Quantifying the Effect of Protuberances and Interfaces from an Aero-Thermal-Structural Design Perspective



William Ivison

Hertford College

University of Oxford

A thesis submitted for the degree of

Doctor of Philosophy

Trinity 2024

Acknowledgements

There are countless people who have contributed in some way to my journey over the last 4+ years, ultimately leading to this single document, but firstly I'd like to thank my two supervisors: Matt McGilvray and Chris Hambidge.

Matt, you've seen me all the way through from my early undergraduate days until now. You encouraged me to undertake this project when I was unsure about my future and since then your guidance has been invaluable. You allowed me to fully explore my work in whatever way I wanted while also making sure I wasn't falling behind.

Chris, I'll miss our weekly StaG do - you've always been 100% invested in whatever problem I might be having and you've indulged my often overly detailed questions. Our long discussions about model design, tunnel operation, data processing, and much more have always left me confident in the way forward.

A big thank you to all the tunnel operators who have had to put up with me during my campaigns, firstly to Harry Kachika and Mailys Buquet, but a special thanks must go to Tristan Crumpton - you made my experiments almost enjoyable, which is a huge achievement.

None of the experimental work in this thesis would have been possible without the technical staff at the Oxford Thermofluids Institute. Dave O'Dell, Leo Verling and Duncan Blake all had to put up with my engineering drawings and manufactured some amazing experimental models. Thanks to Greg King and Andreaa Dabija for their support with all things electronic and for painstakingly hand-painting the thin film gauges. Bill and Hal have always done amazing work actually making the tunnels function properly.

To everyone in the Hypersonics Group - there has always been a helping hand available if needed and I'm grateful for the culture in our group that encourages this. In particular, Luke Doherty, you've always made yourself available and been more than happy to help me when I've asked for advice, even when I'm sure you've always had something more pressing to do.

Andy, it's been a while since our first day at St Hilda's but you've always been there if I need any help and have been a thankful escape from the lab for a coffee or a new lunch spot. Liam, we managed to survive lockdown together - I was always grateful to have a sympathetic ear to moan about work. Jack, you've enabled

my tea break obsession wonderfully over the last couple of years and our treasure hunting escapades have kept me sane. Raggy, your memes always make me laugh and you've looked after me well during experiments. Joe and Alex, I've enjoyed the constant invitations to get a JCT. Simon, we've been on some adventures together, above and below ground, and you've always offered me a place to stay if I'm in town. Seb, I've crashed at your house when I've needed it the most.

My family has been amazingly supportive, especially during the last few months. I have sent many pieces of writing around for proof-reading and I'm grateful to everyone who has had to read anything I've written. So thank you to my mum Frances, my dad David, my step-dad Edward, my brother Thomas, and my sister Katy.

Thank you to Zain and Zara who have helped me proof-read the very final version of this document.

Last but definitely not least, I couldn't have completed this work without the constant love, support, and encouragement of my fiance (and now wife), Sumaiya - you gave me the motivation to finally finish this thesis (and your planning skills are unmatched). We've spent many evenings talking through the problems I've faced with my work, much to your enjoyment I'm sure. This was invaluable in helping me to approach things from different angles and your suggestions for the IR processing are what finally made it all make sense. I look forward to many many more (less stressful) years together.

Thanks to the European Space Agency (ESA) for funding this project (grant no. 4000129548/19/NL/BJ/ig) and to Johan Steelant for advice throughout.

Abstract

Aerodynamic heating of vehicles is a key challenge of hypersonic flight - aircraft experience significant heating when travelling at speeds exceeding Mach 5. Small, unavoidable imperfections are always present on the surface of aircraft in the form of steps, gaps, protuberances, and more complex geometries. These can lead to (i) high levels of localised heat flux augmentation, up to many times the undisturbed level, and (ii) premature boundary layer transition resulting in greater overall heat loads. Designers of vehicles make use of engineering level correlations to account for these effects. However, existing correlations come with large uncertainties and are often lacking in scope, making them not applicable in many cases. This leads to overly conservative vehicle design.

The work presented in this thesis aims to address the need for engineering approaches by collecting high quality experimental heat flux and boundary layer transition data and generating correlations from the results. A sophisticated and highly configurable experimental flat plate model was designed and manufactured which allowed many different surface geometries to be tested by physically raising and lowering two blocks independently of each other. Additionally, the Oxford High Density Tunnel was modified to produce higher total temperature conditions than previously possible to aid in heat transfer measurements. During flat plate experiments, heat flux measurements were taken using IR thermography on, and downstream of, steps, gaps, and 2-dimensional protuberances.

Heat flux augmentations - the ratio of local heat flux with and without a surface geometry - were calculated and a method was developed to produce correlations based on heat flux augmentation, flow parameters, and geometric parameters. In turbulent boundary layers, correlations were developed for seven different heating quantities, each covering a range of geometry types. In laminar boundary layers, a reduced set of geometries was tested and two correlations were developed. Boundary layer transition was also measured, although insufficient data was collected to produce correlations. Various features of interest were observed in the flow downstream of 2-dimensional protuberances using both straight and swept leading edges. Possible mechanisms causing geometry-induced transition are presented.

The newly developed correlations are applicable for use in vehicle design - possibly leading to less conservative design. However, a somewhat limited range of flow conditions was used to generate the correlations. To add more value, a larger dataset could be created with a wider range of flow conditions and geometry scales.

List of Publications

Works published by the author relevant to the thesis

- Ivison, W., Hambidge, C. J., McGilvray, M., Flinton, A., Merrifield, J., Steelant, J.: "Heat Flux Augmentation Caused by Surface Imperfections in Turbulent Boundary Layers". HiSST: 3rd International Conference on High-Speed Vehicle Science & Technology, (2024)

- Flinton, A., Merrifield, J., Ivison, W., McGilvray, M., Jacobs, F., Steelant, J.: "Numerical Study of the Turbulent Phenomena in Hypersonic Boundary Layers from the Presence of Protuberances and Cavities". HiSST: 3rd International Conference on High-Speed Vehicle Science & Technology, (2024)

- Ivison, W., Hambidge, C. J., Doherty, L. J., McGilvray, M.: "Commissioning Ludwieg Mode with Isentropic Compression Heating for the Oxford High Density Tunnel". AIAA SciTech Forum, (2024)

- Ivison, W., Hambidge, C. J., McGilvray, M., Merrifield, J., Steelant, J.: "Experimental Investigation of the Effect of Steps and Gaps on Hypersonic Vehicles". HiSST: 2nd International Conference on High-Speed Vehicle Science & Technology, (2022)

Nomenclature

Acronyms	
BOLT	Boundary Layer Transition Experiment
CFD	Computational fluid dynamics
DNS	Direct numerical simulation
ESA	European Space Agency
FEA	Finite element analysis
HDT	High Density Tunnel
HFA	Heat flux augmentation
IR	Infrared
LICH	Ludwieg tube with isentropic compression heating
MAE	Mean absolute error
MWIR	Mid-wave infrared
NASA	National Aeronautics and Space Administration
PANT	Passive Nosetip Technology Program
PEEK	Polyether ether ketone
PLC	Programmable logic controller
PSD	Power spectral density
RTD	Resistive temperature detector
TFG	Thin film gauge
TPS	Thermal protection system

Latin letters	
a	Correlation constant, speed of sound
A	Area
b	Correlation constant, bluntness
B	IR calibration constant
C	Transmissivity conversion constant, Chapman-Rubesin parameter
C^2	Crocco number
c_f	Friction coefficient
c_p	Specific heat capacity at constant pressure
D	Diameter, boundary layer shape factor
F	IR calibration constant, friction
G	IR calibration constant
h	Enthalpy
H	Height (of step, protuberance, cavity etc.)
k	Thermal conductivity, roughness height
L	Length (of cavity or protuberance)
m	Mass

M	Mach number
Nu	Nusselt number
p	Pressure
Pr	Prandtl number
q	Heat flux
r	Recovery factor
R	IR calibration constant
Re	Reynolds number
S	Cavity shape factor, Reynolds analogy factor
St	Stanton number
t	Time
T	Temperature
u	Velocity
U	IR camera signal
V	Volume
x	Streamwise coordinate
X	Correlation x-axis
y	Wall-normal coordinate
Y	Correlation y-axis
z	Spanwise coordinate

Greek letters	
α	Correlation constant
β	Correlation constant
γ	Ratio of specific heat capacities
δ	Boundary layer thickness
$\delta^\star$	Displacement thickness
ϵ	Emissivity
κ	von Karman Constant
λ	Wavelength
Λ	Leading edge sweep angle
μ	Dynamic viscosity
ρ	Density
σ	Turbulent free layer growth parameter, correlation constant
τ	Shear stress, correlation constant, time constant, transmissivity
θ	Momentum thickness, angle

Subscripts	
0	Total/stagnation condition
1, 2 etc.	Property relating to location in HDT
amb	Ambient
atm	Atmospheric
aw	Adiabatic wall
b	Bluntness
cal	Calibration
D	Detector (of IR camera)
e	Boundary layer edge condition

f	Tunnel fill condition
k	Condition at roughness height
m	Mass
max	Maximum
min	Minimum
o	Condition at plug valve opening
obj	Object
P	Piston
ref	Reference (heat flux or temperature)
$reflect$	Reflected (temperature)
$shot$	During a shot
tr	Compressible transformation
$tran$	Boundary layer transition
w	Wall condition

Contents

List of Figures **xii**

List of Tables **xvii**

1 Introduction **1**
1.1 Motivation . . . 1
1.1.1 Aerodynamic Heating . . . 1
1.1.2 Steps and Gaps . . . 2
1.1.3 Vehicle Design . . . 4
1.2 Research Objectives . . . 7
1.3 Thesis Structure . . . 8

2 Literature Review **10**
2.1 Background . . . 10
2.2 Heat Flux Augmentation . . . 11
2.2.1 Steps . . . 12
2.2.2 Protuberances/Fences . . . 18
2.2.3 Cavities . . . 22
2.2.4 Combined geometries . . . 26
2.2.5 Summary of Heat Flux Augmentation Correlations . . . 27
2.3 Boundary Layer Transition . . . 29
2.3.1 Basics of Boundary Layer Transition . . . 29
2.3.2 Boundary Layer Interaction with Surface Features . . . 31
2.3.3 Correlations for Boundary Layer Transition with Roughness 34
2.4 Summary . . . 40

3 Methodology **42**
3.1 The Oxford High Density Tunnel . . . 42
3.1.1 Ludwieg Mode Operation . . . 44
3.1.2 LICH Mode History . . . 44
3.1.3 LICH Mode Operation . . . 45
3.1.4 LICH Mode Infrastructure . . . 48
3.2 Experimental Model . . . 51

3.2.1 Mechanical Design 52
3.3 Instrumentation 60
3.3.1 Surface Heat Flux Measurements 61
3.3.2 Measurement Uncertainties 72
3.3.3 Surface Pressure Measurements 77
3.3.4 Freestream Characterisation 78
3.3.5 Model Alignment 79
3.3.6 Geometry Height Measurement 80
3.4 Boundary Layer Properties 80
3.4.1 Thickness Parameters 80
3.4.2 Surface Heat Flux 84
3.5 Summary 85

4 LICH Mode Experiments **86**
4.1 Numerical Modelling 87
4.1.1 Model Validation 90
4.1.2 Model Predictions 92
4.2 Experimental Setup 93
4.2.1 Freestream Characterisation 95
4.3 Results from Commissioning Tests 95
4.3.1 Shot Data 95
4.3.2 Performance Maps 96
4.3.3 Freestream Noise 105
4.4 Summary 106

5 Steps and Gaps in Turbulent Boundary Layers **108**
5.1 Test Conditions 109
5.2 Geometries 109
5.3 Heat flux augmentation 110
5.3.1 Camera parallax 112
5.3.2 Camera vibrations 112
5.3.3 Data Extraction 113
5.3.4 Flat plate data 114
5.4 Results 115
5.4.1 Heat Flux Profiles for Basic Geometries 115
5.4.2 Heat Flux Profiles for Combined Geometries 119
5.4.3 Application to Existing Correlations 125
5.4.4 Correlation Development 127
5.5 Summary 135

6 Steps in Laminar Boundary Layers 136
6.1 Measurements of Boundary Layer Transition . . . 137
6.1.1 Heat Flux Data . . . 137
6.1.2 Pressure Fluctuation Data . . . 137
6.2 Natural Flat Plate Transition . . . 140
6.2.1 Effect of Freestream Conditions . . . 140
6.2.2 Effect of Leading Edge Bluntness . . . 144
6.2.3 Effect of Tunnel Blockage . . . 144
6.2.4 Intermittency . . . 148
6.3 Addition of Surface Geometries . . . 150
6.3.1 Effect on Boundary Layer Stability . . . 150
6.3.2 Heat Flux Augmentation . . . 153
6.4 Effect of Swept Leading Edge . . . 156
6.4.1 Flat Plate Transition . . . 157
6.4.2 Addition of Surface Geometries . . . 157
6.4.3 Heat Flux Augmentation . . . 160
6.5 Summary . . . 163

7 Conclusions 164
7.1 Summary of Achievements . . . 164
7.2 Recommendations for Future Work . . . 167

References 170

Appendices

A De-Risk Experiments 184
A.1 Experimental Model . . . 184
A.1.1 Mechanical Design . . . 184
A.1.2 Instrumentation . . . 185
A.2 Experimental Setup . . . 185
A.2.1 Facility . . . 185
A.2.2 Model Configurations . . . 185
A.3 Results . . . 186
A.3.1 Surface Heat Flux . . . 186
A.3.2 Surface Pressure Fluctuations . . . 187

B Deem &Murphy's Method for Estimating Transition 191

List of Figures

1.1 (a) Sample trajectory for antipodean flight of the ESA concept Stratofly vehicle. (b) The ratio of estimated heat loads for the Mach 8 cruise period is also plotted. 4
1.2 Results of blending CFD solutions with transition correlations for calculating the heat load on the HEXAFLY-INT flight model. Adapted from [18]. 6
1.3 An computationally efficient method of accounting for surface imperfections in aircraft design. 7

2.1 Forward- (a) and backward-facing (b) steps and schematics of their respective approximate heat flux profiles. Reproduced from Reference [40]. 13
2.2 Indicative heat flux profiles upstream of forward facing steps in different boundary layers - magnitudes not to scale. Created from data presented by Holloway [42]. 13
2.3 Maximum heating downstream of a backward-facing step, Figure 5 from Jakubowski &Lewis [49]. 17
2.4 Heating rates on a 2D protuberance. Reproduced from Reference [40]. 19
2.5 An engineering approach to predict the location and magnitude of peak heating on surfaces surrounding protuberances. Reproduced from Reference [56]. 21
2.6 Four classifications of cavities, showing their respective flow fields, pressure distributions, and heat flux distributions. Reproduced from Reference [62] 23
2.7 The stepped Shuttle tile setup analysed by Petley et al. [22]. 27
2.8 The different pathways to turbulence, reproduced from Fedorov [82], originally proposed by Morkovin [83]. 30
2.9 A general formulation for transition correlations. Originally printed in [112], reproduced from [114]. 36

3.1 The Oxford High Density Tunnel (HDT). Left: looking upstream from the nozzle. Right: the nozzle and test section 43
3.2 Schematic of HDT showing key infrastructure 43

3.3 Left: oil-filled nylon low temperature piston. Right: anodised aluminium high temperature piston. 50
3.4 CAD image of the downstream end of the HDT barrel, showing the location of the filling plate. 51
3.5 Schematic of the experimental model design, showing how different test geometries can be produced. 52
3.6 Overall dimensions of the flat plate model. 53
3.7 Approximate disturbance areas on the top plate. 54
3.8 Exploded view of the model, showing the subassemblies. 55
3.9 Exploded view of the top plate assembly, showing constituent parts. The swept leading edge is also shown. 56
3.10 Exploded view of the base assembly, showing constituent parts. The configuration for the swept leading edge is also shown. 56
3.11 Exploded view of the test surface and internal assembly, showing constituent parts. The parts labelled 'rear plate' and 'front block' are constructed from PEEK. 57
3.12 The internal parts of the model, colour coded. Red: actuators. Orange: stationary. Blue: horizontal motion. Green: vertical motion. Motion is indicated by arrows on the isometric view. 58
3.13 One of the six manual height adjustment assemblies for the rear plate. 59
3.14 Diagram of the two blunt leading edge modifications. 60
3.15 The experimental model with instrumentation indicated. All dimensions are in mm, with 0 mm being the leading edge. 61
3.16 Calibration curve for a single pixel. 64
3.17 Total transmissivity for the calibration system applied to Planck's Law. Transmittance wavebands for the two IR lenses are shown. . . 66
3.18 Points adjusted by the image transformation. 67
3.19 Construction of the thin film gauge arrays. 68
3.20 Calibration data for a single thin film gauge. 70
3.21 Absolute error of calibrator set-points for a single pixel. 73
3.22 Mean absolute error for a full calibrated frame. 74
3.23 Comparison of thin film gauge data with IR data with uncertainties plotted. 74
3.24 Uncertainty in Mach number for the duration of a shot. 76
3.25 Uncertainty in temperature change for the duration of a shot. . . . 76
3.26 Uncertainty in heat flux for the duration of a shot. 77
3.27 Uncertainty in Stanton number for the duration of a shot. 77
3.28 The twin freestream measurement probe. 79
3.29 The model alignment probe. 80

3.30 Calibration of the linear potentiometers used for block height measurement. 81

4.1 Ludwieg mode shot freestream total pressure and temperature compared with results from the ODE model. 91
4.2 Barrel pressure and freestream total pressure for a cold LICH mode shot compared with ODE model results. 92
4.3 Results from the ODE model for Condition A. Pressure, temperature and mass for all tunnel sections and piston dynamics plotted against time. 94
4.4 Freestream total pressure, temperature, and Re_{unit} of a shot compared with results from the ODE model, both at Condition A. 97
4.5 Map of mean total temperature for the full range of barrel fill temperatures and pressure ratios. 98
4.6 Map of final piston temperature for the full range of barrel fill temperatures and pressure ratios. 99
4.7 Map of Re_{unit} for the full range of mean total temperatures and plug valve opening pressures. 100
4.8 Map of total shot duration for the full range of barrel fill temperatures and pressure ratios. 101
4.9 Map of shot duration for the range of T_4 and Re_{unit} possible using $T_{3,f} = 550\mathrm{K}$. 102
4.10 Map of shot duration for the range of T_4 and Re_{unit} possible using $T_{3,f} = 500\mathrm{K}$. 102
4.11 Map of shot duration for the range of T_4 and Re_{unit} possible using $T_{3,f} = 400\mathrm{K}$. 103
4.12 Map of shot duration for the range of T_4 and Re_{unit} possible using $T_{3,f} = 300\mathrm{K}$. 103
4.13 Full operating range of HDT in LICH mode at Mach 7. Four barrel fill temperatures are shown. The upper limit of Ludwieg mode is shown. 104
4.14 HDT freestream noise compared with other similar facilities: TUSQ [171], VKI H3 [172], HLB [173], BAM6QT [174], and AEDC Tunnel No. 9 [175]. Reproduced from Birch et al [171]. 106

5.1 Range of geometries tested showing heights of the fence and step blocks relative to boundary layer thickness. 111
5.2 Schematic showing H_1 and H_2 for a DU_+ stepped-cavity geometry. 111
5.3 Diagram showing how camera parallax is accounted for with fences. 112
5.4 Diagram showing how camera parallax is accounted for with cavities. 113

5.5 A sample frame from a fence test with the 'centreline' pixels outlined. 114
5.6 Flat plate baseline heat flux with a straight line fitted. 115
5.7 Heat flux augmentation on forward-facing steps. 117
5.8 Heat flux augmentation on backward-facing steps. 117
5.9 Heat flux augmentation on fences. 119
5.10 Heat flux augmentation on cavities. 120
5.11 Heat flux augmentation on double forward-facing steps compared with a single forward-facing step. 121
5.12 Heat flux augmentation on double backward-facing steps compared with a single backward-facing step. 122
5.13 Heat flux augmentation on 1 mm height fences with different rear plate heights. 123
5.14 Heat flux augmentation on 1 mm drop heights following different upstream fence heights. 123
5.15 Heat flux augmentation on forward-facing steps with upstream cavities of different depths. 124
5.16 Heat flux augmentation on backward-facing steps with downstream cavities of different depths. 125
5.17 Heat flux augmentation on prominent forward-facing steps. Re_{unit} = 18.5 - 25.5 million/m. Correlations from Nestler [44] and Hung &Patel [45] are also plotted. 126
5.18 Minimum separation heating using Lamb's correlation [54]. 127
5.19 Data applied to correlations for average cavity floor heating. 129
5.20 Correlations following Equations 5.4, 5.7, and 5.8. 134

6.1 Flat plate heat flux data for a shot at M = 7, Re_{unit} = 25.2 million/m. IR and TFG data is compared with Eckert's heat flux correlations. 138
6.2 PCB power spectral densities of all PCB sensors for the same shot as Figure 6.1. 139
6.3 PCB power spectral densities of all PCB sensors for the same shot as Figure 6.1, plotted in a 3D plot with x location as the third axis. 139
6.4 PCB power spectral densities of PCB 3 for subsequent steady flow periods in the same shot as Figure 6.1. 140
6.5 Natural transition Reynolds number vs unit Reynolds number. Plotted with flat plate transition correlations from Simeonides [179], Charbonnier [110] (Mach 6 only), and Deem &Murphy [180]. 142
6.6 Natural transition distance vs unit Reynolds number. Plotted with flat plate transition correlations from Simeonides [179], Charbonnier [110] (Mach 6 only), and Deem &Murphy [180]. 143
6.7 Transition length ratio for the data plotted in Figures 6.5 and 6.6. . 143

6.8 Transition location, x_{tran}, vs leading edge thickness (diameter), b, at a freestream condition of M = 7, Re_{unit} = 25.2 million/m. Data is compared with correlations from Simeonides [179] and Deem &Murphy [180]. 145
6.9 FEA setup, showing the CAD of the model (a &b), the pressure loads applied (c), and an example of the (scaled) overall deformation (d). 146
6.10 Results from FEA for effective angle of attack of the plate against freestream stagnation pressure when using the slim stand. 147
6.11 Flat plate Stanton number data comparing the original model with the slimmed blockage-reducing configuration. Freestream condition: M = 7, Re_{unit} = 11.7 million/m. 148
6.12 Heat flux maps for different fence heights, straight leading edge, b = 100 µm, M = 7, Re_{unit} = 15.8 million/m. 151
6.13 Heat flux profiles along the lines shown in Figure 6.12. 152
6.14 Heat flux augmentation profile for a fence in a laminar boundary layer, M = 7, Re_{unit} = 15.8 million/m. 154
6.15 Minimum separation heating correlation according to Equation 6.4 . 155
6.16 Peak step heating correlation according to Equation 5.8 156
6.17 Direction of the sweep angle of the leading edge. 156
6.18 H/δ in the spanwise direction for the 1.67 and 3.3 mm fence heights on the swept leading edge. 158
6.19 Heat flux maps for different fence heights, swept leading edge, b = 100 µm, M = 7, Re_{unit} = 15.8 million/m. 160
6.20 Heat flux profiles along the lines shown in Figure 6.19. 161
6.21 Heat flux augmentation comparing swept and straight leading edges for peak heating on a step. 162

A.1 Exploded view of the de-risk model. 184
A.2 Stanton number vs Reynolds number plots for all the geometries tested, compared to laminar and turbulent flat plate correlations. The location of the step/cavity is shown at the bottom of each plot. 188
A.3 Power spectra of surface pressure fluctuations for different geometries. 190

B.1 Effect of leading edge bluntness, b, on transition Reynolds number, Re_{tran}. 191

List of Tables

2.1 Summary of the literature containing heat flux correlations covered in this section. 28

3.1 Overview of some parameters associated with each IR lens. 62
3.2 Details of thin film arrays used on the model. 67
3.3 Thermal products of test materials. 71
3.4 Stanton number uncertainty with contributions from other quantities. 75

4.1 ODE model initial conditions 90
4.2 Tunnel setup for Condition A 92
4.3 Freestream properties of LICH mode Condition A 95

5.1 A summary of the test conditions used for testing in turbulent boundary layers. 109
5.2 Categorisation of different geometries 110
5.3 Constants for average open cavity floor bump factor, taken from Everhart [67]. 128
5.4 Constants for average cavity floor HFA using the modified correlation in Equation 5.4. 130
5.5 Constants for Equation 5.4 133

6.1 Maximum permissible operating pressures when using the slim model stand. 147
6.2 Constants for Equation 6.4 155

A.1 A summary of the test conditions used for testing in turbulent boundary layers. 185
A.2 Range of geometries tested 186

1 Introduction

Contents

1.1 Motivation 1
1.1.1 Aerodynamic Heating 1
1.1.2 Steps and Gaps 2
1.1.3 Vehicle Design 4
1.2 Research Objectives 7
1.3 Thesis Structure 8

1.1 Motivation

1.1.1 Aerodynamic Heating

One of the key challenges to overcome in the pursuit of sustained hypersonic flight is that of aerodynamic heating. At hypersonic speeds, the temperatures attained by gases as they decelerate in the boundary layer are high enough to be a major consideration in the vehicle design process. For example, during its second flight, the experimental vehicle X-43 experienced temperatures on its smooth upper surface of ∼200 - 500 °C for flight Mach numbers of 5 - 7 respectively [1, 2]. At these temperatures, conventional airframe manufacturing techniques become obsolete, with aircraft design requiring the integration of complex thermal management systems to account for structural and thermal loads of similar orders of magnitude.

Calculations by Tauber et al. [3] show that for a nominal "transatmospheric vehicle" (which travels both in the atmosphere and in space), the heat load experienced on ascent would be approximately an order of magnitude greater than that experienced by NASA's Space Shuttle on re-entry. This is mainly due to the duration of sustained hypersonic flight required to accelerate the vehicle to an orbital velocity. Given that the relative mass of the Shuttle's thermal protection system (TPS) was around 11% [4], this implies that for hypersonic cruise vehicles with long flight durations, thermal management and protection systems may make up the majority of the mass of a vehicle.

1.1.2 Steps and Gaps

Although vehicles are designed with smooth bodies and surfaces, in reality they feature steps, gaps, protuberances, cavities, and other surface imperfections. The majority of these features are unavoidable and are, in many cases, intentional and necessary for the function of the aircraft. Examples of such surface features include: gaps between thermal protection system (TPS) tiles on the Space Shuttle to allow for thermal expansion; a backward-facing step at the interface between the nose and the fuselage of the X-15; circular cavities in the heat shields of the Apollo and Orion re-entry capsules for structural supports during take-off. Protuberances can appear in the form of rivets and surface mounted instrumentation. Examples of unintentional geometries include steps between panels caused by manufacturing tolerances or cavities caused by impacts with other objects.

Heat flux augmentation

Steps and gaps have affected hypersonic vehicles since their inception in the early 1960s - the experimental aircraft X-15, which was the first example of hypersonic cruise flight, displayed damage resulting from a gap on the leading edge of one of the wings. The gap, which was present to allow for thermal expansion, caused higher than expected heating in its vicinity resulting in buckling of an adjacent panel. [5]

For re-entry vehicles with ablative heat shields, increased levels of heat flux can accelerate ablation in small areas, leading to an uneven shape change of the heat shield. This could affect the aerodynamics and stability of the aircraft or cause more heat flux augmentation in a positive feedback loop. For example, on the Apollo capsule, heat fluxes near heat shield cavities were up to 6 times greater than on smooth sections. [6] Ablator recession rates from flight tests of simulated cavities were found to be greater than the baseline rate in several places. [7]

Boundary layer transition

In addition to localised heating, imperfections on the surface of an aircraft can also promote early transition from a laminar to a turbulent boundary layer. The exact mechanisms involved are complex and heavily depend on the size and shape of the imperfection. The X-15 also experienced induced transition, with the boundary layer on the majority of the fuselage being turbulent due to a step at an interface on the nose. [8]

Velocity gradients near the wall are much greater in turbulent boundary layers than in laminar boundary layers. This results in steeper temperature gradients and greater heat flux to the surface. The magnitude of this difference is significant. ESA's Stratofly concept vehicle can be taken as an example, which has a nominal trajectory containing a prolonged hypersonic cruise phase shown in Figure 1.1a [9]. Also presented, in Figure 1.1b, is the ratio of the integrated heat load during the Mach 8 cruise period if the boundary layer transitions (plotted as a percentage of the body length) to the heat load of a fully laminar boundary layer. Heat loads were calculated using skin temperatures from Scigliano [10] and Eckert's flat plate heat flux correlations [11]. The difference that an early transition location has on the heat load is striking, with a heat load up to ~ 9 times the fully laminar heat load when transition occurs near the front of the vehicle (such as with the X-15).

Higher heat loads require more thermal management and result in a more substantial TPS being necessary. The TPS of a hypersonic vehicle typically makes up a significant portion of the total mass of the vehicle, meaning that the heat load

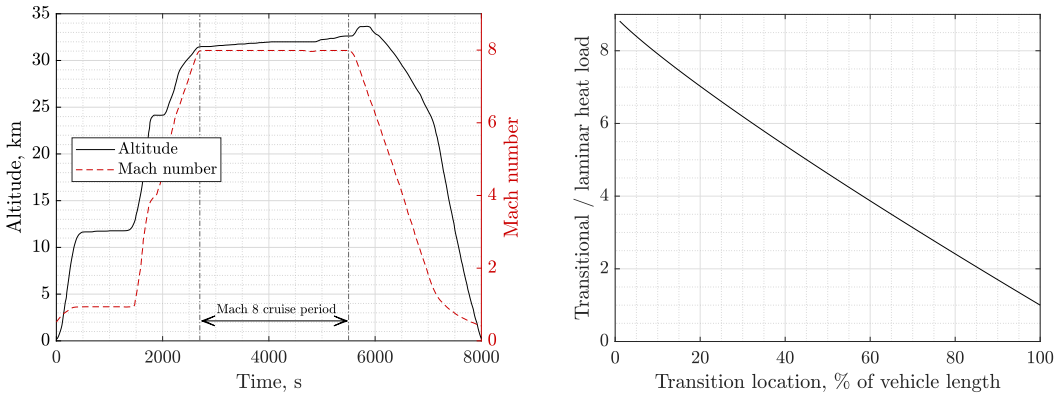

(a) Sample Stratofly trajectory. **(b)** Ratio of transitional and laminar heat loads.

Figure 1.1: (a) Sample trajectory for antipodean flight of the ESA concept Stratofly vehicle. (b) The ratio of estimated heat loads for the Mach 8 cruise period is also plotted.

of an aircraft can have a large impact on its weight. For this reason, one of the outputs from the U.S. National Aerospace Plane (NASP) Program was a general requirement for a deeper understanding of boundary layer transition: [12]

> "The largest uncertainty is the location of the point of transition from laminar to turbulent flow. Estimates range from 20% to 80% along the body span... The assumption made for the point of transition can affect the design vehicle gross take off weight by a factor of two or more."

Given the scale of the potential effects caused by imperfections on the surface of hypersonic aircraft, it is important to account for them during the vehicle design process.

1.1.3 Vehicle Design

Quantifying the effects caused by surface imperfections is difficult due to the complex, and as yet not fully understood, mechanisms behind both localised heat flux augmentations and their impact on boundary layer stability. Due to this, the process of designing hypersonic vehicles historically involved significant amounts of experimental testing, empirically derived approximate rules of thumb, and very conservative estimates. This process results in inefficient design, particularly of thermal protection systems where large factors of safety are included to account for the approximate nature of the correlations used.

In more recent decades, computational fluid dynamics (CFD) has become the tool of choice for aircraft design. Using computational methods allows for rapid changes to vehicle designs to be tested easily. However, one aspect in which computational methods struggle is the addition of small scale geometries to surfaces. The vastly different scales between the vehicle and the surface geometries creates difficulties in producing good quality meshes for simulations. Additionally, including very small elements in the mesh would increase the Courant number for the simulation, proportional to the element size, resulting in significantly increased computation time. This means that, as with historic design methods, correlations remain a useful tool in the design process. In fact, the need for engineering level correlations has consistently been highlighted in design studies. Findings from the Shuttle return-to-flight work in 2006 following the Columbia disaster [13] as well as from ESA's LAPCAT-II program in 2015 [14] indentified that engineering level correlations were an important part of the vehicle design process. As recently as 2022, a key outcome from the Boundary Layer Transition Workshop at the HiSST 2022 conference was the following: [15]

> "During the preliminary and critical design of flight experiments and flight vehicles, engineering approaches are needed, to guarantee or to assess: ... Minimum roughness and/or step/gap/junction requirements to assure an aerodynamically smooth vehicle along its trajectory."

This quote specifically refers to boundary layer transition. However, there is an equal need for similar approaches for estimating heat flux augmentations.

Correlations can be used directly in conjunction with numerical simulations. An approach proposed by researchers at ESA [16, 17, 18] is to perform CFD simulations of the smooth body vehicle for both fully laminar and fully turbulent boundary layers. Local flow and boundary layer properties can be used, along with geometric properties of a proposed surface imperfection, as inputs to engineering level correlations. The outputs of the correlations can estimate both hot spots caused by heat flux augmentation and the effect on the state of the boundary layer. These results can then be blended with the original smooth body solutions to create

a complete vehicle solution. Jacobs & Steelant [18] demonstrated this procedure on the HEXAFLY-INT flight test geometry, shown in Figure 1.2, where the blended solution is made up of either fully laminar or turbulent results, or a proportional amount of each solution in regions where the boundary layer is transitioning. In this example, a blended solution for integrated heat load has been calculated using laminar and turbulent CFD solutions along with correlations for natural transition.

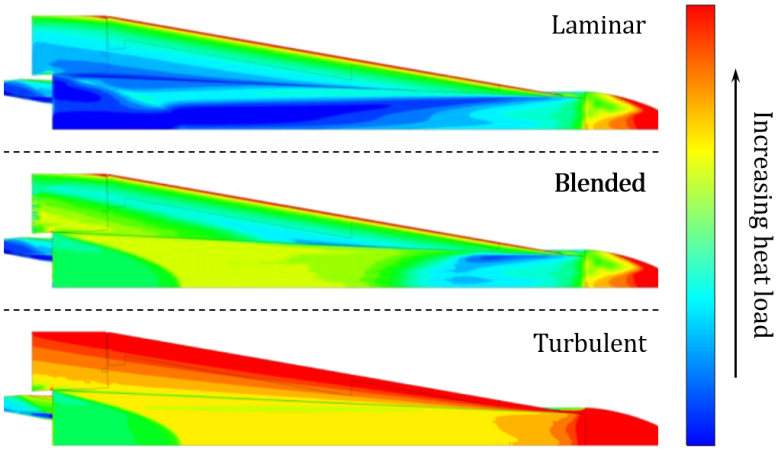

Figure 1.2: Results of blending CFD solutions with transition correlations for calculating the heat load on the HEXAFLY-INT flight model. Adapted from [18].

This approach, presented as a flow diagram in Figure 1.3, is computationally economical as it requires relatively few large scale CFD simulations. Design iterations (of surface features) can be trialled with ease by altering inputs to computationally simple correlations, rather than requiring the entire vehicle to be re-meshed. However, given the magnitude of the effects that surface imperfections can have, the overall result from this approach can be sensitive to the quality of the correlations used. Using robust correlations derived from high quality experimental data will reduce the overall uncertainty of the final result and therefore reduce uncertainty and give confidence to any design decisions made. The overall aim of this type of process would typically be to calculate the maximum permissible sizes of surface features which can then be used to inform any tolerancing during manufacture.

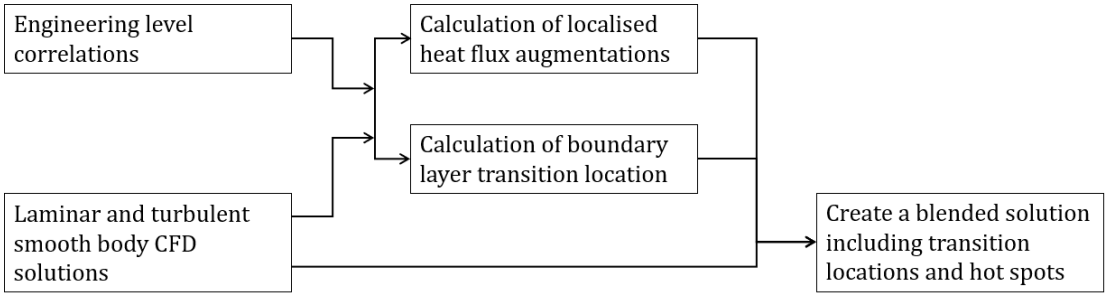

Figure 1.3: An computationally efficient method of accounting for surface imperfections in aircraft design.

1.2 Research Objectives

1 To develop a testbed for introducing steps, gaps, and protuberances to hypersonic flow

An experimental model capable of producing a variety of different surface geometries will aid in further understanding their effects. The model should be highly configurable to allow for rapid changes between different geometries. This will ensure that a wide range of geometry types and scales can be tested. Heat transfer instrumentation in the vicinity and further downstream of the test geometry will allow localised heat flux augmentation and boundary layer stability effects to be measured.

2 To create a unified approach to modelling heat flux augmentation caused by deviations from a smooth body.

There is no single correlation available which describes heat flux augmentation caused by surface geometries. The creation of an adaptable, unified model based on high quality experimental data will allow for easy integration into vehicle design processes. This can be tested against existing correlations for verification.

3 To create a unified approach to modelling boundary layer transition caused by deviations from a smooth body.

There are existing empirical methods which attempt to model roughness induced boundary layer transition. However, these are sometimes contradictory. Using a similar unified method as that used in Objective 2, an attempt will be made to correlate experimental boundary layer transition data.

4 To further develop the hypersonic heat transfer test capability in the UK

Heat transfer instrumentation often suffers from low signal to noise ratios. Increasing the total temperature of the freestream flow can help to improve this. An economical method of increasing the total temperature of Ludwieg tunnels will be explored for implementation on the Oxford High Density Tunnel (HDT). The objective of this is to increase quality of heat transfer data for lower uncertainties in correlation development.

1.3 Thesis Structure

This work consists of the following chapters:

Chapter 2: Literature Review

A review of the relevant literature on the subject of surface imperfections in high speed flows. The literature reviewed covers both heat flux augmentation and boundary layer transition. In each case, the effects are explored for basic geometry types (step, gap, etc.) and relevant correlations are presented. Some key gaps in the literature are then highlighted.

Chapter 3: Methodology

A description of the equipment and methods used during the research. The experimental facility and its operation are described as well as modifications made to extend the total temperature capability. The test model design is presented along with a description of the various instrumentation used, with their respective

data reduction and processing methods. Finally, boundary layer calculations used in the subsequent chapters are presented.

Chapter 4: LICH Mode Experiments

A description of the commissioning process for a new mode operation for the Oxford High Density Tunnel (HDT). Data from experiments carried out in the commissioning process is presented along with estimated performance maps based on a tuned numerical model. The freestream noise level is compared with other similar facilities worldwide.

Chapter 5: Steps and Gaps in Turbulent Boundary Layers

Results of experiments investigating the interaction between surface imperfections and turbulent boundary layers. Heat flux augmentation data for a large number of different 2-dimensional geometries is presented. Various heat flux quantities are then correlated with flow and geometric parameters using an approach which was newly adapted from an existing cavity heating correlation.

Chapter 6: Steps in Laminar Boundary Layers

A discussion of some of the factors which influence natural boundary layer transition, with supporting experimental data, finding that the model configuration did not allow for geometry induced transition experiments to be performed successfully. Flow fields downstream of 2-dimensional protuberances are presented with several features of interest being observed. Heat flux augmentation correlations for a limited range of heating quantities are developed using the same method as that used in Chapter 5. Finally, the effect of leading edge sweep angle is also explored.

Appendix A: De-Risk Experiments

This Appendix describes de-risk experiments which were performed prior to the experimental work carried out in the main body of the thesis. Some preliminary data was collected and is presented in isolation in this Appendix but was not included in the main analysis.

2
Literature Review

Contents

2.1 Background 10
2.2 Heat Flux Augmentation 11
2.2.1 Steps 12
2.2.2 Protuberances/Fences 18
2.2.3 Cavities 22
2.2.4 Combined geometries 26
2.2.5 Summary of Heat Flux Augmentation Correlations . . . 27
2.3 Boundary Layer Transition 29
2.3.1 Basics of Boundary Layer Transition 29
2.3.2 Boundary Layer Interaction with Surface Features . . . 31
2.3.3 Correlations for Boundary Layer Transition with Roughness 34
2.4 Summary 40

2.1 Background

During the development of the Apollo program, experimental work was carried out using scale models of the re-entry capsule to test how external components affected local heat fluxes [6] and heat shield ablation rates [7]. Heat flux augmentation factors (i.e. heat flux levels compared with the equivalent smooth body) of up to 6 were found in some locations, highlighting the potential of surface imperfections to cause problems in vehicle design. The Space Shuttle featured a thermal protection system

(TPS) made of up of tiles rather than an ablative shield. To account for thermal expansion during re-entry, the tiles were mounted with gaps which were large enough to cause disturbances in the boundary layer. A range of studies was carried out looking into the increased local heating rates both on the corners of the tiles and on the underlying surface [19, 20, 21, 22, 23] as well as boundary layer transition caused by imperfections on the TPS [24, 25, 26]. After the Columbia disaster in 2003, which was ultimately caused by a large gap in the TPS on the leading edge of one of the wings of the Shuttle, additional research was carried out to further understand the heating caused by cavities due to impact damage [13, 27, 28]. In the final years of Space Shuttle flight, work was carried out in developing an infrared imaging system to view the heatshield during re-entry [29]. This was used to assess boundary layer transition caused by roughness elements present due to TPS tiles [30].

The recent development of the Orion capsule has once again created interest in cavities on ablative heat shields, with studies looking into boundary layer transition [31, 32] and heat flux augmentation [33] in the vicinity of the cavities.

In addition to the work on isolated surface imperfections, there have been many studies looking into the holistic impact that these imperfections have on the aerodynamic performance of vehicles: in particular, the experimental aircraft X-33 [34], X-43 [35], and HEXAFLY-INT [36], and the ESA concept vehicle LAPCAT-II [37].

Imperfections on the surface of hypersonic vehicles have two main effects: a change in the heat flux in the vicinity of the imperfection; and the introduction of, or interaction with instabilities in the boundary layer, leading to premature boundary layer transition. This chapter aims to review the relevant literature on each of these subjects.

2.2 Heat Flux Augmentation

There has been a huge amount of work carried out looking into the effect that isolated surface roughnesses have on local heating in compressible boundary layers. Two review papers, one by Fletcher in two parts [38, 39] and one by Nestler [40],

cover the majority of the historical work on this topic. However, given the scale of these papers (283 and 81 references in each, respectively) only key findings will be discussed here alongside selected works which are most relevant. These selected works correspond to periods of renewed interest caused by, for example, increased activity in spaceflight, advances in spacecraft design, or accident investigations.

Compared to these, where the tested geometries were typically representative of real flight geometries (e.g. actual Shuttle TPS tiles, or realistic models), the majority of the literature focusses on simplified geometries that can be more applicable to a range of idealised flight geometries. These geometries are typically categorised in one of the following ways:

- Steps (forward and backward facing)
- Protuberances/fences
- Cavities (open, closed, transitional, and gaps)

For each of these categories, the key literature will be presented, along with the expected flow field and heat flux in the vicinity of the geometry and any existing correlations for localised heating. At the end of Section 2.2 the key papers discussed are summarised in Table 2.1.

2.2.1 Steps

Steps are single, sudden changes in the height of a surface and can be either forward facing, where the flow sees an upwards change, or backward facing, where the flow sees a downward change. Steps appear on aircraft when adjoining panels or TPS tiles are mounted at differing heights [22, 41]. Figure 2.1 shows the two configurations of a step geometry and heat flux profiles in turbulent boundary layers.

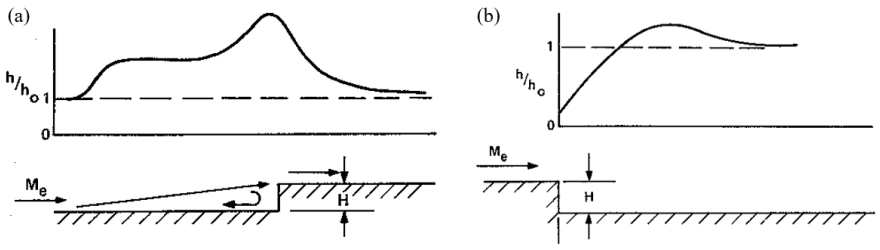

Figure 2.1: Forward- (a) and backward-facing (b) steps and schematics of their respective approximate heat flux profiles. Reproduced from Reference [40].

Forward facing steps

Upstream of a forward-facing step, the flow is diverted upwards and forms a separation bubble. The heat flux upstream of a step depends on whether the incoming boundary layer is laminar or turbulent [42]. In laminar boundary layers, the surface heat flux in the separation bubble decreases compared to the flat plate level before rising rapidly just upstream of the step. However, in turbulent boundary layers, the heat flux increases to a steady plateau in the separation and rises at the step location. In boundary layers which are transitioning between laminar and turbulent at the step location, both phenomena occur: the heat flux decreases initially then briefly increases to a steady level before rising at the step. All three cases are illustrated in Figure 2.2.

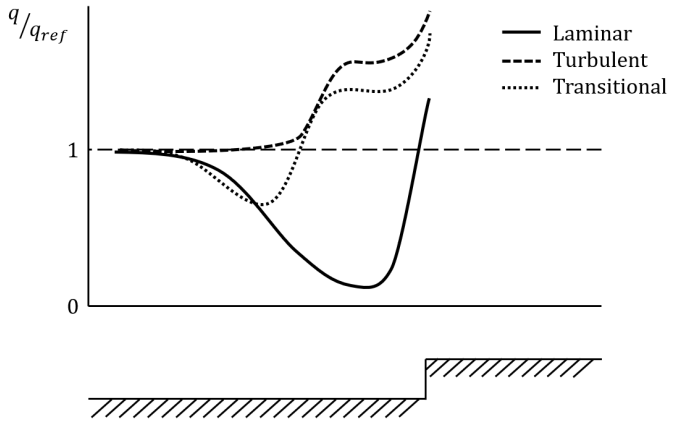

Figure 2.2: Indicative heat flux profiles upstream of forward facing steps in different boundary layers - magnitudes not to scale. Created from data presented by Holloway [42].

In turbulent boundary layers, Zukoski [43] showed experimentally that the size of an upstream separation is independent of Mach number ($M = 1.5 - 6$), giving

$x_s/H = 4.1$, the ratio of separation length and step height, as a constant.

Nestler [44] produced a simple correlation for peak heat transfer just upstream of forward-facing steps larger than the boundary layer as a function of only edge Mach number, M_e, with Mach numbers ranging from 2 - 8.5.

$$\frac{q_{max}}{q_{ref}} = \left(1 + \frac{\gamma}{2} c_p M_e^2\right)^{0.8} \tag{2.1}$$

Where q_{max}/q_{ref} is the ratio of the maximum heat flux on the upstream edge of the step and the reference flat plate heat flux at that position; c_p is the "oblique shock coefficient" which relates the flow turning angle α to the shock angle θ and is given by Equation 2.2; and M_e is the Mach number at the boundary layer edge.

$$c_p = 2/\left(\frac{\cot\alpha}{\tan\theta} + 1\right) \tag{2.2}$$

The correlation fits the relatively few experimental data points reasonably well and is very simple to use. However, the correlation is based on steps that are larger than the local boundary layer thickness. Given that surface imperfections smaller than the boundary layer have the ability to create flow disturbances [32], vehicle design is unlikely to include intentional steps larger than the boundary layer, where possible.

Hung & Patel [45] carried out a large experimental parametric study looking into heating around protuberances in laminar and turbulent Mach 5.3 flow. They generated a number of correlations to describe heating in front of protuberances (see Section 2.2.2), including for wide 2-dimensional protuberances with high ratios of width to height. The heating upstream of wide 2-dimensional protuberances is the same as that on a forward-facing step. Equations 2.3a and 2.3b are correlations for maximum heating upstream of forward-facing steps in laminar and turbulent boundary layers, respectively.

$$\frac{q_{max}}{q_{ref}} = 1.4\left(\frac{H}{\delta}\right)^{1.2} \quad \text{(laminar)} \tag{2.3a}$$

$$\frac{q_{max}}{q_{ref}} = 3.6\left(\frac{H}{\delta}\right)^{0.327} \quad \text{(turbulent)} \tag{2.3b}$$

Where δ is the boundary layer thickness at the location of the step in undisturbed flow. Comparing correlations from Nestler (Equation 2.1)and Hung & Patel (Equation 2.3), which describe the same heating quantity for the same geometries, it is easy to see how correlations can be developed to fit a given dataset without being more generally applicable. Nestler used data for a range of Mach numbers but only for steps much larger than the boundary layer thickness, and determined that heating was only dependent on Mach number. On the other hand, Hung & Patel collected data for a wide range of step heights and showed that heating is dependent on height, but their correlation is only applicable to Mach 5.3 flow.

Backward facing steps

Downstream of a backward-facing step, the flow separates immediately, causing a drop in heat flux. Depending on the step height, the heat flux will either recover to the flat plate level gradually, for smaller steps, or overshoot at the reattachment point and cause a hotspot, for larger steps.

Rom & Seginer [46] proposed, based on flat plate experiments in a shock tunnel at Mach numbers in the range 1.5 - 2.5, that the behaviour of the heat flux profile in the separation behind a backward-facing step in a laminar boundary layer depends solely on the ratio $x/H\mathrm{Re}_x^{1/2}$, which is approximately proportional to the ratio δ/H. They gave a limiting value of $x/H\mathrm{Re}_x^{1/2} = 0.067$, above which the step is small compared to the boundary layer and the heat flux gradually increases back to the flat plate level during flow reattachment. For $x/H\mathrm{Re}_x^{1/2} < 0.067$, a sharp peak in heat flux, greater than the flat plate level, is produced at reattachment. At the largest step height they tested, this peak was ~ 7 times the undisturbed level. Correlations for heat flux in the separation were also developed based on this parameter, given in Equation 2.4.

$$\frac{q}{q_{ref}} = A\left(H\mathrm{Re}_x^{1/2}/x\right)^n \tag{2.4}$$

The constants A and n are different depending on the regime and the location of the heat flux in question. For the average heat flux in the separated region for small

steps ($x/H\mathrm{Re}_x^{1/2} > 0.067$), $A = 0.125$ and $n = 0.8$. For average heat flux behind larger steps ($x/H\mathrm{Re}_x^{1/2} < 0.067$), $A = 0.02$ and $n = 1.3$. Finally, for the peak heat flux at the reattachment point behind larger steps, $A = 0.0465$ and $n = 1.3$.

Further testing by Rom et al. [47], which involved a wider range of test models with separation, including axisymmetric backward-facing steps, found an inverse relation between the peak heat flux at reattachment behind large steps and the distance of this peak, and therefore the reattachment location, from the step.

Wada & Inoue [48] performed similar experiments at a Mach number of 10 and found the limiting value of $x/H\mathrm{Re}_x^{1/2}$ to be ~ 0.03 rather than 0.067. This difference was likely due to the large difference in Mach numbers between experiments.

Jakubowski & Lewis [49] performed experiments with backward-facing steps in Mach 4 laminar flow with and without suction from behind the step. In no-suction cases (i.e. comparable to the work listed above), no overshoot in heat flux was seen in the reattachment region. The maximum heat flux augmentation downstream of a step was plotted against the Reynolds number based on step height alongside data from Rom & Seginer [46], Smith [50], and Holloway et al. [42]. This plot is reproduced in Figure 2.3 and shows a decrease in maximum heat flux for mid-level Reynolds numbers. An overshoot doesn't appear until much higher Reynolds numbers. The data from Rom & Seginer does not follow the general trend shown by the other data, which was justified by saying that their data was collected using a small model in a shock tube. The relation appears to be independent of Mach number, with data points from Holloway ($M = 6$)and Smith ($M = 2.5, 3.5$) following the same trend for larger Reynolds numbers.

Gai et al. [51] performed experimental testing on backward-facing steps in high enthalpy laminar hypersonic flow. Their results also found that the overall heating trend was heavily dependent on the ratio between the boundary layer thickness, δ, and step height, H. Although, even with large step heights, the heat flux was never found to produce an overshoot at reattachment. This difference in behaviour was postulated to be due to the difference in flow enthalpies between the studies. Gai et al. [52] later performed further experiments on a similar test article and again

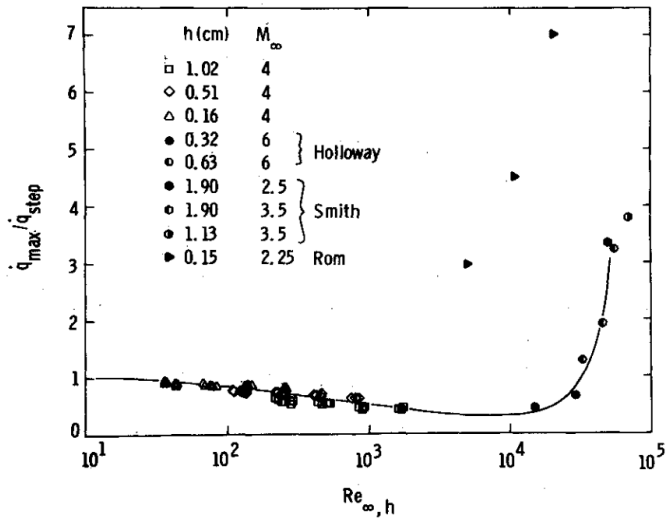

Figure 2.3: Maximum heating downstream of a backward-facing step, Figure 5 from Jakubowski & Lewis [49].

found that there was no overshoot in heat flux present at the reattachment location, even with significant step heights. They found that the downstream heat flux level depended on the flow enthalpy, with higher enthalpies recovering closer to the flat plate heat flux level while lower enthalpies settling at a lower value. Similar high enthalpy experiments were carried out by Redeppa et al. [53]. Once again, the result of no overshoot at reattached was proposed to be because of the high flow enthalpy.

There has been a significant amount of work investigating backward facing steps. However, as with much work on separated flows, there is still much uncertainty in the behaviour of the flow reattachment. Thus, there is no instance of a derived or fitted equation which is able to predict whether an overshoot in heat flux will occur at the reattachment.

There are, however, correlations available to describe the minimum heat flux in the separation behind a backward-facing step. Lamb [54] performed experiments on cylinders in crossflow to assess the separation behind them but also collected historical data for backward-facing steps. Two correlations were generated for the minimum heat flux in the separation behind backward-facing steps: one for laminar incoming boundary layers and one for turbulent boundary layers. These are given in Equations 2.5 & 2.6, respectively:

$$\frac{q_{min}}{q_{ref}} = \begin{cases} 0.1, & D\left(\frac{T_0}{T}\right)_1^{0.3} < 0.45 \\ 0.5\left[D\left(\frac{T_0}{T}\right)_1^{0.3}\right]^2, & 0.45 < D\left(\frac{T_0}{T}\right)_1^{0.3} \end{cases} \tag{2.5}$$

$$\frac{q_{min}}{q_{ref}} = 0.2 \ln\left[45.4 D\left(\frac{T}{T_0}\right)_1\right] \tag{2.6}$$

Where the geometric term, D, is defined by Equation 2.7. It is formulated in this way so that it ranges between 0, for very large step heights, and 1, for very small step heights.

$$D = \frac{\delta_1}{\delta_1 + H} \tag{2.7}$$

The subscript 1 refers to the location of the step, so δ_1 is the boundary layer thickness on a flat plate at the same axial position as the step. The temperature ratio was included to account for different Mach numbers.

In laminar boundary layers, for combinations of larger steps and lower temperature ratios (lower Mach numbers), the minimum heat flux augmentation settles at 0.1. In the case of turbulent boundary layers, there is no apparent minimum, with the lowest data point being $\sim$ 0.04.

2.2.2 Protuberances/Fences

Protuberances consist of isolated protrusions from a surface. They can be in the form of simple shapes like cylinders or rectangular sections or more complex and more representative geometries. In two dimensions, a protuberance is a strip with a constant section, otherwise known as a fence, and in its simplest form a forward facing step directly followed by a backward facing step.

Comparatively little generalised work exists for heat flux on protuberances, likely due to the more specific nature of the geometries. The majority of historical heat transfer work in this area focuses on cylindrical posts protruding from a surface, with Nestler [40] listing a number of this type of study.

For simple 2D protuberances, the upstream heating is identical to that of forward-facing steps. While the downstream heating is more complex than that of backward-facing steps due to the additional upstream separation. Figure 2.4 shows, schematically, the flow over a 2D protuberance.

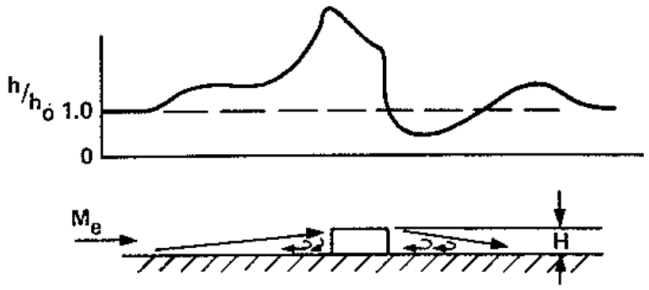

Figure 2.4: Heating rates on a 2D protuberance. Reproduced from Reference [40].

Work on protuberances typically focuses on heating in the vicinity of the protuberance rather than on it. Kumar [55] argues that in most situations the feature creating the protuberance would be more easily protected or shielded from heating so heating on the protuberance is less important.

In addition to the correlation for forward-facing step heating produced by Hung & Patel [45] (Equation 2.3), data was collected for a range of protuberances. Geometries tested were cylindrical and rectangular protuberances of a wide range of heights and widths. Correlations for peak heating upstream of small protuberances (in height and width) for laminar and turbulent boundary layers are given in Equation 2.8.

$$\frac{q_{max}}{q_{ref}} = (2.5 \sim 4.25)\left(\frac{H}{\delta}\right)^{1.5} \quad \text{(laminar)} \tag{2.8a}$$

$$\frac{q_{max}}{q_{ref}} = (5.2 \sim 7.3)\left(\frac{H}{\delta}\right)^{0.863} \quad \text{(turbulent)} \tag{2.8b}$$

The given range of constants for each of these equations is due to the large amount of scatter in the data used to generate the correlations. This approach was used, which covers all data points, rather than giving an average value with an uncertainty.

For peak heating upstream of tall and narrow cylinders, Hung & Patel give the correlation in Equation 2.9 which is applicable in both laminar and turbulent boundary layers.

$$\frac{q_{max}}{q_{ref}} = 4.2\left(\frac{D}{\delta}\right)^{1.38} \tag{2.9}$$

In this case, the heating is dependent on the diameter of the cylinder, D, rather than its height. This is reminiscent of Nestler's [44] correlation in Equation 2.1, where the heating upstream of forward-facing steps was found to be independent of the step height when much larger than the boundary layer.

The work of Hung & Patel [45] only featured heating data on the centreline of the model. However, for 3-dimensional protuberances, hot spots occur in separations which on either side of the protuberance. More recently, Estruch et al. [56, 57] experimentally conducted a parametric study into the heating in the vicinity of 3D rectangular protuberances. They collected heat flux data on the surface around the protuberance, which was of rectangular cross-section in the streamwise direction. The front face was angled backwards, to create a ramp, and forwards, to create an overhang. Two flow regimes were identified based on whether the angle of the front face was at a critical value, calculated based on the state of the incoming boundary layer and freestream flow properties. In cases below this angle, no separation occurs on the front face while for cases above this angle, upstream separation does occur. In both cases, the flow separates on either side of the protuberance. Correlations were developed for peak heating upstream and to the side for both cases. Figure 2.5, taken from [56], shows the calculation of the critical front angle and the heating correlations for each flow regime.

The integrity of these correlations was experimentally tested by Kumar [55, 58] on flat plate and cone configurations but for higher total enthalpies and lower Re_{unit}. Kumar found that although some of the predictions from the correlations matched the test data, due to being outside the range of conditions used to generate the correlations, this close matching was probably due to chance and heating rates at other test points were overpredicted.

A correlation was developed by Mazaheri [59] based on a conceptual design for a Shuttle TPS repair patch - an approximately cylindrical protuberance with a low profile ($H/\delta < 0.28$) and a wide aspect ratio ($108 < L/H < 280$). Experiments

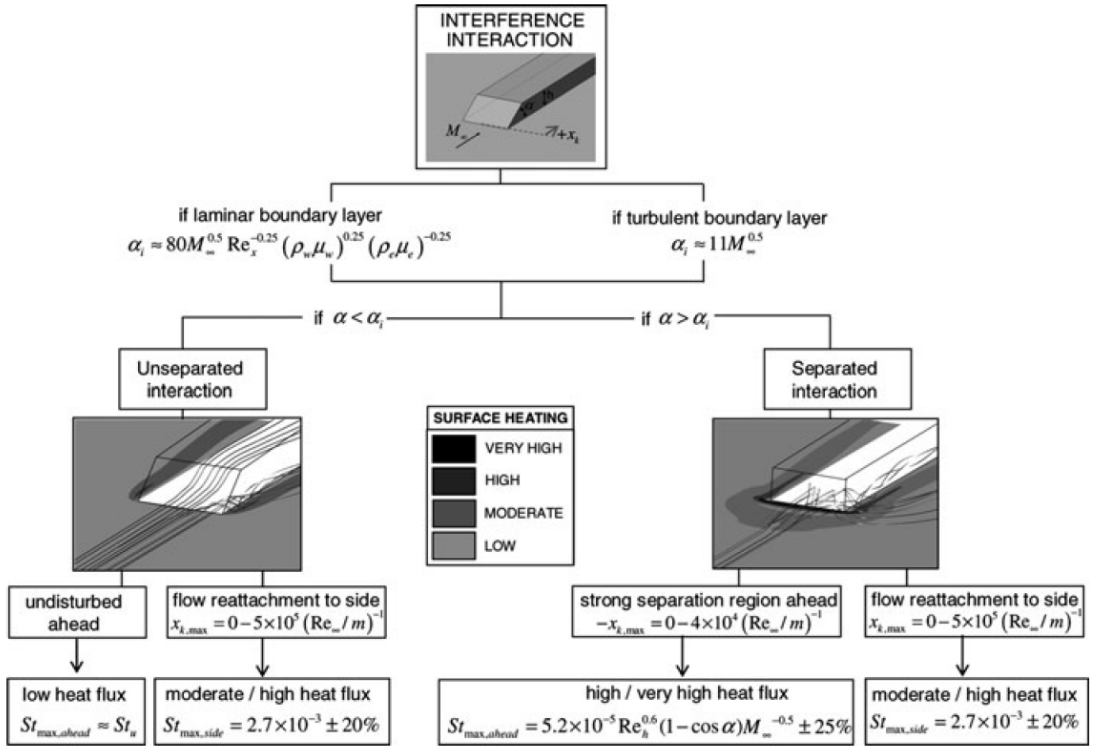

Figure 2.5: An engineering approach to predict the location and magnitude of peak heating on surfaces surrounding protuberances. Reproduced from Reference [56].

were performed to simulate the Shuttle wing leading edge, with $M_\infty =\sim 11.6$. Heat transfer data was collected at various points on the patch geometry, with the data from the gauge with the greatest measured heat flux being used to generate the correlation. The resulting correlation is shown in Equation 2.10.

$$\frac{q_{max}}{q_{ref}} = 0.5e^{0.7h_\eta/h_w} \tag{2.10}$$

Where the ratio in the exponent is the local flow enthalpy in the boundary layer at the height of the peak heating location (η) divided by the enthalpy at the wall. The correlation fits the limited experimental data (4 points) with reasonable accuracy as well as a number of numerical data points: some at the same conditions and some at higher Mach numbers. It is difficult to determine whether this correlation is more generally applicable. Although the geometry tested was very specific, it is likely that this correlation is more generally applicable to simpler cylindrical protuberances (and possibly, due to the aspect ratio, small forward-facing steps).

Unlike the other heating correlations discussed in this chapter which only use freestream conditions and geometric parameters, this correlation depends on the enthalpy being evaluated at two points in the boundary layer. This requires a numerical solution of the flowfield or vehicle is question, which is not always trivial to obtain.

2.2.3 Cavities

As with protuberances, cavities can be either 3- or 2-dimensional, with 2-dimensional cavities being infinite in the spanwise direction. With either type, cavities can be classified according to the ratio of the ratio of height to length. [60, 61, 62, 63] On one extreme, where $L/H < 1$, cavities are referred to as gaps. The flow field in the vicinity of gaps is similar to that of open cavities but the internal flow in gaps features counter-rotating spanwise vortices, the number of which is dependent on L/H.

Cavities with $1 < L/H < 10$ are called open cavities. In open cavities the flow impinges on the end wall before it establishes on the floor. This results in a recirculation region in the majority of the cavity volume.

Cavities with $10 < L/H <\sim 14 - 20$ are transitional, with the flow field fluctuating between open and closed flow periodically. Transitional cavities are generally avoided in the literature due to their difficulty in analysis.

The longest cavities are called closed cavities and have a $L/H >\sim 14 - 20$. In closed cavities the flow fully establishes on the cavity floor before encountering the downstream face of the cavity and can be thought of as two isolated steps (when 2-dimensional – 3-dimensional cavities feature more complex flow from the side walls). Figure 2.6 shows the four cavity/gap configurations.

Lamb [64] performed a survey of cavity heating experiments. Data was collated from a number of previous studies, with Mach numbers ranging from 2.1 - 8.5 and L/H values ranging up to a maximum of 13.3. Correlations were developed for laminar and turbulent boundary layers for heat fluxes in a variety of locations. Equation 2.11 shows Lamb's correlation for laminar boundary layers.

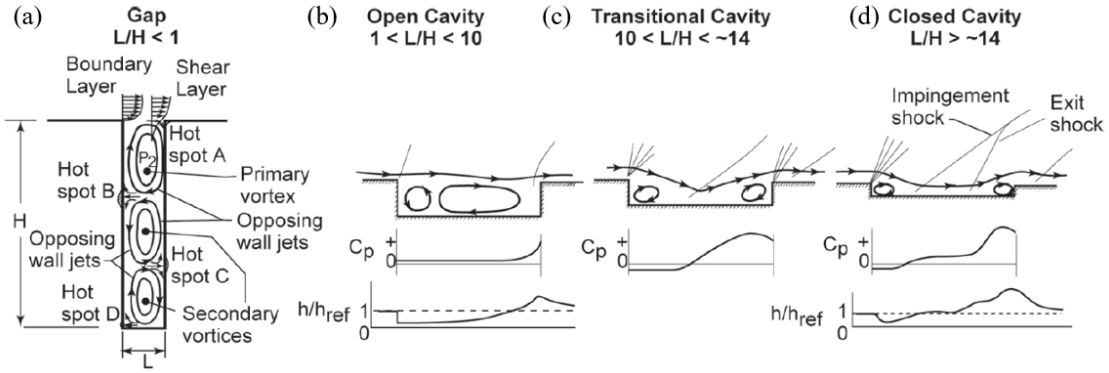

Figure 2.6: Four classifications of cavities, showing their respective flow fields, pressure distributions, and heat flux distributions. Reproduced from Reference [62]

$$\frac{q}{q_{ref}} = A\,(L/\delta)^{0.5}\,(H/\delta)^{n} \tag{2.11}$$

Where the constants A and n depend on the heat flux in question. For peak heat flux on the downstream recompression corner, $A = 0.28$ and $n = -0.25$. For average cavity floor heating, $A = 0.082$ and $n = 0.3$.

For turbulent boundary layers, Equation 2.12 shows the correlation for maximum cavity floor heat flux.

$$\frac{q_{max}}{q_{ref}} = 0.55\,(L/\delta)^{-0.23}\,(L/S)^{0.6}\,(T_0/T)^{0.2} \tag{2.12}$$

Equation 2.13 shows the correlation for minimum cavity floor heat flux.

$$\frac{q_{min}}{q_{ref}} = 0.22 + 0.274\ln\left[1/\left(\frac{L}{\delta}\cdot\frac{S}{L}\cdot\frac{\sigma_i}{\sigma}\right)\right]\cdot\left(\frac{\delta}{H}\right)^{0.2} \tag{2.13}$$

Where σ/σ_i is the ratio of the local and incompressible turbulent free layer growth parameter, defined by Equation 2.14.

$$\sigma/\sigma_i = 1 + 0.056\exp(3.4C^2) \tag{2.14}$$

Where C^2 is the Crocco number defined by Equation 2.15.

$$C^2 = 1 - T/T_0 \tag{2.15}$$

Finally, S is a shape parameter described as the characteristic cavity size, defined by Equation 2.16.

$$S = \frac{LH}{L+H} \sim \frac{\text{cross-sectional area of vortex}}{\text{total perimeter of vortex}} \tag{2.16}$$

The increased complexity of the turbulent correlations is partly due to the dependency on freestream Mach number, which was not the case with the laminar data. In both cases, the derived correlations are a good fit for the data .

Everhart [62, 65, 66, 67, 27] conducted a large number of wind tunnel experiments on cavities to simulate damage due to physical impacts with the Shuttle TPS. Experiments were carried out on a flat plate at angle of attack, resulting in edge Mach numbers between 1.75 and 3.2. Correlations for open and closed cavities in laminar and turbulent boundary layers were created, all using the same framework. In laminar boundary layers, the same correlation was found to be suitable for both open and closed cavities. In turbulent boundary layers, different correlations were required for open and closed cavities. For the open cavities in turbulent flow, additional historical data was found which had sufficient detail to include in the analysis as well. This extended the range of edge Mach numbers to 1.8 - 9. Equation 2.17 gives the general formulation of the correlations.

$$X = \ln\left[M_e^{\sigma} Re_{\theta}^{\tau} \left(\frac{L}{\delta}\right)\right] \tag{2.17a}$$

$$Y = \ln\left[\left(\frac{H}{\delta}\right)^{\alpha} \left(1 + \frac{L}{H}\right)^{\beta} \frac{q}{q_{ref}}\right] \tag{2.17b}$$

$$Y = a + bX \tag{2.17c}$$

Where the constants σ, τ, α, β, a and b depend on the value of q chosen: either average cavity floor heat flux or peak heat flux on the downstream recompression corner. Five sets of constants for combinations of incoming boundary layers and heat flux quantities were fitted.

Hollis has carried out a number of experimental studies on heatshield cavities [68, 69, 70, 33, 71, 72] for several re-entry capsules. The new NASA Orion capsule features compression pads which are a part of the support structure for the capsule

when assembled in the launch vehicle. These take the form of circular cavities. Correlations were developed to describe the average cavity floor heating. Initial investigations [33] on open cavities ($D/H = 2.9 - 15.3$)[1] in laminar boundary layers led to correlations in the form of Equation 2.18.

$$\frac{q}{q_{ref}} = C_1 \mathrm{Re}_\theta^{C_2} \cdot \left(\frac{D}{H}\right)^{C_3} \cdot \left(\frac{H}{\delta}\right)^{C_4} \tag{2.18}$$

Where the constants, C_{1-4} were fitted based on the value of q chosen. Constants for average cavity floor and maximum end wall (recompression corner) heat flux were fitted. Resulting R^2 values for each of these fits were 0.80 and 0.60, respectively. Following subsequent testing, correlations for closed cavities ($D/H = 11.4 - 45.6$) with laminar incoming boundary layers were developed. It was found that for some combinations of cavity sizes and flow conditions, the boundary layer transitioned, or began to transition, to turbulent inside the cavity, leading to non-laminar boundary layers at the cavity exit. This resulted in different trends in heat flux: Equations 2.19 and 2.20 are correlations for average cavity floor heating for fully laminar and transitional boundary layers, respectively.

$$X = \mathrm{Re}_\theta \left(\frac{D}{H}\right)^{-1} \tag{2.19a}$$

$$Y = \frac{q}{q_{ref}} \tag{2.19b}$$

$$Y = \left(1 - \frac{1}{C_1}\right) - \frac{1}{C_1} \tanh\left[\frac{2.718\,(X - C_2)}{C_2}\right] \tag{2.19c}$$

Where $C_1 = 4.0152$ and $C_2 = 2.3589$.

$$X = \frac{\mathrm{Re}_\theta}{M_e} \left(\frac{1}{M_e}\right)^{0.5} \left(\frac{D}{H}\right)^{-0.24} \tag{2.20a}$$

$$Y = \frac{q}{q_{ref}} \tag{2.20b}$$

$$Y = C_1 X^{C_2} \tag{2.20c}$$

Where $C_1 = 0.003574$ and $C_2 = 1.2443$.

[1]The upper limit of L/H used to define open cavities varies significantly between different studies.

The experimental data fits these correlations with a significant amount of scatter. The correlation coefficient for Equation 2.19 is given as 0.787. No goodness of fit for Equation 2.20 is given. In each case, the most scatter comes from data for cavities with $D/H = 11.4$, which are typically classed as transitional cavities (rather than closed cavities, which these correlations were designed for).

As with Everhart's correlations [62, 67], this data comes from blunt body experiments with low boundary layer edge Mach numbers (with the exception of Everhart's turbulent open cavity correlation). Designers of slender cruise vehicles, which feature edge Mach numbers closer to the freestream [35, 36], may not be able to use these correlations with much confidence.

2.2.4 Combined geometries

It is convenient to approximate surface imperfections as simple geometries, however, this is not necessarily representative of features on real vehicles. For example, Smith et al. [73] and Petley et al. [22] conducted numerical analyses of the Shuttle TPS tile array with a stepped tile to account for small differences in tile heights (see Figure 2.7). This work was motivated by post-flight measurements of the TPS, which found that damage to the underlying filler bar (the support structure for the tiles) corresponded with locations of stepped tiles. The steps caused the flow to stagnate, increasing the local pressure and widening the gaps in front of the stepped tiles. Steps were small compared to the boundary layer, with $H/\delta =\sim 0.02 - 0.2$. Results from the study show that even this size of step had a large impact on the heat flux inside the gap, with filler bar temperatures increasing between 280-480 K more when a step is present. Although only a small number of cases were analysed in this study, the impact of combining geometries is clear.

Hinderks conducted numerical simulations of a generic tile array [74] and the X-38 nosecap [75] and found that the heating on downstream recompression corner of a gap between elements in a TPS array can cause excessive thermal expansion, creating an additional step of significant height. Steps were simulated to reach heights the same order of magnitude as the gap width. The simulations were

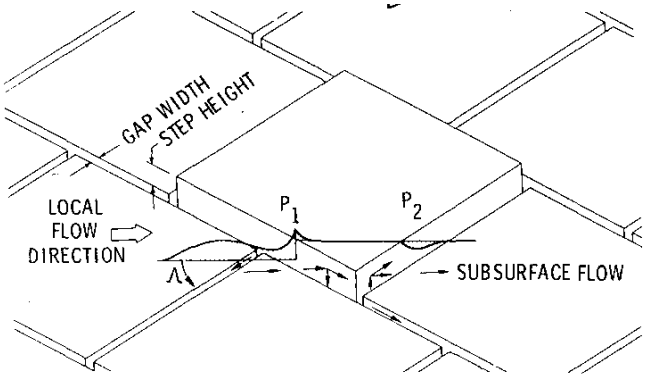

Figure 2.7: The stepped Shuttle tile setup analysed by Petley et al. [22].

partially validated using cold flow wind tunnel testing [76]. On the X-33, which also featured a tile array as its TPS, Palmer et al. [77] conducted a numerical tile heating analysis. They found that the tiles would bow when under thermal load, creating steps and gaps between the tiles.

2.2.5 Summary of Heat Flux Augmentation Correlations

On the following page, Table 2.1 shows a summary of the correlations discussed in this section. For each entry, the geometry is listed: forward-facing step (FFS), backward-facing step (BFS), protuberance (Prot.) or cavity (Cav.). Also listed is the type of boundary layer - laminar (L) or turbulent (T) - that the correlation is applicable for.

Table 2.1: Summary of the literature containing heat flux correlations covered in this section.

Study	Geom.	BL	Correlations
Nestler [44]	FFS	T	Correlation for peak heating on large steps ($H > \delta$) in turbulent boundary layers.
Zukoski [43]	FFS	T	Relation between step height and size of upstream separation.
Hung & Patel [45]	FFS	L,T	Correlations for maximum heating upstream of forward facing steps (also with protuberance data).
Rom & Seginer [46]	BFS	L	Correlations for average heat flux behind small ($x/H\mathrm{Re}_x^{1/2} < 0.067$) and large ($x/H\mathrm{Re}_x^{1/2} > 0.067$) steps.
Jakubowski & Lewis [49]	BFS	L	Line fit for reattachment heat flux vs Re_H. No equation for correlation given.
Lamb [54]	BFS	L,T	Correlations for minimum heat flux in downstream separation.
Hung & Patel [45]	Prot.	L,T	Correlations for peak heating upstream of protuberances (also with FFS data). Narrow short and tall protuberances tested.
Estruch et al. [56, 57]	Prot.	L,T	Correlations for peak heating on the surface in the vicinity of a protuberance. Four flow regimes identified.
Mazaheri [59]	Prot.	L	Correlation for maximum heat flux on the front face of a specific protuberance geometry.
Lamb [64]	Cav.	L,T	Correlations for peak downstream corner & average floor heat flux (laminar) and minimum and maximum floor heat flux (turbulent).
Everhart [65, 62, 66, 26, 67, 27]	Cav.	L,T	Correlations for average and minimum floor heat flux for open and closed cavities.
Hollis [68, 69, 70, 33, 71, 72]	Cav.	L,T	Correlations for average floor & peak downstream corner heat flux (open cavities, laminar) and average floor heat flux (closed cavities, laminar & turbulent).

2.3 Boundary Layer Transition

The second key impact of surface imperfections is on boundary layer transition. The effect of roughness on boundary layer transition is a topic that has attracted a lot of attention over the past decades. Schneider [78] has published a very thorough review of the subject with almost 100 references.

As with heat flux augmentation, historical motivation for research into roughness induced transition was often linked to the development of new spacecraft. The Shuttle experienced transition due to the gap filler between TPS tiles becoming protruded [79, 80, 24, 81]. The new Orion capsule features cavities on its heat shield, as well as roughness due to ablation [31, 72], both of which can cause early transition. Other probes with heat shields experience similar effects [68, 69, 70].

2.3.1 Basics of Boundary Layer Transition

The different routes by which a boundary layer can transition from laminar to turbulent can be summarised by Figure 2.8, where the paths are organised by increasing disturbance levels.

- Path **a** is typical of natural transition in a low disturbance environment, such as on a smooth aircraft surface or on a smooth experimental model in a wind tunnel. In 2-dimensional zero pressure-gradient flows, this type of transition is dominated by two instabilities which were first proposed by Mack [84] following a linear stability theory analysis. These instabilities were thus named first and second Mack mode instabilities. Mack showed that in hypersonic flows, the second mode, which consists of acoustic waves being reflected between the wall and the boundary layer sonic line, was the dominant instability leading to transition. In 3-dimensional boundary layers, crossflow and Görtler instabilities can also be present. The growth of these primary instabilities is slow until 3-dimensional and nonlinear secondary instabilities begin to interact, at which point growth becomes very quick and breakdown to turbulence soon occurs [85, 82, 78].

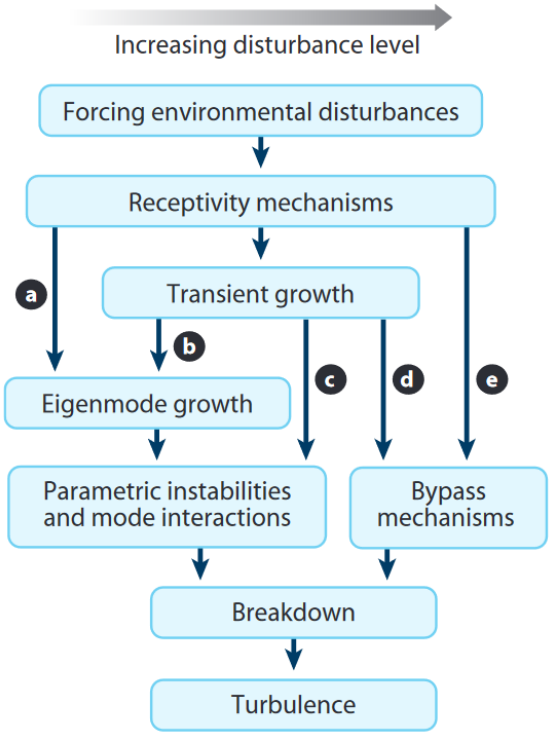

Figure 2.8: The different pathways to turbulence, reproduced from Fedorov [82], originally proposed by Morkovin [83].

- Transient growth occurs when nonorthogonal stable modes interact and grow before decaying. The subsequent path to turbulence depends on the amplitude attained by the transient growth. In path **b**, growth of primary instabilities occurs following the transient growth, followed by interaction with secondary instabilities [86].

- Path **c** leads directly to secondary instabilities following a transient growth with an intermediate amplitude.

- For the largest transient growths, in the case of path **d**, the usual mechanisms by which breakdown is reached are bypassed, with the exact mechanisms being unknown.

- Finally, for the greatest disturbance levels, path **e** corresponds to a boundary layer which experiences no instability growth and transitions immediately. [85]

The effect of surface imperfections is almost always to expedite the transition [78]. However, the mechanisms by which this occurs are not always known. Reshotko [87] proposes that transient growth is an important factor to explain the effect of distributed roughness. Schneider [78] gives three possible reasons that roughness could induce early transition: primary instabilities may grow in the wake of a roughness element; streamwise vorticity that trails the roughness may grow via transient growth; or freestream disturbances may interact with the roughness to create primary instabilities. In any case, the effect of roughness on boundary layer transition depends on its geometry, the flowfield, and the freestream disturbance level, among other things.

2.3.2 Boundary Layer Interaction with Surface Features

This section presents some of the recent work investigating the mechanisms behind roughness induced transition.

Steps

Results from wind tunnel experiments on a 7° half angle cone by Yam et al. [88] found that the inclusion of a step in a laminar boundary layer induced a 250 kHz instability - the approximate frequency expected of a second mode instability for the given flow and model conditions. The instability increased with amplitude for larger step heights, up to a maximum size of $H/\delta = 2.26$. However, even with the largest step height, the boundary layer did not appear to be tripped.

Experimental studies by Xu et al. on sharp [89] and blunt [90] 7° half-angle cones indicate somewhat conflicting results with those of Yam. They found that a forward-facing step can suppress 2nd mode instabilities at values of $H/\delta <\sim 0.75$. This suppressing effect is reduced at higher step heights and at the largest heights tested, $H/\delta = 2$, the effect was to promote earlier transition compared with the smooth case. For backward-facing steps, the effect was to always induce earlier transition, even with the smallest tested step height of $H/\delta = 0.25$. Transition

occurred further upstream in backward-facing steps when compared with forward-facing steps of the same height.

Masutti [91] performed wind tunnel experiments on the EXPERT vehicle, which features a backward-facing step between the nose section and the downstream TPS. It was found that the backward-facing step only induced earlier transition for the highest Reynolds number condition with the largest step height tested of $H/\delta = 4.47$. Following backward-facing steps, streamwise streaks could be seen in heat flux data. Although not discussed, it is likely that these were Görtler vortices, which were observed downstream of backward-facing steps by Ginoux [92, 93]. Wedge-shaped protuberances were also added downstream of the step. These appeared to trip the boundary layer immediately, regardless of the upstream step height. However, larger steps resulted in greater heating in the vicinity of the protuberance. Masutti also carried out experiments on a 7° half angle cone [94] with backward-facing steps. It was found that the step caused earlier transition compared to the smooth cone, and that the streamwise vortices (likely Görlter) interacted with the second mode instabilities already present.

2-dimensional protuberances

The location of a roughness element can determine how it interacts with the boundary layer. Both Holloway [95] and Fujii [96] found during wind tunnel experiments that two-dimensional protuberances on flat plates and cones, respectively, could, in some circumstances, delay transition. Duan [97] and Fong [98, 99] performed direct numerical simulation (DNS) studies on 2-dimensional protuberances with upstream blowing to excite a second mode instability. The studies found that if the location of the protuberance was upstream of the synchronisation point of a particular instability frequency, there will be an amplification. Whereas, if the protuberance is located downstream of the synchronisation point, damping of the instability can occur. Fong further performed a parametric study and concluded that the strength of the amplification or damping was increased with the size of the protuberance. Tang [100] carried out a controlled experimental study, aiming to

capture this effect. They used a flat plate with a slot for blowing, which enhanced the second mode instability further downstream. A 2-dimensional protuberance was placed upstream of the synchronisation point of the first and second modes. Results from the study showed that the protuberance caused a decrease in the frequency of the second mode instability as well as an amplification close to the protuberance. However, the amplitude of the instability recovered back to the smooth plate level further downstream and the transition location was not captured (with or without roughness). These studies suggest that it may be possible, with correct placement, to control boundary layer transition using 2-dimensional roughness.

BOLT flight experiment

The Boundary Layer Transition (BOLT) experiment was a recent effort to measure transition in flight on a hypersonic vehicle with concave surfaces and swept leading edges [101]. Due to different expected heat fluxes during flight, three different materials were used in the construction of the outer shell of the model: a titanium-zirconium-molybdenum alloy (TZM), stainless steel, and aluminium. The different thermal expansion coefficients of each material meant that during the flight, they would expand at different rates. To mitigate the risk of having forward-facing steps at the interfaces, the joints were designed with backward-facing steps. The vehicle had two sides, one of which was selected to investigate the effect of steps due to their inevitable presence [102]. The sizes of the steps for the flight vehicle were informed by ground testing of a scaled model [103], with various step sizes and trajectory points being tested. Results from these experiments were used to create a map for transition due to step height at differing Reynolds numbers. Reda and Shuttle correlations (see Section 2.3.3) were used to extrapolate experimental results to the full scale model which were incorporated into the final design [104]. Unfortunately, during the flight test, the trajectory was not achieved and the vehicle did not manage to reach hypersonic speeds [105].

In addition to this, some ground testing was performed [106] to test the size of protuberance that would trip the boundary layer on the attachment-line (the flow

along the swept leading edge). Two trip heights were tested, sized to be sufficient for transition according to the Reda correlation (see below) with neither of them having any effect on the stability of the boundary layer over the length of the model. This was advantageous for the model design but the phenomenon was unexplained.

A second model, BOLT-II, was designed and flown shortly after the first flight and featured small pizza-box style protuberances while trying to minimise the size of steps [107]. Flight data for the roughness experiment has not been published yet.

2.3.2.1 Shuttle Flight Experiment

During the last years of the flight of the Shuttle, experiments looking into boundary layer transition on the TPS were performed. These involved attaching fence-like protuberances to the TPS tiles and measuring the downstream effect [108]. Results from these experiments showed that the existing prediction methods for transition onset produced good results. However, the heat flux in the vicinity of the protuberances was greatly over predicted by CFD methods, the cause of this being unknown [109].

Combined geometries

Charbonnier [110] tested the effect of a step-gap geometry on boundary layer transition. A parametric study was performed using leading-edge radius, step and gap dimensions, and geometry type (step-gap or raised tile) as variables. Unfortunately, the only geometric parameter presented was the overall height of the step or protuberance, and a critical value $H/\delta = 2.3$ was given. Additionally, no single step or gap was tested, so a useful comparison could not be made.

2.3.3 Correlations for Boundary Layer Transition with Roughness

Given the complexity of the processes involved in boundary layer transition, especially when influenced by rough surfaces, there has always been a high demand for simple engineering correlations.

Roughness Reynolds number: $\mathbf{Re}_k$

In 1932, Schiller [111] first proposed that the Reynolds number based on the height of the roughness (Equation 2.21) could indicate the critical height of a particular roughness to cause transition.

$$\mathrm{Re}_k = \frac{\rho_k u_k k}{\mu_k} \tag{2.21}$$

Where k is the roughness height and the flow properties are taken at the height, k, in the boundary layer. It was thought that above a critical value the roughness would cause vortices to form and be shed into the boundary layer, causing a breakdown to turbulence. This is a very simple approach and has been applied effectively to low speed flows. At hypersonic conditions, there have been a multitude of studies which result in different critical values of Re_k. However, a value of $\sim 10 - 20$ is thought to have very little effect on the stability of the boundary layer [78].

Reda's approach

Reda [112] correlated boundary layer transition for rough nosetips, tested in a ballistic range, using a Re_k method, following the work of Dirling [113] who used it to analyse data from the Passive Nosetip Technology (PANT) program (see below). Reda's approach to correlation development is shown schematically in Figure 2.9. The independent variable is termed the disturbance parameter and typically includes quantities relating to the roughness height and local flow properties. The dependent variable is the transition parameter and typically includes flow properties at the transition location. A power-law relationship between the two parameters is found, with the ideal scenario being $n = -1$, so that a single constant can be used to describe the transition relation.

In Reda's nosetip work, various combinations of transition parameters and disturbance parameters were tested, with the best fit being produced when using Reynolds numbers based on the local momentum thickness, θ, shown in Equation 2.22.

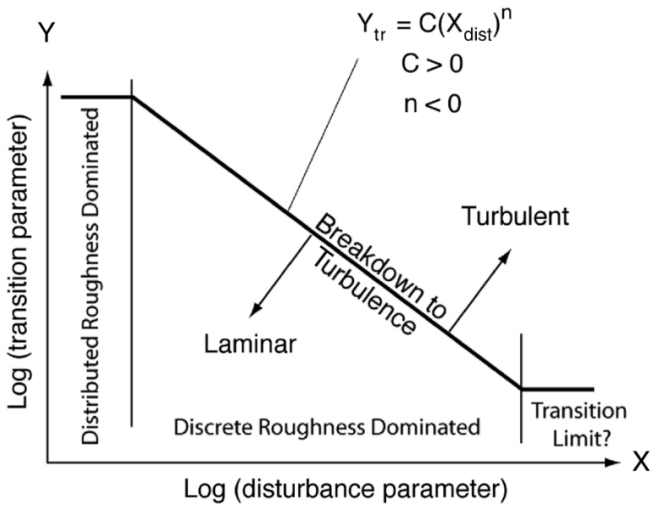

Figure 2.9: A general formulation for transition correlations. Originally printed in [112], reproduced from [114].

$$Y_{tr} = \left[\frac{\rho_e u_e \theta}{\mu_w}\right]_{tr} \tag{2.22a}$$

$$X_{dist} = \left[\frac{\rho_k u_k k}{\rho_e u_e \theta}\right] \tag{2.22b}$$

$$Y_{tr} = 192(X_{dist})^{-0.98} \tag{2.22c}$$

Given the closeness of the fit to $n = -1$, the following approximation can be made:

$$\left[\frac{\rho_k u_k k}{\mu_w}\right]_{tr} = 192 \tag{2.23}$$

This is similar to Re_k given in Equation 2.21 but it uses the viscosity evaluated at the wall temperature rather than the temperature of the boundary layer at the roughness height.

Reda later reviewed a number of datasets using the same approach [115] and found that, in addition to blunt nosetips, this method could also be applied effectively to attachment line, Shuttle, and X-33 transition data. Several versions of the roughness Reynolds number were used with varying success. Some datasets were best correlated when using boundary layer edge conditions, rather than internal boundary layer conditions. While seemingly widely applicable, the datasets featured

relatively low boundary layer edge Mach numbers. Recent work by Passaro [116, 117] investigated boundary layer transition induced by rectangular protuberances on a flat plate in Mach 6 flow. Transition data collected was able to be fitted a constant Reynolds number as shown in Equation 2.23 successfully (dubbed Re_{Reda} by Passaro), showing perhaps an extended regime of applicability of Reda's method.

A concern of the sensitivity of a roughness Reynolds number, discussed by Reda [115], stems from the need for flow properties inside the boundary layer, which are not trivial to produce. The example fit given in Equation 2.23 used an empirical method to calculate the internal boundary layer properties. The same fit was made using values extracted from a Navier-Stokes code and the value of the resulting critical constant differed by 25%.

Shuttle correlation

Following the first few flights of the Shuttle, thermocouple data from the TPS was compared with post-flight inspections. Increased heating, which indicated a turbulent boundary layer, was found in areas downstream of locations where tile gap filler was protruding [79, 80]. This later provided motivation for wind tunnel tests looking into protuberance induced transition on the Shuttle [24, 118]. The results of these experiments, as well as a comparison to flight data, was discussed by Bouslog et al. [25]. Modified versions of the PANT [119] and van Driest & Blumer [120] correlations (see below) were used with some success. Additionally, an alternative approach was used to fit transition data, using Re_θ/M_e as the transition parameter and H/δ as the disturbance parameter, as shown in Equation 2.24.

$$\frac{Re_\theta}{M_e} = C \cdot \left(\frac{H}{\delta}\right)^{-1} \tag{2.24}$$

As with the Re_k approach, the critical value, C, must be determined experimentally, and is dependent on the flowfield and geometry [121]. The correlation appears well suited for predicting transition on geometries similar to that which it was developed for (i.e. high angle-of-attack re-entry bodies) having been also used in the development of the experimental aircraft, X-33 [34, 81].

The Shuttle correlation has since been used for different geometries only somewhat successfully. Passaro [116, 117] succeeded in fitting flat plate transition data for small cylindrical protuberances, while for flat rectangular protuberances transition was not described well by the Shuttle correlation, finding that a Reda-style Reynolds number performed better. Similarly, Tirtey [122] experimentally tested the EXPERT vehicle (a blunt flight experiment vehicle) and found difficulty fitting protuberance induced transition data to the Shuttle correlation, finding instead that a correlation for distributed roughness was better suited [123], even with isolated protuberances.

A later study by King et al. [124] reviewed the previous wind tunnel and flight Shuttle transition data for the purpose of improving the NASA Shuttle-Orbiter Boundary Layer Transition Tool. Seven correlations were proposed and tested against the transition data. Two correlations were chosen: the first correlation was a Shuttle-style correlation with a additional term for total enthalpy ratio to account for variability between facilities: $(h_e/h_w)^m$. This correlation provided the best fit, but one dataset, for large values of H/δ, was omitted. The second correlation was a Reda-style correlation using $\rho_e u_e \theta/\mu_k$ as the transition parameter and $(\rho_k u_k k)/(\rho_e u_e \theta)$ and the disturbance parameter. A value of $n = -0.6$ gave the best fit (referring to Figure 2.9). This correlation was able to account for all the datasets, but performed slightly worse than the Shuttle-style correlation.

Reshotko [87] performed transient growth analysis of roughness induced instabilities and produced transition correlations which were ultimately a Re_k-style critical Reynolds number with an additional term to correct for different wall temperatures. Reshotko is a strong proponent of this type of transition correlation over the Shuttle-style Re_θ/M_e correlations [125]. He argues that the Shuttle approach might be suitable for re-entry vehicles only due to its sensitivity to density changes when travelling through the atmosphere and is not relevant to constant altitude cruise vehicles. In fact, Reda [115] states in his review that the Shuttle correlation can be transformed to a $\mathrm{Re_k}$ by assuming that $\mathrm{M_e}$ and δ/θ are constant and that this holds true for high angle-of-attack hypersonic flows about flat-bottomed lifting-entry

vehicles (such as the Shuttle). It is likely that this assumption can also be made for slender constant altitude cruise vehicles.

Alongside the cavity heat flux correlations developed by Hollis [33, 72] for re-entry capsule heat shields, described in Section 2.2.3, transition data was also collected for open cavities [70]. The Shuttle correlation was the framework for transition fitting for this work. Two transition parameters (Re_θ/M_e and Re_θ) were tested with two disturbance parameters (D/δ and H/δ) in all four combinations. The combination which collapsed the transition data the best was Re_θ and D/δ. This implies that the depth of open cavities is not an important factor for transition. It also suggests that the edge Mach number does not have an influence. This was argued to be because the disturbance caused by such a cavity is near the wall rather than near the boundary layer edge.

Other notable correlations

Some of the first supersonic roughness induced transition experiments were carried out by van Driest & Blumer on sharp cones [120] and spherical blunt bodies [126], using rows of small spheres as the roughness elements. Two separate correlations were used to correlate transition for cones and blunt bodies, shown in Equations 2.25a and 2.25b respectively.

$$\mathrm{Re}_{\delta^*} = 588\frac{1 + 700\,(k/D)}{k/\delta^*} \tag{2.25a}$$

$$\mathrm{Re}_{\delta^*} = 1025\frac{1 + \frac{\gamma-1}{2}M_e^2}{(k/\delta^*)^2} \tag{2.25b}$$

Where δ^* is the displacement thickness and k is the roughness height (commonly used for distributed roughness). These correlations, while in good agreement with the dataset they were generated from, are fairly specific and have not been widely tested for use with other data [78].

The Passive Nosetip Technology (PANT) Program was an effort in the early 1970s to quantify some of the phenomena associated with ablative nosetips during reentry [127]. One of the objectives was to assess boundary layer transition caused

by the ablative material becoming rough. The result of this work was a correlation describing transition on rough nosetips: the so-called PANT correlation [119]. This is shown in Equation 2.26.

$$\mathrm{Re}_{\theta\, tr} = 215\Psi^{-0.7} \tag{2.26a}$$

$$\Psi = \frac{k}{\theta} \cdot \frac{T_e}{T_w} \tag{2.26b}$$

Where additional terms can be added to Ψ for blowing effects due to ablation. The correlation was successfully applied to a number of datasets on spherical nosetips with distributed roughness caused by ablation.

2.4 Summary

The scope of this chapter was to perform a review of the literature which investigates the effect of surface features on the flow over hypersonic vehicles. While not complete (there is a great deal of work which has been covered by previous reviews), it is hoped that the gaps in the topics reviewed here reflect the gaps in current knowledge base. These are summarised below.

Heat flux augmentation

- It is well known that combined geometries occur - specifically stepped gaps, which are well documented on tile-based TPS systems. However, there is little work looking into the additional effect that combining geometries has on localised heating.

- A great deal of the recently developed heat flux augmentation correlations were done so using data for blunt bodies or vehicles with high angle-of-attack with low edge Mach numbers. Although the correlations provide a very good fit for this data, they cannot be extrapolated to higher Mach number flows with any confidence. There have been no studies to verify (or refute) the applicability of the correlations to more general flow fields.

- Additionally, the majority of heating studies focus on large scale elements (of significant size compared to the boundary layer thickness) [55]. Although still important, the effects of small scale features have been shown to have a large impact on heating as well as boundary layer stability [32, 59].

Boundary layer transition

- The mechanisms by which roughness causes transition are unknown [87, 91]. Recent experimental investigations aiming to isolate different effects have provided some insight (e.g. the effect of 2-dimensional steps and protuberances on second mode instabilities [100, 88, 90]). However, there is still much to be learned.

- The majority of the data used to generate correlations for boundary layer transition is for blunt bodies, ablatives, or high angle of attack vehicles [115, 24, 119]. As with correlations for heat flux augmentation, the transition correlations typically describe these types of flows well, but have not been tested, to a great extent, on flows relevant to slender vehicles with hypersonic boundary layer edge Mach numbers.

- There is a range of correlations which have been used to predict roughness induced transition. They are not all suitable in all situations, and there have been many disagreements in the community about which approach is the most suitable [125]. It is not known whether a universal correlation for transition actually exists.

3 Methodology

Contents

3.1 The Oxford High Density Tunnel 42
3.1.1 Ludwieg Mode Operation 44
3.1.2 LICH Mode History 44
3.1.3 LICH Mode Operation 45
3.1.4 LICH Mode Infrastructure 48
3.2 Experimental Model 51
3.2.1 Mechanical Design 52
3.3 Instrumentation 60
3.3.1 Surface Heat Flux Measurements 61
3.3.2 Measurement Uncertainties 72
3.3.3 Surface Pressure Measurements 77
3.3.4 Freestream Characterisation 78
3.3.5 Model Alignment 79
3.3.6 Geometry Height Measurement 80
3.4 Boundary Layer Properties 80
3.4.1 Thickness Parameters 80
3.4.2 Surface Heat Flux 84
3.5 Summary 85

3.1 The Oxford High Density Tunnel

The experimental testing carried out for this work was performed in the Oxford High Density Tunnel (HDT), shown in Figure 3.1 and schematically in Figure 3.2.

The HDT consists of a 152.4 mm internal diameter x 17.4 m long, electrically heated barrel (**2** & **3**) capped, on the downstream end, by a pneumatically operated fast-acting plug valve. A contoured nozzle sits downstream of the plug valve via an intermediate plenum (**4**). Nozzles exist for Mach numbers of 4, 5, 6, and 7 which can be interchanged as necessary. All nozzles have a 0.351 m exit diameter and exit into a free jet test section (**5**). The test section leads to a dump tank of 28 m^3. McGilvray [128] and Wylie [129] give more details on the construction and operation of the tunnel.

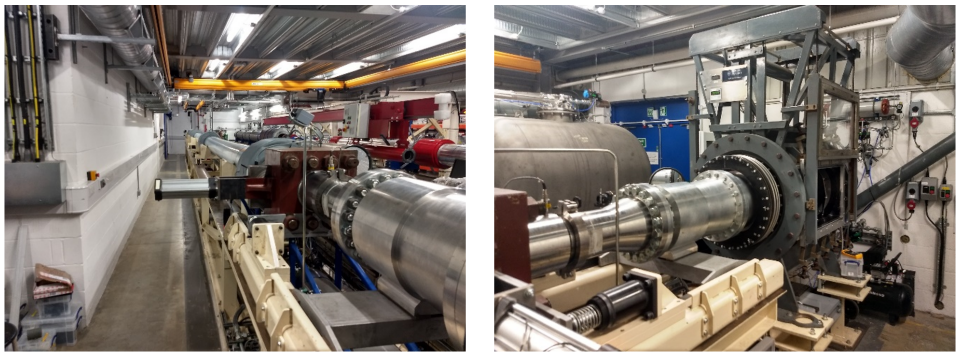

Figure 3.1: The Oxford High Density Tunnel (HDT). Left: looking upstream from the nozzle. Right: the nozzle and test section

HDT typically operates as a Ludwieg tunnel but modifications were made, as a part of this work, to allow for different mode of operation to be used. Ludwieg mode with Isentropic Compression Heating (LICH mode) includes a piston stroke in the test gas during the firing sequence, heating the gas past the temperature attainable by electric heating alone, and extending the total temperature capability of the facility.

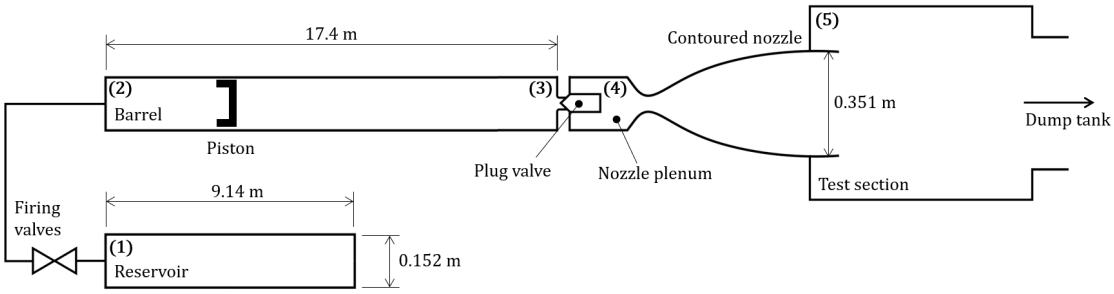

Figure 3.2: Schematic of HDT showing key infrastructure

3.1.1 Ludwieg Mode Operation

A Ludwieg tunnel consists of a high pressure reservoir which is isolated from a converging/diverging nozzle, typically via a diaphragm or a fast-acting valve. A shot occurs when the test gas is allowed to pass through the nozzle into the test section. A feature of HDT, which is not typical of Ludwieg tunnels, is a plenum located between the plug valve and the nozzle throat (region 4 in Figure 3.2). The presence of the plenum is necessitated by the design of the plug valve. The flow stagnates in the plenum, causing two effects: firstly, a large unsteady temperature spike occurs during flow initialisation; secondly, the additional flow path and surface area causes total temperature losses. Additionally, the freestream noise levels (in terms of RMS (p_{pitot}) $/\overline{p_{pitot}}$) have been measured to be lower than other Ludwieg tunnels which is postulated to be due to the presence of the nozzle plenum.

As the plug valve opens, rarefaction waves begin to travel upstream through the test gas in the barrel. These waves are reflected once they reach the upstream end of the barrel and travel back to the nozzle plenum. During the time between the rarefaction wave leaving and returning to the plug valve, the supply pressure to the nozzle plenum remains constant. During a shot, this process occurs multiple times, leading to a series of steady flow periods of subsequently lower and lower pressures of between 30-70 ms in length depending on fill conditions. The strength of the pressure drop between reflected waves depends on the speed at which the plug valve opens and as shown by Hillyer [130, 131], can be altered to extend the steady test time.

3.1.2 LICH Mode History

Wind tunnels using isentropic piston strokes have been used since the early 1970s, with several key improvements being incorporated in developments since then. The addition of a piston stroke to isentropically heat test gas for wind tunnels was first investigated by Jones et al. [132] after employing a similar technique for producing engine-realistic flows in gas turbine cascades. A trial facility was built which produced steady, high temperature, supersonic (M > 1.8) flows. Oldfield et al. [133] then incorporated this into the Oxford University Gun Tunnel, producing

similar but more steady stagnation conditions than the gun tunnel was capable of. Following this success, a dedicated LICH tunnel was built at Southampton University [134] which added electric heaters to the barrel to preheat the test gas, allowing even greater total temperatures to be achieved. All of the tunnels up to this point used a diaphragm to release the test gas into the test section when the tube pressure reached a certain threshold. At Syracuse University [135, 136] a LICH tunnel was developed which used a fast acting ball valve instead. This increased the opening time, extending the length of the rarefaction wave which propagates along the barrel. This had the result of decreasing the magnitude of reflected waves from the piston and producing steadier flow. Currently, the TUSQ facility at the University of Southern Queensland uses a light piston to heat test gas in a Ludwieg tube and can produce Mach 6 flows with total temperatures above 500 K [137]. More recently, work on the TUSQ facility has allowed it to operate at Mach 3 [138] and Mach 7 [139].

3.1.3 LICH Mode Operation

To operate in LICH mode, a light piston is placed inside the barrel which separates the test gas in volume 3 from the driver gas in volume 2 (see Figure 3.2). The shot firing sequence includes a piston stroke to compress and heat the test gas. The piston can operate inside the already pre-heated barrel, meaning that the temperature of the test gas can exceed that which is possible in Ludwieg mode. Compared with gun tunnels, which operate in a similar way [140], the piston in a LICH tunnel moves relatively slowly - the piston stroke can take several seconds. This is to ensure the test gas is compressed isentropically and avoids the production of compression waves, resulting in a prolonged steady test time and a uniform temperature distribution in the test gas.

The following paragraphs detail some of the key differences in operation between Ludwieg mode and LICH mode:

3.1.3.1 Tunnel Setup

In LICH mode, there are four independent inputs that may be adjusted to alter the test condition achieved. They affect the resulting nozzle supply conditions in the following ways, where numbered subscripts indicate labelled regions in Figure 3.2:

- $p_{3,o}$ - the barrel pressure at which the plug valve is set to open. The nozzle supply pressure, p_4, is purely a function of $p_{3,o}$.
- $p_{3,f}$ - the initial barrel fill pressure. The compression of the test gas is set by the ratio of initial to final barrel pressure, $p_{3,o}/p_{3,f}$. Greater compression ratios lead to higher nozzle supply temperatures, T_4. The compression ratio also influences the total test time available - see *Test Time* below.
- $T_{3,f}$ - the initial barrel fill temperature. The temperature of the test gas at the beginning of the piston stroke dictates the final temperature after compression. A given T_4 is achievable using multiple combinations of $p_{3,o}/p_{3,f}$ and $T_{3,f}$, the implications of which are discussed further in Section 4.3.2.
- $p_{1,f}$ - the initial reservoir fill pressure. This gives control over the piston stroke, with larger pressures leading to faster strokes. Additionally, the reservoir pressure affects the rate of change of p_4 during a shot - see *Matched Conditions* below.

Fill conditions are all set prior to the shot and a threshold for $p_{3,o}$ is input into the programmable logic controller (PLC) which controls HDT. A GEMS 3100 Series pressure sensor monitors the barrel pressure during the piston stroke and once the preset threshold is measured, the PLC performs an automated sequence to actuate the valves that allow the plug valve to open and initiate the shot.

3.1.3.2 Test Time

The test time in LICH mode can be defined by either the total flow time or the duration of the steady flow periods caused by rarefaction waves. The total flow time, defined as the time taken for the test gas to exit the facility nozzle, is a function

of two variables: compression ratio and nozzle throat area. The compression ratio determines the piston displacement when the plug valve is opened, with higher compression ratios corresponding to greater displacements from the initial position and resulting in a shorter total flow time. Nozzles with a smaller throat have a lower mass flow rate for given supply conditions which results in a longer test time. In the case of HDT, for which the nozzle exit diameters are constant across the range of nozzles, this means that higher Mach number nozzles in HDT have a longer test time in LICH mode compared with lower Mach number nozzles.

3.1.3.3 Piston Mass

An ideal piston for LICH mode acts purely as a barrier between the driver gas and the test gas and is massless. In reality, the mass and consequent momentum of the piston result in bulk oscillation of the piston when subject to a rapid differential pressure. This happens at two occasions during a piston stroke: firstly, at beginning of the piston stroke when the firing valves connecting the reservoir to the barrel are opened; secondly, when the plug valve is opened to begin the shot. In the first case, the piston oscillations have little effect on performance. However, in the second case, the piston oscillations are transferred to the test gas and lead to oscillations in stagnation pressure, typically at a higher frequency than rarefaction wave transmission.

Another effect of the piston having mass is that the rarefaction waves created at the beginning of a shot are partially reflected by the piston. Acoustic analysis carried out by Oldfield et al. [133] and later by Magari & LaGraff [136] show that this effect is dependent on the ratio of the plug valve opening time, τ_d, to the time constant associated with the piston mass, τ_m, given by Equation 3.1.

$$\tau_m = \frac{m_P}{2A_P\ \rho_{3,o}\ a_{3,o}} \tag{3.1}$$

Where m_P and A_P are the piston mass and cross-sectional area and $\rho_{3,o}$ and $a_{3,o}$ are the density and speed of sound of the barrel test gas at plug valve opening. Results from the analysis showed that the reflected waves are only significant if the piston mass time constant is of a similar magnitude to the plug valve opening time.

At values of $\tau_d/\tau_m >> 1$, the strength of reflected rarefaction waves diminished greatly, being negligible at $\tau_d/\tau_m = 10$. The high temperature piston (right in Figure 3.3) has a mass of 0.68 kg, resulting in τ_d/τ_m values of between $\sim 10 - 80$ depending on the tunnel conditions chosen, indicating minimal wave reflections.

3.1.3.4 Matched Conditions

After the plug valve opens, mass is lost from the barrel. The flow is said to be matched if the volumetric flow rate from the reservoir to the barrel is equal to that from the barrel to the nozzle. This means that the test gas barrel pressure is constantly being replenished during the shot from further piston compression, leading to a steady barrel pressure and consequently constant nozzle supply pressure during the shot. If the volumetric flow rate from the reservoir is greater than that through the nozzle, the pressure will rise during a shot, and if it is lower, the pressure will fall during a shot.

Achieving a matched condition in HDT is made difficult due to a relatively high mass flow rate through the nozzle. In order to match this using the current tunnel setup, the reservoir pressure must be $\sim 6 - 8.5$ times the nozzle supply pressure at plug valve opening, depending on tunnel conditions. A high reservoir pressure causes a fast piston stroke, which is undesirable in LICH mode. A method, proposed by Jones et al. [132], to achieve both a slow piston stroke and matched conditions is to perform the piston stroke with a small reservoir flow area and increase it once the shot begins. This could be achievable in HDT by operating the two reservoir firing valves independently.

3.1.4 LICH Mode Infrastructure

When HDT was built originally in Oxford, operation in LICH mode was built into the design of the tunnel and, as such, some additional infrastructure has existed for a number of years. Additional infrastructure for LICH mode includes the piston and the piston reservoir (**1**). The piston is driven using an external reservoir of high pressure gas, which consists of a 152 mm bore, 9.14 m long tube situated below

the barrel. Unlike the barrel, the reservoir is unheated and remains at ambient temperature. This is advantageous for maintaining the temperature of the piston during the stroke, allowing lower temperature materials to be used and keeping a consistent fit between the piston and the barrel. The reservoir is connected to the barrel via 2 Hale Hamilton MV22 pilot-operated solenoid valves and 2 Douglas-Chero 2500 manually operated globe valves. The Hale Hamilton valves are fast-acting (with opening times < 250 ms) and are used to initiate the piston stroke, while the Douglas-Chero valves are used to adjust the mass flow rate and enable tuning of the piston motion. The maximum effective diameter of the barrel feed pipework is 17.7 mm. This was determined by measuring the rate of pressure rise during piston strokes. In addition to the reservoir and pipework, some basic logic was implemented into the programmable logic controller (PLC) which controls the tunnel.

In order for the full commissioning of LICH mode, there were several pieces of infrastructure which needed to be manufactured or altered which were carried out as a part of this work. The following paragraphs describe new modifications to the tunnel infrastructure during LICH mode commissioning.

Piston

The piston was designed to minimise mass while maintaining enough strength to both survive an impact with the end of the barrel and withstand a significant pressure differential during barrel filling and venting. Shown in Figure 3.3, two different pistons were designed - a “low” temperature piston suitable for use with the barrel cold and a “high” temperature piston, suitable for use with the barrel heated to 500 K.

The low temperature piston was designed primarily as a test piston for the initial stages of commissioning and is a fairly simple single-piece design. It is constructed from oil impregnated nylon which is self-lubricating, ensuring a smooth piston stroke, but limits its use to when the barrel is unheated. The piston has a free-running sliding fit with the barrel while maintaining a low level of leakage

with the three channels in the outer face acting as a rudimentary labyrinth seal. The mass of the low temperature piston was 0.28 kg.

The high temperature piston was designed to be able to run with the barrel pre-heated and consists of an anodised aluminium body and two brass rings, which are shrink fitted onto the body, to provide the sliding contact between the piston and the barrel. The piston has a loose fit with the barrel at room temperature and, due to the different rates of thermal expansion of the aluminium piston body and the steel barrel, a close sliding fit at the design point of 500 K. The high temperature piston has a mass of 0.68 kg.



Figure 3.3: Left: oil-filled nylon low temperature piston. Right: anodised aluminium high temperature piston.

Balance Line

During filling and venting of the barrel, the presence of the piston results in relatively small, trapped volumes of gas. This ultimately caused one of the low temperature pistons to break when the piston experienced a large pressure differential. To alleviate this problem, a balance line was added to the barrel. This consists of a length of fixed pipe connecting one of the ports along the length of the barrel to the rear flange, creating a path for gas to bypass the piston during filling and venting while being closed off during the firing sequence. The line is controlled via a remotely operated shut-off valve for safe operation while there is high pressure gas present in the facility.

Filling Plate

The downstream flange of the barrel contains a separate, removable plate through which the barrel is filled and vented. This is called the filling plate and was originally manufactured with a smaller bore (152.00 mm) than the rest of the barrel (152.76 mm) - this is shown in Figure 3.4 and the bore is indicated with *ID*. This created a step which the piston would impact if it travelled too far during a stroke. A new filling plate was manufactured with the same bore as the barrel. Additionally, a buffer was manufactured to stop the piston blocking the filling and vent lines.

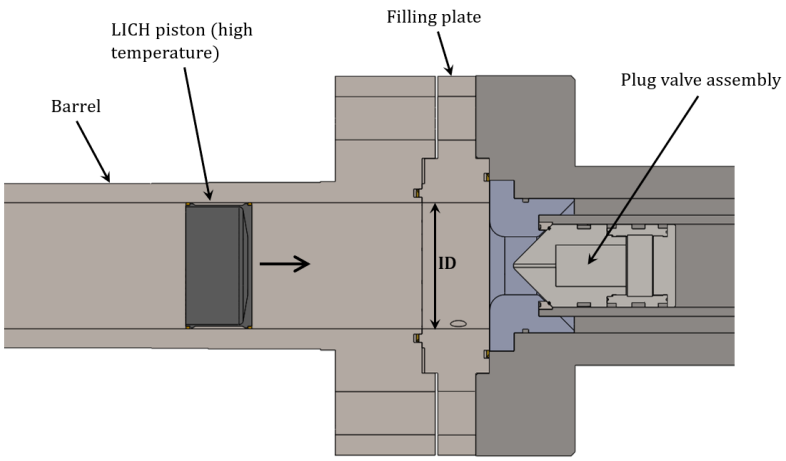

Figure 3.4: CAD image of the downstream end of the HDT barrel, showing the location of the filling plate.

3.2 Experimental Model

The purpose of the experimental model was to be able to rapidly produce test geometries of varying scales and configurations while being able to measure heat flux and flow properties in the vicinity of the geometries. This section describes how this was achieved. The model was completely designed and manufactured for this project, using only an existing stand for mounting in the tunnel.

3.2.1 Mechanical Design

3.2.1.1 Model Configuration

Experimental models for fundamental aerodynamic research are typically either flat plates or cones. Each configuration has advantages, depending on the exact nature of the study. Some optical diagnostic methods, such as schlieren imaging, are more easily achieved on cones (integration over the optical path can interfere with schlieren imaging on a flat plate), whereas IR thermography is better suited to flat surfaces where viewing angles are constant. Cones are less prone to picking up freestream disturbances, with transition distances being up to ~ 30 % further downstream in conventional wind tunnels when compared with flat plates [141]. Ultimately, the model configuration was decided in conjunction with the method of creating surface test geometries. Two blocks, making up the outer surface of the model, are raised and lowered in order to generate steps, gaps, and protuberances in different combinations. This is only achievable on a flat plate model due to the 2-dimensional motion of the blocks. A schematic of the general configuration of the model are presented in Figure 3.6.

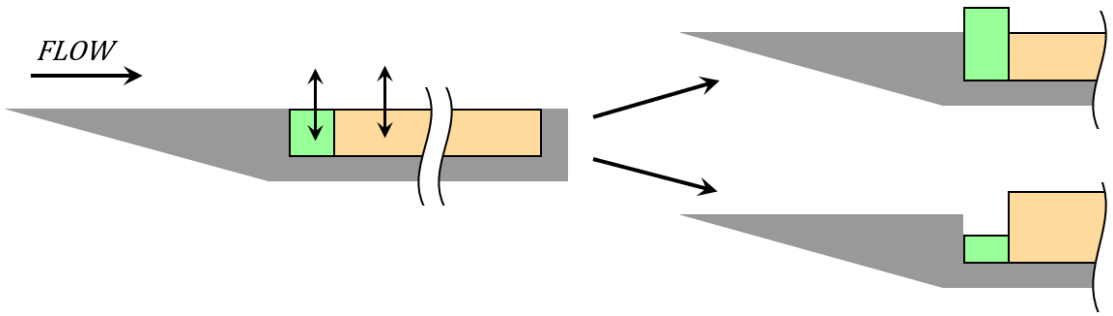

Figure 3.5: Schematic of the experimental model design, showing how different test geometries can be produced.

The test geometry constitutes a short front block located at an axial distance of 150 mm from the leading edge. The block has a length (in the flow direction) of 5 mm and width of 160 mm. This block is immediately followed by a longer rear plate of length 390 mm and width 110 mm. Both parts can be moved in and out of the plane of the plate, creating steps of different heights. By moving each block/plate independently, a number of different combinations of steps, gaps, protuberances and

other geometries can be tested. Figure 3.6 shows the overall dimensions of the model with the front block and rear plate highlighted in green and peach, respectively.

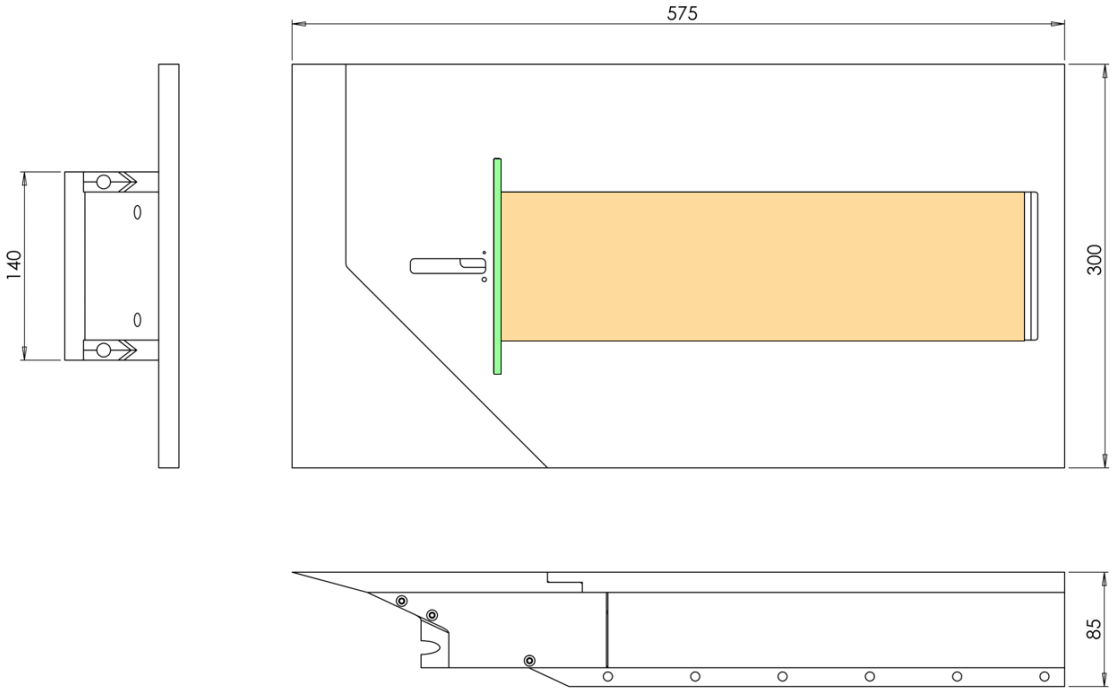

Figure 3.6: Overall dimensions of the flat plate model.

In order to obtain the most value from the experiments, the aim was to maximise the number of geometry scales and configurations tested. Changing the configuration of a model between tests would typically be a manual task. In the HDT this requires the test section to be vented up to atmospheric pressure and pumped back down to a vacuum, adding a significant amount of time to each test. Therefore, to achieve greater testing efficiency, the model incorporates externally controlled actuators to alter the test geometry. The internal mechanism that accomplishes this is described in Section 3.2.1.3.

The top plate of the model is significantly wider than the rear plate of the test geometry. This is to avoid edge effects emanating from the lead edge influencing the flow over the test surface. Figure 3.7 shows approximate areas where the flow might be affected.

The top half of the diagram corresponds to Mach 5 flow and the bottom corresponds to Mach 7 flow. The bounding lines are determined by the Mach angle,

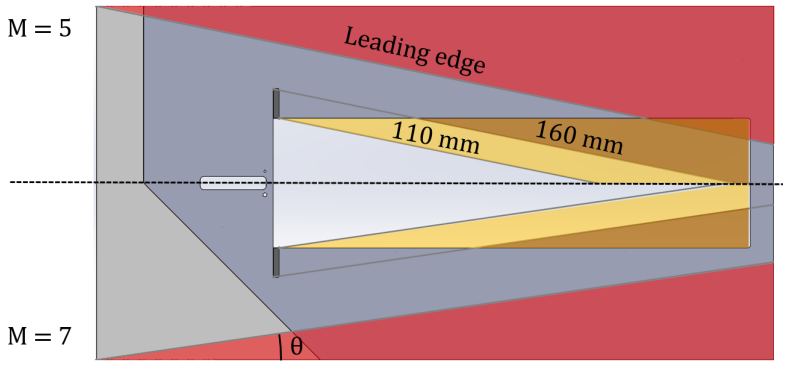

Figure 3.7: Approximate disturbance areas on the top plate.

defined by Equation 3.2, giving an upper bound to the area of potential disturbances.

$$\theta = \sin^{-1}\left(\frac{1}{M}\right) \tag{3.2}$$

It can be seen that, due to the width of the main plate, the influence of the leading edge only affects a small portion of the rear plate. Also shown are lines originating from the upstream corners of the front test block. This illustrates the reason for the front block being wider than the rear plate: the wider front block results in a significantly smaller disturbance area than if it was the same width as the rear plate.

3.2.1.2 Construction

The model is constructed from four subassemblies, shown in Figure 3.8: the top plate, the base/housing for the internal cavity, the internal mechanism, and the stand. As seen, the model is in a vertical orientation. This is to allow the 'top' surface to be visualised with an IR camera, which has optical access through the side of the test section. It was decided that data from the IR camera would be the most important and that the potential advantages of mounting the model horizontally could be neglected - this primarily being the capture of schlieren imagery. A sturdy stand and attachment arrangement were prioritised over additional measurement and flow visualisation techniques.

Figure 3.9 shows an exploded view of the top plate subassembly. The top plate itself is made up of two parts: the main plate and the interchangeable leading edge. Two versions of the leading edge piece were made: one straight and one

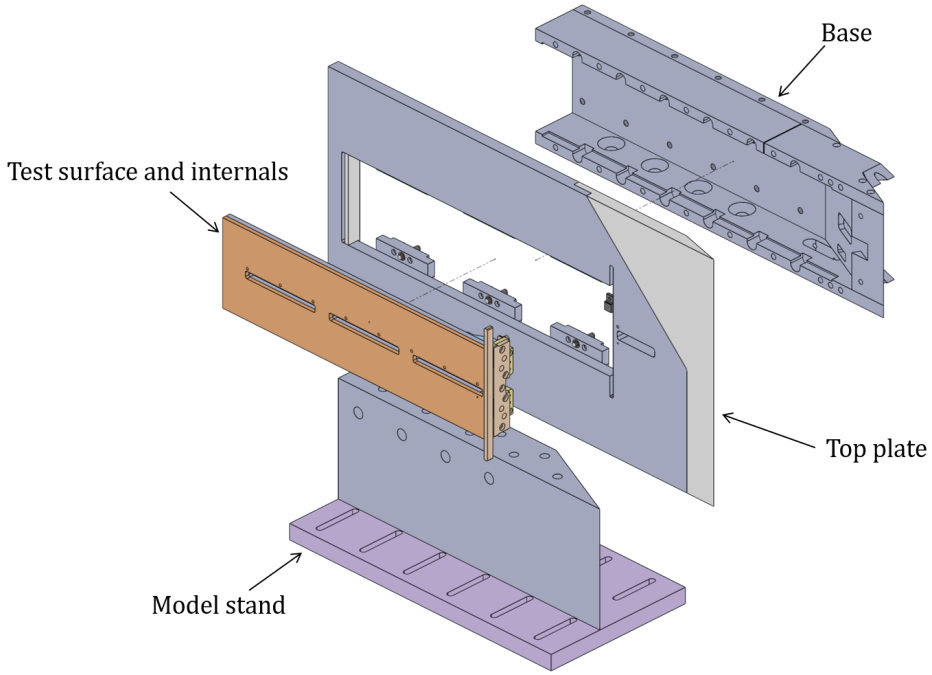

Figure 3.8: Exploded view of the model, showing the subassemblies.

with a sweep angle of 45 degrees. These are interchangeable due to the design of the lap joint joining the leading edge with the main plate, which accounts for the reduced running length on one side. The centreline running length (150 mm to the front block) is maintained between both leading edges. The main plate and the leading edges are constructed from 17-4 PH H1150. This is a precipitation hardening, heat treated, stainless steel with a yield stress of 725 MPa and was chosen due to its high strength and resistance to corrosion, providing a durable surface finish. The parts were finished with a surface grinder to achieve an average surface roughness (Ra) of 0.8 µ m. Additional parts in the top plate subassembly are mounting brackets for the rear plate adjustment and the rear cable interface plate. See Section 3.2.1.3 for a description of the adjustment mechanism.

The base, shown in Figure 3.10, is made up of two side walls, a front plate, and a back plate. The right wall is structural while the other three parts are simply cover plates which enclose the interior volume of the model. This volume houses the cabling for the instrumentation. The side walls contain holes for forward facing probes (see twin probe and model alignment probes in Sections 3.3.4 and 3.3.5).

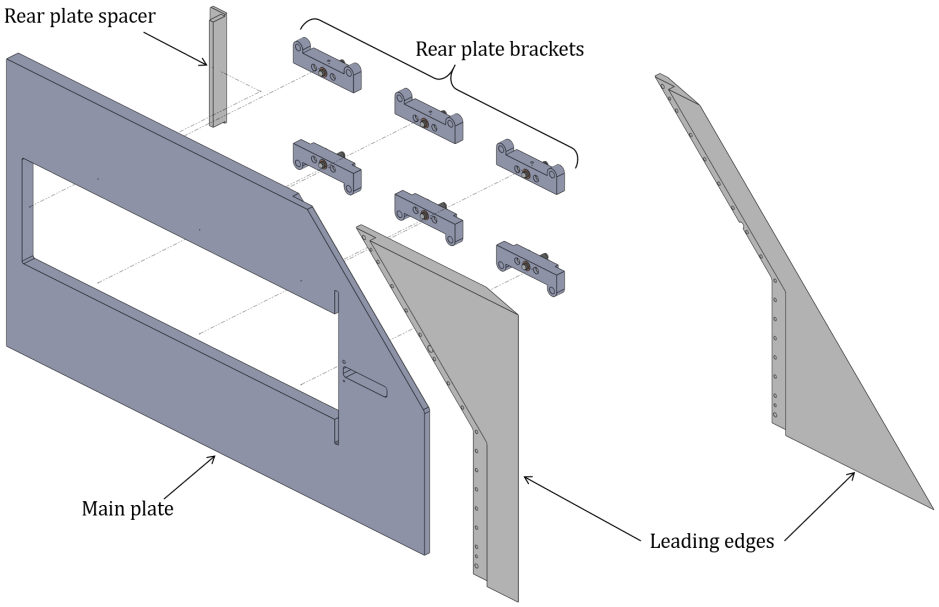

Figure 3.9: Exploded view of the top plate assembly, showing constituent parts. The swept leading edge is also shown.

The left side wall is split to allow the front section to be interchanged when using the swept leading edge. Components of the base assembly are made of 6082-T6 aluminium, which has a high yield strength of 300 MPa and has good machinability.

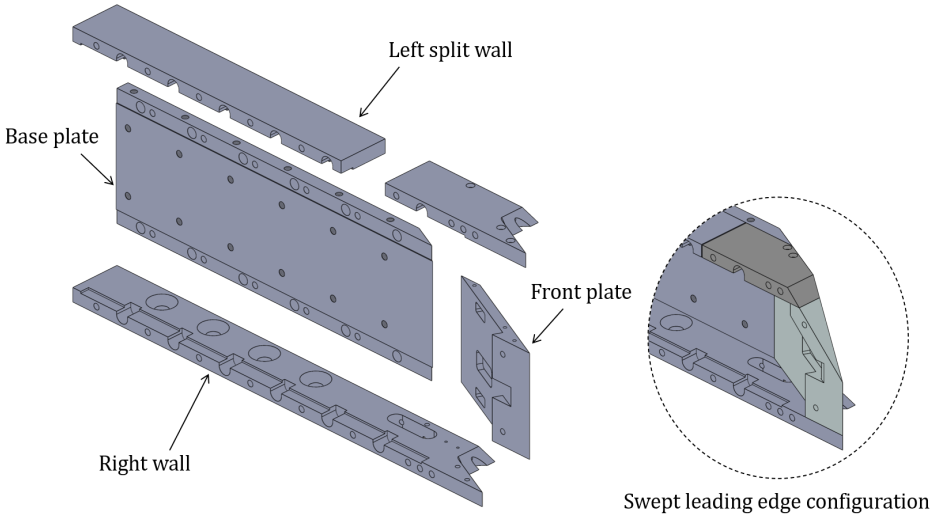

Figure 3.10: Exploded view of the base assembly, showing constituent parts. The configuration for the swept leading edge is also shown.

The internal assembly also constitutes the test surfaces, with the PEEK parts being directly attached to the adjustment mechanism. This assembly is shown in

Figure 3.11 and is described in more detail in the following section.

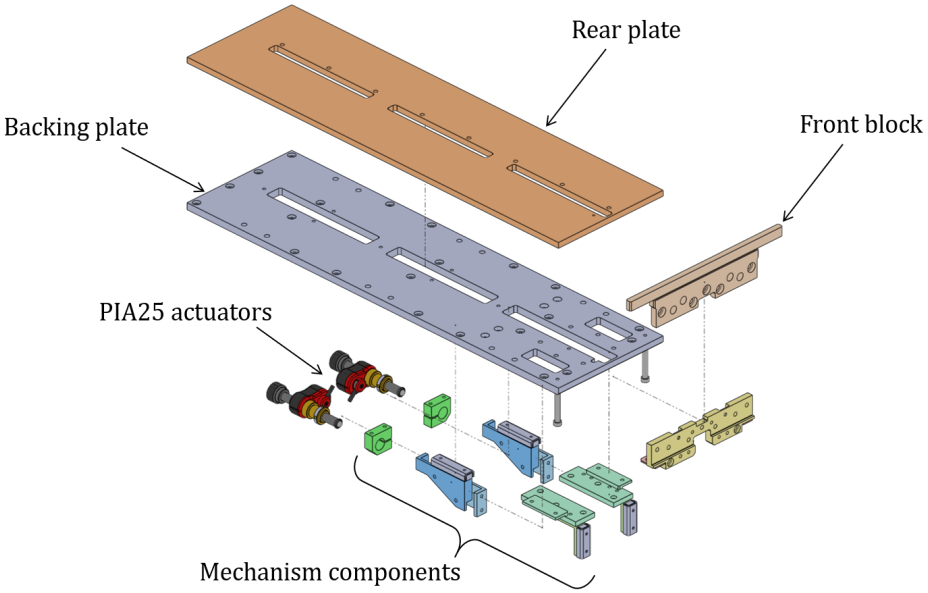

Figure 3.11: Exploded view of the test surface and internal assembly, showing constituent parts. The parts labelled 'rear plate' and 'front block' are constructed from PEEK.

3.2.1.3 Block Actuation

Front Block

The front block is adjusted remotely using two Thorlabs PIA25 piezoelectric inertia actuators. The actuators function by repeatedly exciting a piezoelectric crystal which pushes laterally on a screw thread. This rotates the thread by a small amount each cycle, translating the screw and moving the end of the actuator. The step size is given as 20 nm, but this is not repeatable and can change by up to ±20 %, depending on the load. Additionally, the actuators are open loop and do not provide feedback, so require an independent measurement to determine their position. The actuators are positioned in a horizontal orientation to allow them to fit inside the model cavity. A mechanism converts their horizontal motion into the vertical motion required to raise and lower the block. The mechanism is shown in Figure 3.12 and is colour-coded to highlight the different components.

The actuators are shown in red; the 'static' parts in orange; the front test block in green; and the intermediate parts in blue. The motion of each part relative to

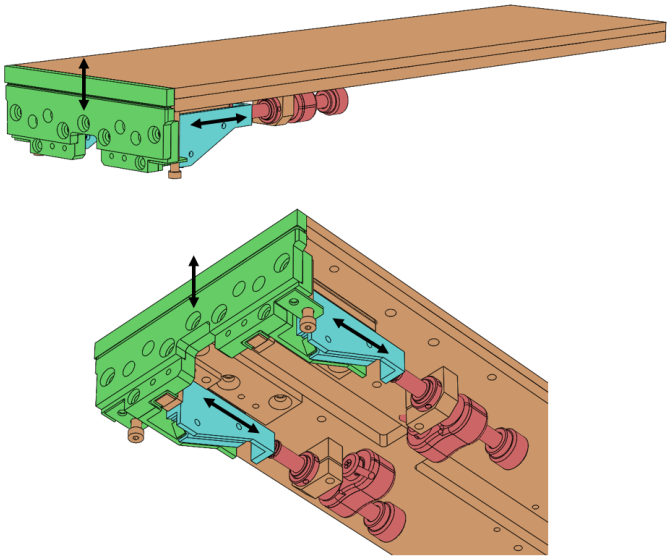

Figure 3.12: The internal parts of the model, colour coded. Red: actuators. Orange: stationary. Blue: horizontal motion. Green: vertical motion. Motion is indicated by arrows on the isometric view.

the orange parts is indicated by arrows. The blue intermediate parts contain three linear slides (per actuator): one horizontal, one vertical, and one at an angle of 26.6°. This arrangement transforms the horizontal motion into vertical motion at a ratio of 2:1, meaning that the front block moves half the distance that the actuators move. Compared to a direct connection between the actuator and the block, this allows for more precise positioning of the front block and reduces the force required by the actuators. Two springs provide the returning force for the front block and exert $\sim 6 - 12$ N each, depending on the position of the mechanism.

Having two actuators side-by-side allows for any offset in the lateral angle of the front block to be corrected. This also requires two height measurements at the location of each actuator (see Section 3.3.6). The overall repeatability of the position of the front block is estimated to be ± 10 µm.

Rear Block

Due to its size and need for stability during shots, the rear block (or plate) is manually adjusted. This is achieved using six Thorlabs F6MSS30 fine adjustment screws, with M6 x 0.25 mm threads, arranged around the perimeter of the plate.

The fine adjustment screws are used in conjunction with a pair of standard pitch M5 holding screws, as shown in Figure 3.13.

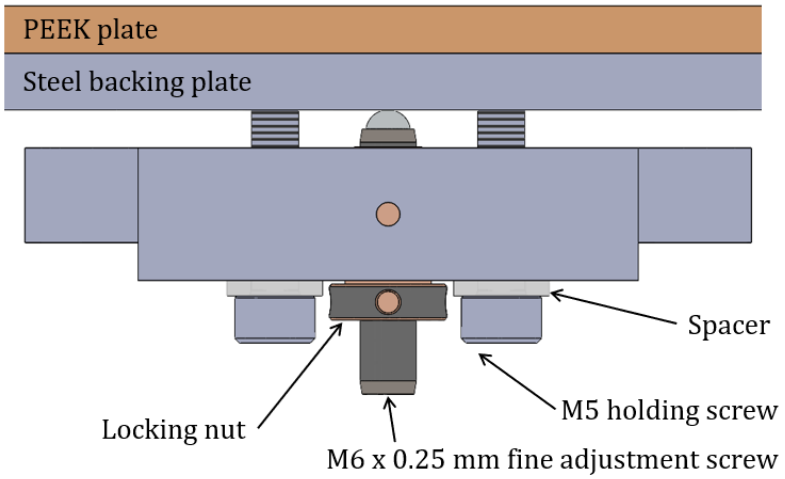

Figure 3.13: One of the six manual height adjustment assemblies for the rear plate.

To move the plate, first the holding screws and locking nut are loosened, then the fine adjustment screw is moved to the required position. Finally, the holding screws and locking nut are tightened. The screws are tightened according to a torque sequence in order to prevent any warping of the upper surface of the plate. This arrangement of manually adjusted and clamped screws provides more stability and control over the exact height of the plate than a remotely actuated system. The flatness of the plate is measured during adjustment using a dial indicator.

3.2.1.4 Leading Edges

Both the straight and swept leading edges were manufactured to be nominally sharp. However, in order to have more control over boundary layer transition, some modifications were made to add a larger radius to the leading edges. Three additional bluntnesses were used with 100 µm, 2 mm, and 6 mm diameters. The 2 and 6 mm bluntnesses were achieved by affixing a steel rod underneath the leading edge, backed by a 3D printed support. The 100 µm leading edge was achieved using Kapton tape of 50 µm thickness. This resulted in a backward-facing step of height 50 µm at an axial position of ±20 mm but a step of this size was determined to be insignificant. Figure 3.14 presents diagrams of both configurations.

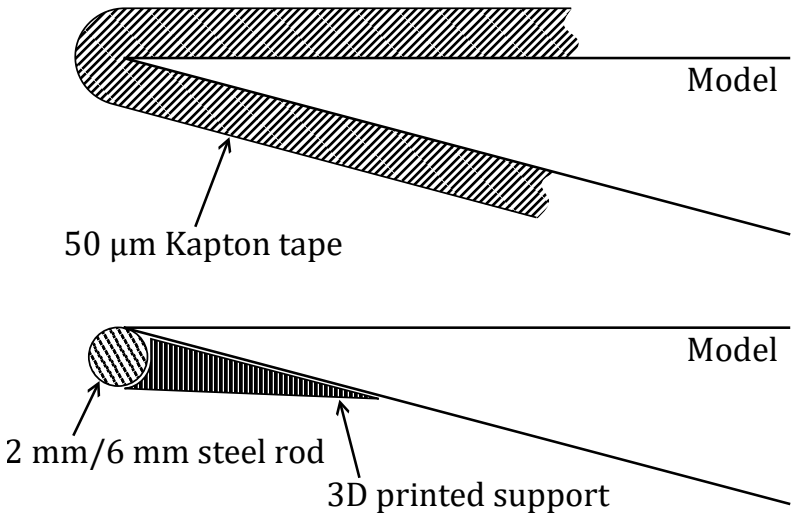

Figure 3.14: Diagram of the two blunt leading edge modifications.

3.3 Instrumentation

The model was instrumented to measure the following quantities:

- Surface heat flux both on the plate (upstream and downstream of the geometry) and on the test geometry itself to evaluate the heat flux augmentation.
- Properties of the boundary layer on the top surface of the flat plate, including high frequency pressure fluctuations, whether the boundary layer has transitioned from laminar to turbulent and, if possible, the location of the transition.
- Angle of attack of the model.
- Freestream flow properties.
- The height of each block making up the feature geometry.

A diagram of the model with top-plate instrumentation indicated is given in Figure 3.15. This section details the methods used to measure each of the listed quantities.

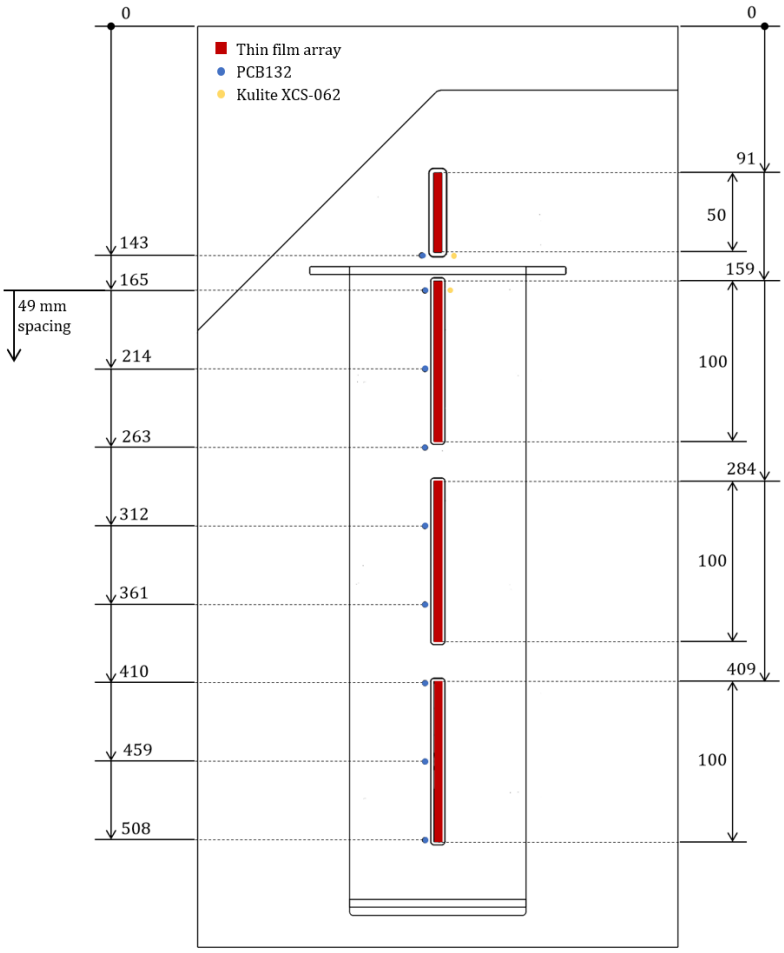

Figure 3.15: The experimental model with instrumentation indicated. All dimensions are in mm, with 0 mm being the leading edge.

3.3.1 Surface Heat Flux Measurements

3.3.1.1 IR Thermography

IR thermography was the primary heat flux measurement, providing a high spatial resolution for heat flux measurements on the PEEK test surfaces. A Telops M3k FastCam was used to view mid-wave infrared (MWIR) in the range 1.5 - 5.2 µm. The camera recorded a windowed frame of 320 x 128 pixels at 4000 frames per second with an integration time of 90 µs. The camera was positioned outside the test section and viewed the model through a 5 mm thickness UQG Optics sapphire window with an anti-reflective coating. The camera was oriented so that the incident angle was less than 50° – this is the approximate limit at which the emissivity of an insulator can be assumed to be constant [142]. Two lenses were used with focal

lengths of 13 and 50 mm. The 13 mm lens allowed the entire test surface to be imaged while the 50 mm lens provided a higher resolution near the step location. Table 3.1 provides some of the relevant parameters for each lens.

Table 3.1: Overview of some parameters associated with each IR lens.

Lens focal length [mm]	Waveband [µm]	FOV [mm]	Pixel size [mm]	τ_{shot}/τ_{cal}
13	3.0 - 4.9	440 x 150	1.2 - 1.4	0.9722
50	1.5 - 5.15	120 x 50	0.4	0.9764

The IR thermography setup used in HDT was pioneered by Naved [143, 144]. However, a slightly different data reduction scheme was used in this work. This is detailed in the following pages.

Fundamental Concepts

The total amount of electromagnetic radiation emitted from a black body is described by Planck's Law, the wavelength form of which is shown in Equation 3.3:

$$I_s(\lambda) = \frac{2\pi hc^2}{\lambda^5} \cdot \frac{1}{\exp\left(\frac{hc}{\lambda k_B T}\right) - 1} \tag{3.3}$$

Where I_s is the emitted intensity of radiation per unit wavelength, h is the Planck constant, c is the speed of light in a vacuum, and k_B is the Boltzmann constant. The sensors which make up the focal plane array (FPA) of an IR camera directly measure incident radiation. This means that the measured camera signal, U, can be described by an equation of the same form as Planck's Law:

$$U = \frac{R}{e^{B/T} - F} \tag{3.4}$$

Where the constants R, B, and F are all a function of the optical system. In reality, the radiation measured by the camera is made up of contributions from other sources in addition to the object of interest. The two main additional components come from radiation reflected from the object being measured and radiation being emitted from objects in the optical path - primarily from the atmosphere and any windows being used. Emissivity and transmissivity terms can also be included to

account for the fact that the object being measured is not a black body and that the optical path does not transmit all emitted radiation. A more complete equation describing the IR setup is given by Astarita [145], shown in Equation 3.5:

$$U_D = \epsilon_{obj}\tau_{atm}\frac{R}{e^{B/T_{obj}} - F} + (1 - \epsilon_{obj})\tau_{atm}\frac{R}{e^{B/T_{reflect}} - F} + (1 - \tau_{atm})\frac{R}{e^{B/T_{atm}} - F} \tag{3.5}$$

The terms on the right-hand side of Equation 3.5 describe (with associated temperatures), in order: the emitted radiation from the object of interest (T_{obj}); the radiation from the environment which is reflected from the object of interest ($T_{reflect}$); and the emitted radiation from the atmosphere (T_{atm}). During calibrations and shots, the reflected and atmospheric temperatures are both the ambient temperature of the system and remain constant. This reduces the last two of the three terms in Equation 3.5 to constants which can replaced by a single constant, G, as proposed by Zaccara et al. [146].

IR Calibration Procedure

To calibrate the IR system, a CI Systems SR-33N-7A extended area blackbody calibrator was placed in the test section in place of the experimental model. The calibrator consists of a flat surface of size 178 x 178 mm which can be set to specified temperatures. The emissivity is given as 0.98, the spatial uniformity is given as 0.01 K, and the temperature accuracy is given as 0.05 K. During calibration, the blackbody was set to a number of temperatures spanning the range of surface temperatures expected during model testing. Images were recorded at each temperature set-point, giving data points for camera measurement, U, as a function of observed temperature for the particular optical system. The calibration equation is given in Equation 3.6.

$$U_{D,\,cal} = \frac{R}{e^{B/T_{cal}} - F} + G_{cal} \tag{3.6}$$

This is analogous to Equation 3.5 with the last two terms being absorbed into the constant G. The constants R, B, F, and G are determined by fitting

Equation 3.6 to the U and T_{cal} data on a pixel-by-pixel basis. The Levenberg-Marquardt least squares fitting method is used. Figure 3.16 shows the fitted calibration curve for a single pixel.

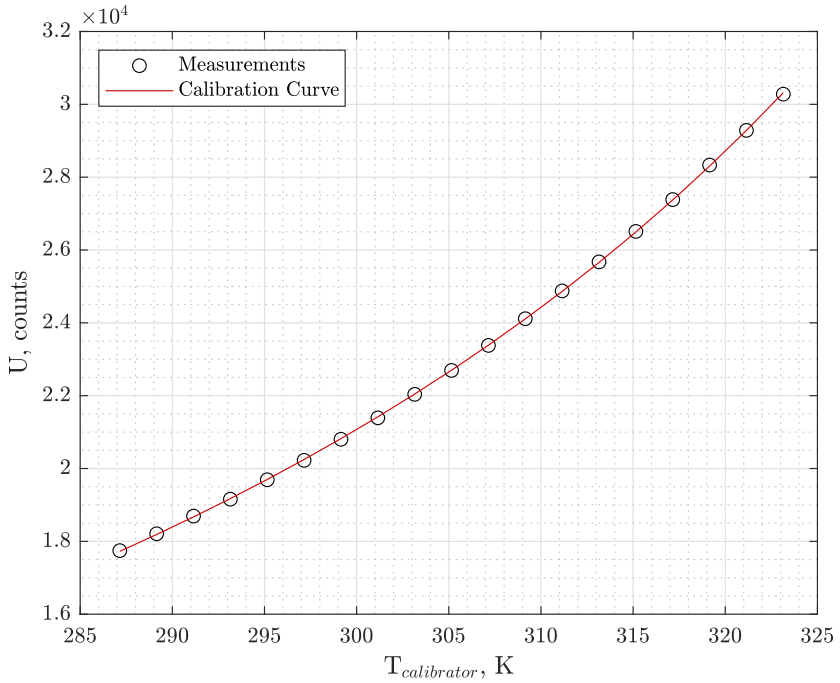

Figure 3.16: Calibration curve for a single pixel.

If an in-situ calibration is carried out (where all properties of the optical system are kept constant between the calibration and the test), the emissivity and transmissivities of the optical system can be ignored. For this work, a so-called semi in-situ calibration was performed [147]. This involves a calibration using the majority of the optical setup as is used in the shot but with a change in total transmissivity of the system. The total transmissivity changes due to the fact that the calibration is carried out in ambient air, whereas shots use nitrogen as the test gas. Atmospheric air contains significant quantities of CO_2 and water vapour which absorb heavily in MWIR. The total radiated intensity is also affected by the material being observed: materials with higher emissivities emit more IR radiation for a given temperature. These factors all have an influence on the measured counts from the camera. Equation 3.7 describes the measured IR signal during a shot:

$$U_{D,\,shot} = \frac{CR}{e^{B/T_{shot}} - F} + G_{shot} \tag{3.7}$$

Where C is a constant which converts between calibration and shot optical systems, defined by Equation 3.8.

$$C = \frac{\epsilon_{shot}\tau_{shot}}{\epsilon_{cal}\tau_{cal}} \tag{3.8}$$

The difference in transmissivity between calibrations and shots is entirely caused by the difference in test section gas composition [148]. To calculate the difference in transmissivities, spectral transmittance data for 0.5 m of air (simulating the air in the test section during a calibration) was multiplied by the curve given by Planck's Law. The total transmissivity is the ratio of the integrated spectral intensities of Planck's Law and the new curve across the waveband of the lens.[1] Figure 3.17 shows the two curves as well as the wavebands for each lens. Transmissivity data for atmospheric air and nitrogen was generated using the online tool, SPECTRA [149], created by Mikhailenko et al. [150]. Values of emissivity are 0.98 and 0.93 for the calibrator and PEEK model surface, respectively. The emissivity of the PEEK was previously determined by Naved [143] using a bench top calibration device which heats a sample to a range of specified temperatures and measures the emitted radiation using the same Telops camera. Emissivity was assumed to be constant due to the minimal temperature change (< 5 K) experienced by the material during testing.

The constant G_{shot} in Equation 3.7 is different to G_{cal} in Equation 3.6 due to the differences in optical setup and ambient temperature. In order to assess the magnitude of G_{shot}, two assumptions are made: the value of G_{shot} remains constant for the duration of the shot; and the pre-shot surface temperature of the model is the same as the measured ambient temperature. G_{shot} can then be defined by Equation 3.9:

$$G_{shot} = U_{D,pre-shot} - \frac{CR}{e^{B/T_{amb}} - F} \tag{3.9}$$

[1]This ratio should also include the transmissivity of nitrogen. However, the difference this makes does not appear until the 12th significant figure.

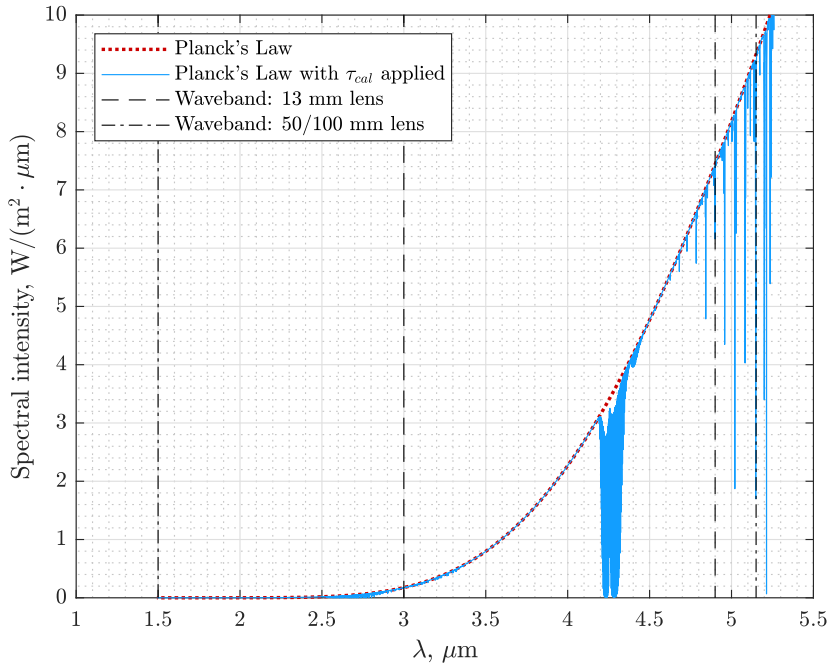

Figure 3.17: Total transmissivity for the calibration system applied to Planck's Law. Transmittance wavebands for the two IR lenses are shown.

Applying this to Equation 3.7 and rearranging for object temperature results in Equation 3.10, which provides a relationship between the measured camera signal and the temperature of the object of interest during a shot.

$$T_{obj} = \frac{B}{\ln\left(\frac{CR}{U_{D,shot} - U_{D,pre-shot} + \frac{CR}{e^{B/T_{amb}} - F}} + F\right)} \tag{3.10}$$

Image Adjustment

IR footage captured through the 13 mm lens featured distortion in the form of a fish-eye effect. To remove this, images were transformed onto a real-world coordinate system. This was achieved by capturing an image of a grid of known dimensions in place of the model. The alignment grid consisted of a piece of paper with aluminium tape, which provided a high contrast with the paper, arranged in an array at known locations. This was affixed to the surface of the model to provide reference locations for alignment. The pixel locations of the grid points

on the image were transformed to the real world coordinates with a polynomial transformation generated using the Matlab function `fitgeotform2d`. Figure 3.18 shows the original grid of points and the transformed points. The polynomial transformation could then be applied to shot data.

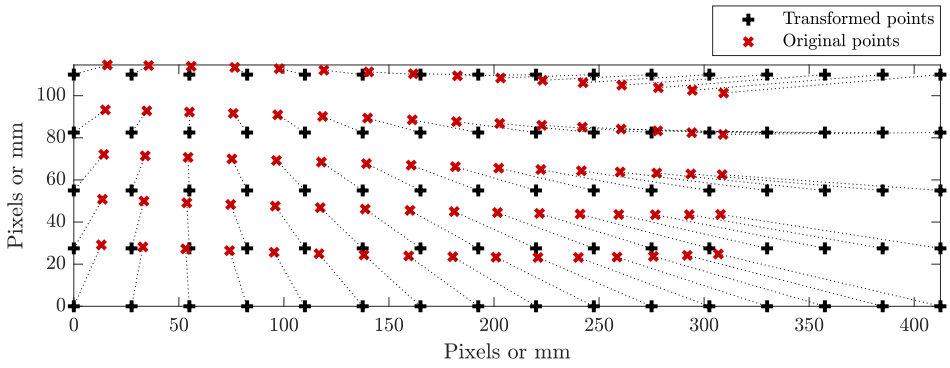

Figure 3.18: Points adjusted by the image transformation.

3.3.1.2 Thin Film Heat Transfer Gauges

A series of thin film heat transfer gauges were located on the model centreline, upstream and downstream of the step. Upstream gauges were placed to assess the state of the incoming boundary layer. Downstream gauges were used to quantify levels of heat flux augmentation. Four arrays were used, the details of which are summarised in Table 3.2.

Table 3.2: Details of thin film arrays used on the model.

Array	x_{start}, mm	length, mm	Spacing, mm	# gauges	# gauges used
Up	90	50	∼1.6	32	14
Down 1	159	100	5	20	9
Down 2	284	100	10	10	7
Down 3	409	100	10	10	5
Total	-	-	-	62	35

Not all gauges were used due to a limit on the number of channels available in the data acquisition system.

Gauges were manufactured by applying thin layers of platinum paint, by hand, onto a Macor substrate before curing at a high temperature. Thicker layers of gold

paint were applied around the corners of the Macor so that wires could be soldered to the underside of the array. The painted Macor was enclosed in a 3D printed housing and the rear cavity was potted using Stycast 2850 FT. Figure 3.19 shows a schematic of the array in cross-section and a sample from one of the existing arrays.

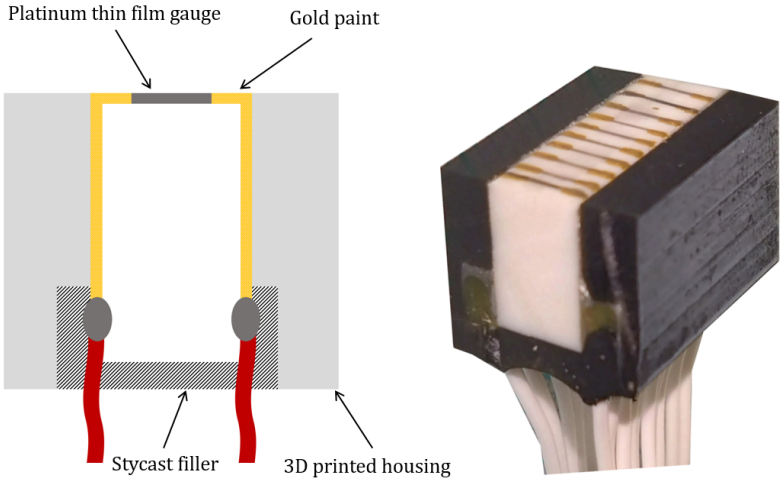

Figure 3.19: Construction of the thin film gauge arrays.

Thin film gauges operate as resistive temperature detectors (RTDs) in that the resistivity of the platinum from which the gauge is made from is highly sensitive to temperature. The temperature of a gauge during a test can be calculated using coefficients for a straight line relating temperature to resistance, given in Equation 3.11

$$T_{gauge} = mR_{gauge} + c \tag{3.11}$$

Where the gradient, m, and the offset, c, are determined through pre-calibration.

Gauge Calibration

Gauges were calibrated using a Friocell FC222 high-uniformity oven, which cycled through a number of temperature set-points exceeding the range of expected temperatures that the gauges would experience during a test. For flat plates in HDT, a range of 10 - 50 °C is suitable. The oven was set to hold at each temperature for 2 hours, allowing the temperature of the entire model to stabilise before data was recorded. Figure 3.20a shows typical temperature traces of the gauges during

a calibration and Figure 3.20b shows the temperature vs resistance relationship for a gauge on the upstream array.

Data Acquisition

Data was recorded using the in-house Lancaster HTA5 system, which acts as an amplifier and data acquisition system for thin film gauges.

The amplifiers provide a constant current to each sensor, the level of which can be set independently, along with a DC voltage offset, to tune the supply to be appropriate to the gauge resistance. The constant current sources allow the resistance of the sensors to be calculated by measuring the voltage. This then allows Equation 3.11 to be used to calculate the temperature. Sensor voltages are boosted before entering the ADC with a frequency dependent gain. Higher frequencies are amplified more than lower frequencies, with DC voltages having a gain of unity. This is done to reduce the effect of electrical noise on higher frequency components of the signal. Prior to any analysis, the data is passed through a deboost filter, returning the sensor voltage.

3.3.1.3 Conversion of Temperature to Heat Flux

Both measurement techniques in this section, IR thermography and thin film gauges, measure a change in temperature rather than the heat flux to the surface directly. The conversion between a temperature history to a heat flux is an inverse heat transfer problem. In most cases these problems are ill-posed and difficult to solve. However, certain assumptions can be made to simplify the process. Firstly, the substrate can be assumed to transfer heat 1-dimensionally: through the thickness of the material. Secondly, the time scales involved with short duration wind tunnel testing can be assumed to be short enough that the thermal penetration depth is less than the material thickness during the test time. This criterion is given in Reference [151] by Equation 3.12.

$$t = \frac{L^2 \rho c_p}{16k} \tag{3.12}$$

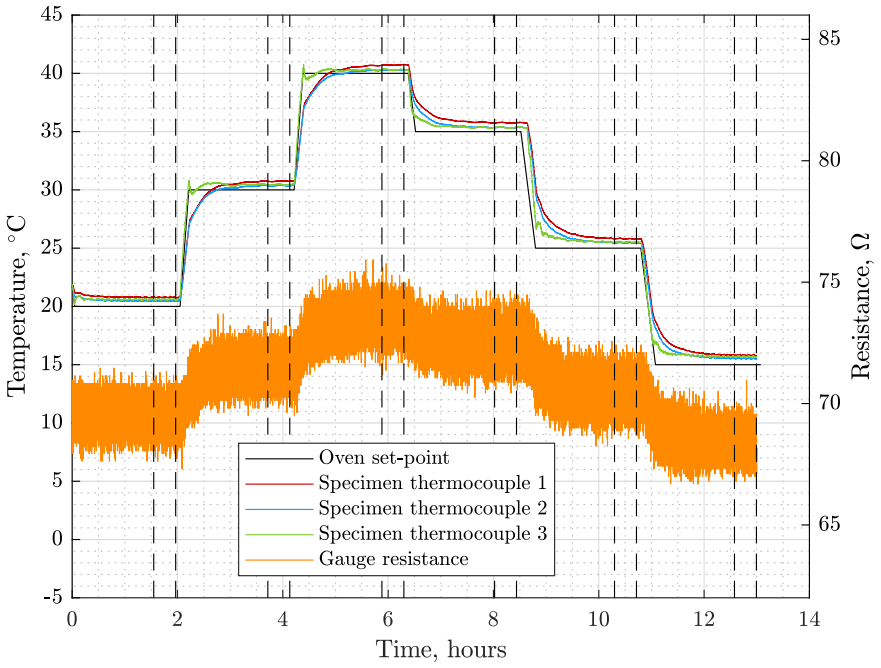

(a) Temperature history for a calibration, showing the averaging periods. The resistance of the gauge shown below is also plotted.

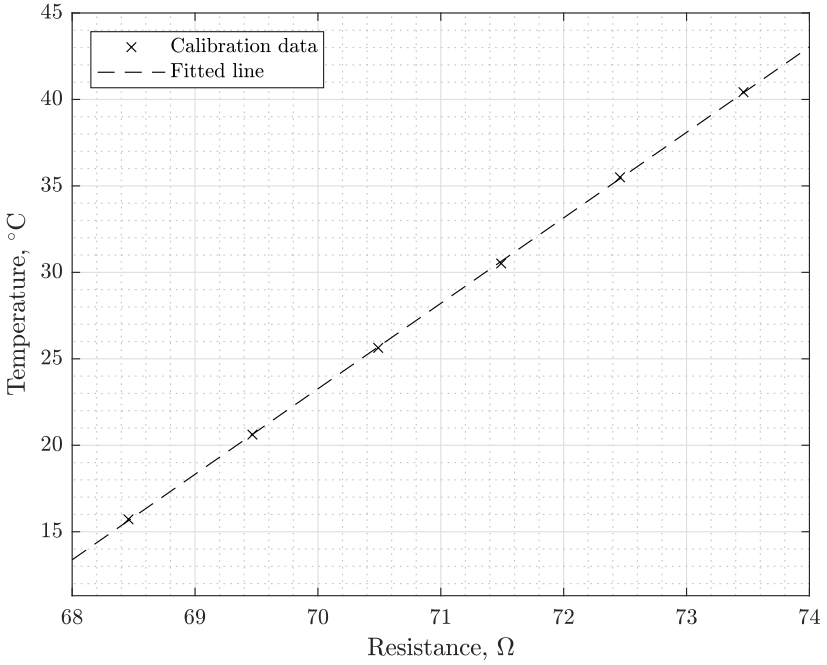

(b) Temperature vs resistance relationship for a thin film gauge on the upstream array. $m = 4.9437$ °C/Ω and $c = -322.8$ °C (referring to Equation 3.11).

Figure 3.20: Calibration data for a single thin film gauge.

Where t is the time taken for the change in temperature to propagate through a substrate of thickness L.

Given these two assumptions, the relationship between surface temperature and surface heat flux is given by Equation 3.13, from Schultz & Jones [152].

$$T_s = \frac{2\dot{q}_s}{\sqrt{\pi}}\sqrt{\frac{t}{\rho c_p k}} \tag{3.13}$$

To apply this to shot data, a method, developed by Oldfield [153], is employed which applies a filter to dT data based on the expected impulse response of the system, dT being calculated by subtracting the initial averaged value from the temperature history of each gauge or pixel.

The properties ρ, c_p, and k determine the rate of heat transfer to a specific material with the thermal products, $\sqrt{\rho c_p k}$, of PEEK and Macor being shown in Table 3.3.

Table 3.3: Thermal products of test materials.

Material	$\sqrt{\rho c_p k}$ [J m^{-2}K^{-1}s$^{-0.5}$]
PEEK	624
Macor	1705

The Stanton number, a non-dimensionalised form of heat flux, is then calculated. This is given by Equation 3.14

$$St = \frac{\dot{q}}{\rho_e u_e c_p \left(T_{aw} - T_w\right)} \tag{3.14}$$

Where ρ and u are evaluated at the boundary layer edge. T_{aw} is the adiabatic wall, or recovery, temperature given by Equation 3.15.

$$T_{aw} = T_e\left(1 + r\left(\frac{\gamma - 1}{2}\right)M_e^2\right) \tag{3.15}$$

Where r is the recovery factor and is given by $\mathrm{Pr}^{1/2}$ for laminar flow, which gives reasonable accuracy for T_{aw}. For turbulent flow, the value of $r = 0.885 \pm 0.015$ is used, which is a result from a survey of hypersonic test data carried out by Leontiev et al. [154]. Alternative methods of calculating T_{aw} using experimental data (such as regression of heat flux vs wall temperature) were attempted but were ultimately

not possible to perform due to the very small temperature change experienced by each sensor or IR pixel during a shot (< 2 K).

3.3.2 Measurement Uncertainties

This section details the uncertainty analysis carried out on the IR and thin film gauge heat transfer measurements. The known uncertainties in directly measured quantities are used to calculate uncertainties in subsequently derived results. The method, described by Coleman and Steele [155], used to propagate uncertainties from their sources to derived quantities involves summing the squares of contributions from each variable.

$$u_r^2 = \sum_{i=1}^{J} \left(\frac{\partial r}{\partial X_i} \right)^2 u_{X_i}^2 \tag{3.16}$$

Where u_r is the overall uncertainty of the variable r, which itself is a function of multiple measured variables: $r = f(X_i, X_{i+1}, ...X_J)$. The total uncertainties attributed to each measured quantity, X, are denoted by u_X and the partial derivative term quantifies the influence of each variable, X, on the derived quantity r.

The process which takes the raw data from the IR camera through to a Stanton number is complicated and involves a number of independently measured quantities. The calculation of the uncertainty of the resulting Stanton number was carried out by perturbing inputs to each of the Matlab functions which perform the basic operations in the processing chain (e.g. the calculation of calibration constants R, B, and F from black body calibration data). By perturbing the inputs, the partial derivative, and therefore contribution to total uncertainty, can be calculated following Equation 3.16. The majority of sources of uncertainty were taken from datasheets for materials and sensors or from calibrations carried out externally. The exception is the uncertainty in $U_{D\ shot}$ where the black body calibration was used.

IR Calibration Uncertainty

The pixel-wise calibration curves (see Figure 3.16) have an uncertainty associated with the quality of the fit. This is quantified by calculating the expected temperature

from the measured camera input, U, for each pixel based on the fitted constants R, B, F, and G. The mean absolute error (MAE) is calculated for each pixel. This is defined as the average of the difference between the calculated temperature and the calibrator set-point temperature. Figure 3.21 shows the absolute error for the fitted curve shown in Figure 3.16 as well as the mean value (the MAE). The MAE is a quantity associated with a single pixel. To quantify the total error for a camera position, the MAE is plotted as a colour map for the full camera frame. The average value of the MAE taken over the frame is used as the total error originating from the calibration process. Figure 3.22 shows this for one of the camera positions. In this case, the total error (mean MAE) is 0.047 K.

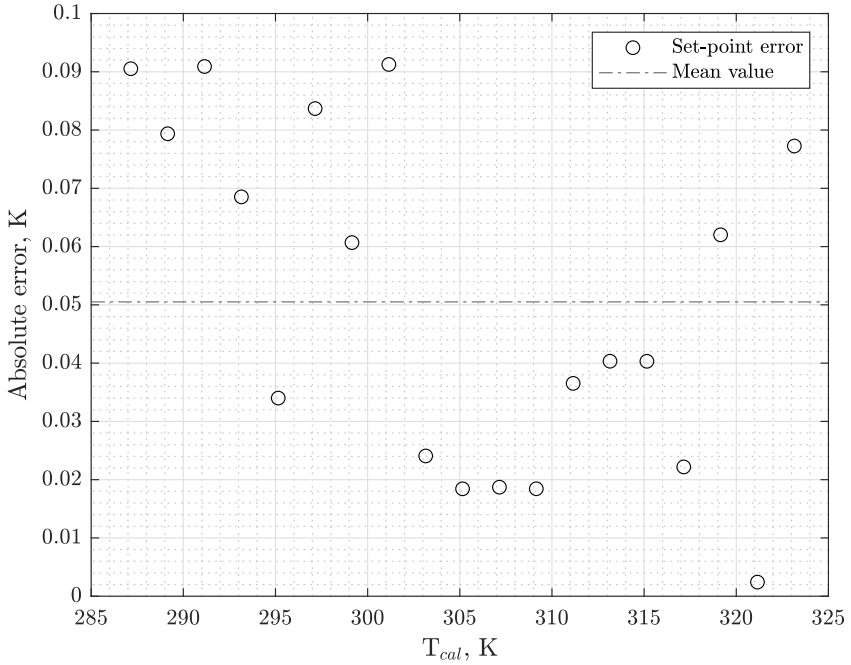

Figure 3.21: Absolute error of calibrator set-points for a single pixel.

The MAE calculated from the curve fitting process was fed into the calibration equation (Equation 3.6) along with uncertainties for R, B, and F to estimate an overall uncertainty in $U_{D\ shot}$.

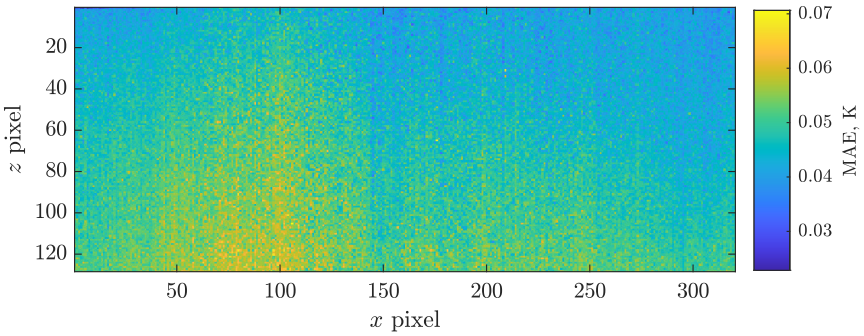

Figure 3.22: Mean absolute error for a full calibrated frame.

Comparison Between IR and Thin Film Gauges

A part of the uncertainty analysis carried out was the validation of the IR processing technique. Time varying IR and thin film gauge data from the same shot and location are plotted in Figure 3.23 along with their respective uncertainties.

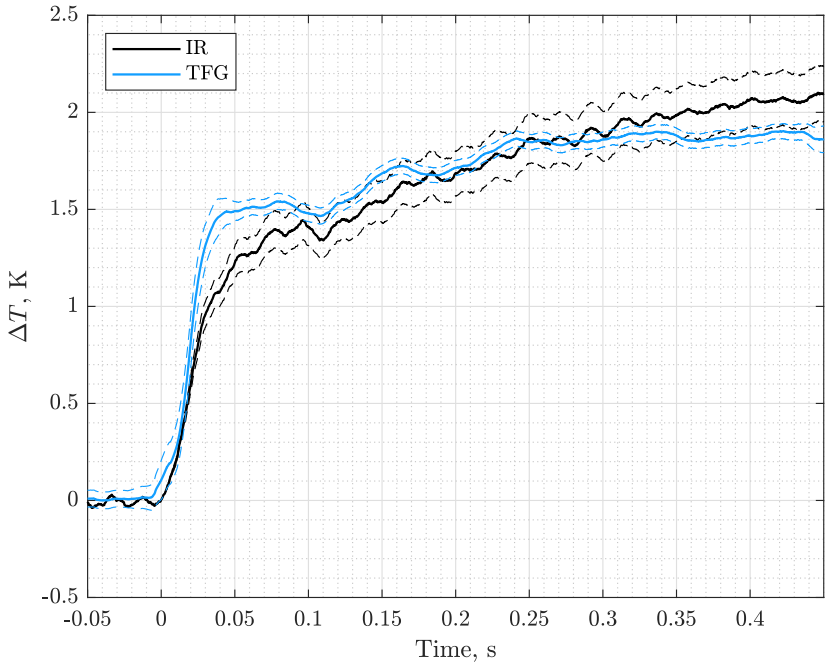

Figure 3.23: Comparison of thin film gauge data with IR data with uncertainties plotted.

Close agreement can be seen between both the calculated change in temperature and the uncertainties (with the exception of the change in temperature during

tunnel start up) of each measurement technique. This gives confidence to the assumption made in Section 3.3.1.1 that G_{shot} remains constant during a shot.

Total Uncertainties

Total uncertainties in the resulting Stanton number were calculated and are plotted with some of the results shown in later chapters. Uncertainty results for a typical IR data point are presented in Table 3.4, with the contribution from each variable shown in the last column. The overall uncertainty in Stanton number is dominated by the uncertainty in total temperature measurement followed by that of the recovery factor, with a contribution to the overall uncertainty of 71.9% and 16.9% respectively. Regardless, the overall uncertainty of 15.4% is reasonably low and gives confidence to the IR measurements.

Table 3.4: Stanton number uncertainty with contributions from other quantities.

Quantity	Unit	Value	Uncertainty	%	% contribution
$U_{D,\,cal}$	-	-	-	0.025	-
T_{cal}	K	-	0.051	-	-
R	-	1.32×10^{5}	1760	1.33	-
B	K	870	3.02	0.347	-
F	-	8.98	0.0699	0.745	-
$U_{D,\,shot}$	-	19754	13.5	0.0683	5.37×10^{-6}
τ_{cal}	-	0.97637	0.00229	0.234	6.32×10^{-5}
ϵ_{cal}	-	0.98	0.02	2.04	0.00479
ϵ_{shot}	-	0.93	0.05	5.38	0.0333
T_{amb}	K	297.19	2.20	0.740	2.46
$\sqrt{\rho c_p k}$	J m^{-2}K^{-1}s$^{-0.5}$	624	24.6	3.94	6.54
p_{pitot}	Pa	7.43×10^{3}	700	0.942	0.414
p_0	Pa	2.74×10^{6}	4.2×10^{4}	1.53	2.09
T_0	K	435	15.0	3.45	71.9
r	-	0.885	0.015	1.69	16.9
St	-	4.73×10^{-4}	7.31×10^{-5}	15.4	-

Figures 3.24, 3.25, 3.26, and 3.27 present Mach number, surface temperature change, heat flux, and Stanton number, respectively, as time-varying quantities for the duration of a shot along with their respective uncertainties.

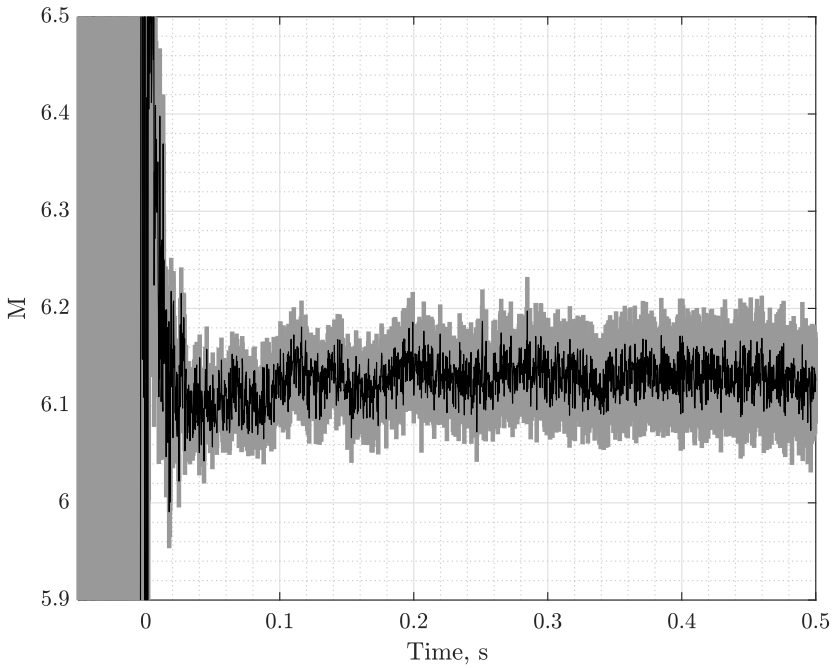

Figure 3.24: Uncertainty in Mach number for the duration of a shot.

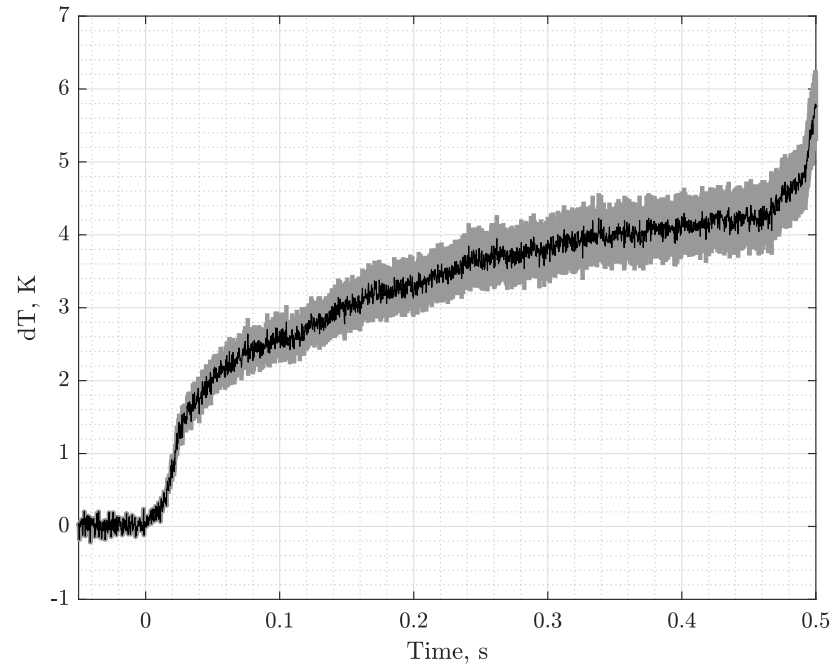

Figure 3.25: Uncertainty in temperature change for the duration of a shot.

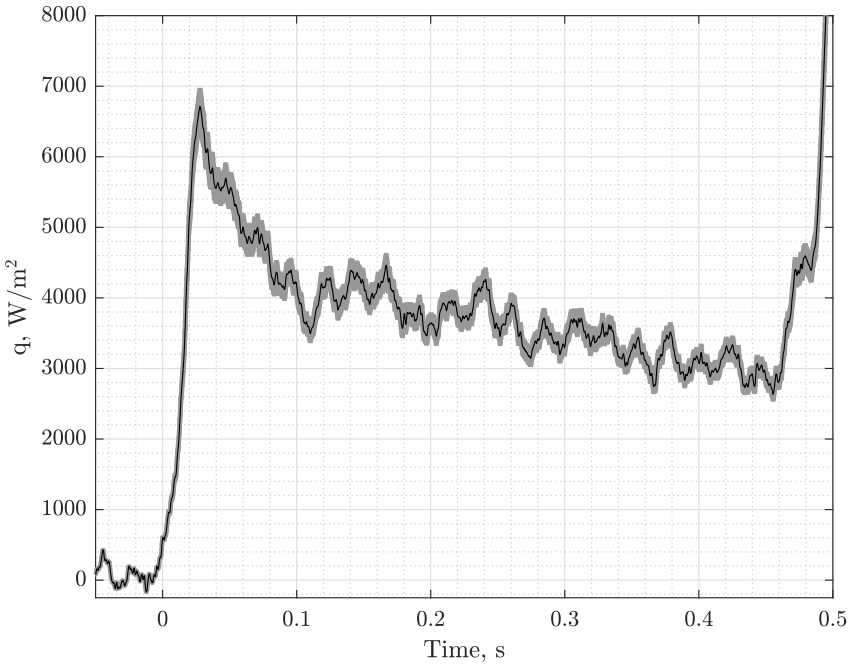

Figure 3.26: Uncertainty in heat flux for the duration of a shot.

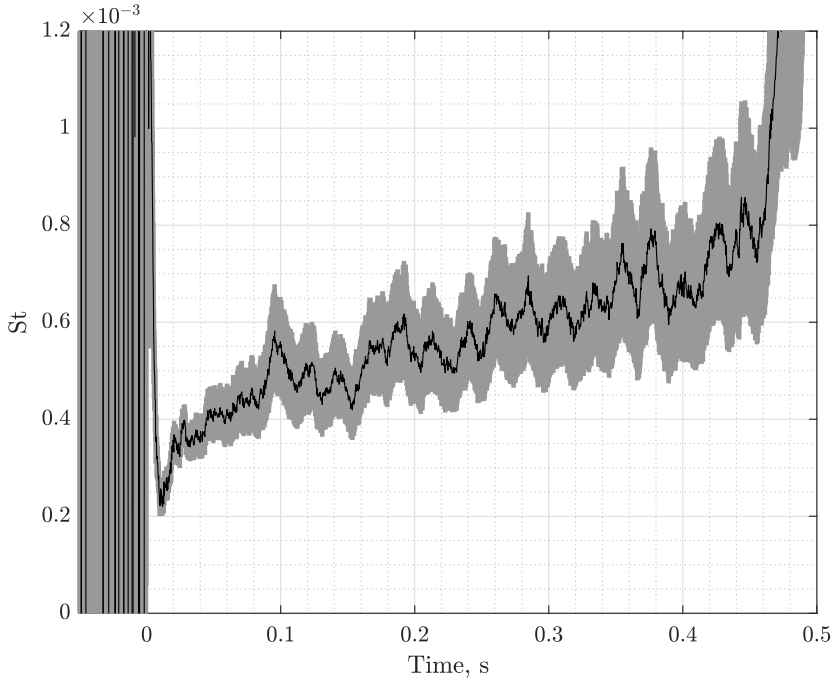

Figure 3.27: Uncertainty in Stanton number for the duration of a shot.

3.3.3 Surface Pressure Measurements

Two Kulite XCS-062-5A pressure sensors, with an uncertainty of 0.5% of the full scale output of 5 psi, were flush mounted in the model surface. Both sensors were

located close to the step, with one upstream and one downstream, allowing the separation and wake of different step geometries to be characterised. All Kulite sensors were amplified using Fylde FE-H379-TA full-bridge amplifiers which applied a low-pass filter with a cut-off frequency of 30 kHz. Data from Kulite sensors was averaged over steady flow periods. This data was primarily used to aid in assessing the angle of attack of the plate by comparing with calculated static pressure.

To measure high frequency pressure fluctuations in the boundary layer, 9 PCB 132A31 sensors were placed at an even spacing of 49 mm near the model centreline. These were amplified using PCB 482C15 ICP signal conditioners. The absolute magnitude of data from these sensors is less important than the relative magnitudes of the different frequency contributions to the signal. The frequency content was extracted from the steady flow periods using Welch's method [156] to approximate the power spectral density (PSD).

3.3.4 Freestream Characterisation

Stagnation pressure measurements were taken using a Kulite XCQ-080-70BARA piezo-resistive pressure sensor, amplified using a Fylde FE-H379-TA transducer amplifier which applied a low-pass filter with a cut-off frequency of 30 kHz to the signal. The sensor has a measurement uncertainty of 0.5 % of the full scale output of 70 bar.

Measurements of the freestream were taken using a Pitot probe and an aspirated thermocouple. These sensors were part of a twin probe mounted below the leading edge of the flat plate model - downstream of the leading edge but upstream of the leading edge shock. Figure 3.28 shows the twin freestream measurement probe.

Pitot pressure was measured using a Kulite XCQ-093-100A piezo-resistive pressure sensor which was also amplified using a Fylde FE-H379-TA amplifier with the same 30 kHz low-pass filter applied. The sensor has an associated measurement uncertainty of 0.5 % of the full scale output of 100 psi ($\sim$700 kPa).

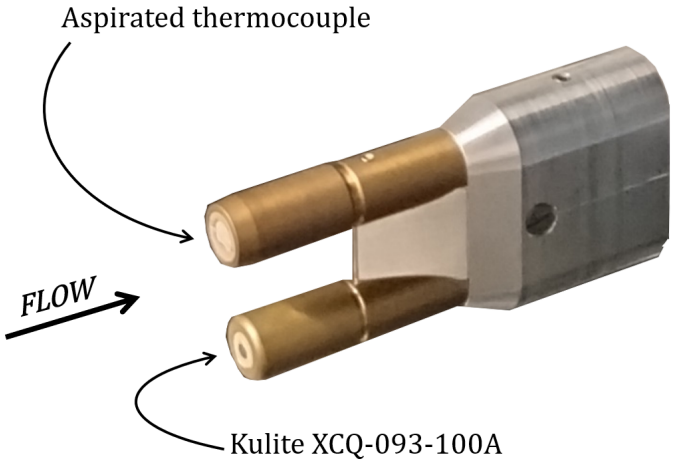

Figure 3.28: The twin freestream measurement probe.

The aspirated thermocouple consists of a pre-heated 0.076 mm (3 thou) diameter K-type thermocouple suspended across a hollow cylinder through which the post-shock freestream can flow (hence "aspirated"). The flow over the thermocouple is approximated as a cylinder in cross-flow of which the diameter is known. Effective cylinder length and heat transfer coefficients were calculated using an optimisation process which attempts to fit data from three differently heated thermocouples to a derived total temperature trace. Data at three initial thermocouple temperatures typically requires three identical shots to be carried out in succession. Hermann et al. [157] describe this process in more detail and give an overall uncertainty of ±15 K for the resultant total temperature.

3.3.5 Model Alignment

The angle of attack of the model was measured using a model alignment probe designed by Bustard [158], shown in Figure 3.29. This probe was also mounted beneath the leading edge of the model in a location alongside the twin probe. It consists of a 32 mm diameter, 30° half-angle cone, with four Kulite XCEL-152-25A pressure sensors equally spaced by 90° around the conical surface. These sensors have an uncertainty of 0.5 % of the full scale output of 25 psi. By comparing opposite sensors, the approximate angle of attack of the probe (and therefore the model) could be estimated using a pre-calibrated empirical relationship.



Figure 3.29: The model alignment probe.

3.3.6 Geometry Height Measurement

The height of the front actuated block was measured using two Alps Alpine RDC1014A09 linear potentiometers mounted on the underside of the rear plate, approximately in line with each actuator. The arrangement of the potentiometers provided a measurement relative to the rear plate rather than to the main top plate. To acquire an absolute height measurement, the height of the rear plate was measured manually during adjustment using a calibrated RS PRO dial indicator with a quoted accuracy of ±0.005 mm. The potentiometers were calibrated using the same dial indicator by measuring the relative height between the front block and rear plate for a number of locations spanning the range of motion. The height of the block is proportional to the ratio of supply voltage to output voltage of each potentiometer, as shown in Figure 3.30.

3.4 Boundary Layer Properties

Various properties of the boundary layer are used throughout the presentation of results in the following chapters. This section summarises how these quantities are calculated.

3.4.1 Thickness Parameters

Laminar

Laminar boundary layer thickness, δ, was calculated using a correlation given by White [159], shown in Equation 3.17.

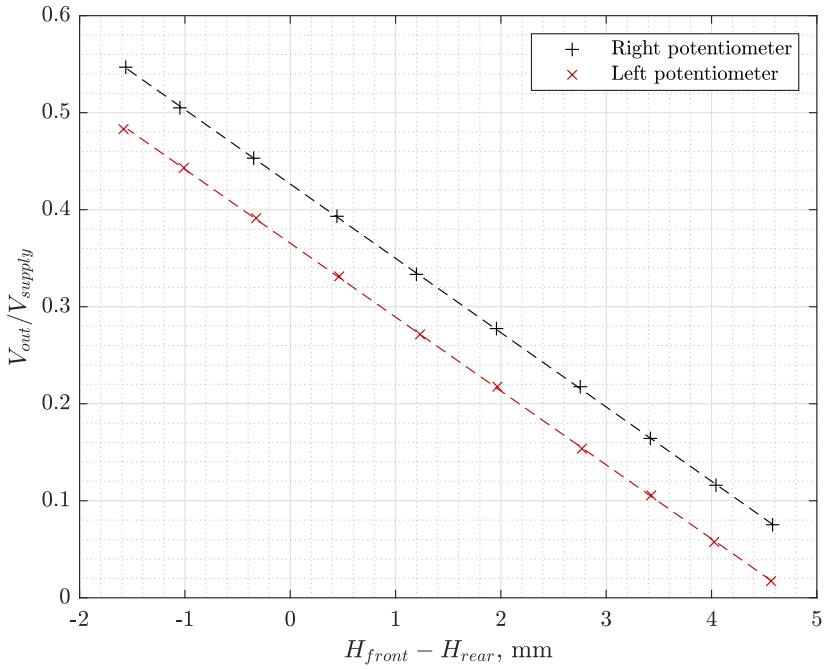

Figure 3.30: Calibration of the linear potentiometers used for block height measurement.

$$\delta_{laminar} = \frac{x}{\sqrt{\mathrm{Re}_x}} C_w^{1/2} \left[5 + \left(0.2 + 0.9 \frac{T_w}{T_{aw}} \right) (\gamma - 1) M_e^2 \right] \tag{3.17}$$

Where C_w is the Chapman-Rubesin parameter evaluated at wall conditions, given by Equation 3.18.

$$C_w = \frac{\rho_w \mu_w}{\rho_e \mu_e} \tag{3.18}$$

Momentum thickness, θ, for laminar boundary layers was given by Equation 3.19, following Qiao et al. [160], requiring the boundary layer thickness to have been calculated.

$$\frac{\delta}{\theta} = -0.02125M^3 + 0.8084M^2 - 0.3505M + 8.2 \tag{3.19}$$

Turbulent

In turbulent boundary layers, the process of calculating boundary layer properties is more complex. Laminar properties are first calculated up to the transition location. The subsequent growth of θ is then calculated, followed by the ratio θ/δ.

Following the method described by Reshotko & Tucker [161], first a transformed momentum thickness, θ_{tr}, is calculated, defined by Equation 3.20. This accounts for compressibility effects in the boundary layer.

$$\theta_{tr} = \theta / \left(1 + \frac{\gamma - 1}{2} M_e^2\right)^3 \tag{3.20}$$

This is evaluated at the transition location, using the laminar θ, given by Equations 3.17 and 3.19, to give $\theta_{tr,\, x_{tran}}$. The growth in θ_{tr} with x is then given by Equation 3.21, which is the solution of an integral.

$$\theta_{tr,\, x} = \left[\frac{0.01173}{Re_{unit}^{0.2155}} \frac{(T_e/T_{ref})^{0.732}}{(T_0/T_e)^{3.268}} (x - x_{tran}) + \theta_{tr,\, x_{tran}}^{1.2155}\right]^{1/1.2155} \tag{3.21}$$

Where, T_{ref} is a reference temperature, described in Section 3.4.2. Finally, $\theta_{tr,\, x}$ is converted back to θ_x using the inverse of Equation 3.20.

To calculate the boundary layer thickness, the method of Huang et al. [162] was used, implemented using a slightly altered version summarised by Roy & Blottner [163]. The method iterates through several steps until the solution converges. First, a theoretical law-of-the-wall compressible transformed velocity profile is defined:

$$\frac{\mathrm{d}u_{cb}^+}{\mathrm{d}y^+} = \frac{2}{1 + \sqrt{1 + 4l^{+\,2}}} \tag{3.22a}$$

$$l^+ = \kappa y^+ \left(1 - e^{-y^+/A^+}\right) \tag{3.22b}$$

$$A+ = 25.53,\ \kappa = 0.41 \tag{3.22c}$$

$$u^+ = \frac{u}{u_\tau} \tag{3.22d}$$

The transformed velocity profile is updated to include a wake profile, which accounts for differences outside the viscous sublayer:

$$u_c^+ = u_{cb}^+(\eta) + \frac{\Pi}{\kappa} w(\eta) \tag{3.23a}$$

$$\eta = \frac{y}{\delta} \tag{3.23b}$$

Where Π is a function which is dependent on Re_θ, defined by Equation 3.24.

$$\Pi = 0.55\left[1 - \exp\left(-0.24\sqrt{z_1} - 0.298 z_1\right)\right] \tag{3.24a}$$

$$z_1 = \frac{\mathrm{Re}_\theta}{425} - 1 \tag{3.24b}$$

And w is a wake function given by Equation 3.25 which ranges from 0 at the wall to 2 at the boundary layer edge.

$$w = 2\sin^2\left(\eta\frac{\pi}{2}\right) \tag{3.25}$$

Next, the reverse transformation of the velocity profile is performed:

$$u^+ = \frac{1}{R}\sin\left(Ru_c^+\right) - H\left[1 - \cos\left(Ru_c^+\right)\right] \tag{3.26a}$$

$$R = u_\tau\sqrt{\frac{\mathrm{Pr}_T}{2c_pT_w}} \tag{3.26b}$$

$$H = \left[\frac{1 - \frac{T_e}{T_w}}{R^2u_e^+} - u^+\right]/2 \tag{3.26c}$$

The temperature profile is then updated:

$$T = T_w\left(1 - \alpha u^+ - R^2u^{+2}\right) \tag{3.27a}$$

$$\alpha = 2R^2H \tag{3.27b}$$

Finally, the ratio between boundary layer and momentum thickness is calculated:

$$\frac{\theta}{\delta} = \int_0^1 \frac{\rho\, u^+}{\rho_e u_e^+}\left(1 - \frac{u^+}{u_e^+}\right)\mathrm{d}\eta \tag{3.28}$$

This process is repeated, updating the shear velocity, u_τ, after each iteration until convergence of the ratio θ/δ.

3.4.2 Surface Heat Flux

Measured heat flux levels were compared with theoretical values to aid in the calculation of heat flux augmentations. A reference temperature approach is used, where certain properties of compressible boundary layers can be estimated by evaluating incompressible solutions at a reference temperature. Eckert [11] defines the reference temperature using Equation 3.29.

$$T_{ref} = T_e \left(1 + 0.58 \left(\frac{T_w}{T_e} - 1\right) + 0.2r\frac{\gamma - 1}{2}M_e^2\right) \tag{3.29}$$

Laminar

To calculate heat flux, first the local skin friction coefficient is found:

$$c_f = \frac{0.664}{\sqrt{\mathrm{Re}_{ref}}} \tag{3.30}$$

Where Re_{ref} is the local Reynolds number evaluated at the reference temperature. The skin friction is related to heat flux using:

$$St = \frac{c_f}{2S} \tag{3.31}$$

Where S is the Reynolds analogy factor. The value of S has been the subject of multiple experimental investigations [164] but a value of $\mathrm{Pr}^{2/3}$ is typically suitable.

Turbulent

The Schultz-Grunow relationship is used for skin friction in turbulent boundary layers, and is suitable for Re$< 10^9$.

$$c_f = \frac{0.370}{\log_{10}\mathrm{Re}_{ref}^{2.584}} \tag{3.32}$$

The same conversion to Stanton number is used as in Equation 3.31.

3.5 Summary

This chapter has summarised the methods used to approach the problem defined in Chapter 1. An experimental model was designed and manufactured to be tested in HDT in two modes of operation. The model was instrumented to measure surface heat flux, as well as a number of other flow properties.

4

LICH Mode Experiments

Contents

4.1 Numerical Modelling 87
4.1.1 Model Validation 90
4.1.2 Model Predictions 92
4.2 Experimental Setup 93
4.2.1 Freestream Characterisation 95
4.3 Results from Commissioning Tests 95
4.3.1 Shot Data 95
4.3.2 Performance Maps 96
4.3.3 Freestream Noise 105
4.4 Summary 106

A new mode of operation, Ludwieg mode with Isentropic Compression Heating (LICH), has been commissioned for the Oxford High Density Tunnel (HDT). LICH mode can extend the total temperature range of Ludwieg tunnels by including a piston stroke in the shot sequence, compressing the test gas and heating it above the level achievable by electrically pre-heating Ludwieg tubes alone. A numerical model for HDT has been developed for rapid assessment of conditions, aiding in the design of a lightweight piston. Initial testing has been carried out, producing ∼600 K Mach 7 flow and proving the capability of LICH mode in HDT. An assessment has been carried out of the overall performance of HDT operating in LICH mode at

Mach 7. Condition maps have been generated using the numerical model, validated from experimental data. Finally, the freestream noise is compared to various other facilities which produce similar flow conditions.

LICH mode has been implemented in the Oxford High Density Tunnel (HDT) to address the need for higher total temperatures, allowing for a greater range of wall to total temperature ratios and unit Reynolds numbers to be tested. Higher temperatures also allow higher Mach number nozzles to be used while avoiding liquefaction of the test gas as it expands through the nozzle.

This chapter presents a description of HDT, how LICH mode operation is achieved, and a simple numerical model of the tunnel. Sample experimental data is then presented, followed by performance maps calculated using the validated numerical model. Finally, the effectiveness of LICH mode is compared to Ludwieg mode by looking at freestream noise levels and signal to noise ratios of thin film gauge data.

4.1 Numerical Modelling

A numerical model has been developed which uses a system of ordinary differential equations (ODEs) to describe the mass flow of gas between regions of the tunnel, the temperature of gas in each region, and the dynamics of the piston. The model was originally created by Buttsworth [165] for modelling TUSQ at the University of South Queensland, and is described in detail in Reference [165]. As part of an initial investigation of the implementation of LICH mode in HDT, McGrath [166] updated the model to reflect the geometry and plug valve operation of HDT.

The mass flow rate between volumes 1 and 2 is described by Equation 4.1. The p_{th} is a throat pressure which is used to distinguish between choked and unchoked flow, shown in Equation 4.2. When $p_2 \lesssim 0.58 p_1$, the flow is choked and doesn't depend on the ratio of p_1 to p_2. Equation 4.1 is also applicable to mass flow between volumes 3 and 4 and volumes 4 and 5.

$$\dot{m}_{12} = A_{12}\sqrt{2p_1\rho_1\frac{\gamma}{\gamma-1}\left(\frac{p_{th}}{p_1}\right)^{\frac{2}{\gamma}}\left[1-\left(\frac{p_{th}}{p_1}\right)^{\frac{\gamma-1}{\gamma}}\right]} \tag{4.1}$$

$$p_{th} = \begin{cases} p_1 \cdot \left(\frac{2}{\gamma+1}\right)^{\left(\frac{\gamma}{\gamma-1}\right)} & \text{for } p_2 \leq p_1 \cdot \left(\frac{2}{\gamma+1}\right)^{\left(\frac{\gamma}{\gamma-1}\right)} \\ p_2 & \text{for } p_2 > p_1 \cdot \left(\frac{2}{\gamma+1}\right)^{\left(\frac{\gamma}{\gamma-1}\right)} \end{cases} \tag{4.2}$$

The change in temperature of the gas in volume 3 is described by carrying out an energy balance on the volume. The result of this is Equation 4.3:

$$\dot{T}_3 = \frac{\dot{Q}_{in,\,3}}{m_3 c_v} + \frac{\dot{m}_3}{m_3}(\gamma-1)\,T_3 - \frac{p_3}{m_3 c_v}\dot{V}_3 \tag{4.3}$$

The first term is the heat transfer from the tunnel walls (described below by Equation 4.5), the second term comes from energy added from mass flow into the volume, and the third term comes from the change in volume due to the piston compression. This equation is applicable to the other volumes with slight changes to the second term and the removal of the third term, as necessary.

Key updates to the current version of the model, used in this work, are presented in the following paragraphs.

HDT Geometry

The majority of geometry updates were made by McGrath [166] with the exception of the nozzle plenum (region 4). This was included, which involved an additional set of mass flow and heat transfer equations being added into the system of ODEs.

Piston Heat Transfer

Heat transfer to the piston was modelled to aid in piston design. The correlation shown in Equation 4.4, from Taylor [167], describes heat transfer to pistons in internal combustion engines and, in the absence of a more specific model, is taken to be valid for this work.

$$\mathrm{Nu}_P = 10.4 \cdot \mathrm{Re}_P^{3/4} \tag{4.4}$$

Re_P refers to the Reynolds number based on the piston velocity and the piston diameter. For implementation into the ODE model, the correlation was used to calculate heat transfer to the front and the rear faces of the piston using gas properties from volumes 2 and 3, with the overall heat transfer being the sum of that to the front and rear faces. The piston was assumed to be thermally thin, having a uniform internal temperature distribution at all times.

Heat Transfer Scale Factors

Heat transfer between gas and the barrel walls can be approximated as that of a gas flowing through a cylinder in steady state, given by the commonly named Dittus-Boelter equation [168] shown in Equation 4.5.

$$\mathrm{Nu}_D = 0.023 \cdot \mathrm{Re}_D^{4/5} \cdot \mathrm{Pr}^n \tag{4.5}$$

Where $n = 0.4$ for gas heating and $n = 0.3$ for gas cooling. This approximation does not fully capture the transient nature of the flow in the vicinity of the piston, in particular a vortex ring which is generated by the boundary layer being "scooped" off the barrel walls as the piston moves [132]. Additionally, some parts of the tunnel (such as the plug valve) have more complex geometries, leading to higher levels of heat flux. These heat transfer effects are modelled by including heat flux augmentation factors for certain gas volumes - this approach gives reasonable results with sufficient tuning to experimental data. Scale factors were applied to the heat transfer coefficients calculated from Equation 4.5.

Piston Friction Model

A new friction model for the piston which is proportional to the piston velocity was implemented for use in the equation of motion for the piston. The friction model is given by Equation4.6 and produced accurate piston stroke dynamics.

$$F = 10 \cdot \dot{x}_P \tag{4.6}$$

Various friction models were trialled based on various quantities such as: constants, the pressure difference across the piston, and piston acceleration. The chosen velocity-dependent model was used due to the agreement between the behaviour of simulated and experimental barrel pressure during the piston stroke.

Implementation

The system of ODEs was solved using the `ode15s` function within MATLAB. This particular solver was chosen due to its efficiency with stiff differential equations which helped during periods of rapid variation (e.g. just after the plug valve opens or at piston impact). Outputs of the model are (referring to Figure 3.2 for subscripts): x_P, $\dot{x}_P$, m_1, m_4, m_5, T_1, T_2, T_3, T_4, and T_P. Pressures in each volume are calculated from the mass and temperature solutions using ideal gas assumptions. The model is terminated when the piston impacts the end of the barrel and the total simulated time is typically between 1 and 10 seconds, depending on initial conditions. Table 4.1 presents the range of initial conditions investigated in this work.

Table 4.1: ODE model initial conditions

Variable	Units	Range
$p_{3,o}$	bar	$8 - 50$
$p_{3,f}$	bar	$1 - 0.95 \cdot p_{3,o}$
$p_{1,f}$	bar	$1.1 \cdot p_{3,o} - 200$
$T_{3,f}$	K	$300 - 550$

4.1.1 Model Validation

Prior to LICH mode shots being undertaken in HDT, the ODE model was validated using data from both a Ludwieg mode shot and an unheated LICH shot. For the Ludwieg mode validation case the ODE model was simplified by setting the piston velocity to 0 and removing gas volumes 1 and 2 (the reservoir and the barrel upstream of the piston).

Figure 4.1 shows the results from the model compared with Ludwieg mode shot data. The ODE model does not calculate any acoustic effects so does not follow the more transient changes in pressure and temperature caused by rarefaction waves

being reflected in the barrel. However, the overall trends in both pressure and temperature are captured with reasonable accuracy.

Figure 4.2 shows the barrel pressure and the nozzle supply pressure for a cold LICH shot compared with results from the ODE model. Once again, the model follows the overall trend: a steady pressure rise during the piston stroke followed by a sudden drop when the plug valve opens at $t = 0$. It is still unable to capture the shorter duration transients in pressure. The sudden change in barrel pressure in the shot data at $t = -1.5$ is an aberration caused by the piston passing over the barrel pressure sensor.

These validation cases were used to tune the effective diameter of the reservoir to barrel contraction, the heat flux augmentation factors in different parts of the tunnel, and plug valve opening times.

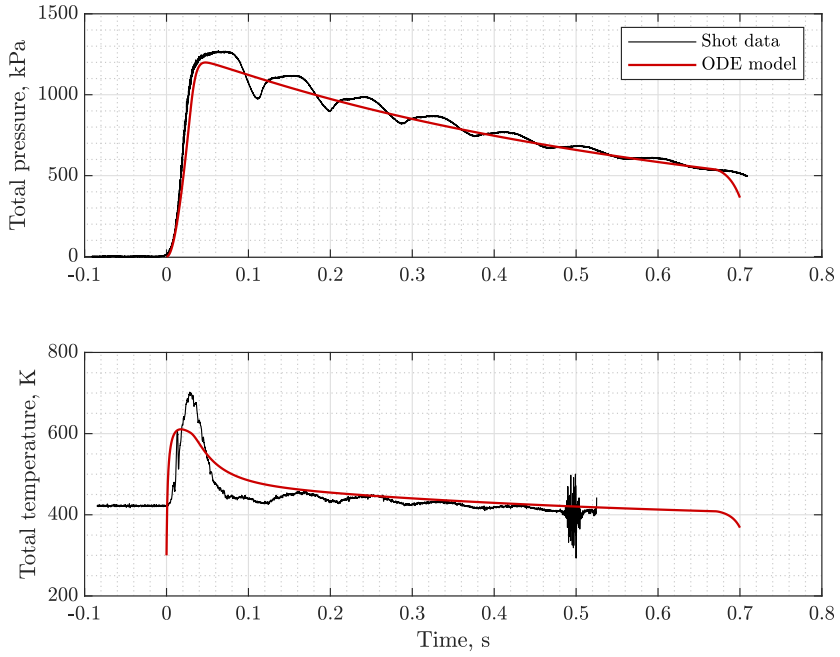

Figure 4.1: Ludwieg mode shot freestream total pressure and temperature compared with results from the ODE model.

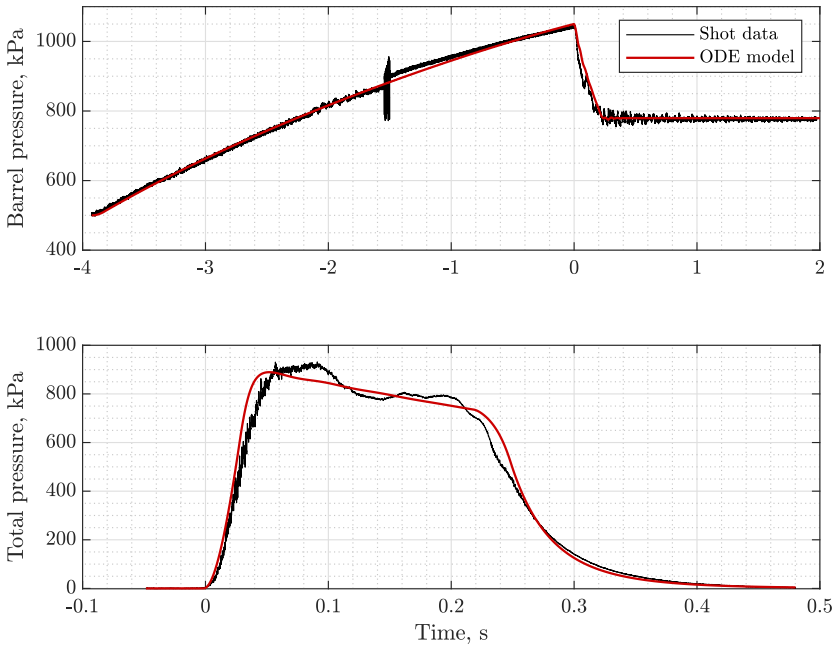

Figure 4.2: Barrel pressure and freestream total pressure for a cold LICH mode shot compared with ODE model results.

4.1.2 Model Predictions

Typical results from the ODE solver are presented in Figure 4.3 for the initial conditions given in Table 4.2. This tunnel setup is referred to as Condition A and is the condition chosen for experimental testing. Plots of pressure, temperature, and piston dynamics are shown. The legend in the pressure plot (top) also applies to the temperature plot. The time axis has been adjusted such that $t = 0$ corresponds to the first rise in the nozzle supply pressure. This enables consistent comparison with Ludwieg mode shots and experimental data.

Table 4.2: Tunnel setup for Condition A

Variable	Units	Value
$p_{3,o}$	bar	9.5
$p_{3,f}$	bar	1.5
$p_{1,f}$	bar	25
$T_{3,f}$	K	500

During the piston stroke, the reservoir pressure, p_1, decreases while both barrel pressures, p_2 and p_3, increase simultaneously. At the beginning of the shot, at $t = 0$,

the nozzle plenum pressure, p_4, increases to a level slightly lower than p_3. p_4 is seen to decrease, along with p_2 and p_3 while the plug valve is open. This indicates that the condition is not matched as if it were, p_4 would stay constant.

The difference in temperature between the upstream, T_2, and downstream, T_3, barrel gas is consistently large due to the flow of cold reservoir gas into the barrel behind the piston. One benefit of a cold driver is that the reservoir gas acts to cool the piston which has a temperature of just over 500 K at the end of the stroke. Thermal energy is lost from the test gas when it flows past the plug valve, resulting in the nozzle supply temperature, T_4, being significantly lower than the temperature of the test gas in the barrel, T_3. There is also a more pronounced drop in T_4 over the test time compared with the p_4. This is partly due to the presence of the spike in temperature as the gas first enters the nozzle plenum (seen more clearly in Figure 4.1) and partly due to large rates of heat transfer in the nozzle plenum.

The piston begins the stroke with a rapid acceleration after which the velocity gradually falls to a very low level at the end of the stroke. When the plug valve opens, the piston accelerates again and large oscillations occur which are strongly attenuated. The piston is predicted to impact at a velocity of 12.5 m/s. Although the magnitude of the oscillations is large, the velocity remains positive, and the piston continues travelling downstream.

4.2 Experimental Setup

Experiments were conducted in the HDT with a heated barrel to prove the operation of LICH mode and to characterise the freestream conditions produced by LICH mode. A series of commissioning shots were undertaken with increasingly larger compression ratios over the range $p_{3,o}/p_{3,f} = 1.25 - 6.33$. Taking this staged approach enabled risk to the facility infrastructure to be appropriately managed. The initial conditions for the largest compression ratio tested are provided in Table 4.2. Only results from this condition will be presented here.

The commissioning tests were also used to evaluate the new, LICH-specific infrastructure, control system logic and high-temperature piston design. This was

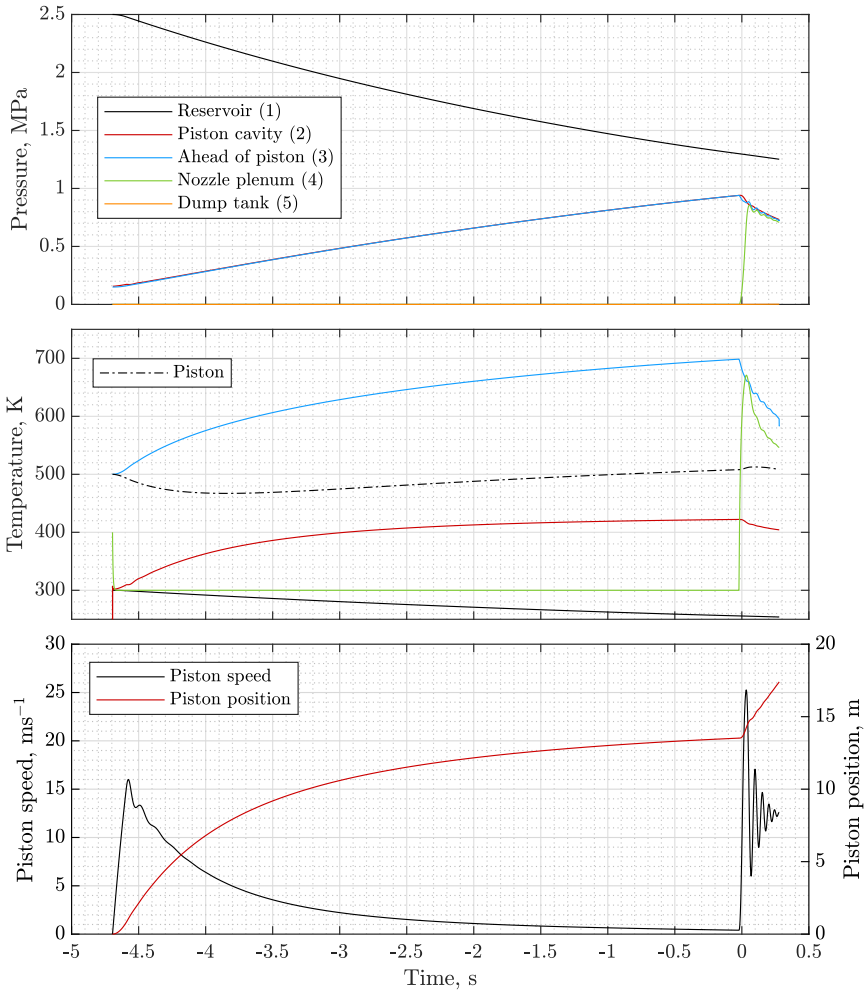

Figure 4.3: Results from the ODE model for Condition A. Pressure, temperature and mass for all tunnel sections and piston dynamics plotted against time.

mostly successful with the infrastructure and logic performing as expected. However, during the highest-compression ratio testing, the piston impacted the downstream end of the facility, damaging the piston but not the facility barrel. The impact was not intentional and a consequence of lack of fine control on the closing time of the plug valve, which may be mitigated in future by the addition of a buffer to catch the piston. Further work is required to enable consistent operation of the LICH mode in HDT, however the results presented in the next section prove the capability.

4.2.1 Freestream Characterisation

LICH mode testing was carried out as part of the main test campaign using the flat plate model. The freestream was characterised in the same way as described in Section 3.3.4. A Kulite XCQ-080-70BARA sensor was used measure total pressure. The twin probe mounted on the model included a Kulite XCQ-093-100A and an aspirated thermocouple to measure pitot pressure and total temperature, respectively.

4.3 Results from Commissioning Tests

Presented in this section are shot data compared with solutions from the ODE model and predicted tunnel performance maps calculated using the ODE model.

4.3.1 Shot Data

Figure 4.4 presents experimental freestream data from a shot at Condition A compared with results from the ODE model. Freestream quantities presented are total pressure (top), total temperature (middle) and unit Reynolds number (bottom). The pressure and temperature from the ODE model are p_4 and T_4 in Figure 4.3 respectively. The viscosity for Re_{unit} was calculated using Keyes' relation [169]. Table 4.3 shows the time averaged freestream properties for Condition A.

Table 4.3: Freestream properties of LICH mode Condition A

Variable	Units	Value
p_0	bar	7.32
T_0	K	595
Re_{unit}	$10^6 \cdot \mathrm{m}^{-1}$	3.01
Shot duration	s	0.26

The three peaks in the experimental pressure trace are caused by the rarefaction waves in the barrel. These flow periods are much less pronounced than those of the Ludwieg mode pressure trace in Figure 4.1. This is primarily due to a much longer plug valve opening time for the LICH shots ($\sim$ 80 ms rather than $\sim$ 30 ms) which has the effect of spreading out the rarefaction waves. The cause of the

difference in plug valve opening speeds is purely that the LICH mode shot was operating at a significantly lower barrel pressure than the Ludwieg mode shot. The effect of piston oscillations and reflected rarefaction waves is not apparent in the experimental pressure. In contrast, the pressure oscillations in the ODE data are caused solely by piston oscillations. Although the acoustic effects aren't modelled, the overall downwards trend in pressure is captured by the ODE model.

At $t = 0.25$ s, the shot ends when the piston impacts the end of the barrel. The pressure abruptly falls as the nozzle plenum empties. The ODE model currently overpredicts the test time by ~ 30 ms which is likely due to a slight mismatch in the barrel temperatures between the shot data and ODE model. The temperature of the test gas in the barrel during the piston stroke is not experimentally measured so this was difficult to tune in the model. A difference in barrel temperature would lead to a difference in mass flow rate during the shot, and therefore a difference in test time.

The stagnation temperature trace is also different to what is usually seen in Ludwieg mode (see Figure 4.1 for a typical shot). The initial unsteady peak in total temperature does not appear in the LICH mode shot data. Instead, the temperature is reasonably steady for the entire duration of the shot. In this case, the ODE model overpredicts the initial temperature rise but falls more quickly towards the end of the shot, indicating that the heat transfer scaling in the barrel and the nozzle plenum may need further tuning.

Re_{unit} is derived from the pressure and temperature data and approximately follows the pressure history in shape. The dependency of viscosity on temperature results in the downward trends of both the pressure and temperature somewhat cancelling out in the calculation of Re_{unit}.

4.3.2 Performance Maps

The current operational range of HDT in LICH mode at Mach 7 was examined by running cases with the tuned ODE model spanning the range of inputs in Table 4.1. Figures 4.5-4.8 show maps of various tunnel conditions plotted against initial

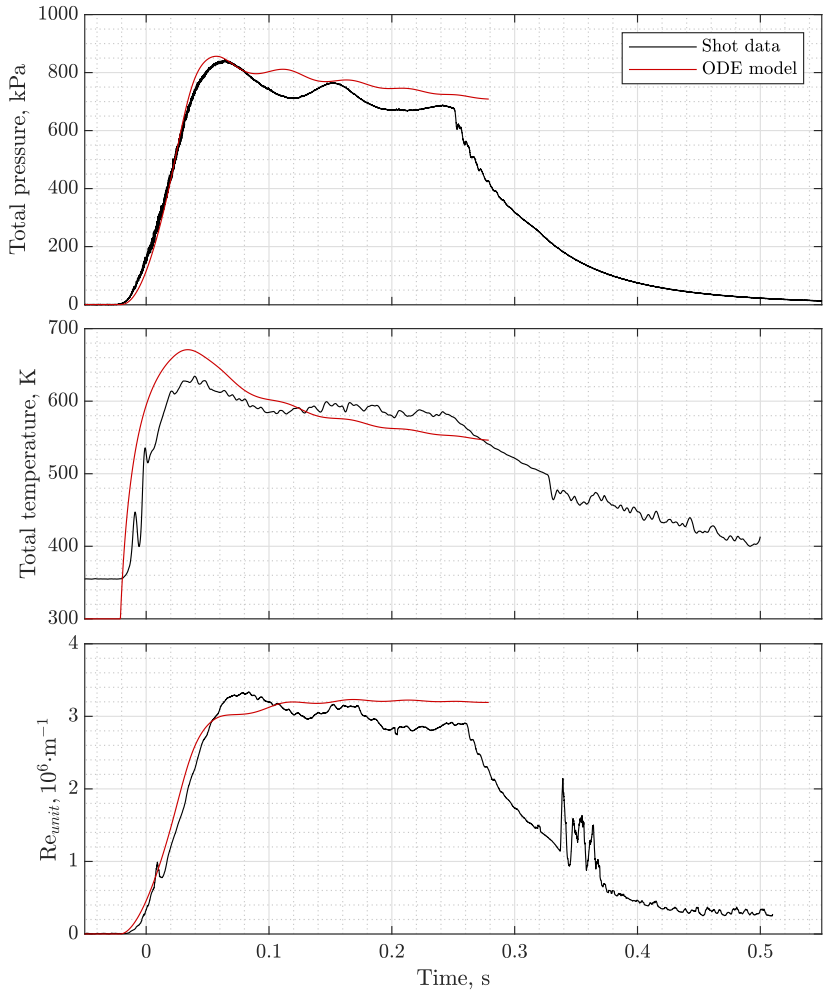

Figure 4.4: Freestream total pressure, temperature, and Re_{unit} of a shot compared with results from the ODE model, both at Condition A.

tunnel conditions, with the location of Condition A being indicated by a black cross. The maps are intended to be used as guides for tunnel operation.

Figure 4.5 shows a map of the mean total temperature during a shot plotted as a function of $T_{3,f}$ and $p_{3,o}/p_{3,f}$. The mean is taken from the end of the initial rise until piston impact- referring to Figure 4.4, this is the mean of the total temperature between $t = 0.04$ s and the end of the shot at $t = 0.28$ s. As discussed earlier, T_4 is a function of both $T_{3,f}$ and $p_{3,o}/p_{3,f}$. This is seen here, with the highest available temperatures of just under 1100 K being produced at $T_{3,f} = 550$ and

$p_{3,o}/p_{3,f} = 50$. The isotherms lie on approximately diagonal lines, showing that there are multiple combinations of initial conditions which are able to produce a given T_4. From an operational perspective, lower compression ratios are more desirable due to the associated decreased risk to infrastructure. Additionally, lower compression ratios produce longer test times (see below in Figure 4.8). Condition A lies at the lower end of possible compression ratios (with $p_{3,o}/p_{3,f} = 6.33$) but produces a total temperature of $\sim$ 600 K due to a higher $T_{3,f}$. Ludwieg mode operates on the y-axis of this map, with an effective compression ratio of 1. This shows the capability of LICH mode, with even small compression ratios producing greater temperatures than possible in Ludwieg mode.

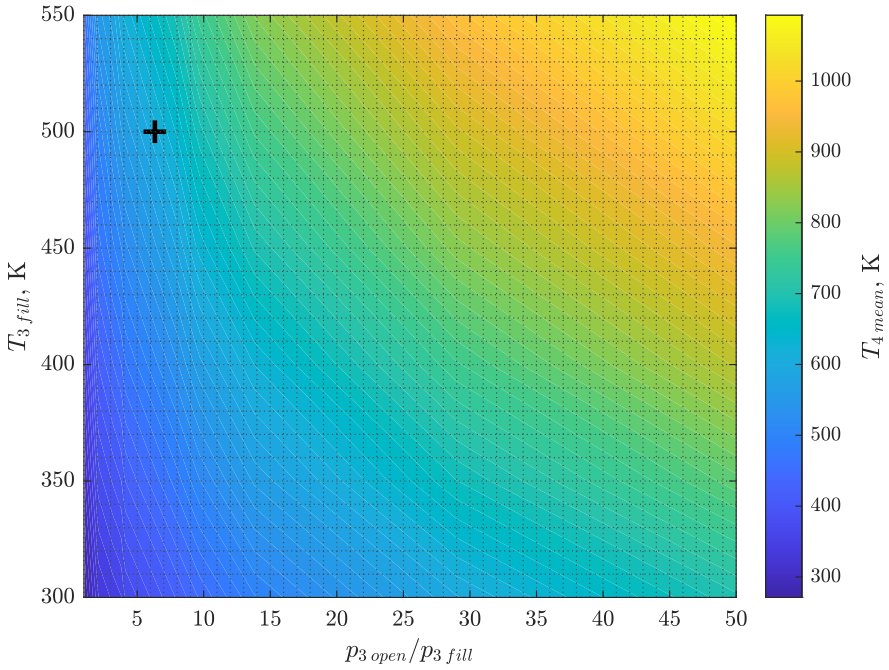

Figure 4.5: Map of mean total temperature for the full range of barrel fill temperatures and pressure ratios.

Figure 4.6 shows a map of the piston temperature at the beginning of a shot and uses the same axes as Figure 4.5. Both maps look largely the same, with large T_P and large T_4 being produced by the same mechanisms. It is interesting to note that the piston temperature never rises by more than $\sim$ 150 K at even the highest compression ratios. This is attributed to the cold reservoir gas cooling

the piston from the rear. This is advantageous as it allows the use of lightweight materials, such as aluminium, to be used in the construction of the piston. This plot displays some apparent non-linear behaviour at an x-axis value of 8. This appears to be a boundary between two conditions: at values of $p_{3,o}/p_{3,f} < 8$, $T_P < T_{3,f}$ while the opposite is true for $p_{3,o}/p_{3,f} > 8$.

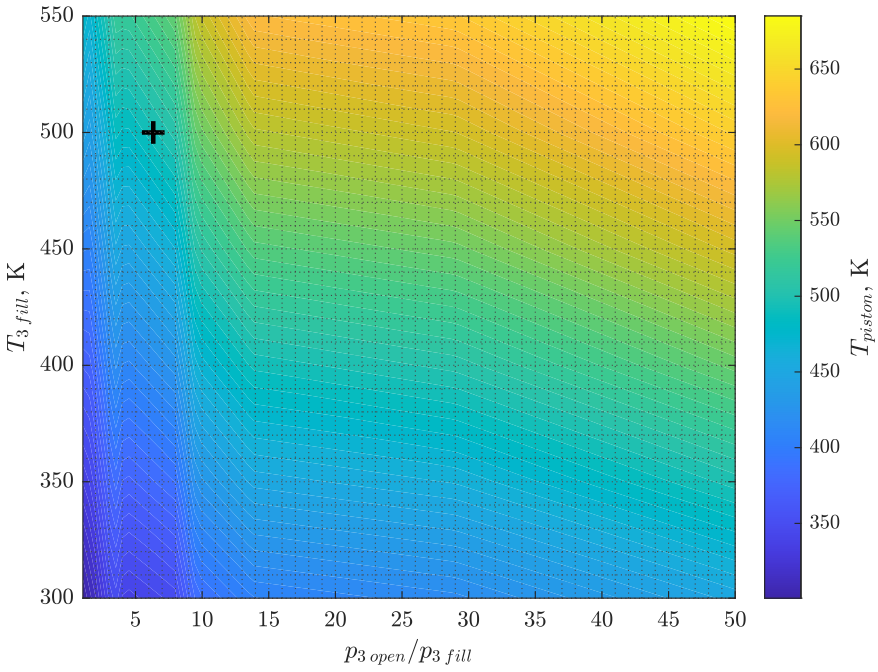

Figure 4.6: Map of final piston temperature for the full range of barrel fill temperatures and pressure ratios.

A map of Re_{unit} plotted as a function of $T_{4\,mean}$ and $p_{3,o}$ is shown in Figure 4.7. To use this map for estimating conditions, first $T_{4\,mean}$ must be read from Figure 4.5. High Re_{unit} are generated from high pressures and low temperatures while low Re_{unit} are generated from low pressures and high temperatures. A white dashed line shows the approximate upper temperature limit of Ludwieg mode. LICH mode allows for lower Re_{unit} to be achieved than is possible in Ludwieg mode - the area in the upper left corner, containing Condition A, produces lower Re_{unit} than anything below the white line.

The final performance map is given in Figure 4.8 and shows total shot duration as a function of $T_{3,f}$ and $p_{3,o}/p_{3,f}$. The x-axis is plotted on a log scale as most of

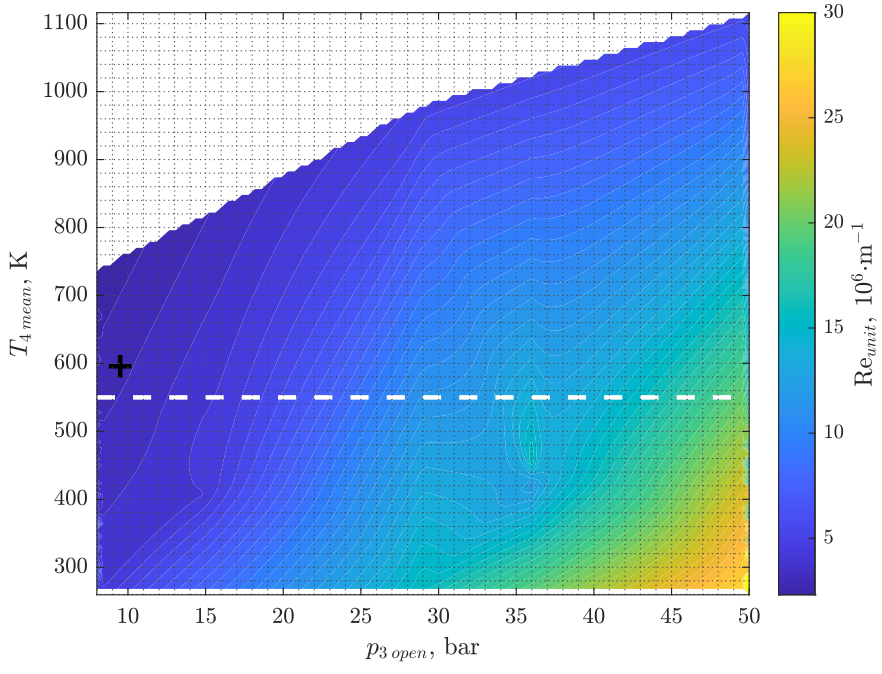

Figure 4.7: Map of Re_{unit} for the full range of mean total temperatures and plug valve opening pressures.

the variation in shot duration occurs at low compression ratios. Shot duration is primarily a function of compression ratio, with only a small dependency on $T_{3,f}$. At very low compression ratios, the piston does not move very far before the shot begins, leading to long shot durations of several seconds. However, for useful LICH conditions which produce higher total temperature flows, $p_{3,o}/p_{3,f}$ must be greater than ~ 5. In this regime, shot lengths are below 1 s, with that for Condition A being predicted at 0.28 s. For the highest total temperatures possible using LICH mode, shot durations are well below 0.1 s. However, this is still comparable to the duration of the steady flow periods produced in Ludwieg mode.

If the above performance maps are combined, the flow quantities of total temperature, unit Reynolds number, and shot duration can be plotted together. These quantities are perhaps the most useful from the perspective of designing an experiment. Due to given values of T_4 being achievable using different combinations of $T_{3,f}$ and compression ratios, the data for these maps does not collapse for the full range of operation. Four maps are presented, each showing the relationship between

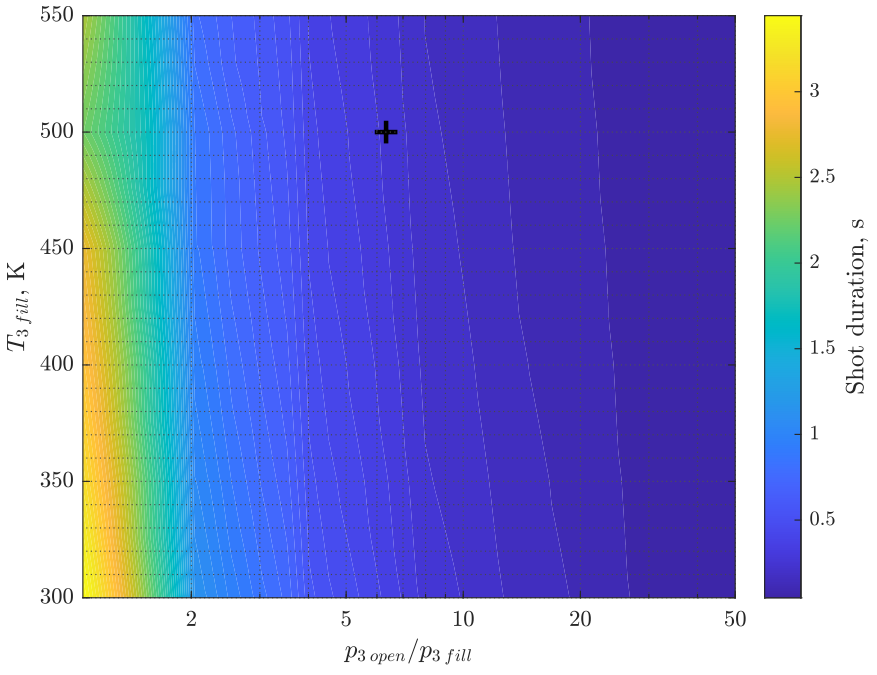

Figure 4.8: Map of total shot duration for the full range of barrel fill temperatures and pressure ratios.

T_4, Re_{unit}, and shot duration for a single initial barrel temperature, $T_{3,f}$. Figures 4.9 - 4.12 show these maps for $T_{3,f}$ of 550K, 500K, 400K, and 300K, respectively. As above, the location of Condition A is indicated in Figure 4.10 by a black cross. For all maps, the axes and colour scales are the same. This highlights the differences in the possible range of generated freestream conditions between values of $T_{3,f}$. In contrast, the shot duration is somewhat consistent between different $T_{3,f}$ values, with lower T_4 values corresponding to lower compression ratios and therefore longer shot durations.

An indication of the full operating range in the T_4-Re_{unit} space is given by extracting the boundaries of the shapes in Figures 4.9 - 4.12. These are plotted together in Figure 4.13 and show that, generally, there is a trade-off between achievable T_4 and Re_{unit}. There is a large dependence of achievable conditions on $T_{3,f}$, with greater Re_{unit} only being possible using colder barrel temperatures and greater T_4 only being possible using greater barrel temperatures. However, the upper T_4 limit of Ludwieg mode of 480 K (shown by the black dashed line), shows that if higher Re_{unit} are required (above $\sim 15 \times 10^6 \cdot \mathrm{m}^{-1}$), then the use

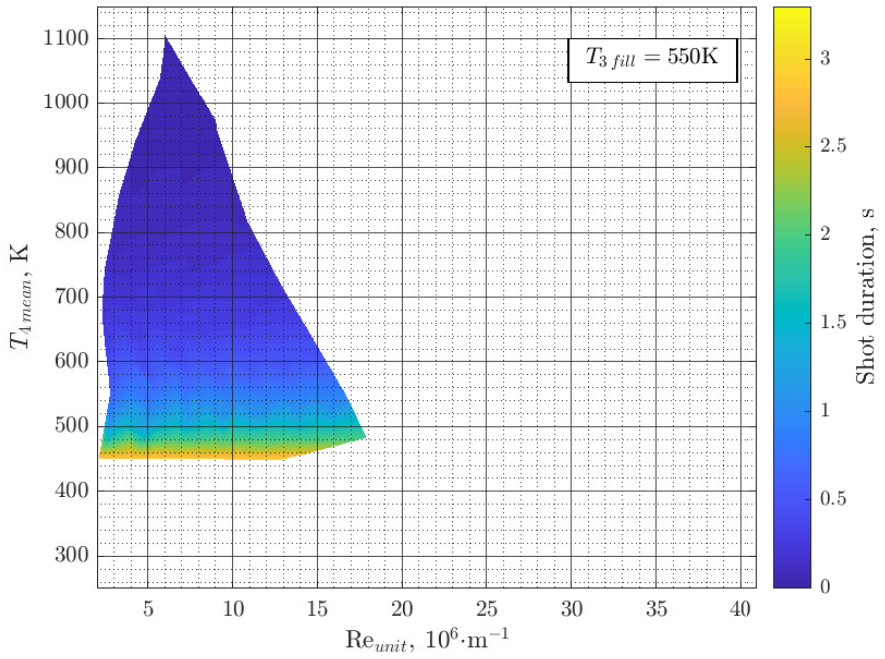

Figure 4.9: Map of shot duration for the range of T_4 and Re$_{unit}$ possible using $T_{3,f}$ = 550K.

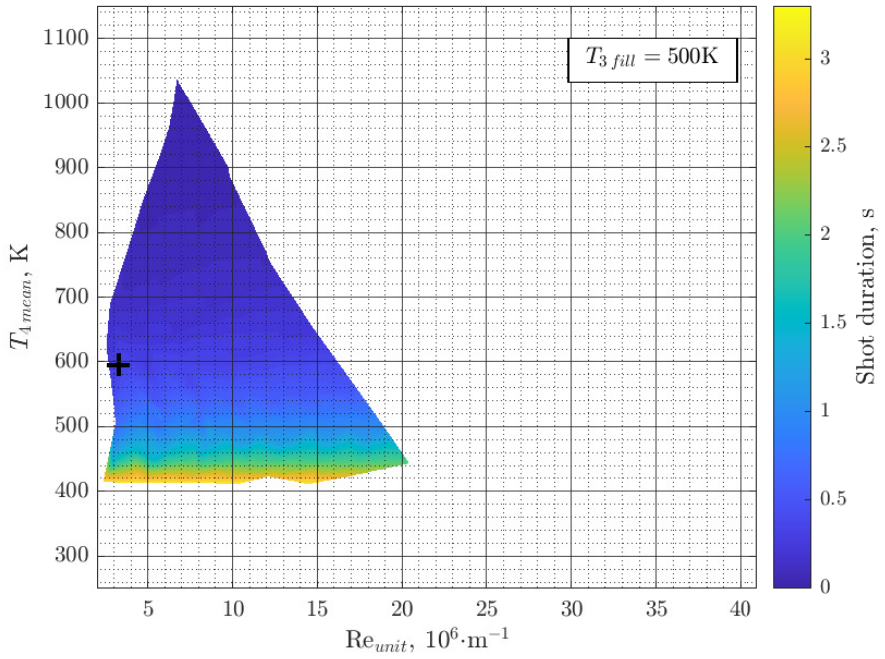

Figure 4.10: Map of shot duration for the range of T_4 and Re$_{unit}$ possible using $T_{3,f}$ = 500K.

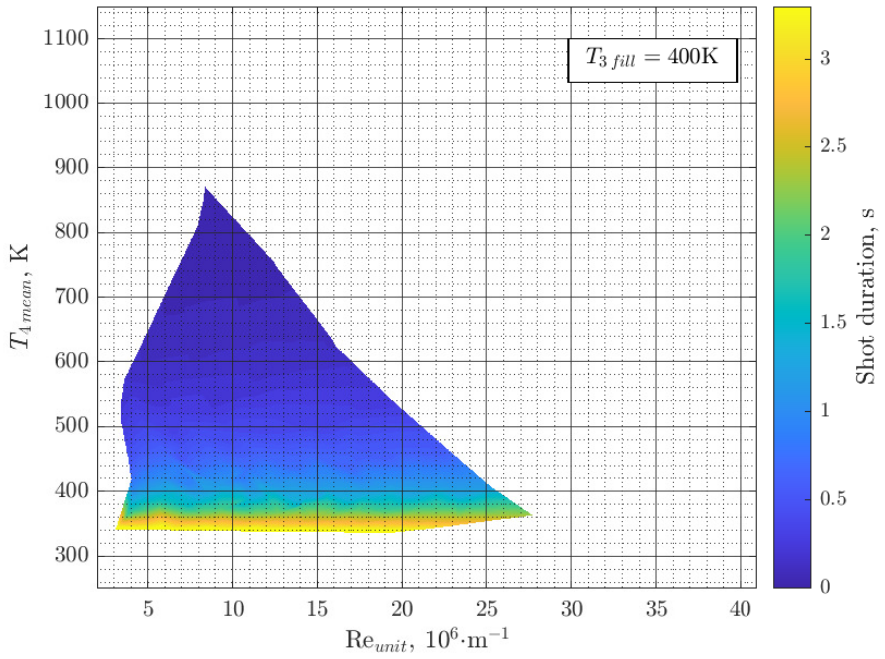

Figure 4.11: Map of shot duration for the range of T_4 and Re$_{unit}$ possible using $T_{3,f} = 400$K.

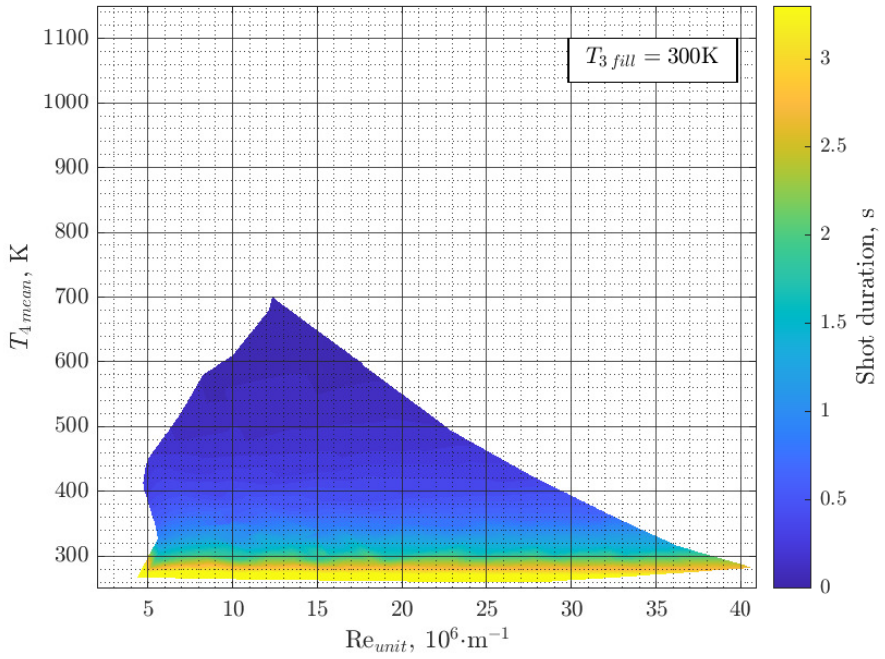

Figure 4.12: Map of shot duration for the range of T_4 and Re$_{unit}$ possible using $T_{3,f} = 300$K.

of LICH mode may not be necessary.

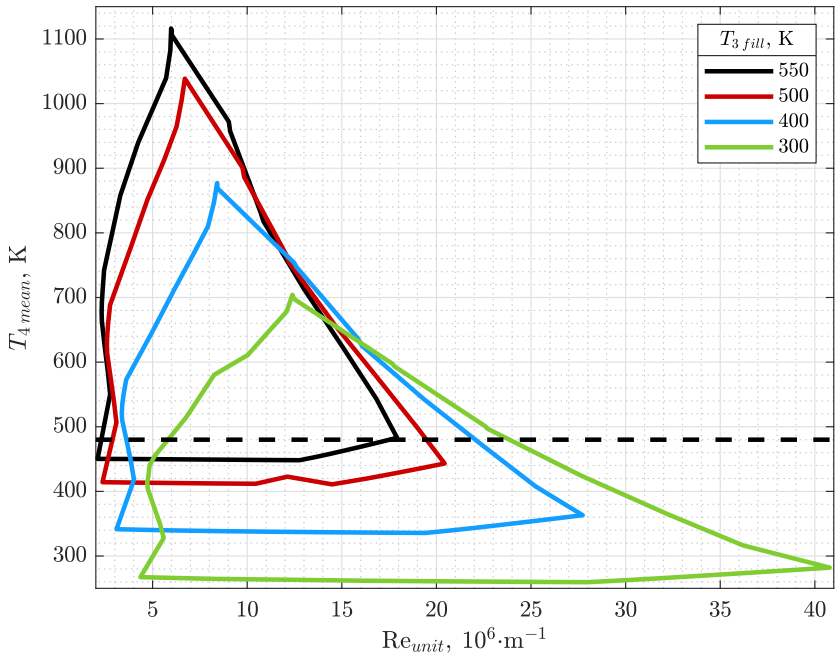

Figure 4.13: Full operating range of HDT in LICH mode at Mach 7. Four barrel fill temperatures are shown. The upper limit of Ludwieg mode is shown.

4.3.2.1 Using the Performance Maps

The performance maps presented in this section can be used either to estimate the freestream properties generated from an initial tunnel setup or, in reverse, to estimate the tunnel setup required for a desired freestream condition. In the first case, the black crosses give an example of estimating freestream conditions for the tunnel setup given for Condition A in Table 4.2.

To do the reverse, Figure 4.13 can be used to assess the most suitable $T_{3,f}$ for a desired combination of Re_{unit} and T_4. As mentioned above, higher $T_{3,f}$ values are desirable for safer and more reliable tunnel operation. Following the selection of a $T_{3,f}$, the value of $p_{3,o}$ can be determined using Figure 4.7 then the required compression ratio, and value of $p_{1,f}$, can be found using Figure 4.5.

4.3.3 Freestream Noise

The freestream noise experienced during LICH mode is expected to be greater than during Ludwieg mode due to the piston interacting with and reflecting rarefaction waves in the barrel, leading to significant pressure oscillations. There are multiple methods used in the literature to quantify the freestream noise of wind tunnels. One such method, proposed by Laderman [170], uses a normalised noise defined by Equation 4.7.

$$\text{Normalised noise} = \frac{RMS(p)/\overline{p}}{\gamma M^2/2} \tag{4.7}$$

The pressure can be any measured pressure - pitot pressure was used in this case. The Kulite sensor used for this measurement has a maximum bandwidth of 20 kHz. This does not give a full picture of all the noise present in the facility but does allow for quick qualitative comparisons between different modes of operation or different facilities. A more complete nozzle survey test campaign with an appropriately instrumented rake is planned for the future. However, due to the relatively low frequency effects that the piston causes, much of the differences in noise levels between Ludwieg mode and LICH mode are thought to be measurable using the current setup.

Figure 4.14, adapted from Birch et al [171], shows the normalised noise evaluated for a number of facilities similar to HDT along with some HDT data. The x-axis is the freestream Reynolds number based on nozzle exit diameter. Several Ludwieg mode shots for a range of Re_D at Mach 6 and 7 are displayed, along with two LICH shots at Condition A. For LICH mode shots, pitot pressures were taken across the entire test time: from the end of the intial pressure rise to the piston impact. For Ludwieg mode shots, pressures were taken from the second steady flow period (e.g. $\sim 0.13 - 0.15$ s in Figure 4.1). Pitot pressure signals were filtered using a bandpass filter with cutoff frequencies of 1 and 20 kHz. The `bandpass` function in Matlab was used, with a steepness factor of 0.98.

The noise level for Ludwieg mode shots is self-consistent, with a trend of higher Re_D conditions leading to lower levels of normalised noise. Although the Re_D of

the LICH mode condition is below the limit of operation for Ludwieg mode, the LICH mode data points appear to fall on the same line. This suggests that there is no significant increase in freestream noise levels at frequencies below 20 kHz when operating in LICH mode. It is encouraging, however, to see that noise levels in LICH mode are very comparable to other facilities.

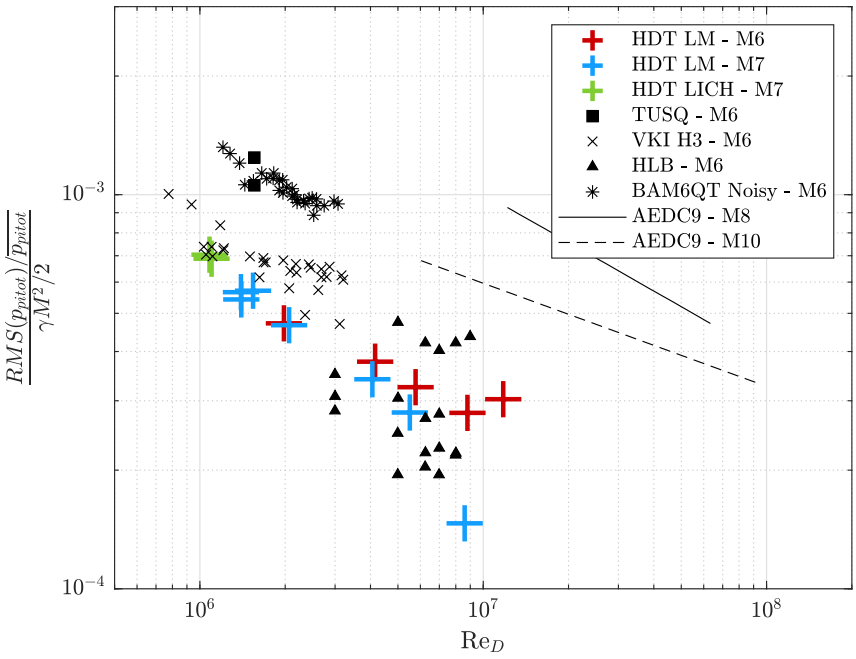

Figure 4.14: HDT freestream noise compared with other similar facilities: TUSQ [171], VKI H3 [172], HLB [173], BAM6QT [174], and AEDC Tunnel No. 9 [175]. Reproduced from Birch et al [171].

4.4 Summary

This chapter has described the successful implementation of LICH mode of operation in the HDT. New tunnel infrastructure has been proven and a design for a piston has been assessed, showing a need for some improvement. A LICH condition, which provides increased total temperature flow in HDT, has been tested and characterised. Experimental data has been collected which was used to validate a simple numerical ODE model to simulate the key processes which happen during a shot. The ODE model was used to generate performance maps for estimating flow conditions in

LICH mode operation at Mach 7. An increase in operating range compared to Ludwieg mode has been shown. Experimental data was also used to assess levels of freestream noise, which was found to be comparable to operation in Ludwieg mode.

To further develop LICH mode, a clearer understanding of the acoustic effects which have a large influence on various aspects of LICH operation would be valuable. Simulations using tools such as L1d would give an insight into these effects. For HDT to operate in LICH mode more regularly, the piston design will need to be re-assessed to ensure greater survivability. Finally, LICH mode will be most effective if matched conditions are able to be used. The implementation of additional logic to control the reservoir firing valves would make this more easily achievable while maintaining tunnel performance.

5

Steps and Gaps in Turbulent Boundary Layers

Contents

5.1 Test Conditions 109
5.2 Geometries 109
5.3 Heat flux augmentation 110
5.3.1 Camera parallax 112
5.3.2 Camera vibrations 112
5.3.3 Data Extraction 113
5.3.4 Flat plate data 114
5.4 Results 115
5.4.1 Heat Flux Profiles for Basic Geometries 115
5.4.2 Heat Flux Profiles for Combined Geometries 119
5.4.3 Application to Existing Correlations 125
5.4.4 Correlation Development 127
5.5 Summary 135

The effect of steps and gaps in turbulent boundary layers is primarily a change in the heat flux in the vicinity of the geometry in question. This chapter presents heat flux augmentation data from experimental work carried out in the Oxford High Density Tunnel.

5.1 Test Conditions

For this section of work, a fully turbulent boundary layer was desired at the step geometry at an axial position of 150 mm. The two higher Re_{unit} conditions (Conditions B & C) transitioned to full turbulence far enough upstream of the step, at $x = 0.1$ and 0.08 m, respectively. However for the lowest Re_{unit} condition (Condition A), a boundary layer trip consisting of a 1 mm diameter wire was placed at an axial position of 42 mm to ensure complete transition, which occurred at $x = 0.08$ m. Boundary layer transition was confirmed using heat flux measurements from the upstream thin film gauge array. Table 5.1 summarises the conditions used for this work.

Table 5.1: A summary of the test conditions used for testing in turbulent boundary layers.

Condition	Mach number	p_0 [bar]	T_0 [K]	Re_{unit} [10^6/m]	δ [mm]	# of tests
A	6.1445	18.095	434.60	16.372	2.5074	10
B	6.1290	27.078	432.76	24.814	1.8773	41
C	6.1728	37.606	435.78	33.495	2.1076	10

5.2 Geometries

Geometries covering a wide range of scales and types were tested. Table 5.2 shows how the different geometries are categorised and Figure 5.1 shows the range of sizes tested plotted graphically, with the x- and y-axes showing the heights of the step and fence relative to the boundary layer thickness, respectively. Figure 5.2 shows the step heights, H_1 and H_2 schematically. The codes listed in Table 5.2 describe the change in height experienced by the flow as it travels downstream over the surface of the plate. The subscripts signify the height relative to the fixed upstream portion of the plate. For example, UF represents an upwards change followed by no change (flat) - a forward-facing step - and DU$_-$ represents a downward change followed by an upward change lower than the fixed plate - a backward-facing step with an intermediate gap. The forward- and backward-facing steps have two configurations each (UF & FU and DF & FD). Both configurations of each step

are the same but allow different instrumentation to be used. The UF and DF geometries allow for easier comparison with other geometries due to the point of initial deviation from the flat plate being the same.

Table 5.2: Categorisation of different geometries

Description	Code	Relative Heights	Diagram
Flat plate	FF	$H_1 = H_2 = 0$	
Fence	UD_F	$H_1 > 0, H_2 = 0$	
Forward-facing step	UF	$H_1 = H_2 > 0$	
Forward-facing step	FU	$H_1 = 0, H_2 > 0$	
Backward-facing step	DF	$H_1 = H_2 < 0$	
Backward-facing step	FD	$H_1 = 0, H_2 < 0$	
Double step forward	UU	$H_2 > H_1 > 0$	
Double step backward	DD	$H_2 < H_1 < 0$	
Fence-step forward	UD_+	$H_1 > H_2 > 0$	
Fence-step backward	UD_-	$H_1 > 0 > H_2$	
Step-gap forward	DU_+	$H_2 > 0 > H_1$	
Step-gap backward	DU_-	$H_1 < H_2 < 0$	
Gap/cavity	DU_F	$H_1 < 0, H_2 = 0$	

5.3 Heat flux augmentation

Surface heat flux is calculated according to the process outlined in Section 3.3.1. In the majority of cases in this section, in order to compare different geometries efficiently, a non-dimensionalised heat flux augmentation (HFA) is used. This is defined in Equation 5.1 as:

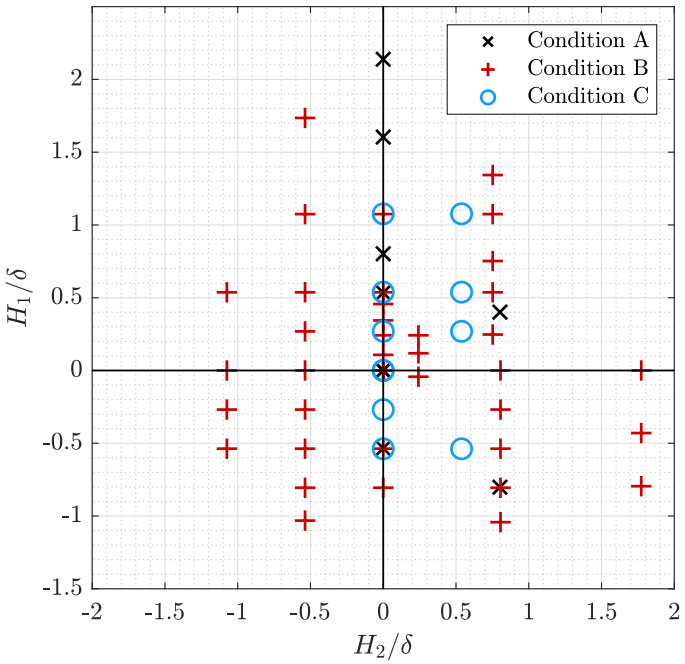

Figure 5.1: Range of geometries tested showing heights of the fence and step blocks relative to boundary layer thickness.

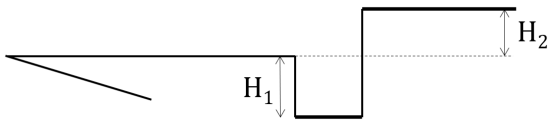

Figure 5.2: Schematic showing H_1 and H_2 for a DU_+ stepped-cavity geometry.

$$HFA = \frac{\mathrm{St}}{\mathrm{St}_{ref}} \cdot \left(\frac{\mathrm{Re}_{unit\,ref}}{\mathrm{Re}_{unit}} \right)^{1/5} \tag{5.1}$$

Where the subscript *ref* refers to a reference heat flux. In most cases, this is the heat flux on a flat plate at the same freestream conditions and with the same incoming boundary layer. To account for slight variations in freestream conditions between nominally identical shots, the heat flux ratio is multiplied normalised by the ratio of Re_{unit} between the two shots, raised to the power 1/5. This exponent comes from Eckert's heat flux correlation for turbulent boundary layers.

5.3.1 Camera parallax

Due to the camera being at an angle to the surface of the model, different geometries caused either the upright surfaces to appear in the IR image or some portions of the top surface to be obscured. For geometries in which the fence was higher than the step, certain portions of the data were removed. Figure 5.3 shows a sketch of this process: the rear face of the fence is visible and the corresponding heat flux data is removed. This process was performed on all geometries where the fence was higher than the step (geometries with codes ending in D). For geometries with the fence lower than the step (codes ending in U), a small part of the top of the fence block was obstructed by the corner of the step. To account for the hidden data, a gap was added into the HFA profile for these geometries. Figure 5.4 illustrates this procedure for both cases.

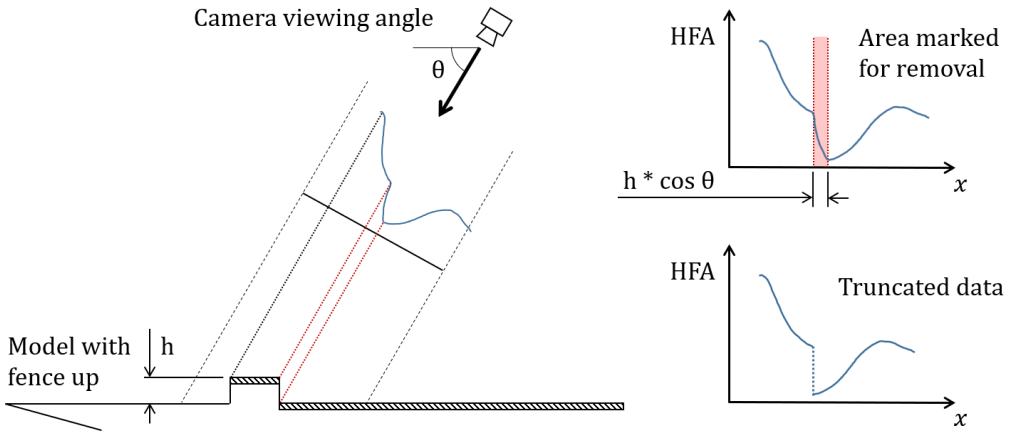

Figure 5.3: Diagram showing how camera parallax is accounted for with fences.

5.3.2 Camera vibrations

During shots, vibrations generated by the tunnel were transferred through the optics table to the camera mount. This caused the camera, and therefore the image of the model in the camera frame, to move during testing. The locations of physical hot spots in the image moved, meaning that subsequent heat flux calculations (which use the pixel-wise change in temperature) were affected. The images were stabilised

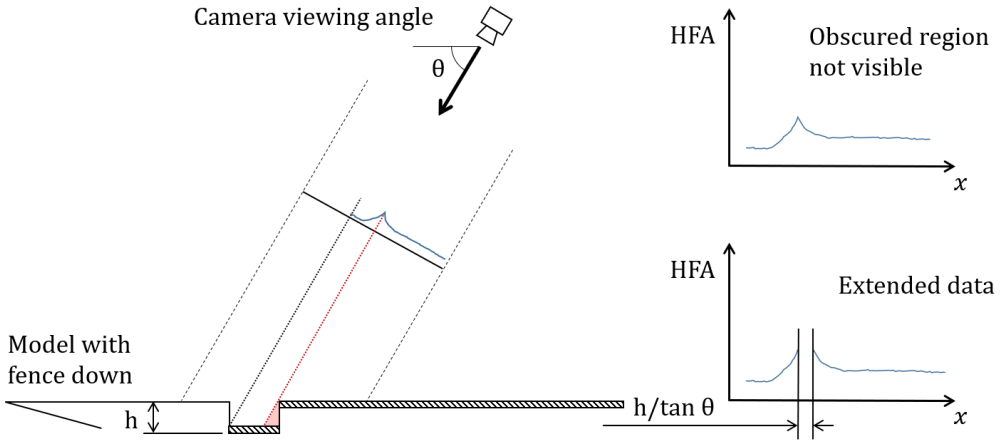

Figure 5.4: Diagram showing how camera parallax is accounted for with cavities.

using a subpixel image registration algorithm, developed by Guizar et al [176], which uses cross-correlation to calculate the relative shift between each video frame.

In addition to camera vibrations, the movement of the fence and step heights between different geometries placed the locations of interest (e.g. hotspots on the corners of steps) in different places in the camera frame.

To account for both of these issues and to ensure different shots could be normalised with respect to each other, the heat flux profiles were interpolated and given unified x-coordinates. The Akima method was used for interpolation due to its ability to avoid overshoots [177].

5.3.3 Data Extraction

Data for heat flux profiles was taken as the average heat flux over a number of pixels across the width of the model. Given that the model and geometry were 2-dimensional, the heat flux was determined not to vary in the spanwise direction. Using the average over a number of pixels near the model reduced the influence of occasional random hot spots. Figure 5.5 shows a frame from a shot and the pixels which were chosen. This example shows the heat flux and temperature for a fence (UD_F) geometry, with flow going from left to right. The darker strip along the middle of the image is one of the centreline thin film gauge arrays and the smaller circles near the centreline are PCB and Kulite pressure sensors. The

sensors heated the surface of the model by 1-5 °C, depending on the sensor - this temperature increase can be seen in the lower right-hand half of the image. Pixels were chosen to avoid the influence of this self-heating. The high heat flux line towards the left of the image is the leading edge of the fence and the slightly wider low heat flux line just downstream of this is the separation in the wake of the fence. The image is slightly tilted due to the camera mount. Pixel strips were taken at an angle to account for this.

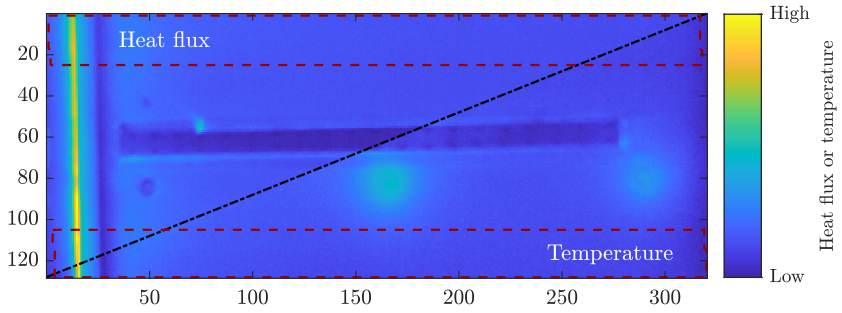

Figure 5.5: A sample frame from a fence test with the 'centreline' pixels outlined.

5.3.4 Flat plate data

When moving the fence and step into a flat configuration for the baseline cases, a small vertical offset between the different sections of the plate was always present. This was always measured to be $< 20\mu m$ in each case ($\sim 2\%$ of the boundary layer thickness), so any downstream effects were determined to be negligible. However, small hot and cold spots were present in the heat flux profiles - up to an 8% deviation from the correct level. As these were to be used for normalisation, any deviations from the true flat plate heat flux would produce non-physical artefacts in the resulting heat flux augmentations. A curve based on Eckert's correlation, fitted to downstream heat flux data, was used as the heat flux baseline case. The fitted curve is described by Equation 5.2:

$$q_{fit} = c_1 q_{Eckert} + c_2 \tag{5.2}$$

Where q_{Eckert} is Eckert's solution for turbulent heat flux based on boundary layer edge properties and c_1 and c_2 are fitted constants. q_{fit} is the fitted curve and, in most cases presented in this chapter, is used as q_{ref} in Equation 5.1. Figure 5.6 shows an example of flat plate heat flux with the fitted curve overlaid.

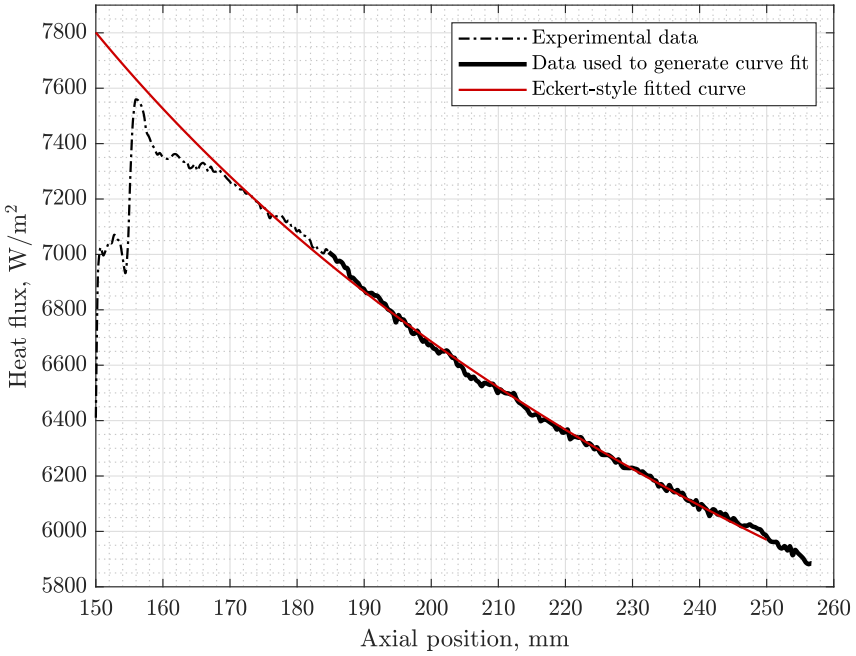

Figure 5.6: Flat plate baseline heat flux with a straight line fitted.

5.4 Results

5.4.1 Heat Flux Profiles for Basic Geometries

In each of the plots in this section, the heat flux augmentation profile is plotted against axial position as a distance from the model leading edge. For each profile, a schematic diagram of the geometry is given, along with the heights of the fence and step components relative to the upstream plate listed in the legend. Geometries are also shown in which a change in behaviour was observed when testing different geometry scales.

Thin film gauge data is plotted alongside IR data in many cases. Where thin film gauge data is not displayed this is either because data wasn't collected for

that shot or the data that was collected was of very low quality and did not produce physically representative results. Error lines for the first listed shot in each figure are also plotted.

5.4.1.1 Forward-Facing Steps

Experimental heat flux augmentation data for a forward-facing step (FU) is shown in Figure 5.7. At location of the step, $x = 155$ mm, there is a peak in heat flux, which decreases rapidly at first and steadily relaxes to the flat plate level. Upstream of the step, a separation bubble creates an increased plateau in heat flux at an intermediate level between the baseline and the peak, which then increases again up to the peak. This plateau begins at around $x = 140$ mm after rising over the preceding $\sim$10 mm. The rise is visible in thin film gauge data (crosses) but the plateau is located between the thin film gauges and IR data. The location of the end of the plateau is captured in the IR data at around $x = 152$ mm, where the heat flux begins to rise to its peak.

The prediction of separation distance by Zukoski [43] seems to be accurate to the point at which the plateau of heat flux begins. Maximum heat flux predictions of Nestler [44] and Hung & Patel [45] are both lower than measured, although the Hung data point lies within the error band.

5.4.1.2 Backward-Facing Steps

Experimental heat flux augmentation data for a backward-facing step (DF) is shown in Figure 5.8. A separation directly behind the step causes a sudden drop in heat flux. The shape of the heat flux as it recovers back to a steady level is dependent on the ratio of the step height to the boundary layer thickness. Typically, larger steps cause an overshoot in heat flux at the reattachment location. In this dataset, step heights were large enough to produce only a small overshoot. Due to a thinner boundary layer following reattachment, the downstream heat flux is greater than the flat plate level. Predictions of minimum separation heat flux by Lamb [54] are good, with a close agreement for both step heights.

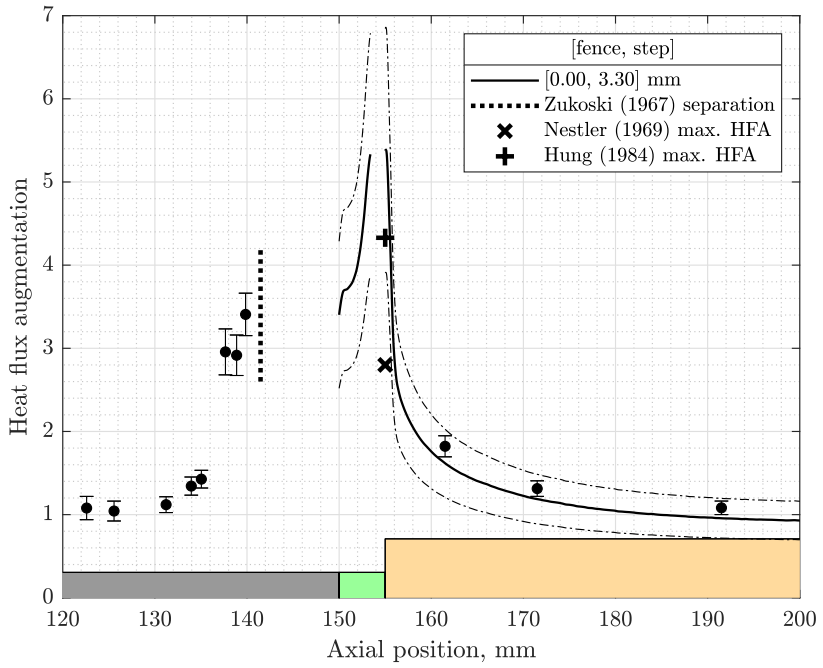

Figure 5.7: Heat flux augmentation on forward-facing steps.

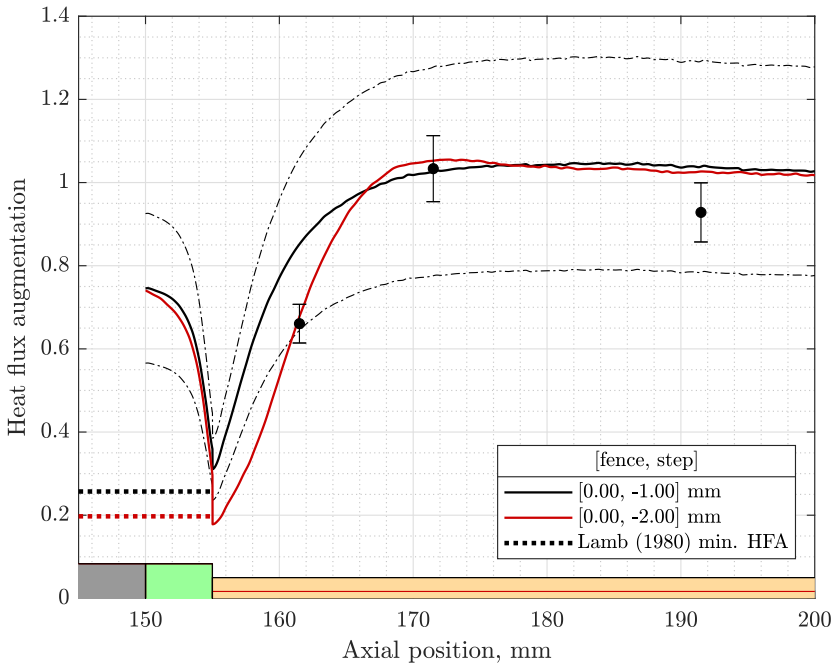

Figure 5.8: Heat flux augmentation on backward-facing steps.

5.4.1.3 Fences (2-Dimensional Protuberances)

A 2-dimensional protuberance (protuberances can also be defined with a 3rd width dimension), or fence, (UD_F) can be thought of as a forward-facing step followed by a backward-facing step. The same features as each isolated step are present in the heat flux profile, with similar dependencies on step height. The heat flux peaks on the leading edge of the fence, decreases towards the trailing edge, and drops due to a separation in the wake of the fence. Similarly to backward-facing steps, the reattachment causes an overshoot if the fence is high enough compared to the boundary layer. Figure 5.9 shows the heat flux on two fence geometries of different heights: 0.2 mm and 2.0 mm. Compared to the larger fence, the smaller fence has a lower peak heat flux, a smaller decrease in heat flux in the separated region and doesn't overshoot the flat plate level at reattachment. The larger fence also causes a decrease in the recovered level following the reattachment overshoot. The 2.00 mm fence in Figure 5.9 displays a large overshoot whereas the backward-facing step of the same size in Figure 5.8 shows no overshoot. This suggests a dependency on the flow upstream of a backward-facing step when looking at flow reattachment.

Predictions from existing correlations for peak heating are once again lower than measured, although the Hung & Patel correlation is very close. Both of the Hung & Patel predictions lie within the error band of the IR data while the Nestler correlation does not.

5.4.1.4 Cavities

As with fences, cavities (DU_F) can be viewed as a backward-facing step followed by a forward-facing step. Cavities in this work are all categorised as open cavities - with $L/H < 10$ [60]. The flow over open cavities separates but does not fully establish again on the floor before it reaches the downstream corner. This leads to the heat flux profile shown in Figure 5.10. The cavity floor experiences a drop in heat flux, caused by a separation, which increases along the length of the cavity to the peak augmentation level on the upper edge of the downstream face. The heat flux downstream of the cavity relaxes to a level close to the flat plate baseline.

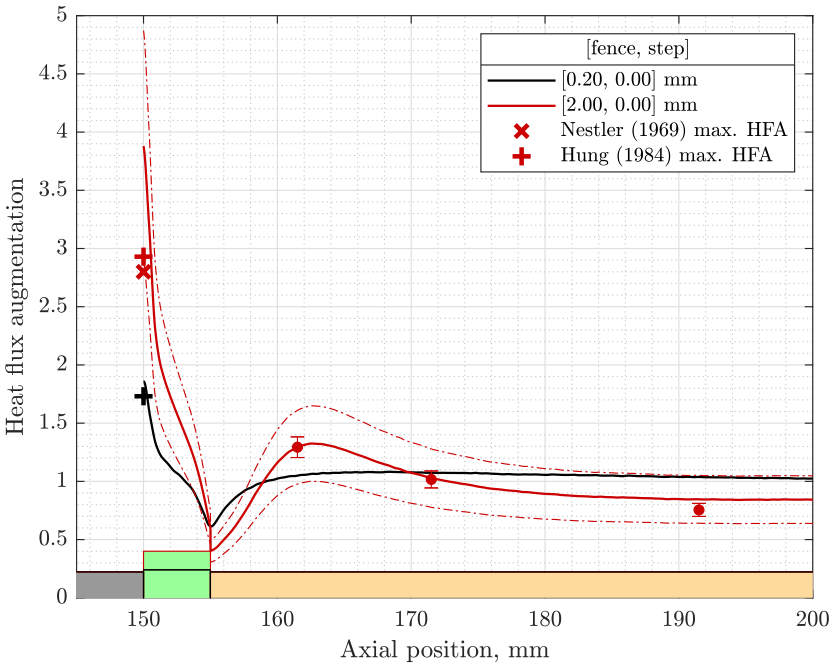

Figure 5.9: Heat flux augmentation on fences.

Predictions from correlations are plotted for minimum heat flux inside the cavity and maximum heat flux on the downstream edge of the cavity, both from Lamb [64]. This time, the minimum heat flux on the cavity separation is predicted to be significantly lower than experimentally measured and is outside the error bands of the data. The peak heating on the downstream cavity lip is predicted with good accuracy with $< 5\%$ difference between measured and predicted values.

5.4.2 Heat Flux Profiles for Combined Geometries

In addition to the four simple geometries described above, a number of combined cases were tested.

5.4.2.1 Double Forward-Facing Steps

Steps with smaller intermediate steps will be referred to as double steps. The heat flux profiles for forward-facing double steps (UU geometries) compared with that of a single step of the same total height are shown in Figure 5.11. The inclusion of an intermediate step creates an additional hot spot. It can be seen that the

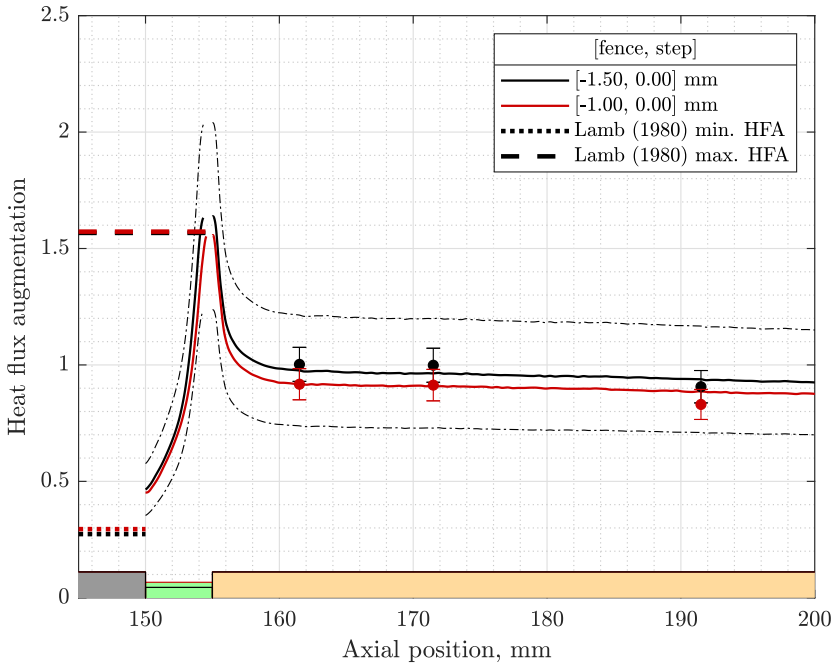

Figure 5.10: Heat flux augmentation on cavities.

relative heights of each step are important: the smaller intermediate step of 0.46 mm increases the peak HFA value (now at $x = 155$ mm rather than $x = 150$ mm) compared to the larger intermediate step of 1.00 mm in which the second peak is lower than the first. In all three cases, the initial peak is approximately the same height, indicating that the heat flux on double steps primarily affects downstream heat loads. The heat flux upstream of double steps was not measured in this work, so any differences in upstream separation cannot be speculated. Note that the small bump in the blue profile at $x = 155$ mm is due to the interface between the two adjustable blocks.

5.4.2.2 Double Backward-Facing Steps

Heat flux profiles for a backward-facing step compared with two heights of double backward-facing step are presented in Figure 5.12. Compared to the single step (in blue), intermediate steps appear to extend the overall separation length. At both step locations ($x = 150$ and $x = 155$ mm) a larger change in height creates a more pronounced separation and a lower minimum heat flux. The most downstream

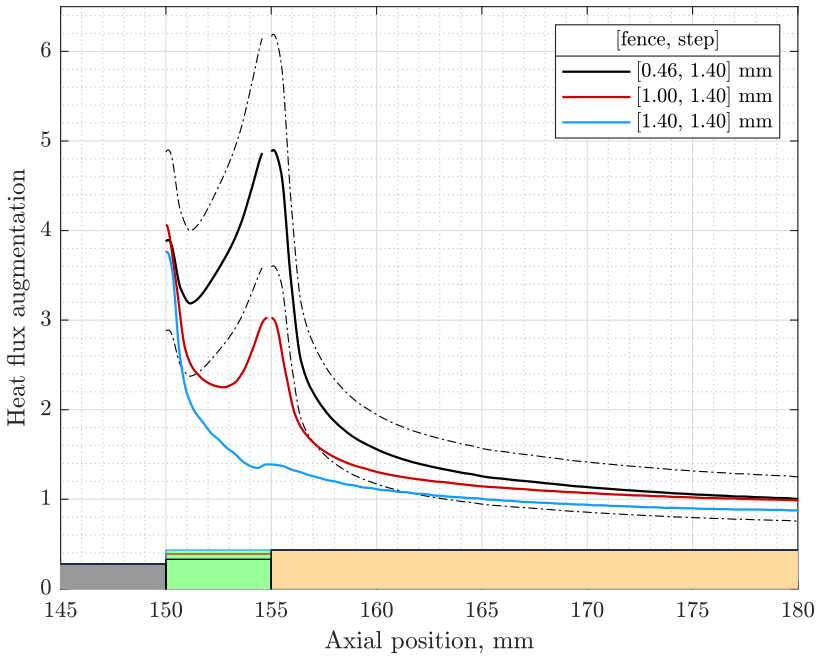

Figure 5.11: Heat flux augmentation on double forward-facing steps compared with a single forward-facing step.

of these steps, at $x = 155$ mm, has a larger impact on the overall heat load experienced by the model.

5.4.2.3 Steps with Intermediate Fences

Figure 5.13 shows three fences with differing rear drop heights. The flow field over all three of the geometries is similar until $x = 155$ mm, causing the heat flux profile across the top of the fences ($x = 150$ - 155 mm) to be identical in each case. The heat flux in the downstream separation is directly affected by the drop height, with the larger downward steps causing larger separations, greater reattachment heating, and lower minimum heat flux in the internal corner of the rear step.

In contrast, Figure 5.14 shows heat flux profiles for two different fence heights and one flat fence (FD geometry), all with a ~1 mm drop at $x = 155$ mm. In this case, the flow fields are substantially different to each other further upstream compared to the fences shown in Figure 5.13. Even with similar sized downward steps, the overall heat flux profiles are completely different. Larger initial steps cause a higher level of heat flux in the entire vicinity of the fence: the blue 2.50 mm height line is

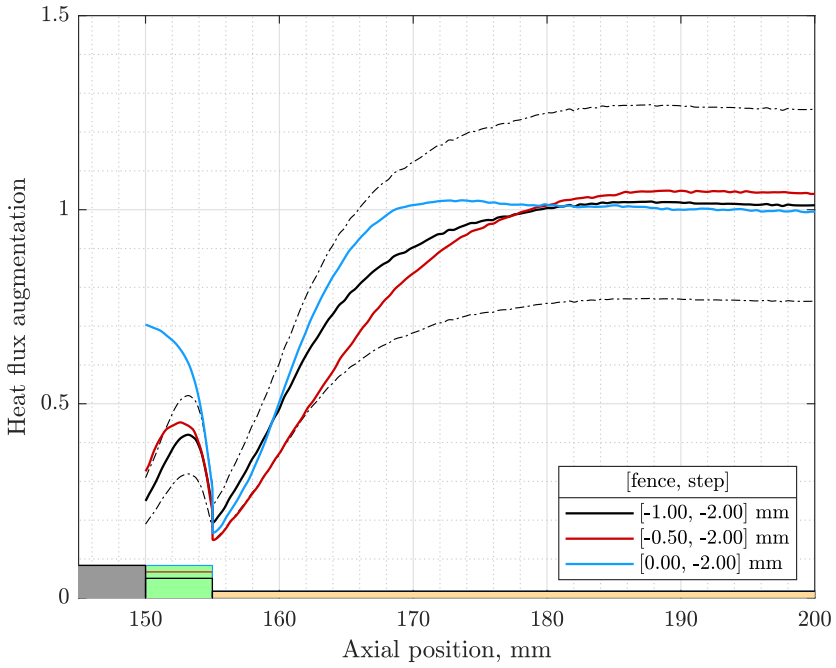

Figure 5.12: Heat flux augmentation on double backward-facing steps compared with a single backward-facing step.

consistently higher than the red 1.00 mm line until about $x = 170$ mm. However, the location of the reattachment overshoot, and therefore the size of the separation, appears to be the same for each step. In contrast to the fences, the rear-facing step (in black) has a completely different profile, not overshooting at reattachment and settling at a higher heat flux further downstream. A finding consistent with that of fences (Figure 5.9) is that a larger initial fence height results in a lower downstream heat flux. This could potentially be of interest in vehicle design, where this effect could be used to reduce the heat flux downstream of a know protuberance location.

5.4.2.4 Forward-Facing Steps with Upstream Gap

The effect of including a recess upstream of a forward-facing step (DU_+ geometries) is examined in Figure 5.15. Any size of upstream cavity appears to cause a separation over the cavity, which reduces the local heat flux, including that on the peak of the step at $x = 155$ mm. Above a cavity depth of 0.5 mm, there is no additional reduction of heat flux caused by further increasing the depth. Additionally, the downstream effect of these cavities is negligible, with almost identical heat flux

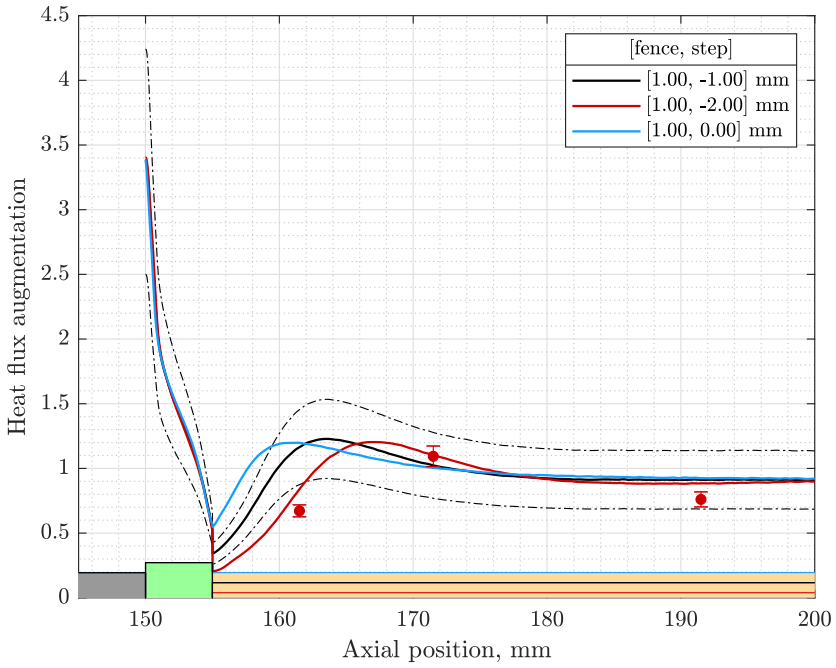

Figure 5.13: Heat flux augmentation on 1 mm height fences with different rear plate heights.

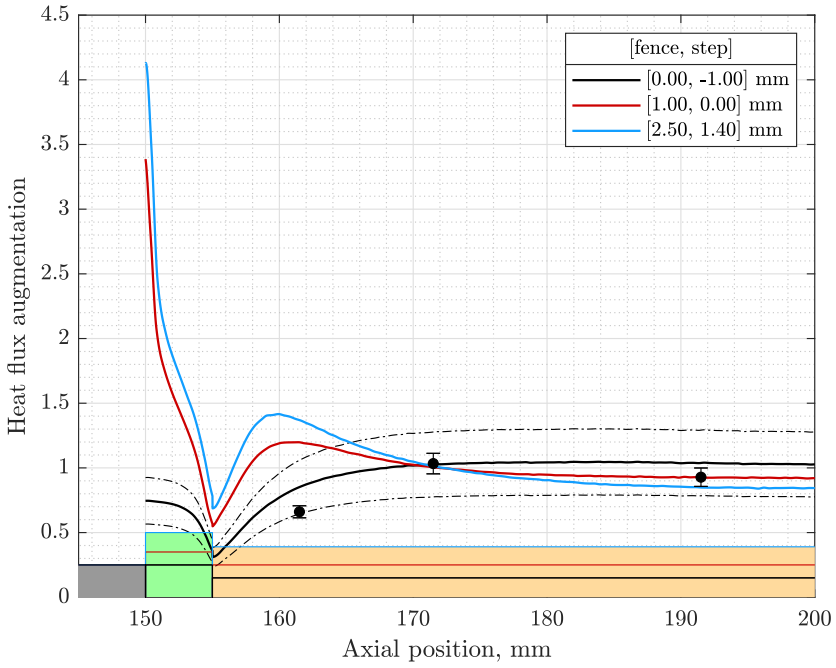

Figure 5.14: Heat flux augmentation on 1 mm drop heights following different upstream fence heights.

profiles immediately downstream of the step. This result may be useful in vehicle design, where the addition of a small cavity upstream of a step could be used to reduce the integrated heat flux in an area without impacting the downstream flow.

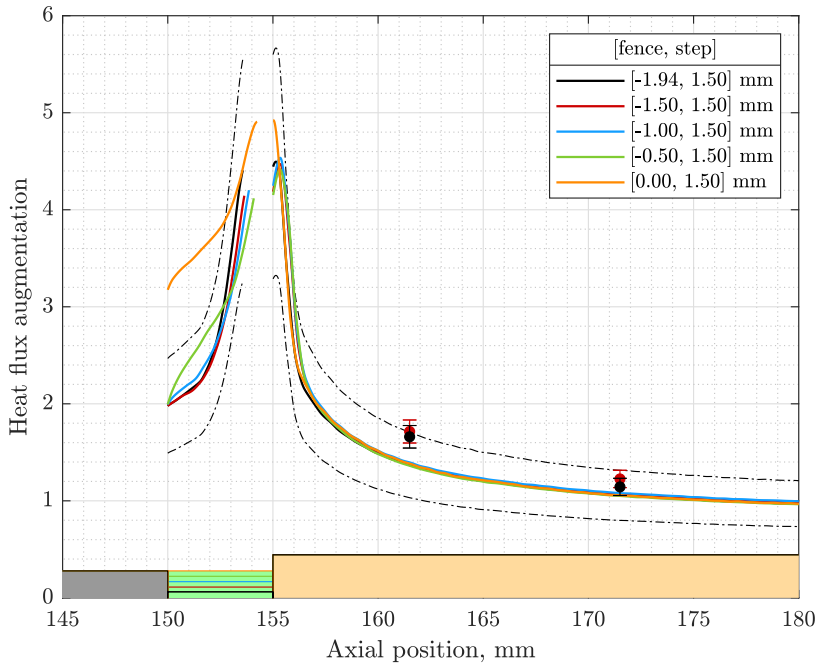

Figure 5.15: Heat flux augmentation on forward-facing steps with upstream cavities of different depths.

5.4.2.5 Backward-Facing Steps with Downstream Gap

Intermediate cavities were also tested on backward-facing steps (DU_ geometries). Figure 5.16 shows two backward facing step-gaps compared to a single step, all with an overall step height of -1 mm. Similarly to the forward step-gaps shown in Figure 5.15, the inclusion of an intermediate cavity reduces the heat flux in the cavity itself. Small hot spots occur on the downstream lip of the cavity at $x = 155$ mm, but not to a level of heat flux higher than the single step. Further downstream, the heat flux profiles recover to the same level within around 15 mm. Once again, this may be a useful result from the perspective of vehicle design.

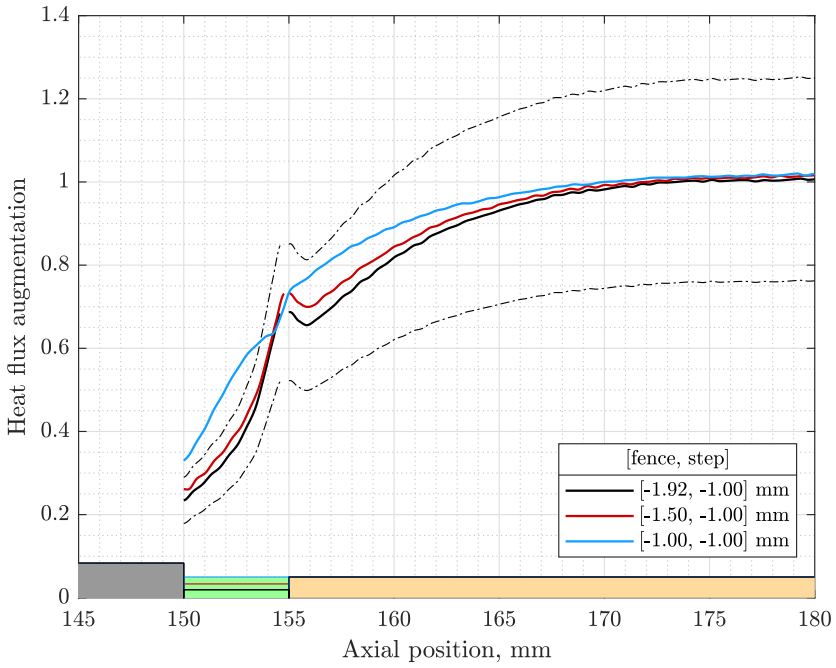

Figure 5.16: Heat flux augmentation on backward-facing steps with downstream cavities of different depths.

5.4.3 Application to Existing Correlations

5.4.3.1 Peak Heating on Prominent Forward-Facing Steps

Figure 5.17 shows the peak heating on prominent forward-facing steps (forward-facing steps with no upstream intermediate steps or gaps/cavities). Geometries included are: UD_F, UF, UD_+, and UD_-. Heat flux augmentation on the maximum heating location is plotted against the ratio of step height to boundary layer thickness at the step location on a flat plate. For these geometries, peak heating always occurs at the leading edge of the step.

Heating on steps significantly smaller than the boundary layer thickness is heavily dependent on step height. This dependency reduces as the step height approaches the boundary layer thickness, where the value of HFA appears to reach steady level. Nestler [44] also shows step height independence for steps larger than the boundary layer and gives a correlation to describe the heat flux augmentation just upstream of large steps, depending only on freestream Mach number (see Equation 2.1 in Section 2.2.1). For Mach 6 freestream flow the value of peak HFA

calculated using this correlation is 2.8. This is plotted in Figure 5.17 as a dashed line beginning at $h/\delta = 1$. The current data shows significantly higher levels of heat flux augmentation than Nestler. This is explained by the Nester correlation describing heat flux just upstream of the step rather than on the step itself - this was probably a limitation of the instrumentation used. Additionally, experimental data used in the creation of the correlation has significant spread: data at M = 6.3 gives a HFA of ∼2.8 whereas data from a different study at M = 6.0 gives a HFA of ∼3.4, which is closer to the current data.

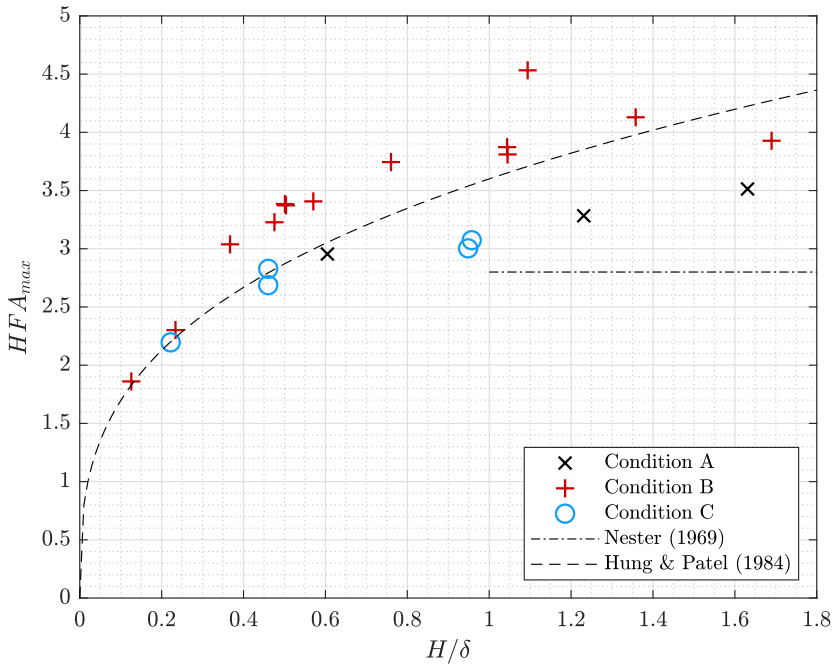

Figure 5.17: Heat flux augmentation on prominent forward-facing steps. Re_{unit} = 18.5 - 25.5 million/m. Correlations from Nestler [44] and Hung & Patel [45] are also plotted.

5.4.3.2 Minimum Heat Flux Downstream of Backward-Facing Steps

Lamb's correlation, discussed in Section 2.2.1, describes the minimum heat flux in the separated region following backward-facing steps in turbulent boundary layers. Figure 5.18 shows this correlation (Equation 2.5) compared with minimum separation heat flux data for geometries tested which feature a single backward-facing step. Geometries included are: $\mathrm{UD_F}$, FD, $\mathrm{UD_+}$, and $\mathrm{UD_-}$. The presented

data points correspond to the minimum values of heat flux augmentation at $x = 155$ mm in Figures 5.8 and 5.9. Data points are coloured according to the height of the fence block. Backward-facing steps, which Lamb's correlation was designed for, are displayed in dark blue and circled in red. These are the closest of the points presented: the correlation appears to predict the heat flux reasonably well, although there are only two data points, so this could be by chance.

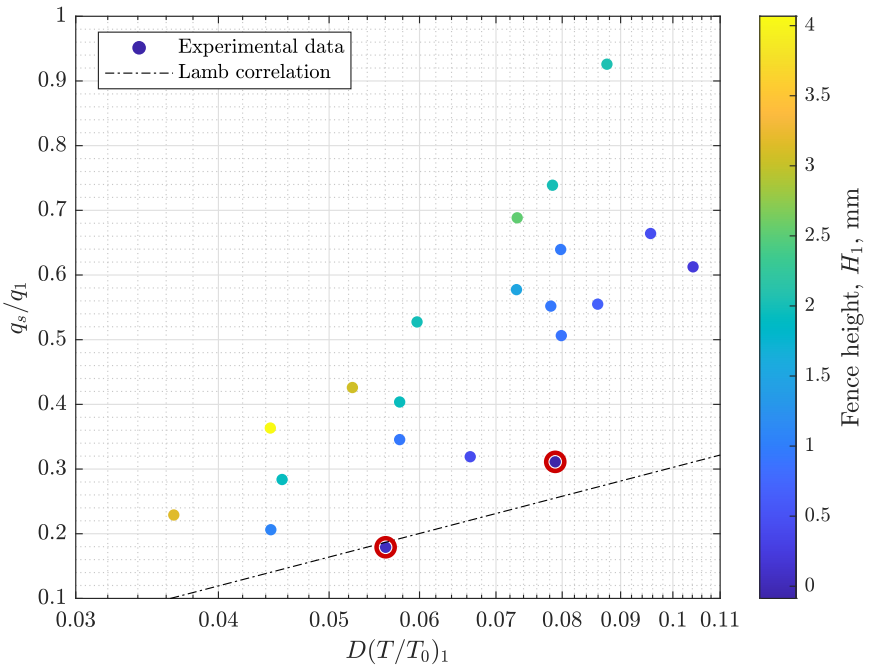

Figure 5.18: Minimum separation heating using Lamb's correlation [54].

Lamb's correlation was developed uniquely for minimum heat flux after backward-facing steps in turbulent boundary layers. Everhart [67] employed a more generally applicable method of producing cavity heating correlations, using it to correlate the average and maximum heat flux augmentation in open and closed cavities in laminar and turbulent boundary layers.

5.4.4 Correlation Development

The correlation formulated by Everhart [67] (discussed in Section 2.2.3) to describe various heating quantities in 3-dimensional cavities is shown in Equation 5.3.

Variables X and Y are defined using flow and geometric quantities and are then fitted to a straight line.

$$X = \ln\left[M_e^{\sigma} Re_{\theta}^{\tau} \left(\frac{L}{\delta}\right)\right] \tag{5.3a}$$

$$Y = \ln\left[\left(\frac{H}{\delta}\right)^{\alpha} \left(1 + \frac{L}{H}\right)^{\beta} BF\right] \tag{5.3b}$$

$$Y = a + bX \tag{5.3c}$$

Where, L is the length of the cavity, H is the height of the cavity, and BF is the "bump factor" - analogous to HFA. Re_{θ} is the Reynolds number based on the local momentum thickness. The value of momentum thickness used to calculate this is approximated as $\theta = 0.097\delta$ [159]. The constants α, β, σ, τ, a, and b are calculated by fitting the function to experimental data. Fitted constants for the average bump factor on the floor of open cavities are listed in Table 5.3.

Table 5.3: Constants for average open cavity floor bump factor, taken from Everhart [67].

α	β	σ	τ	a	b
3.70	2.70	0.00	0.10	-2.3741	2.6034

Applying this correlation to the current dataset indicates that this method is not applicable to combined stepped cavity geometries. Figure 5.19a shows average HFA for cavity-type geometries plotted according to Equation 5.3. Geometries included in this figure are (referring to Table 5.2): DU_F, DU_+, and DU_-. Data points are coloured according to the height of the rear plate, H_2 (see Figure 5.2 above). The points circled in red, corresponding to plate heights of 0 mm (DU_F), can be compared with Everhart's dataset. These points generally lie the closest to the central line, indicating that the correlation is applicable to 2-dimensional cavities as well as 3-dimensional cavities. However, geometries with different rear plate heights deviate significantly and do not appear to follow a trend.

The current dataset tested flow conditions at a single Mach number (M = 6) and geometries of a single length (L = 5 mm), resulting in a small range in X. The variety of geometry types and scales tested (and therefore range of HFA)

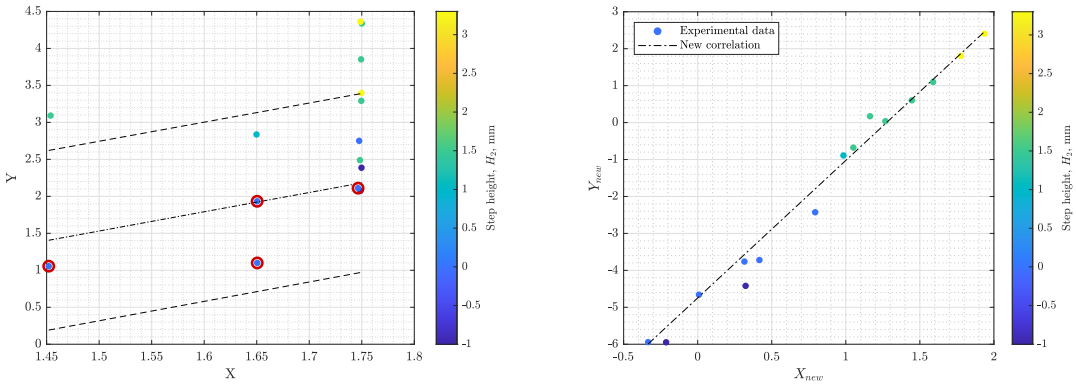

(a) Equation 5.3 using constants in Table 5.3. **(b)** Equation 5.4 using constants in Table 5.4.

Figure 5.19: Data applied to correlations for average cavity floor heating.

leads to larger range in Y. To make this correlation scheme more applicable to combined geometries, various modifications were made to Equation 5.3 to account for the different entrance and exit heights of geometry configurations. The modified correlation scheme is shown in Equation 5.4.

$$X_{new} = \ln\left[M_e^{\sigma} Re_{\theta}^{\tau}\left(\frac{|\Delta H|}{\delta}\right)\right] \tag{5.4a}$$

$$Y_{new} = \ln\left[\left(\frac{|\Delta H|}{\delta}\right)^{\alpha}\left(\frac{L}{S_{new}}\right)^{\beta} HFA\right] \tag{5.4b}$$

$$Y_{new} = a + bX_{new} \tag{5.4c}$$

The geometry scale, H, is now split into H_1 and H_2 (shown in Figure 5.2) which are defined as the heights of each adjustable block with respect to the upstream plate - postive values being above the flat plate level. ΔH is the height of the rear face of the cavity, $H_2 - H_1$. In the above formulation, the absolute, scalar height is used.

The term $|\Delta H|/\delta$ appears in both X_{new} and Y_{new}. The height of the fence block H_1 is contained within the S_{new} term. This term was adapted from that used by Lamb in the development of previous cavity heating correlations [64] and is defined, approximately, as the ratio between the cross-sectional area of the separation vortex in a cavity and the perimeter of that vortex. While this ratio is simply defined

for regular cavities, for geometries with differing front and rear heights, the non-rectangular cavity cross-section must be factored into the ratio. Equation 5.5 shows the formulation which accounts for non-zero values of H_2.

$$S_{new} = \frac{L(|H_1| + |\Delta H|)}{L + |H_1| + |\Delta H| + \sqrt{L^2 + (|H_1| - |\Delta H|)^2}} \tag{5.5}$$

To apply the modified correlation to experimental data, Equation 5.4 is rearranged for HFA, this is shown in Equation 5.6:

$$HFA = e^a \left[M_e^\sigma Re_\theta^\tau \left(\frac{|\Delta H|}{\delta} \right) \right]^b \left(\frac{|\Delta H|}{\delta} \right)^{-\alpha} \left(\frac{L}{S_{new}} \right)^{-\beta} \tag{5.6}$$

Constants are fitted to this equation using the Levenberg-Marquardt least-squares fitting method. Constants α, β, τ, a, and b were calculated while σ was set to 0 due to M_e being constant throughout the current dataset. When applied to the data presented in Figure 5.19a, the modified correlation produces a much better fit, seen in Figure 5.19b. Constants for this fit are shown in Table 5.4 along with the R^2 value for the straight line fit (Equation 5.4c).

Table 5.4: Constants for average cavity floor HFA using the modified correlation in Equation 5.4.

α	β	τ	a	b	R^2
2.56	-1.03	0.143	-5.05	3.72	0.981

5.4.4.1 Other Geometries

Following the success in fitting data for average cavity floor HFA, other flow quantities can be correlated using the same methodology. Figure 5.20 shows the quantities plotted according to Equation 5.4. Table 5.5 shows the fitted constants and R^2 in each case.

Minimum cavity heating

Minimum cavity floor heating for geometries in which the fence is the lowest point (types DU_F, DU_+, and DU_-) is shown in Figure 5.20a. Points are coloured according to the height of the rear step, H_2. The minimum heat flux occurs at

the most upstream internal corner of a cavity, for example at $x = 150$ mm in Figures 5.10, 5.15, and 5.16.

Peak cavity heating

Peak end wall cavity heating for the same geometry types (DU_F, DU_+, and DU_) is presented in Figure 5.20b. This peak in heat flux happens on the upstream external corner of the rear step of the cavity geometry: $x = 155$ mm in Figures 5.10, 5.15, and 5.16.

Minimum separation heating

The minimum heat flux caused by the separation downstream of a step is correlated in Figure 5.20c. Points are coloured according to fence height, H_1. Geometries included contain a single backward facing element, with either no upstream or positive upstream steps ($H < 0$ and $H_1 \geq 0$). This corresponds to geometry types of FD, UD_F, UD_+, and UD_. This minimum heating occurs at $x = 155$ mm in Figures 5.8, and 5.14.

Peak reattachment heating

The correlation for peak heating at the reattachment location following a separation is shown in Figure 5.20d. As with minimum separation heating, geometries included are ones which experience a separation with no intermediate steps or cavities: FD, UD_F, UD_+, and UD_. However, only cases which produce an overshoot in heat flux at the separation location are included. Figure 5.14 provides an example of geometries either side of this criterion and the difference in peak reattachment heating between different geometry scales.

Reattachment length

The reattachment distance, or separation length, following a backward facing geometry can also be correlated. The same geometries are used as for peak reattachment heating, with the same restrictions regarding an overshoot at reattachment. Figure 5.20e shows the correlated data. Unlike each other correlation presented, this time

the HFA term in Equation 5.4b is replaced with a non-dimensional distance term and the Y axis, shown in Equation 5.7, is defined slightly differently.

$$Y_{new,\,reattach} = \ln\left[\left(\frac{|\Delta H|}{\delta}\right)^{\alpha}\left(\frac{L}{S_{new}}\right)^{\beta}\left(\frac{x_{reattach}-x_{step}}{|\Delta H|}\right)\right] \tag{5.7}$$

Where $x_{reattach} - x_{step}$ is the distance between the backward facing step and the reattachment location and ΔH is the height of the backward facing step (referring to Figure 5.2). For the purpose of simplicity, $x_{reattach}$ is defined as the location of the peak in heat flux following a separation: for example, $x_{reattach} \approx 162$ mm in Figure 5.9. Figure 5.13 illustrates different peak heating locations, and therefore different reattachment lengths, for different rear step heights.

Peak step heating

The peak heating on prominent forward facing steps (steps with no upstream intermediate steps or larger downstream steps) is independent on any downstream geometry changes. As such, the only geometry dependent quantity is the initial step height, H_1. Both the X and Y correlation parameters have been redefined to account for this, shown in Equation 5.8.

$$X_{new,\,step} = \ln\left[M_e^{\sigma} Re_{\theta}^{\tau}\left(\frac{H_1}{\delta}\right)\right] \tag{5.8a}$$

$$Y_{new,\,step} = \ln\left[\left(\frac{H_1}{\delta}\right)^{\alpha}\left(\frac{L}{S_{new}}\right)^{\beta} HFA\right] \tag{5.8b}$$

For this formulation, the height terms use H_1 rather than $|\Delta H|$, and the exponent for the second term in the Y axis, β, is set to 0. This correlation is plotted in Figure 5.20f. Geometries included are types UF, UD_{+}, UD_{F}, and UD_{-} where peak heat flux occurs, for example, at $x = 150$ mm in Figures 5.9 and 5.13.

Table 5.5: Constants for Equation 5.4

	Eqn.	Fig.	α	β	τ	a	b	R^2
Min. cav.	5.4	5.20a	2.44	-1.17	0.115	-4.93	3.84	0.979
Peak cav.	5.4	5.20b	2.57	-1.13	0.0873	-3.11	3.71	0.987
Min. sep.	5.4	5.20c	3.64	0.958	0.0553	-0.719	2.65	0.997
Peak reattach.	5.4	5.20d	3.23	0.433	-0.00133	0.895	3.08	1.00
Reattach. loc.	5.7	5.20e	3.15	-0.952	-0.117	2.93	3.09	1.00
Peak step	5.8	5.20f	0.705	-	-	-0.204	3.33	0.988

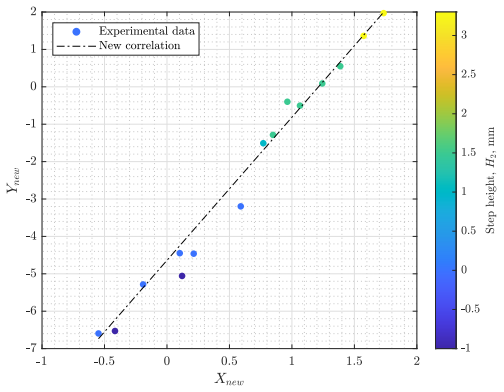

(a) Minimum cavity HFA.

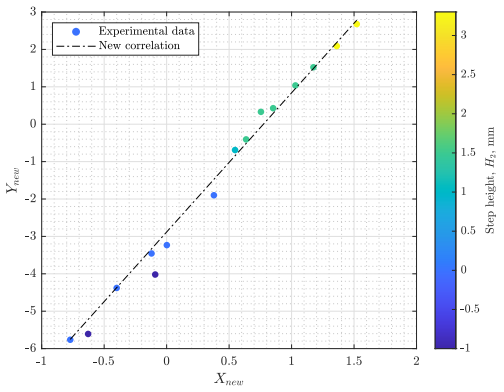

(b) Peak cavity HFA.

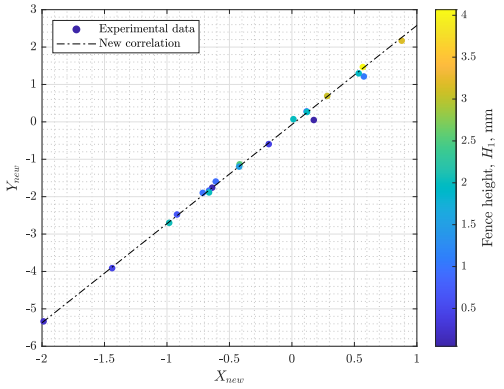

(c) Minimum separation HFA.

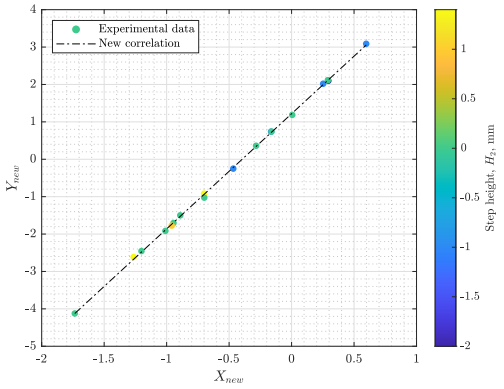

(d) Peak reattachment HFA.

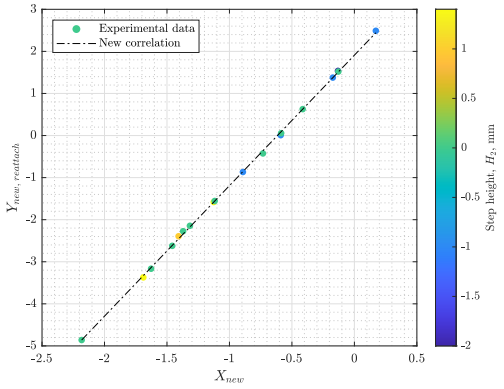

(e) Reattachment location.

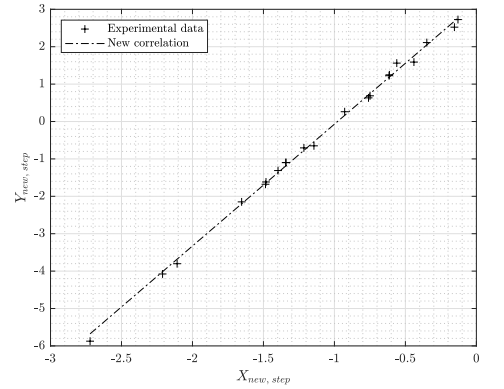

(f) Peak step HFA.

Figure 5.20: Correlations following Equations 5.4, 5.7, and 5.8.

5.5 Summary

Surface heat flux data has been collected in the vicinity of a wide range of surface geometries. Three flow conditions were tested, all producing a fully turbulent boundary layer at the geometry location. Streamwise heat flux augmentation profiles were calculated, allowing the overall qualitative and quantitative effect of surface imperfections to be assessed. Combinations of the canonical geometries were tested, finding that heat flux profiles can be sensitive to small upstream changes.

A number of quantities extracted from the heat flux profiles, useful for CFD validation, material selection, and aircraft design processes, have been correlated with geometric and flow properties. These correlations are applicable to both better understood simple geometries and more complex combined geometries. A modified version of Everhart's correlation method [67] was the most readily adaptable and has produced the best fit for a range of different geometry categories and heat flux quantities.

6

Steps in Laminar Boundary Layers

Contents

6.1 Measurements of Boundary Layer Transition 137
6.1.1 Heat Flux Data 137
6.1.2 Pressure Fluctuation Data 137
6.2 Natural Flat Plate Transition 140
6.2.1 Effect of Freestream Conditions 140
6.2.2 Effect of Leading Edge Bluntness 144
6.2.3 Effect of Tunnel Blockage 144
6.2.4 Intermittency 148
6.3 Addition of Surface Geometries 150
6.3.1 Effect on Boundary Layer Stability 150
6.3.2 Heat Flux Augmentation 153
6.4 Effect of Swept Leading Edge 156
6.4.1 Flat Plate Transition 157
6.4.2 Addition of Surface Geometries 157
6.4.3 Heat Flux Augmentation 160
6.5 Summary 163

This chapter presents various aspects of the effects of steps on laminar boundary layers. The purpose of this set of experiments was to investigate the effect of surface imperfections on both heat flux augmentation in laminar boundary layers and on transition from laminar to turbulent boundary layers. Also discussed is the effect of a swept leading edge on both the heat flux and boundary layer stability when steps are introduced.

6.1 Measurements of Boundary Layer Transition

6.1.1 Heat Flux Data

Transition from a laminar to a turbulent boundary layer was detected by the magnitude of the surface heat flux. Laminar and turbulent boundary layers have well characterised heat flux profiles for flat plate flows, with several correlations having been proposed for each. Eckert's correlations, described in Section 3.4.2 were used to compare theoretical heat fluxes with experimental data. Transition onset was defined by the initial deviation of the heat flux from Eckert's laminar level. When transition occurred upstream of the step, this location was detected using the upstream thin film gauge (TFG) array. When transition occurred downstream of the step, IR thermography was used instead. The greater spatial resolution of the IR thermography measurements made the determination of transition location more precise when further downstream ($\pm$ $\sim$2.5 mm for TFGs and $\pm$ $\sim$0.5 mm for IR data). Additionally, the high levels of electrical noise in the thin film gauges caused reasonably high scatter in the data points, making the exact location of the first deviation from the laminar level difficult to determine.

Figure 6.1 shows heat flux data for a Mach 7 shot, showing TFG and IR data, compared with Eckert's laminar and turbulent flat plate heat flux correlations.

In this case, transition occurs at $x \simeq 140$ mm, between the upstream gauges and the PEEK plate where IR can be measured.

6.1.2 Pressure Fluctuation Data

An alternative method of assessing transition is using the frequency content of pressure fluctuations. Figure 6.2 shows the power spectra (calculated using the method in Section 3.3.3) for pressures measured by seven of the PCB gauges. The shot is the same as that used to generate Figure 6.1. The colours of the triangles in Figure 6.1 and the lines in Figure 6.2 correspond to the same gauges - the triangles indicating the axial position of the gauges. Figure 6.3 shows the same data plotted

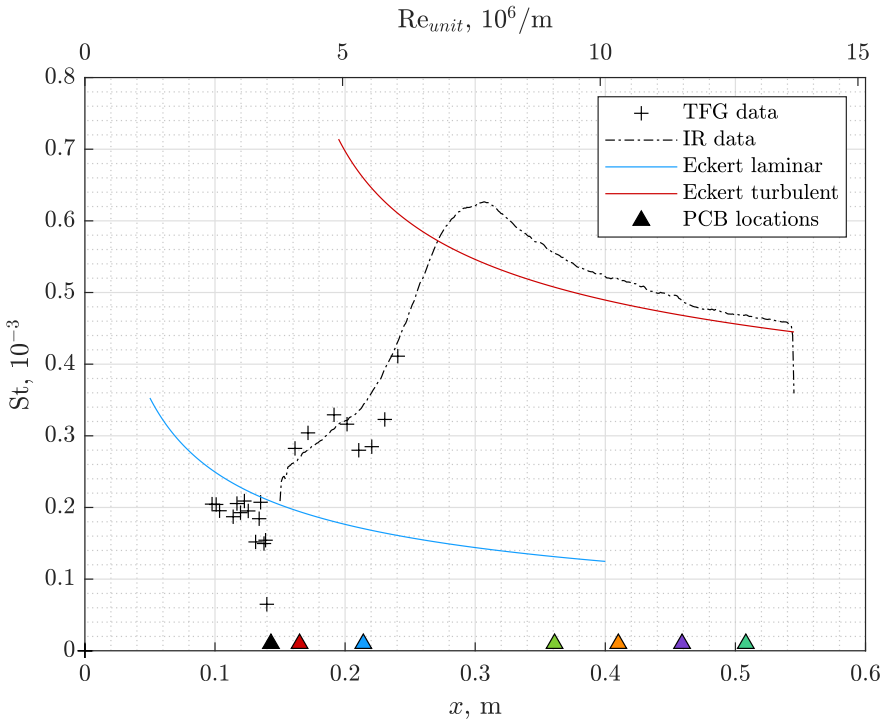

Figure 6.1: Flat plate heat flux data for a shot at M = 7, Re$_{unit}$ = 25.2 million/m. IR and TFG data is compared with Eckert's heat flux correlations.

slightly differently on a 3D line plot. This makes the different behaviours of the each sensor more clear and it is much easier to see the peak in PCB 3.

There is a peak in the spectrum of PCB 3 at $x = 214$ mm at a frequency of ∼200-210 kHz. The expected frequency for a second mode instability is given by Equation 6.1.

$$f_{II} \simeq \kappa \frac{u_e}{2\delta} \tag{6.1}$$

Where κ is a constant in the range 0.7 - 1.0. [178]. For the shot presented in Figure 6.2, this estimated frequency would be in the range 201 - 287 kHz, meaning that the peak displayed in PCB 3 could correspond to a second mode instability. By plotting the PSDs of the same sensor at later periods during the shot, motion of the peak can be observed. Shown in Figure 6.4, the peak moves towards lower frequencies later in the shot as the Re$_{unit}$ decreases. This is typical of a second

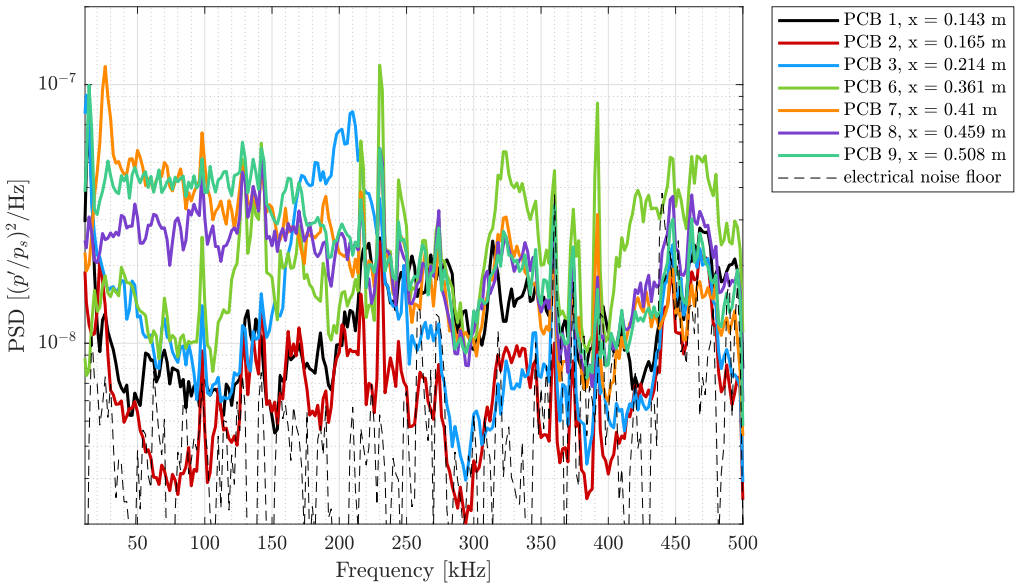

Figure 6.2: PCB power spectral densities of all PCB sensors for the same shot as Figure 6.1.

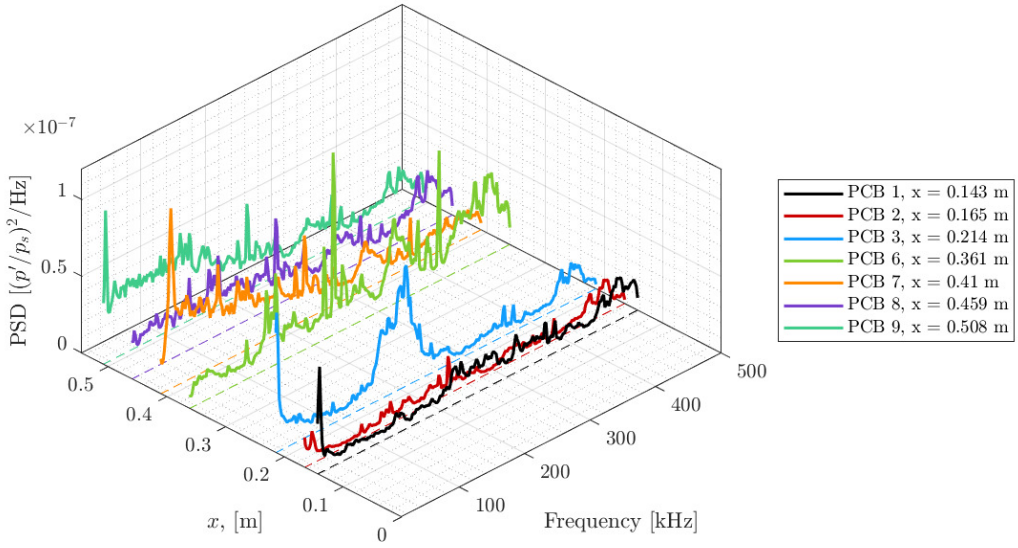

Figure 6.3: PCB power spectral densities of all PCB sensors for the same shot as Figure 6.1, plotted in a 3D plot with x location as the third axis.

mode instability: the boundary layer thickness increases with decreasing Re_{unit} leading to lower second mode frequencies following Equation 6.1.

PCB 3 is the only sensor which displays any evidence of a second mode instability, with the downstream gauges displaying a higher broadband level, suggesting full

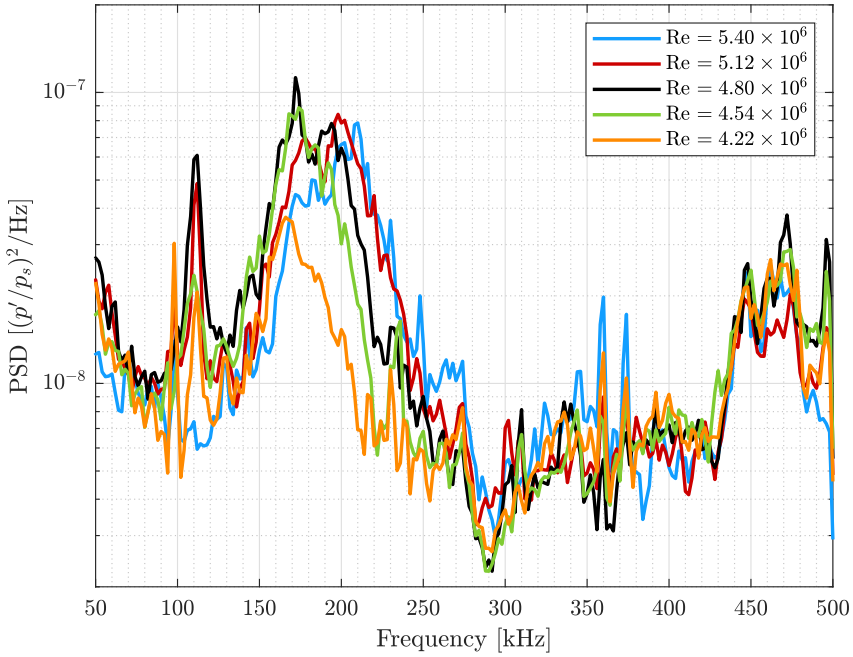

Figure 6.4: PCB power spectral densities of PCB 3 for subsequent steady flow periods in the same shot as Figure 6.1.

turbulence. Unfortunately, the data exhibits extremely high electrical noise which likely originated from the IR camera, and the PCB gauge data from most of the shots was unusable.

6.2 Natural Flat Plate Transition

An investigation into the effect of of surface imperfections on boundary layer transition would require the natural flat plate transition to be positioned significantly downstream of the step location. The following sections describe attempts to achieve this by altering various flow and model variables.

6.2.1 Effect of Freestream Conditions

Freestream total pressure, total temperature, and Mach number were altered to observe the effect on transition location. Figure 6.5 shows natural transition Reynolds number plotted against freestream unit Reynolds number for Mach 6 and Mach 7 conditions. Also plotted for each Mach number are transition correlations

from Simeonides [179] (Equation 6.2), Charbonnier [110] (Mach 6 only, Equation 6.3), and Deem & Murphy [180] (see Appendix B).

$$\mathrm{Re}_{tran} = 0.9\frac{\mathrm{Re}_{unit}}{M} \quad \text{(weak bluntness)} \quad \frac{\mathrm{Re}_b}{M^2} < 50 \tag{6.2a}$$

$$\mathrm{Re}_{tran} = 7 \times 10^4 M^{0.08}\mathrm{Re}_b^{0.46} \quad \text{(modest bluntness)} \quad 50 < \frac{\mathrm{Re}_b}{M^2} < 1000 \tag{6.2b}$$

$$\mathrm{Re}_{tran} = 6 \times 10^6 M^{1.38}\mathrm{Re}_b^{-0.19} \quad \text{(strong bluntness)} \quad 1000 < \frac{\mathrm{Re}_b}{M^2} \tag{6.2c}$$

$$\mathrm{Re}_{tran} = 2 \times 10^5 + 0.124\mathrm{Re}_{unit} + 105 \times 10^5 b^2 \mathrm{Re}_{unit} \tag{6.3}$$

Where data points are in linked pairs, the lower point shows the location of transition onset (where the heat flux first deviated from the laminar baseline) and the upper point shows the end of transition. Single points are for shots where the end of transition occurred downstream of the instrumentation and was not captured.

For higher freestream Reynolds numbers, transition Reynolds numbers are also higher, with an approximately linear trend. This trend breaks down at lower Re_{unit} at Mach 7, where Re_{tran} begins to increase again.

The correlations of Simeonides and Charbonnier appear to predict transition Reynolds numbers with reasonable accuracy around $\mathrm{Re}_{unit} \simeq 10$ million/m. Deem & Murphy's method was based on the location of the peak in pitot pressure in the transition region, rather than transition onset, and is closer to the end of transition. Their model appears to be able to predict the end of transition.

Transition data can also be plotted as a transition distance, x_{tran}, rather than a Reynolds number. Figure 6.6 shows the data plotted in this way. The same correlations are plotted again, in addition to horizontal lines marking the upstream and downstream edges of the PEEK parts of the model. Presenting the data in this way is more useful for visualising transition location. For example, for three of the shots, transition onset was upstream of the step location at $x = 150$ mm. Transition onset occurred within 100 mm of the step for all conditions with $\mathrm{Re}_{unit} > 4.3$ million/m, which was deemed to be too close for investigating the effect of surface imperfections. One shot was performed at a slightly lower condition of $\mathrm{Re}_{unit} = 4.1$

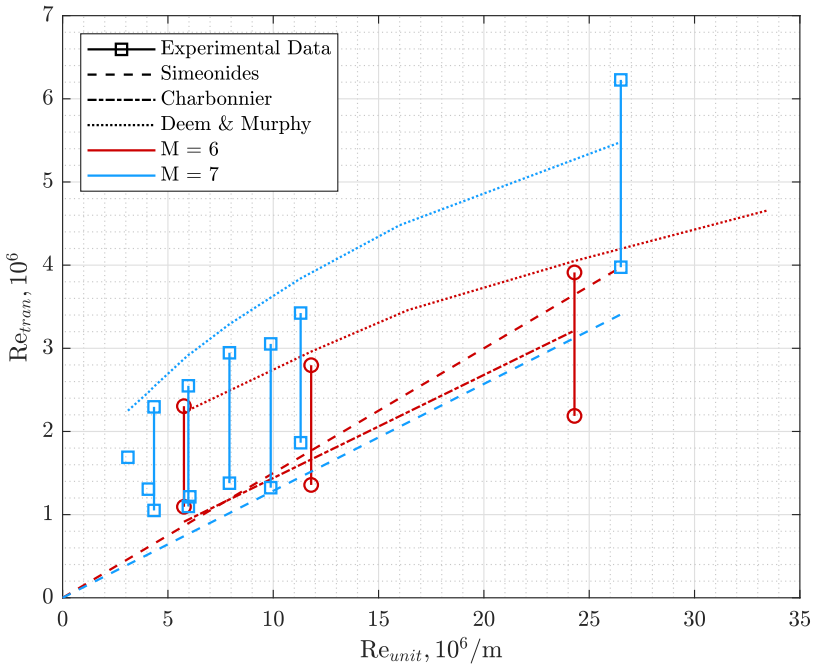

Figure 6.5: Natural transition Reynolds number vs unit Reynolds number. Plotted with flat plate transition correlations from Simeonides [179], Charbonnier [110] (Mach 6 only), and Deem & Murphy [180].

million/m and resulted in transition at $x = 321$ mm. This location would have been suitable, however, the shot was at the lower limit of the operation of HDT in Ludwieg mode and the plug valve was found to perform with a low repeatability. The data point at the lowest Re_{unit} was performed in LICH mode (Condition A, see Section 4.3.1) and remained laminar for the entire duration of the PEEK plate.

In addition to transition onset, the transition length is also of interest to investigations into step induced transition. Transition length, the distance between the start and end of transition, is typically the same as the length of the upstream laminar boundary layer [178]: i.e. $x_{tran\ end} - x_{tran\ start} = x_{tran\ start}$. Figure 6.7 shows the ratio of transition length to onset plotted against unit Reynolds number. The experimental data behaves approximately as expected but has a dependency on freestream conditions, with higher Re_{unit} resulting in relatively shorter transition lengths. Referring back to Figure 6.6, if the entirety of the transition region is captured on the PEEK insert for a given condition, then the location of transition onset is too close to the step for that condition to be useful.

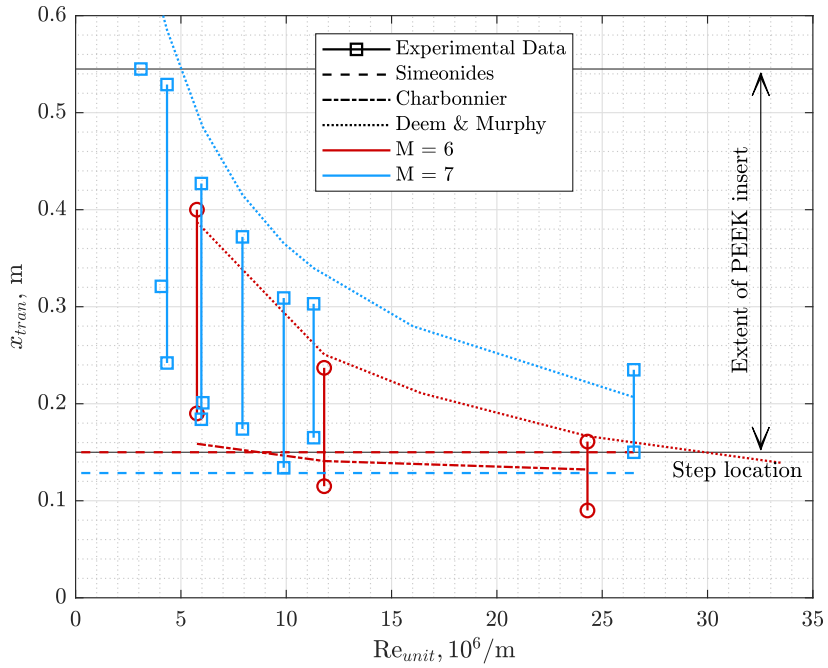

Figure 6.6: Natural transition distance vs unit Reynolds number. Plotted with flat plate transition correlations from Simeonides [179], Charbonnier [110] (Mach 6 only), and Deem & Murphy [180].

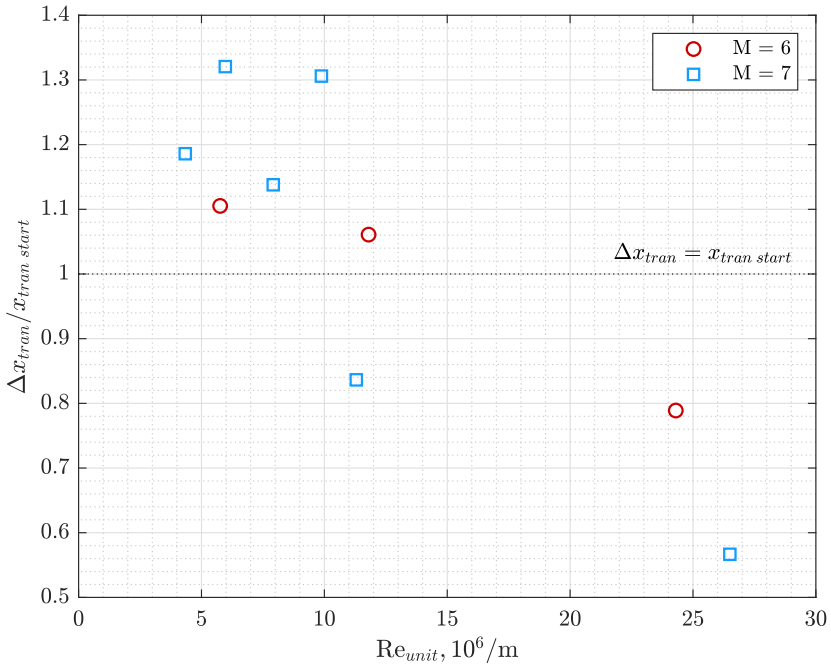

Figure 6.7: Transition length ratio for the data plotted in Figures 6.5 and 6.6.

6.2.2 Effect of Leading Edge Bluntness

The experimental model featured a nominally sharp leading edge. This had an estimated thickness of 0.5 µm, based on its ability to cleanly slice free-hanging paper [181]. Boundary layer transition data shown above used this leading edge. The leading edge was modified to add bluntness in an attempt to delay transition. Bluntnesses tested were 100 µm, 2 mm, and 6 mm in thickness (diameter). Figure 6.8 shows the effect of the different leading edge bluntnesses on transition at a single freestream condition. Note that the x-axis uses a log scale. In all cases where a blunt leading edge was used, the boundary layer was laminar for the entire extent of the plate. Also plotted are predictions from Simoenides [179] and Deem & Murphy [180] for transition location based on leading edge bluntness. Simeonides' correlation has three regimes: for weak- , moderate-, and strong-bluntness effects. For the sharp leading edge, this correlation predicts the transition location well. However, for larger bluntnesses, the experimental data deviates from predicted values. Deem & Murphy's correlation appears to capture the seemingly large effect on transition caused by even small bluntnesses. Using their method, a value of bluntness in the range of $\sim 10 - 50$µm would be expected to produce transition in a sensible location. However, 100 µm was the smallest bluntness achievable without completely manufacturing a new leading edge and was done by wrapping 50 µm Kapton tape around the leading edge.

Once again, a suitable transition location was unable to be achieved by altering the leading edge bluntness.

6.2.3 Effect of Tunnel Blockage

The large size of the experimental model caused significant blockage of flow in the test section. This resulted in a smaller core flow, which impinged on the downstream end of the PEEK plate. This was apparent in the IR data by the appearance of a large increase in heat flux. With the model in its most upstream position, the impingement of the shock from the nozzle rendered approximately 100 mm of the downstream data unusable. This presented a problem in the search for a suitable

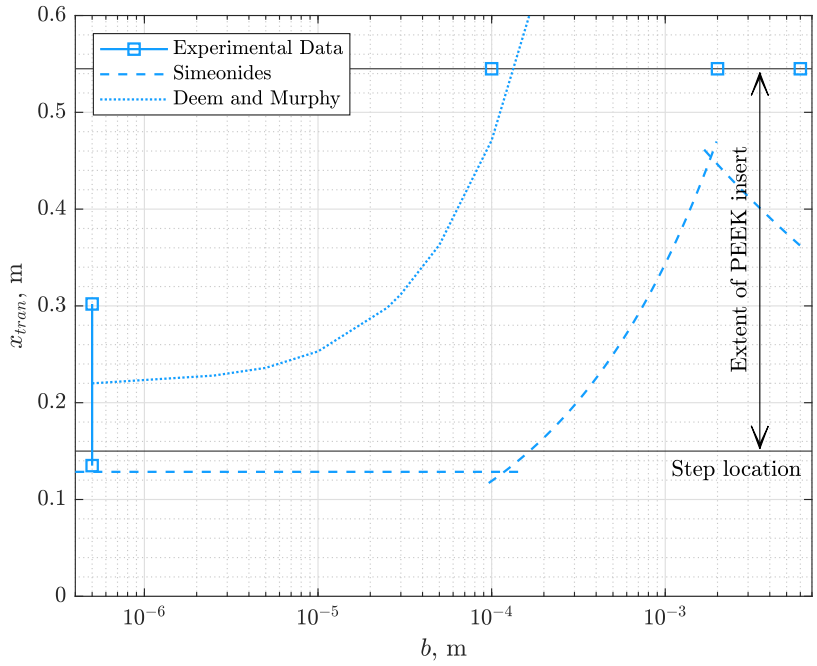

Figure 6.8: Transition location, x_{tran}, vs leading edge thickness (diameter), b, at a freestream condition of M = 7, Re_{unit} = 25.2 million/m. Data is compared with correlations from Simeonides [179] and Deem & Murphy [180].

condition for investigating boundary layer transition by effectively reducing the size of the measurement area. To alleviate this problem, various parts of the model were modified to reduce the total frontal area of the model, outlined below.

6.2.3.1 Modifications to Reduce Blockage

To reduce blockage, two modifications were made to the model assembly: a newly manufactured slimmer model stand, and a reduction in the thickness of the back plate. These modifications resulted in a reduction in the frontal area of $\sim 21\%$.

Model stand

The model stand was reduced in thickness from 55 mm to 25 mm. This significant reduction in size posed a similarly significant reduction in the stiffness of the stand, which was originally designed to withstand the full operating range of HDT. FEA was performed to assess the stiffness of the new stand using the Ansys Mechanical solver. A simplified version of the model CAD was used, which featured the major

model parts and assembly screws without the more complex internal parts. Pressure loads were applied based assumed isentropic oblique shocks and expansions over the model. FEA was conducted with pressure loads corresponding to freestream total pressures of $5 - 65$ bar and Mach numbers of 5, 6, and 7. Figure 6.9 shows the setup and an example solution.

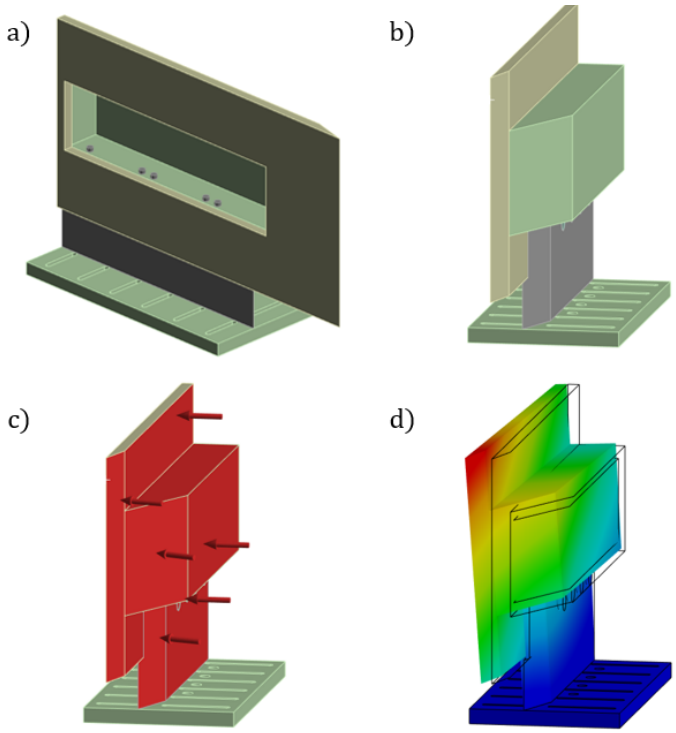

Figure 6.9: FEA setup, showing the CAD of the model (a & b), the pressure loads applied (c), and an example of the (scaled) overall deformation (d).

Figure 6.10 shows results from FEA performed on the top plate attached to the slim stand assembly. Results are displayed as an effective angle of attack of the leading edge, calculated from the tip deflection assuming the plate bends from half its length.

Also plotted is a horizontal line lying at an angle of attack of 0.1°. This was decided to be the maximum permissible angle caused by deflection of the plate during a shot. Due to the setup of the FEA (not all parts were included), this provided a conservative estimation of the maximum permissible stagnation pressure for each Mach number: where each curve intersects the 0.1° line. Table 6.1 gives lists these maximum stagnation pressures along approximate corresponding barrel fill pressures.

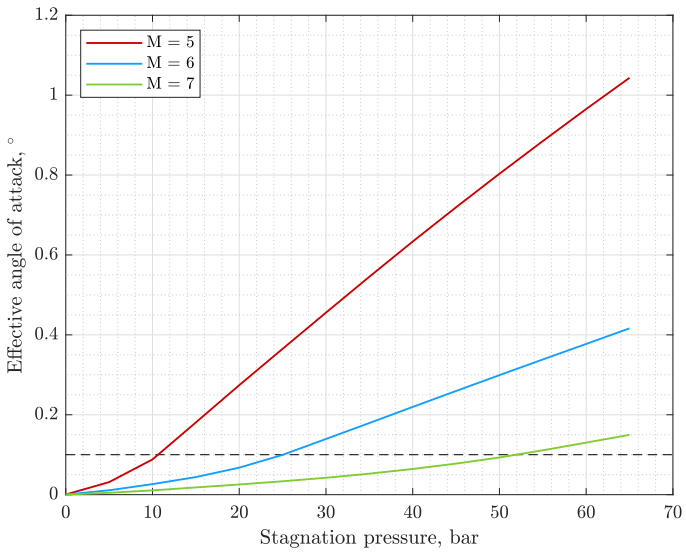

Figure 6.10: Results from FEA for effective angle of attack of the plate against freestream stagnation pressure when using the slim stand.

Table 6.1: Maximum permissible operating pressures when using the slim model stand.

Mach number	p_0 [bar]	p_{fill} [bar]
5	10.6	14.9
6	25.1	27.6
7	51.9	54.6

Reduced thickness base plate

The second modification was a reduction in thickness of the base plate (refer to Figure 3.10) from 15 mm to 7 mm. This part is not structural and acts as a cover plate for the internal cavity of the model. FEA was not performed for the modified back plate.

6.2.3.2 Effect

The modifications were effective in reducing the total blockage caused by the model and allowed for more of the model surface to be used for data gathering. Figure 6.11 shows two shots, at the same condition, using the original and the modified slim model. The IR camera position used for the slim model did not have a calibration associated with it, so the heat flux level is not exactly correct. However, the sharp increase in heat flux due to blockage is clearly not present.

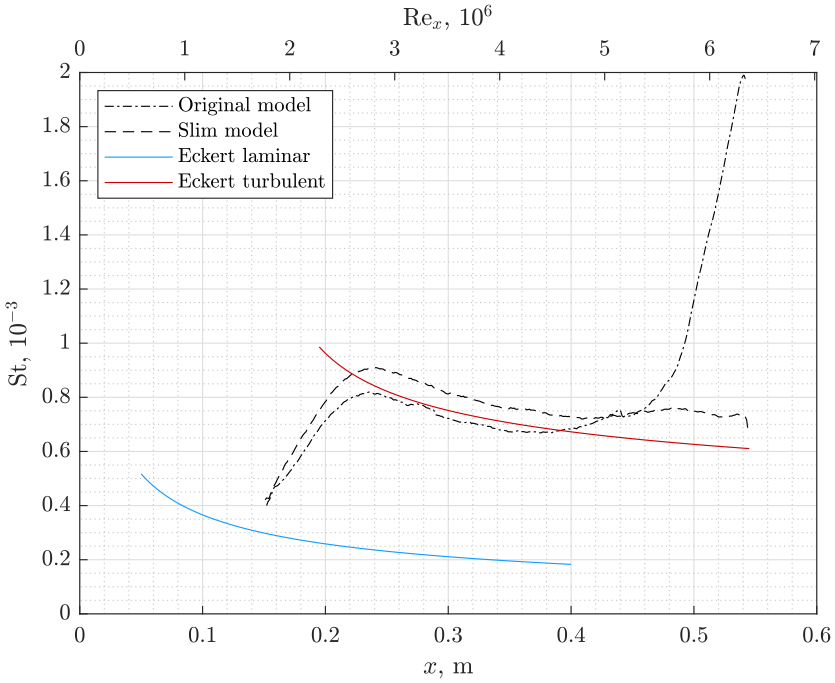

Figure 6.11: Flat plate Stanton number data comparing the original model with the slimmed blockage-reducing configuration. Freestream condition: M = 7, Re_{unit} = 11.7 million/m.

Due to the nozzle shock impinging at the downstream portion of the plate, tunnel blockage did not affect the data collected in Chapter 5, which focused on the flow in the close vicinity of the step.

6.2.4 Intermittency

Of interest in boundary layer transition studies is the intermittency of the boundary layer in the transition region - intermittency being the proportion of the local flow that is at a turbulent level (of a given flow parameter such as heat flux). This is often measured experimentally using high frequency measurements: either surface pressure or heat flux. The experimental model featured these measurements in PCB pressure gauges and thin film heat transfer gauges, which were both sampled at 1 MHz. However, as stated previously, the noise levels on both sets of gauges were too high to gain any useful insight into the measurements. Some data processing, outlined here, was carried out in order to verify that this was the case.

A general scheme for quantifying intermittent behaviour in a flow signal is described by Hedley & Keffer [182]. First, a detector function is synthesised from the intermittent signal. Various formulations of this function have been used in the literature, but they are typically derivatives of velocity or pressure. A criterion function is constructed by applying a filter to the detector function. Finally, a threshold is applied to the criterion function, generating an indicator for intermittency. Typically, for turbulent flows, the probability density function (PDF) of the detector function has a broader and has a peak at higher values of the detector function.

For this work, various detector functions were trialled involving derivatives of surface pressure from PCB gauges and surface heat flux from thin film gauges. The process which had the most success was as follows:

- The detector function took the form of the squared derivative of heat flux.
- Criterion functions were created by calculating the probability density function of the detector function and finding the location of the peak in the PDF.
- The produce a time varying criterion function, PDFs were calculated on windowed portions of the signal, sweeping along the length of the signal. Points in the time axis correspond to the locations of peaks of the PDF for a particular window.

By varying the threshold for the criterion function, this process produced some limited results which were self-consistent (i.e., subsequent, more turbulent gauges producing more intermittent signals). However, most gauges did not follow this pattern and the threshold required varied greatly between shots. The lack of a robust methodology for finding intermittency supports the conclusion that the signals were too noisy to extract any useful information of this type.

6.3 Addition of Surface Geometries

For testing of laminar boundary layers, surface imperfections were only introduced to the flow in the form of fences (UD_F geometries - refer to Table 5.2). The reason for this is that the majority of the testing in laminar boundary layers was performed using the flat configuration in order to achieve a suitable natural transition location. Due to the block adjustment mechanism only allowing for remote actuation of the front block, only this block was moved in attempts to trip the boundary layer. Given that a suitable natural transition location was not achieved, only fence tests were performed.

6.3.1 Effect on Boundary Layer Stability

The primary aim of this portion of work was to assess the effect of steps on the stability of the boundary layer and how the transition location is subsequently affected. However, given the difficulties experienced in producing a suitably located flat plate transition location (see Section 6.2), this aim was not fully realised. Instead, this section explores some of the flow features present when fences are introduced.

Heat flux data from three shots, performed at M = 7.06 and Re_{unit}= 15.8 million/m using the 100 µm leading edge, are presented in Figure 6.12. Fence heights of 0 (flat), 1.67, and 3.30 mm were tested, corresponding to $H/\delta \simeq 1$ and 2 for the fence heights. Additionally, Figure 6.13 shows heat flux profiles at the locations of the spanwise (vertical) lines and the mean of the strip between the streamwise (horizontal) lines in Figure 6.12. The mean of the streamwise strips is used rather than a single line to remove any error from local high or low streaks (which are discussed below). The colours of the triangular marks at the edges of the maps correspond to the colours of the line plots. The fish-eye effect of the 13 mm lens used for this work was removed using the process outlined in Section 3.3.1.1. However, the images in Figure 6.12 still display a very slight amount of warping, with 1-2 pixels of vertical deviation between the left and right edges of the images. Given that the majority of the discussion in this section is qualitative, the remaining distortion was ignored.

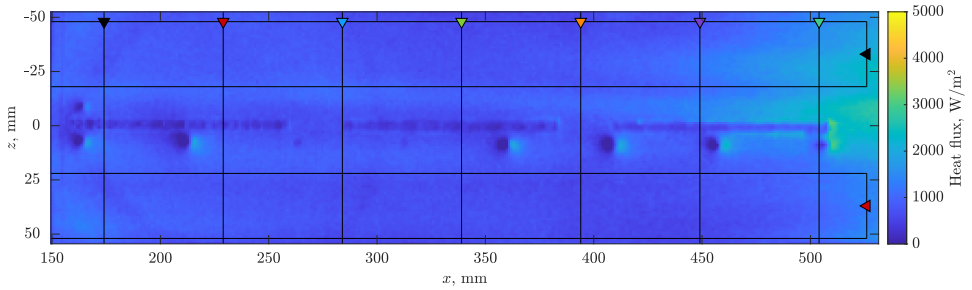

(a) Flat plate.

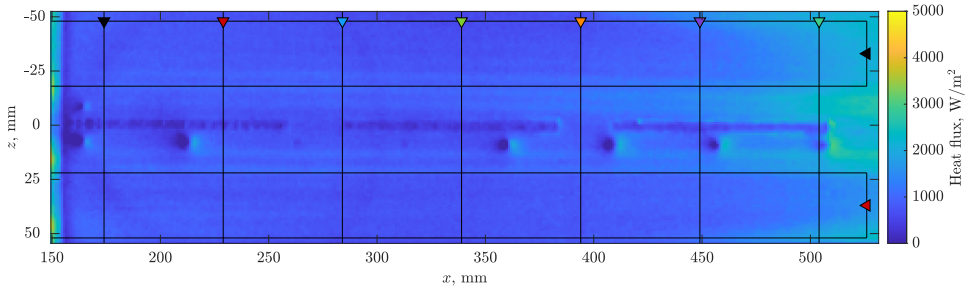

(b) 1.67 mm fence.

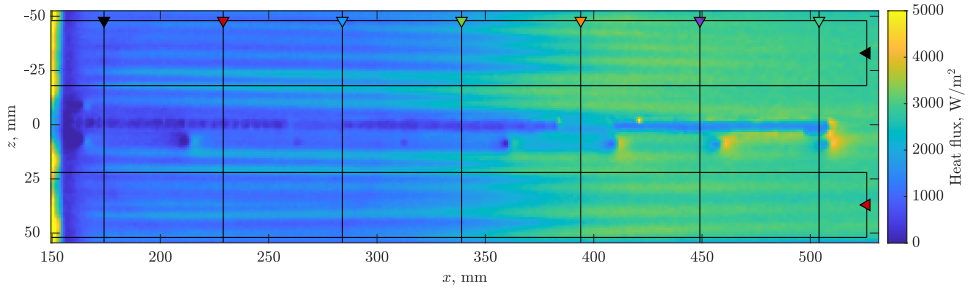

(c) 3.3 mm fence.

Figure 6.12: Heat flux maps for different fence heights, straight leading edge, $b = 100$ µm, M = 7, $\mathrm{Re}_{unit} = 15.8$ million/m.

When a fence is introduced to a laminar boundary layer, the flow first experiences a compression as it approaches the fence. When the flow reaches the downstream face of the fence, it expands and turns towards the plate. At reattachment after a downstream separation bubble, the flow is turned upwards by the plate and is subject to a pressure gradient. This causes the boundary layer to curl up into counter-rotating streamwise vortices, otherwise known as Görtler vortices [183]. These appear as streamwise streaks in Figures 6.12b and 6.12c, beginning around 20 - 30 mm downstream of the fence. When caused by surface imperfections, Görtler vortices are typically associated with backward-facing steps [92, 93, 91], so it is

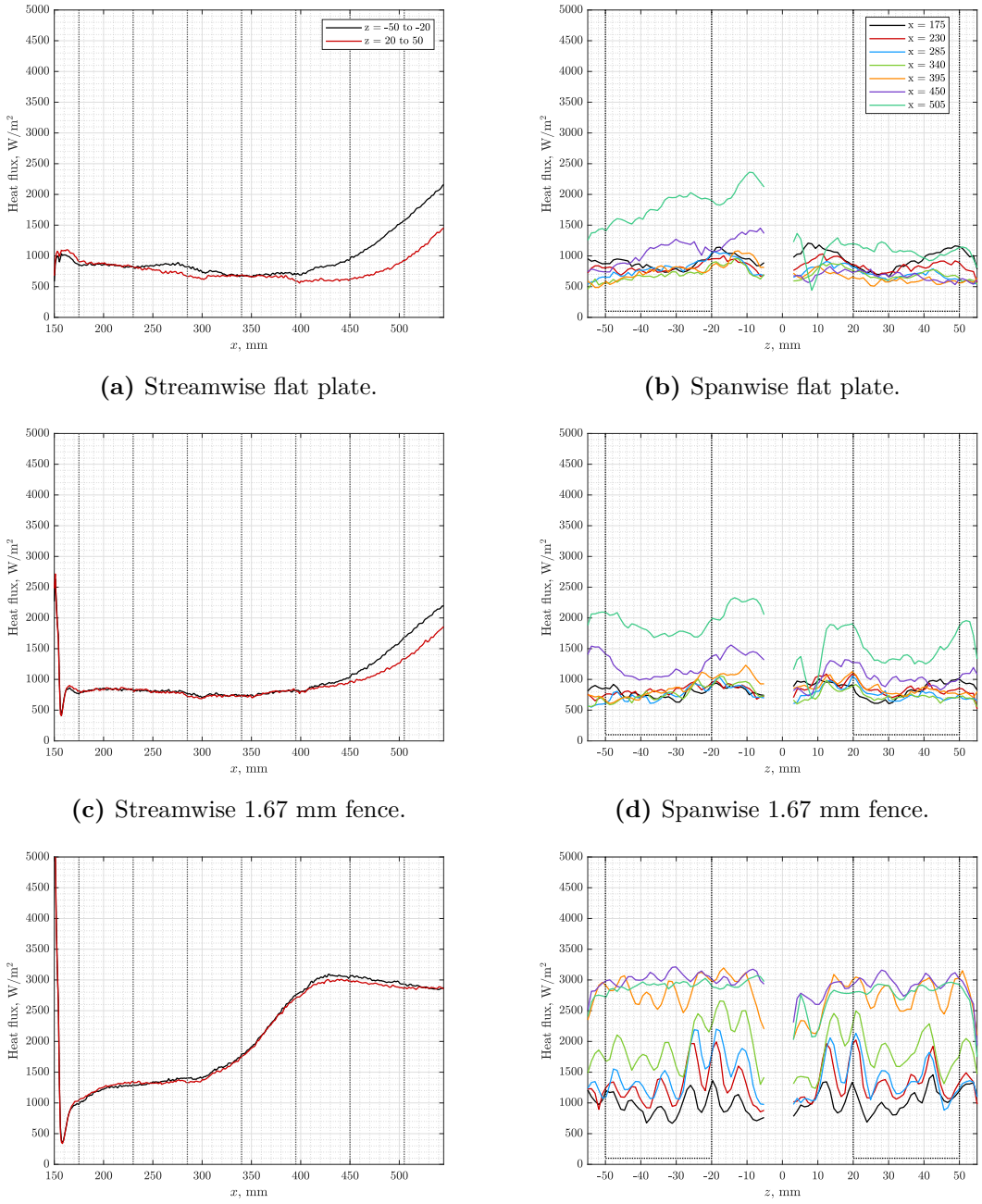

(a) Streamwise flat plate.

(b) Spanwise flat plate.

(c) Streamwise 1.67 mm fence.

(d) Spanwise 1.67 mm fence.

(e) Streamwise 3.3 mm fence.

(f) Spanwise 3.3 mm fence.

Figure 6.13: Heat flux profiles along the lines shown in Figure 6.12.

interesting to see them being caused by 2-dimensional protuberances.

In Figure 6.13, Görtler vortices appear as peaks and troughs in heat flux in the z direction (spanwise). The peak-to-trough height is much greater with the larger fence in Figure 6.13f, indicating that the vortices extend further into the boundary layer. The amplitude of the streaks is also greater closer to the centreline of the

model, for $-30 < z < 30$ mm. This corresponds to similarly high levels of heat flux for the flat plate in the same region, indicating that there is perhaps an existing instability present which interacts with the growing Görtler vortices. This could possibly be caused by the instrumentation upstream of the fence, in particular, the PCB and Kulite sensors which are located at $z = \pm 10$ mm.

An obvious effect of the larger 3.3 mm step is earlier transition. The exact transition locations of the flat plate and 1.67 mm step tests are unclear. For the flat plate case, a turbulent spot appears at $x \simeq 400$ mm and grows in width and magnitude moving downstream. This can be seen in the negative z line in Figure 6.13a as an early increase, and in the $x = 450$ and 505 mm lines in 6.13b as a low, wide, growing peak at $z \simeq -30$ mm.

The intermediate 1.67 mm fence does not appear to affect the transition location when compared with the flat plate. The streamwise heat flux profiles (Figure 6.13c) display the same overall shape as the flat plate but with a slightly flatter profile for $200 < x < 350$ mm. Görtler vortices have the effect of increasing the mean heat flux, with the heat flux in the trough being approximately the same as the flat plate heat flux [93]. Moving downstream from the step, the additional heat flux from the growing Görtler vortices makes up for the decrease in heat flux which occurs moving downstream on smooth walls. In addition, the turbulent spot from the flat plate case does not appear here. Instead, the heat flux rises both near the edges of the plate and towards the centreline where the Görtler vortices are stronger.

For the 3.3 mm fence, transition clearly occurs much earlier, at $x \simeq 300$ mm. Once again, the heat flux between the fence and the transition location is elevated due to the Görtler vortices. Transition close to the centreline where the vortices are stronger begins earlier but ends at $x \simeq 410$ mm regardless of spanwise position.

6.3.2 Heat Flux Augmentation

Heat flux augmentation data was collected as a byproduct of transition testing. Thus, only fences (UD_F geometries) were tested. However, this meant that a range of Re_{unit} was tested at Mach numbers of 6 and 7. The dataset covers Re_{unit} in the

range 4.07 – 24.4 million/m and H/δ in the range 0.42 - 2.1. For definitions of quantities relating to heat flux augmentation in this section, see Chapter 5.

6.3.2.1 Heat Flux Profile

The heat flux profile in the vicinity of a fence in a laminar boundary layer is largely the same as that in a turbulent boundary layer with two exceptions. Firstly, while in a turbulent boundary layer the separation causes an increase in heat flux, the opposite is true for laminar boundary layers. Instead, the heat flux drops significantly before rising just upstream of the step [42]. This can be seen in Figure 6.14 in thin film gauge data. Secondly, the heat flux downstream of the fence rises above the flat plate level. This is due to Görtler vortices (see above) causing a mean increase in heat flux.

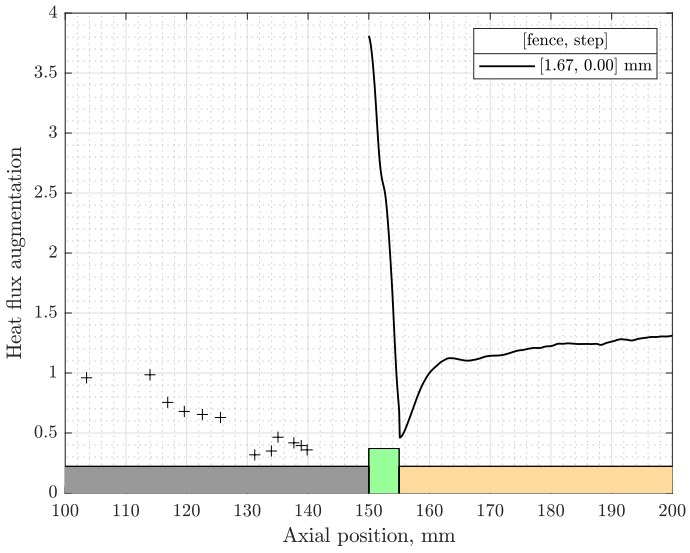

Figure 6.14: Heat flux augmentation profile for a fence in a laminar boundary layer, M = 7, Re_{unit} = 15.8 million/m.

6.3.2.2 Correlations

Data was reduced using the modified version of Everhart's correlation described in Section 5.4.3.2. The equations are repeated here for convenience:

$$X_{new} = \ln\left[M_e^{\sigma} Re_{\theta}^{\tau}\left(\frac{|\Delta H|}{\delta}\right)\right] \tag{6.4a}$$

$$Y_{new} = \ln\left[\left(\frac{|\Delta H|}{\delta}\right)^{\alpha}\left(\frac{L}{S_{new}}\right)^{\beta} HFA\right] \tag{6.4b}$$

$$Y_{new} = a + bX_{new} \tag{6.4c}$$

Laminar boundary layer tests were conducted using both Mach 6 and Mach 7 nozzles meaning that the boundary layer edge Mach number, M_e, varied between different data points. The exponent σ from Equation 6.4 was thus used for this data set. Due to the lack in variety of geometries tested compared to those tested in turbulent boundary layers, only minimum separation heating and peak step heating correlations have been fitted. With fence geometries, ΔH is equivalent to H_1. Table 6.2 shows the fitted constants and R^2 values for minimum separation and peak step heat flux augmentation and Figures 6.15 and 6.16 show the line fits, respectively. Due to the lack of variety in geometries, the correlation for minimum separation heating is less generally applicable than that developed for turbulent boundary layers.

Table 6.2: Constants for Equation 6.4

	Figure	α	β	σ	τ	a	b	R^2
Min. sep.	6.15	3.020	-1.349	0.1248	-0.1264	2.067	3.257	0.9907
Peak step	6.16	3.354	0	0.1824	0.0286	-1.942	4.269	0.9918

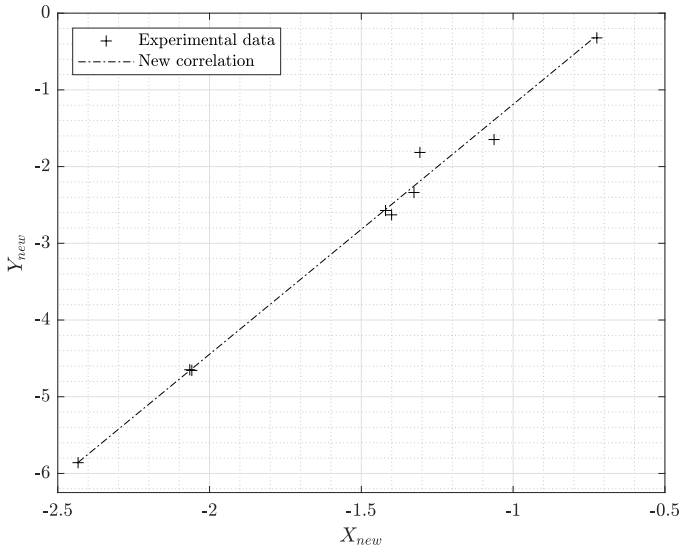

Figure 6.15: Minimum separation heating correlation according to Equation 6.4

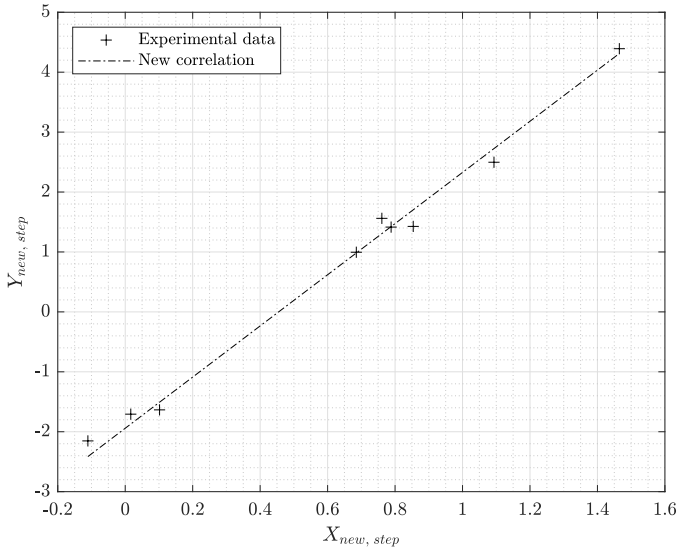

Figure 6.16: Peak step heating correlation according to Equation 5.8

6.4 Effect of Swept Leading Edge

This section presents data from experiments using the flat plate model in its configuration with a swept leading edge. As described in Section 3.2.1.4, the alternative leading edge has a sweep angle of 45° and maintains the centreline step position of 150 mm. The shots presented in this section feature a blunt leading edge with a thickness of 100 µm. The leading edge is angle so that the longer running length is at the top of the images presented (negative z values). Figure 6.17 shows this schematically.

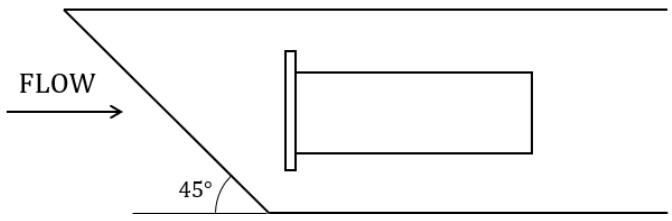

Figure 6.17: Direction of the sweep angle of the leading edge.

The two effects of a swept leading edge are the difference in flow running length to the step/fence in the spanwise direction and the addition of crossflow.

6.4.1 Flat Plate Transition

Given that natural boundary layer transition is typically the result of growing instabilities in the boundary layer, the local flow running length is an important factor in the transition location. On a flat plate, this length is the distance from the leading edge, meaning that when a swept leading edge is used, transition is expected to occur in a swept line, parallel to the leading edge. This has been seen in flat plate experiments in the literature, with Lu [184] being a recent example.

Referring to Figure 6.19a, which shows a 2-dimensional heat flux map of the model, the transition front (the region of increasing heat flux at $x \simeq 300$ mm) seems to span the model laterally, without regard to the leading edge sweep angle. This could be due to additional factors promoting transition, such as the interfaces between parts of the model or the instrumentation upstream of the step.

Comparing Figure 6.12a and 6.19a, natural transition with the swept leading edge is significantly earlier than the straight leading edge. This indicates that there is some interaction involving a crossflow instability which causes transition with the swept leading edge. Bowcutt et al. [185] give a correlation relating the leading edge sweep angle and its effect on transition location, shown in Equation 6.5.

$$\frac{\mathrm{Re}_{tran,\,\Lambda}}{\mathrm{Re}_{tran,\,\Lambda=0}} = 0.787\left(\cos\left(\Lambda\right)\right)^{4.346} - 0.7221e^{-0.0991\Lambda} + 0.9464 \tag{6.5}$$

Where Λ is the leading edge sweep angle in radians. For $\Lambda = 45°$, the ratio of Re_{tran} becomes 0.453. Assuming that the increase in heat flux at $x \simeq 450$ mm in Figure 6.13a indicates transition onset, Bowcutt's correlation would estimate a transition location of $\sim$ 204 mm. This approximately corresponds with the increase in heat flux in Figure 6.20a

6.4.2 Addition of Surface Geometries

With the swept leading edge, the boundary layer thickness varies along the length of the fence due to the difference in flow running length - the fence is perpendicular to the flow rather than parallel with the leading edge. At the end of the fence closer to the leading edge, at $z = 55$ mm, the fence is larger relative to the boundary

layer thickness, creating a larger obstruction to the flow. Figure 6.18 shows the H/δ across the width of the fence for each fence height. The curves are plotted for the entire 160 mm span of the fence block and the vertical lines indicate the extent of the rear PEEK plate on which IR data was collected. Boundary layer thickness was assumed to be unaffected by the leading edge sweep and is calculated using Equation 3.17 evaluated at each z location.

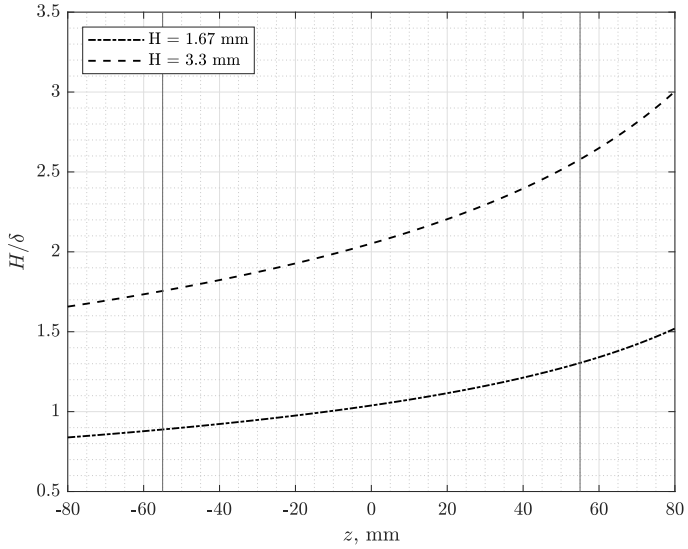

Figure 6.18: H/δ in the spanwise direction for the 1.67 and 3.3 mm fence heights on the swept leading edge.

As with the straight leading edge (Section 6.3.1), Figures 6.19b and 6.19c show heat flux maps for the swept leading edge for two fence heights of 1.67 and 3.3 mm with Figure 6.20 showing similar line plots. In this case, dashed lines indicate data from the straight leading edge and are plotted for comparison with the swept leading edge. Once again, the inclusion of a fence causes Görtler vortices to appear downstream of the step, resulting in earlier transition. For the swept leading edge the effect now varies in the spanwise direction: for negative z (longer running length), where the step is smaller relative to the boundary layer, the vortices produced are much weaker than for positive z. However, this does not vary smoothly across the span of the model, as would be expected from a continuously varying H/δ. Instead there appears to be a split along the centreline, with the upper and lower

halves exhibiting bulk behaviour, i.e. no spanwise variation within each half. This is more apparent in the line plots shown in Figures 6.20d and 6.20f, where the peaks and troughs associated with Görtler vortices are much more pronounced for values of positive z and there is a clear divide between the two halves of the plate. Görtler vortices appear further upstream in the positive z half of the plate, and begin at the same axial location for each half of the plate. The fact that the transition location and production of vortices does not change linearly across the plate suggests that there is some additional mechanism affecting them. It is not clear what the cause of this is.

Another difference between the straight and the swept leading edge is that the vortices for the swept leading edge are affected by crossflow and move in the spanwise direction towards positive z values as they travel downstream. The peaks moving from $z = -52$ to -47 mm on the $x = 175$, 230, and 285 mm lines in Figure 6.20f illustrate this.

For low values of H/δ ($z < 0$ with the 1.67 mm fence), there is very little change in transition location when compared to the flat plate. As soon as the fence becomes larger than the boundary layer ($H/\delta > 1$), there is a definite upstream movement of the transition location.

For $z > 0$ on the 3.3 mm step, transition occurs almost instantly, the heat flux being significantly greater than the laminar level immediately after the fence. The Görtler vortices are also the strongest directly after the fence, at $x = 175$ mm. Referring to Figure 6.19c, the vortex streaks begin at the reattachment location at $x \simeq 160$ mm and immediately grow in magnitude to full turbulence.

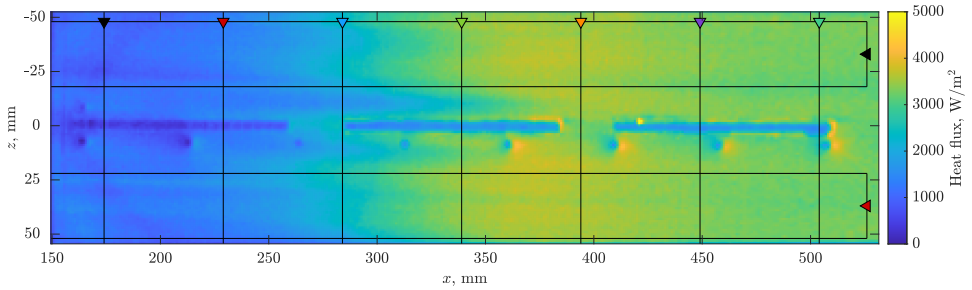

(a) Flat plate.

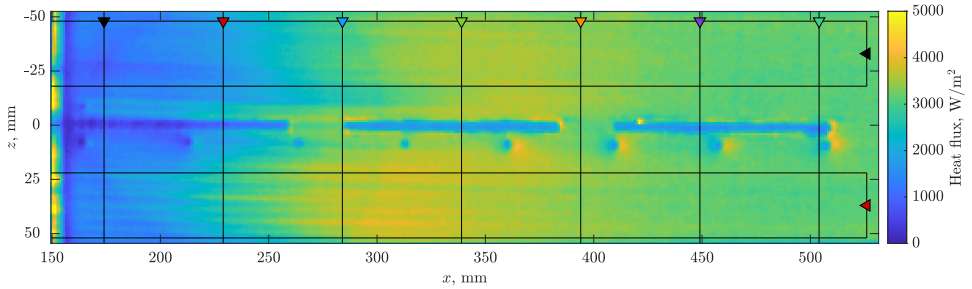

(b) 1.67 mm fence.

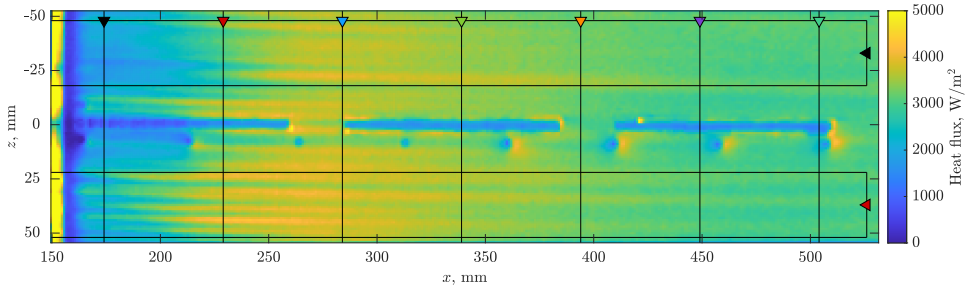

(c) 3.3 mm fence.

Figure 6.19: Heat flux maps for different fence heights, swept leading edge, $b = 100$ µm, M = 7, $\mathrm{Re}_{unit} = 15.8$ million/m.

6.4.3 Heat Flux Augmentation

In addition to the effect on boundary layer stability. The swept leading edge has the effect of increasing heat flux augmentation on a step. Figure 6.21 shows the swept to straight heat flux augmentation for peak heating on the upstream corner of the fences presented in Figures 6.12 and 6.19. Instead of HFA defined by Equation 5.1, Figure 6.21 uses the ratio of HFAs for the straight and swept leading edges, defined by Equation 6.6. This is plotted against spanwise distance, z. Due to the large spanwise variation in the data, the mean value for each line is also shown.

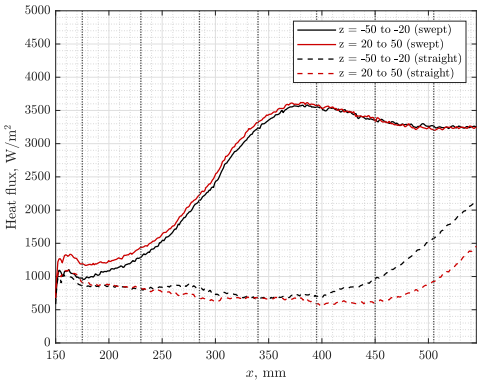

(a) Streamwise flat plate.

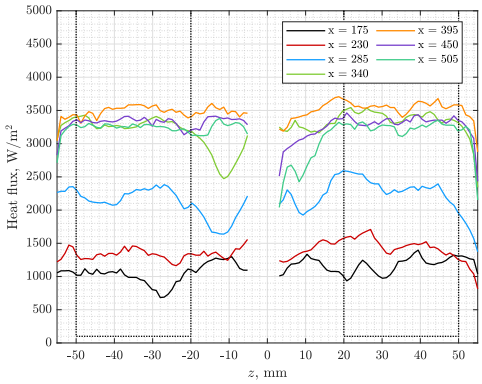

(b) Spanwise flat plate.

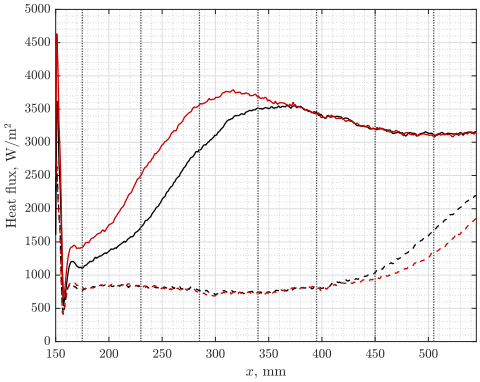

(c) Streamwise 1.67 mm fence.

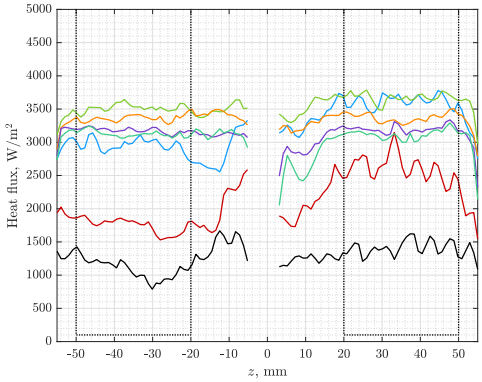

(d) Spanwise 1.67 mm fence.

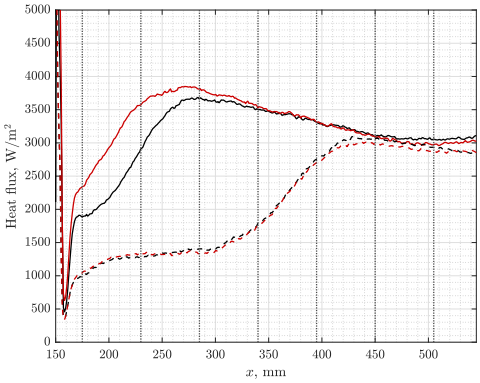

(e) Streamwise 3.3 mm fence.

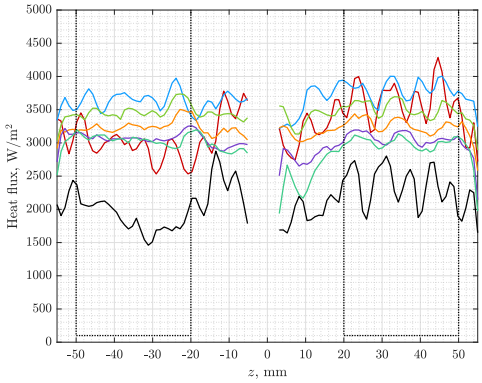

(f) Spanwise 3.3 mm fence.

Figure 6.20: Heat flux profiles along the lines shown in Figure 6.19.

$$HFA_{swept/straight} = \frac{HFA_{swept}}{HFA_{straight}} = \frac{q_{swept,\,step}}{q_{swept,\,flat}} \Big/ \frac{q_{straight,\,step}}{q_{straight,\,flat}} \tag{6.6}$$

Immediately obvious in the HFA data is the two large peaks, which appear for both fence heights at $z = -16$ and 26 mm. These peaks most likely originate from

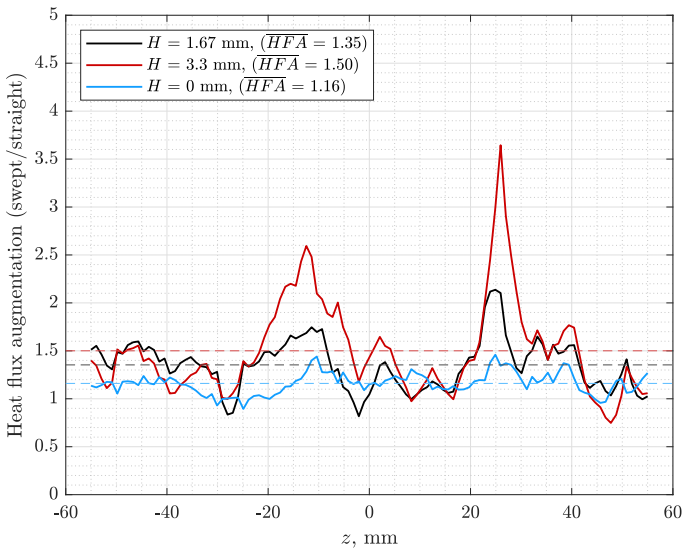

Figure 6.21: Heat flux augmentation comparing swept and straight leading edges for peak heating on a step.

an upstream disturbance on the swept leading edge which is not present on the straight leading edge. Damage to the leading edge was not observed. However, the interface between the leading edge and top plate parts could have influenced the downstream heat flux. Unfortunately, the leading edge was swapped before any measurements of the interface could be taken.

The lines in Figure 6.21 are all above 1, meaning that for a given geometry, the swept leading edge produces a greater heat flux than the straight leading edge. This is the case even for $z < 0$, where H/δ is lower for the swept leading edge. This suggests that the addition of crossflow adds significantly to the heat flux experienced by a step, perhaps due to increased mixing between different parts of the boundary layer. As the step height becomes larger, the increase in heat flux augmentation compared to a flat plate becomes larger as well: the 1.67 mm step experiences a 35% increase in heat flux augmentation whereas the 3.3 mm step experiences a 50% increase in heat flux augmentation. Referring to Figure 6.20c, which shows that transition may have begun at $x = 150$ mm, could explain the fact that the flat plate HFA in Figure 6.21 is above 1. This may also be the reason for the large difference when steps are introduced.

6.5 Summary

In summary, experiments investigating the effect of steps on boundary layer transition were less successful than planned. The dimensions of the model resulted in the natural flat plate transition location being too close to the step for any useful conclusions to be made regarding the overall effect of steps. To improve the performance of the model for this purpose, there are several modifications which could be made. Some examples of modifications are: moving the step location further upstream so that the obtained transition locations were suitable; extending the model further downstream so that transition at lower Re_{unit} conditions could be measured; manufacturing leading edges with highly toleranced leading edge bluntnesses to add more control.

Heat flux data exposed the occurrence of Görtler vortices behind fence geometries which appeared to be a factor in the promotion of earlier transition. Heat flux augmentation data were collected for peak heating on the upstream corner and minimum separation heating behind fence geometries. Correlations based on freestream conditions and geometry scales were developed for predicting these two heat flux quantities.

The effect of a swept leading edge was investigated. The overall effect was an earlier transition location, induced by crossflow. When steps were introduced, their influence on both heat flux augmentation and boundary layer transition was amplified when using a swept leading edge. Consistently higher levels of heat flux were experienced on steps on the swept model when compared to the straight model: up to ~ 4 times higher for the largest step tested. Transition occurred consistently further upstream on the swept model compared to the straight model.

7 Conclusions

Contents

7.1 Summary of Achievements 164
7.2 Recommendations for Future Work 167

This chapter summarises the achievements made during the project with respect to the research objectives outlined in Chapter 1 and presents some recommendations for any future work on the subject.

7.1 Summary of Achievements

A sophisticated experimental model was successfully designed and manufactured which enabled heat flux data to be collected in the vicinity of and downstream of 2-dimensional surface geometries. The model is highly configurable and adjustable, with many different geometry types able to be produced with ease with a precision of 10 µm. Leading edges with four different bluntnesses were manufactured, adding to the possible test matrix: sharp (0.5 µm), 100 µm, 2 mm and 6 mm. A leading edge with a 45° angle of sweep was also manufactured. The overall design of the model allows for easy alterations to be made to the instrumentation layout and

the test pieces without affecting its performance. The model can therefore be a diverse testbed for any future testing on this topic.

A new mode of operation for HDT called LICH mode, which increases the total temperature capability of the tunnel, was developed and commissioned. The addition of a piston stroke produced higher total temperature flows than were previously possible using only electric heating of the barrel. A simple numerical model of the tunnel, tuned using Ludwieg and LICH mode data, was used to generate theoretical performance maps of the facility. These maps show that the new development has increased the operational range of the tunnel, both in higher temperatures and lower Reynolds numbers, while also improving heat transfer measurements. Commissioning tests proved a capability increase to a total temperature of 600 K, above the previous maximum of around 500 K.

In turbulent boundary layers, heat flux augmentations were measured for a large range of geometry types and scales at three different Mach 6 freestream conditions ranging from $\mathrm{Re}_{unit} = 16.4-33.5$ million/m. Geometries tested were both basic individual geometries like steps, gaps, and 2D protuberances and geometries involving combinations of these. Some qualitative conclusions were made when comparing heat flux augmentations for different scales of similar geometries. Some of these conclusions represent potential value in aircraft design processes. For example, data shows that having even a very small cavity upstream of a forward-facing step can reduce the peak heating on the step by around 10 % without an impact further downstream. Similarly, a small cavity downstream of a backward-facing step can reduce the heat flux in the immediate separation region with an additional effect downstream. The presence of a small intermediate step on a forward-facing step can be detrimental by causing greatly increased heating on the peak of the larger step: a $> 20\%$ increase was seen in data.

The key result of turbulent experiments was the development of a method which produced easily usable correlations relating heat flux augmentation, geometric parameters, and flow parameters. The approach enabled heat fluxes at different locations to be correlated using the same set of equations, with a different set of

correlating constants in each case. Six different quantities were correlated using this method, with a seventh needing a slightly altered set of equations. These were: minimum heat flux on a cavity floor; peak heat flux on the downstream corner of a cavity; minimum heat flux in a downstream separation; peak heat flux at flow reattachment following a separation; the location of the reattachment location; and the peak heat flux on the corner of a forward-facing step. All of these correlations incorporated not only basic individual geometries but also combined cases. For example, correlations for cavities included stepped cavities with different rear step heights. All correlations were fitted with R^2 values above 0.979. Test conditions used to generate the datasets limit their applicability but additional data can be collected and incorporated into the correlations. In their current form, they are still in a useful range of Mach and Reynolds numbers for hypersonic cruise applications. Flow parameters required for the correlations would be attainable from standard CFD solutions of vehicles making them usable for the CFD blending process outlined in the Introduction.

In laminar boundary layers, the primary focus of the experimental work was an investigation into boundary layer transition. Freestream Reynolds numbers, Mach numbers, and leading edge bluntnesses were altered in order to achieve a natural flat plate transition location which was in a good location for investigating geometry induced transition. Unfortunately, this was not achieved and it was determined that the overall dimensions of the model and location of the test geometry prevented a desirable transition location from occurring. During the investigation, some data was collected which gave insight into natural transition on flat plates in HDT. This is a useful result from the perspective of experimental design and will help to inform future experiments carried out in the tunnel.

Fence geometries (2D protuberances) were tested in laminar boundary layers and in some cases were seen to induce earlier transition. Heat flux data downstream of the geometry gave an indication of the possible mechanisms behind induced transition, with Görtler vortices being present downstream of 2D protuberances. Although this is not a surprising result, this is the first observation and measurement

of Görtler vortices caused by 2D protuberances rather than backward-facing steps. Higher fences induced these vortices sooner resulting in earlier transition.

A swept leading edge was also tested, which had the effect of causing earlier transition compared to the straight leading edge. This was due to the addition of crossflow which adds to the overall disturbance level in the boundary layer. The transition data collected agrees with existing correlations which describe the effect of swept leading edges. In this case, the 45° leading edge induced transition at approximately 45 % of the distance of the straight leading edge. The same flow features were observed with the swept leading edge, with Görtler vortices being present prior to transition.

Heat flux augmentation data was collected for 2D protuberances in laminar boundary layers. This data was correlated using the same method as that used for turbulent boundary layers. When compared with the turbulent dataset, a larger variety of freestream conditions, but only set of geometries, were used in the correlation development. Only a correlation for peak heat flux on forward-facing steps was created. For the swept leading edge, heat flux both on the flat plate and the forward corner of a step was seen to be consistently higher than for the straight leading edge, with a 16 % increase in baseline heat flux and a 50 % increase in heat flux on the highest step tested.

In summary, the research objectives laid out in the Introduction have all been addressed, with heat flux augmentation being explored thoroughly in both turbulent and laminar boundary layers. Boundary layer transition was difficult to control in a way which could be investigated as initially expected. However, useful data and some insightful qualitative results were collected.

7.2 Recommendations for Future Work

The work carried out in this project highlighted some areas for further study on the topic as well as some areas for possible improvement. This section outlines some recommendations for additional work.

- The heat flux augmentation correlations developed in Chapter 5 are only applicable to flow parameters and geometric scales within the dataset collected in this work. While a wide variety of different geometry types and scales were tested, the range of freestream flow conditions was limited to only three different Re_{unit} and one Mach number. This represents a small portion of the trajectory points which are relevant to a flight vehicle. For a more useful set of correlations, the dataset would cover more trajectory points. Further testing of the same experimental model at different Mach numbers and Re_{unit}, even with a more limited set of geometries, would vastly improve the applicability of the correlations for use in aircraft design.

- With minor alterations to the experimental model, 3D geometries could be investigated. Some examples of possible geometries of interest are: the corner of a stepped tile; an isolated 3D protuberance or cavity; and streamwise steps and gaps.

- There are some additional heat flux measurements which would add value to the dataset. IR measurements could be made upstream of the step by modifying the top plate to include a PEEK layer. Higher resolution heat flux measurements (both spatially and temporally) would also aid in understanding some of the mechanisms involved, especially with cavities where the flow can be unsteady. This could be achieved by using a lens with a longer focal length to achieve a higher image resolution and with locally mounted TFGs to achieve higher sample rates.

- Data from the boundary layer transition experiments did not produce the required results and was not of sufficient quality to properly investigate step induced transition. An experimental model designed differently may have performed differently to produce the desired data. However, there are several possible alterations both to the physical model and to the experimental procedure which may help in this regard. In particular, a leading edge with a precisely machined bluntness would reduce the number of unknown variables

involved in transition. IR thermography was the primary measurement used during the experiments and a large amount of good quality IR data was produced. However, the availability of good quality IR data lead to less of a focus on the other measurements resulting in greatly reduced quality of data from PCB and TFG sensors: high levels of electrical noise rendered data from these sources unusable for most of the shots carried out. Both the PCB and TFG measurements could have given useful insight into any mechanisms involved in transition given their high temporal resolution. In any future testing, more priority would be given to measurements from sensors like these, which will provide a greater understanding of step induced transition than bulk heat flux measurements alone.

- Value could be added to the experimental data by assessing the flow structure in the vicinity of the geometry element. This could be achieved by using a flow visualisation technique such as schlieren imaging, but numerical simulations could also give additional insight. Both techniques could aid in understanding some of the mechanisms behind the heat flux augmentation and separation phenomena observed during experiments.

References

[1] McClinton, C.R., Rausch, V.L., Nguyen, L.T., Sitz, J.R.: "Preliminary X-43 flight test results". Acta Astronautica, 57(2-8):266–276 (2005)

[2] Karlgaard, C.D., Tartabini, P.V., Blanchard, R.C., Kirsch, M., Toniolo, M.D.: "Hyper-X Post-Flight-Trajectory Reconstruction". Journal of Spacecraft and Rockets, 43(1):105–115 (2006)

[3] Tauber, M.E., Menees, G.P., Adelman, H.G.: "Aerothermodynamics of Transatmospheric Vehicles". Journal of Aircraft, 24(9):594–602 (1987)

[4] Curry, D.M.: "Thermal Protection Systems-Manned Spacecraft Flight Experience". NASA Conference Publication, pp. 19–19. NASA (1992)

[5] Weil, J.: "Review of the X-15 Program". Tech. Rep. TN-D-1278, NASA (1962)

[6] Bertin, J.J.: "The Effect of Protuberances, Cavities, and Angle of Attack on the Wind-Tunnel Pressure and Heat-Transfer Distribution for the Apollo Command Module". Tech. Rep. TM-X-1243, NASA (1966)

[7] Walton, T.E., Witte, W.G., O'Hare, B.J.: "Flight Investigation of the Effects of Apollo Heat-Shield Singularities on Ablator Performance". Tech. Rep. TN-D-4791, NASA (1968)

[8] Braslow, A.L.: "Analysis of boundary-layer transition on X-15-2 research airplane". Tech. Rep. TN-D-3487, NASA (1966)

[9] Viola, N., Ferretto, D., Fusaro, R., Scigliano, R.: "Performance Assessment of an Integrated Environmental Control System of Civil Hypersonic Vehicles". Aerospace, 9(4):201 (2022)

[10] Scigliano, R., De Simone, V., Marini, M., Fusaro, R., Ferretto, D., Viola, N., et al.: "Aero-thermal design of STRATOFLY MR3 hypersonic vehicle". Titolo volume non avvalorato, pp. 1–12. European Space Agency (2022)

[11] Eckert, E.: "Engineering Relations for Heat Transfer and Friction in High-Velocity Laminar and Turbulent Boundary-Layer Flow over Surfaces with Constant Pressure and Temperature". Transactions of the American Society of Mechanical Engineers, 78(6):1273–1283 (1956)

[12] on the National Aerospace Plane, U.S.D.S.B.T.F.: Report of the Defense Science Board Task Force on the National Aerospace Plane (NASP). Office of the Under Secretary of Defense for Acquisition (1988)

[13] Campbell, C., Anderson, B., Bourland, G., Bouslog, S., Cassady, A., Horvath, T., Berry, S., Gnoffo, P., Wood, W., Reuther, J., et al.: "Orbiter return to flight entry aeroheating". 9th AIAA/ASME Joint Thermophysics and Heat Transfer Conference, p. 2917 (2006)

[14] Steelant, J., Varvill, R., Walton, C., Defoort, S., Hannemann, K., Marini, M.: "Achievements obtained for sustained hypersonic flight within the LAPCAT-II project". 20th AIAA International Space Planes and Hypersonic Systems and Technologies Conference, p. 3677 (2015)

[15] Sandham, N., Van den Eynde, J.: "Outcome of high-speed boundary layer transition workshop at HiSST 2022". CEAS Space Journal, 15(6):989–991 (2023)

[16] Hoffmann, J.P., Van den Eynde, J., Steelant, J.: "An analysis tool for boundary layer and correlation-based transition onset assessment on generic geometries". CEAS Space Journal, 15(6):923–945 (2023)

[17] Jacobs, F., Steelant, J.: "Temporal Evolution of Transition Onset along Trajectories of Generic Flight Vehicles" (2023)

[18] Jacobs, F., Steelant, J.: "A Boundary Layer Analysis on the HEXAFLY-INT Experimental Flight Test Vehicle" (2024)

[19] Avery, D.E.: Aerodynamic Heating in Gaps of Thermal Protection System Tile Arrays in Laminar and Turbulent Boundary Layers, vol. 1187. National Aeronautics and Space Administration, Scientific and Technical ... (1978)

[20] Brewer, R., Saydah, A., Nestler, D., Florence, D.: "Thermal Performance Evaluation of REI Panel Gaps for Space Shuttle Orbiter.". Journal of Spacecraft and Rockets, 10(1):23–28 (1973)

[21] Dunavant, J.C., Throckmorton, D.A.: "Aerodynamic Heat Transfer to RSI Tile Surfaces and Gap Intersections". Journal of Spacecraft and Rockets, 11(6):437–440 (1974)

[22] Petley, D., Smith, D., Edwards, C., Carlson, A., Hamilton, H.: "Surface Step Induced Gap Heating in the Shuttle Thermal Protection System". Journal of Spacecraft and Rockets, 21(2):156–161 (1984)

[23] Pitts, W., Murbach, M.: "Flight Measurements of Tile Gap Heating on the Space Shuttle". 3rd Joint Thermophysics, Fluids, Plasma and Heat Transfer Conference, p. 840 (1982)

[24] Berry, S.A., Bouslog, S.A., Brauckmann, G.J., Caram, J.M.: "Shuttle Orbiter Experimental Boundary-Layer Transition Results with Isolated Roughness". Journal of Spacecraft and Rockets, 35(3):241–248 (1998)

[25] Bouslog, S., Bertin, J., Berry, S., Caram, J., Bouslog, S., Bertin, J., Berry, S., Caram, J.: "Isolated Roughness Induced Boundary-Layer Transition-Shuttle Orbiter Ground Tests and Flight Experience". 35th Aerospace Sciences Meeting and Exhibit, p. 274 (1997)

[26] Everhart, J.: "Transition Induced by Fence Geometries on Shuttle Orbiter at Mach 10". 48th AIAA Aerospace Sciences Meeting Including the New Horizons Forum and Aerospace Exposition, p. 1577 (2010)

[27] Everhart, J.: "Supersonic/Hypersonic Correlations for In-Cavity Transition and Heating Augmentation". 42nd AIAA Thermophysics Conference, p. 3480 (2011)

[28] McGinley, C., Berry, S., Kinder, G., Barnwell, M., Wang, K.C., Kirk, B.: "Review of Orbiter Flight Boundary Layer Transition Data". 9th AIAA/ASME Joint Thermophysics and Heat Transfer Conference, p. 2921 (2006)

[29] Horvath, T., Tomek, D., Splinter, S., Zalameda, J., Krasa, P., Schwartz, R., Gibson, D., Tietjen, A., Berger, K.: "The HYTHIRM Project: Flight Thermography of the Space Shuttle During Hypersonic Re-entry". 48th AIAA Aerospace Sciences Meeting Including the New Horizons Forum and Aerospace Exposition, p. 241 (2010)

[30] Horvath, T.J., Zalameda, J.N., Wood, W.A., Berry, S.A., Schwartz, R.J., Dantowitz, R.F., Spisz, T.S., Taylor, J.C.: "Global Infrared Observations of Roughness Induced Transition on the Space Shuttle Orbiter". RTO AVT-200 RSM-030 Specialists"Meeting on Hypersonic Laminar-Turbulent Transition, NF1676L-13455 (2012)

[31] Amar, A., Horvath, T., Hollis, B., Berger, K., Berry, S., Calvert, N., Calvert, N.: "Protuberance Boundary Layer Transition for Project Orion Crew Entry Vehicle". 46th AIAA Aerospace Sciences Meeting and Exhibit, p. 1227 (2008)

[32] Chang, C.L., Choudhari, M., Venkatachari, B.S., Li, F.: "Effects of Cavities and Protuberances on Transition over Hypersonic Vehicles". 41st AIAA Fluid Dynamics Conference and Exhibit, p. 3245 (2011)

[33] Hollis, B.: "Heating Augmentation in Laminar Flow Due to Heat-Shield Cavities on the Project Orion CEV". AIAA Atmospheric Flight Mechanics Conference and Exhibit, p. 6558 (2008)

[34] Berry, S.A., Horvath, T.J., Hollis, B.R., Thompson, R.A., Hamilton, H.H.: "X-33 Hypersonic Boundary-Layer Transition". Journal of Spacecraft and Rockets, 38(5):646–657 (2001)

[35] Berry, S., Daryabeigi, K., Wurster, K., Bittner, R.: "Boundary-Layer Transition on X-43A". Journal of Spacecraft and Rockets, 47(6):922–934 (2010)

[36] Steelant, J., Langener, T., Hannemann, K., Marini, M., Serre, L., Bouchez, M., Falempin, F.: "Conceptual Design of the High-Speed Propelled Experimental Flight Test Vehicle HEXAFLY". 20th AIAA international space planes and hypersonic systems and technologies conference, p. 3539 (2015)

[37] Steelant, J., Passaro, A., Fernandez Villace, V., Gubanov, A., Ivanyushkin, D., Shvalev, Y., Voevodenko, N., Marini, M., Di Benedetto, S.: "Boundary Layer Transition Assessment on a Slender High-Speed Vehicle". 21st AIAA International Space Planes and Hypersonics Technologies Conference, p. 2133 (2017)

[38] Fletcher, L., Briggs, D., Page, R.: "A Review of Heat Transfer in Separated and Reattached Flows". 3rd Fluid and Plasma Dynamics Conference, p. 767 (1970)

[39] Fletcher, L., DG, B., RH, P.: "Heat Transfer in Separated and Reattached Flows: An Annotated Review" (1974)

[40] Nestler, D.: "The Effects of Surface Discontinuities on Convective Heat Transfer in Hypersonic Flow". 20th Thermophysics Conference, p. 971 (1985)

[41] Sourgen, F., Fontaine, J., Garçon, F., Verant, J., Pelissier, C., Tribot, J.P., Hauwaert, P.V., Spel, M., Vos, J.: "Effect of steps and gaps on aerothermodynamics for the IXV hypersonic vehicle". International Journal of Aerodynamics, 2(2-4):130–151 (2012)

[42] Holloway, P.F., Sterrett, J.R., Creekmore, H.S.: An Investigation of Heat Transfer within Regions of Separated Flow at a Mach Number of 6.0. National Aeronautics and Space Administration (1965)

[43] Zukoski, E.E.: "Turbulent Boundary-Layer Separation in Front of a Forward-Facing Step.". AIAA journal, 5(10):1746–1753 (1967)

[44] Nestler, D., Saydah, A., Auxer, W.: "Heat transfer to steps and cavities in hypersonic turbulent flow.". AIAA Journal, 7(7):1368–1370 (1969)

[45] Hung, F., Patel, D.: "Protuberance Interference Heating in High-Speed Flow". 19th Thermophysics Conference, p. 1724 (1984)

[46] Rom, J., Seginer, A.: "Laminar Heat Transfer to a Two-Dimensional Backward Facing Step from the High-Enthalpy Supersonic Flow in the Shock Tube". AIAA Journal, 2(2):251–255 (1964)

[47] Rom, J., Green, M., Seginer, A.: Investigation of Heat Transfer in Base Type Supersonic Laminar and Transitional Separated Flows. Technion, Israel Inst. of Technology, Department of Aeronautical Engineering (1970)

[48] Wada, I., Inoue, Y.: "Heat transfer behind the backward facing step in the hypersonic flow". International Symposium on Space Technology and Science, 10 th, Tokyo, Japan, pp. 425–432 (1973)

[49] Jakubowski, A.K., Lewis, C.H.: "Experimental study of supersonic laminar base flow with and without suction". AIAA Journal, 11(12):1670–1677 (1973)

[50] Smith, H.E.: The flow field and heat transfer downstream of a rearward facing step in supersonic flow. Aerospace Research Laboratories, Office of Aerospace Research, United States ... (1967)

[51] Gai, S., Reynolds, N., Ross, C., Baird, J.: "Measurements of heat transfer in separated highenthalpy dissociated laminar hypersonic flow behind a step". Journal of Fluid Mechanics, 199:541–561 (1989)

[52] Gai, S., Hayne, M., Gardener, A., Morgan, R., Mee, D.: "Heat Transfer Behind A Step in High Enthalpy Super-Orbital Flow". 39th Aerospace Sciences Meeting and Exhibit, p. 509 (2001)

[53] Reddeppa, P., Nagashetty, K., Saravanan, S., Jagadeesh, G., Gai, S.: "Measurement of Heat Transfer Rate on Backward-Facing Steps at Hypersonic Mach Number". Journal of thermophysics and heat transfer, 25(3):321–328 (2011)

[54] Lamb, J.: "Convective Heat Transfer Correlations for Planar, Supersonic, Separated Flows" (1980)

[55] Kumar, C., Reddy, K.: "Experimental Investigation of Heat Fluxes in the Vicinity of Protuberances on a Flat Plate at Hypersonic Speeds". Journal of heat transfer, 135(12):121701 (2013)

[56] Estruch-Samper, D., Stollery, J., MacManus, D., Lawson, N., Garry, K.: "Hypersonic Interference Heating: A Semi-Empirical Hot Spot Predictive Approach". 16th AIAA/DLR/DGLR International Space Planes and Hypersonic Systems and Technologies Conference, p. 7444 (2009)

[57] Estruch-Samper, D.: "Reattachment heating upstream of short compression ramps in hypersonic flow". Experiments in Fluids, 57:1–17 (2016)

[58] Kumar, C.S., Singh, T., Reddy, K.: "Investigation of the separated region ahead of three-dimensional protuberances on plates and cones in hypersonic flows with laminar boundary layers". Physics of fluids, 26(12) (2014)

[59] Mazaheri, A., Wood, W.A.: "Heating Augmentation for Short Hypersonic Protuberances". Journal of Spacecraft and Rockets, 46(2):284–291 (2009)

[60] Charwat, A., Roos, J., Dewey Jr, F., Hitz, J.: "An Investigation of Separated Flows-Part I: The Pressure Field". Journal of the Aerospace Sciences, 28(6):457–470 (1961)

[61] Charwat, A., Dewey Jr, C., Roos, J., Hitz, J.: "An Investigation of Separated Flows-Part II: Flow in the Cavity and Heat Transfer". Journal of the Aerospace Sciences, 28(7):513–527 (1961)

[62] Everhart, J.L.: "Supersonic/Hypersonic Laminar Heating Correlations for Rectangular and Impact-Induced Open and Closed Cavities". Journal of spacecraft and Rockets, 46(3):545–560 (2009)

[63] Stallings Jr, R.L., Wilcox Jr, F.J., Forrest, D.K.: "Measurements of Forces, Moments, and Pressures on a Generic Store Separating from a Box Cavity at Supersonic Speeds". Tech. rep. (1991)

[64] Lamb, J.: "Analysis and Correlation of Convective Heat Transfer Measurements of Open Cavities in Supersonic Flow". 15th Thermophysics Conference, p. 1526 (1980)

[65] Everhart, J., Alter, S., Merski, R., Wood, W., Prabhu, R.: "Pressure Gradient Effects on Hypersonic Cavity Flow Heating". 44th AIAA Aerospace Sciences Meeting and Exhibit, p. 185 (2006)

[66] Everhart, J.L., Berger, K.T., Merski Jr, N., Woods, W.A., Hollingsworth, K.E., Hyatt, A., Prabhu, R.K.: "Aero-Heating of Shallow Cavities in Hypersonic Freestream Flow". Tech. rep. (2010)

[67] Everhart, J.L., Greene, F.A.: "Turbulent Supersonic/Hypersonic Heating Correlations for Open and Closed Cavities". Journal of Spacecraft and Rockets, 47(4):545–553 (2010)

[68] Hollis, B., Liechty, D.: "Boundary Layer Transition Correlations and Aeroheating Predictions for Mars Smart Lander". 32nd AIAA Fluid Dynamics Conference and Exhibit, p. 2745 (2002)

[69] Hollis, B.R., Liechty, D.S.: "Transition Due to Heat-Shield Cavities on a Mars Entry Vehicle". Journal of Spacecraft and Rockets, 43(2):354–366 (2006)

[70] Hollis, B.R., Liechty, D.S.: "Correlations for Boundary-Layer Transition on Mars Science Laboratory Entry Vehicle Due to Heat-Shield Cavities". Tech. rep. (2008)

[71] Hollis, B.: "Heating Augmentation Due to Compression Pad Cavities on the Project Orion CEV Heat Shield". 41st AIAA Thermophysics Conference, p. 3843 (2009)

[72] Hollis, B.R.: "Compression pad cavity heating augmentation on orion heat shield". Journal of thermophysics and heat transfer, 25(3):329–340 (2011)

[73] Smith, D., Petley, D., Edwards, C., Patten, A.: "An Investigation of Gap Heating Due to Stepped Tiles in Zero Pressure Gradient Regions of the Shuttle Orbiter Thermal Protection System". 21st Aerospace Sciences Meeting, p. 120 (1983)

[74] Hinderks, M., Gülhan, A., Radespiel, R.: "Simulation of Hypersonic Gap Flow with Consideration of Fluid Structure Interaction". 34th AIAA Fluid Dynamics Conference and Exhibit, p. 2238 (2004)

[75] Hinderks, M., Radespiel, R.: "Investigation of Hypersonic Gap Flow of a Reentry Nosecap with Consideration of Fluid Structure Interaction". 44th AIAA Aerospace Sciences Meeting and Exhibit, p. 188 (2006)

[76] Schäfer, R., Mack, A., Esser, B., Gülhan, A.: "Fluid-structure interaction on a generic model of a reentry vehicle nosecap" (2003)

[77] Palmer, G., Kontinos, D., Sherman, B.: "Surface Heating Effects of X-33 Vehicle Thermal-Protection-System Panel Bowing". Journal of Spacecraft and Rockets, 36(6):836–841 (1999)

[78] Schneider, S.P.: "Effects of Roughness on Hypersonic Boundary-Layer Transition". Journal of spacecraft and rockets, 45(2):193–209 (2008)

[79] Goodrich, W., Derry, S., Bertin, J.: "Shuttle Orbiter Boundary-Layer Transition - A Comparison of Flight and Wind Tunnel Data". 21st Aerospace Sciences Meeting, p. 485 (1983)

[80] Goodrich, W.D., Derry, S.M., Bertin, J.J.: "Shuttle Orbiter Boundary Layer Transition at Flight and Wind Tunnel Conditions". NASA. Langley Research Center Shuttle Performance: Lessons Learned, Pt. 2 (1983)

[81] Horvath, T., Berry, S., Merski, N., Berger, K., Buck, G., Leichty, D., Schneider, S.: "Shuttle Damage/Repair from the Perspective of Hypersonic Boundary Layer Transition - Experimental Results". 9th AIAA/ASME Joint Thermophysics and Heat Transfer Conference, p. 2919 (2006)

[82] Fedorov, A.: "Transition and Stability of High-Speed Boundary Layers". Annual review of fluid mechanics, 43:79–95 (2011)

[83] Morkovin, M.V.: "Transition in open flow systems-a reassessment". Bull. Am. Phys. Soc., 39:1882 (1994)

[84] Mack, L.M.: Boundary-Layer Stability Theory. Jet Propulsion Laboratory (1969)

[85] Saric, W.S., Reed, H.L., Kerschen, E.J.: "Boundary-Layer Receptivity to Freestream Disturbances". Annual review of fluid mechanics, 34(1):291–319 (2002)

[86] Reshotko, E.: "Transient growth: A factor in bypass transition". Physics of Fluids, 13(5):1067–1075 (2001)

[87] Reshotko, E., Tumin, A.: "Role of Transient Growth in Roughness-Induced Transition". AIAA journal, 42(4):766–770 (2004)

[88] Yam, C., Schneider, S.P., Jewell, J.S.: "Effects of Forward-and Backward-Facing Steps on BOLT at Mach 6". AIAA Scitech 2022 Forum, p. 0346 (2022)

[89] Xu, X., Yi, S., Zhang, F., Zhang, B., Liu, X.: "Influences of Steps on the Hypersonic Boundary-Layer Transition on a Cone". AIAA Journal, 59(2):439–446 (2021)

[90] Xu, X., Yi, S., Han, J., Quan, P., Zheng, W.: "Effects of steps on the hypersonic boundary layer transition over a cone at 10° angle-of-attack". Physics of Fluids, 34(3) (2022)

[91] Masutti, D., Chazot, O., Asma, C., Spinosa, E.: "Criteria Evaluation of 2D Roughness Induced Transition for EXPERT Vehicle Design". 16th AIAA/DLR/DGLR International Space Planes and Hypersonic Systems and Technologies Conference, p. 7212 (2009)

[92] Ginoux, J.J.: Laminar Separation in Supersonic and Hypersonic Flows. Von Karman Institute for Fluid Dynamics (1966)

[93] Ginoux, J.J.: "On Some Properties of Reattaching Laminar and Transitional High Speed Flows.". Tech. rep., Von Karman Institute for Fluid Dynamics (1969)

[94] Masutti, D.: "Ground Testing Investigation of Hypersonic Transition Phenomena for a Re-entry Vehicle" (2013)

[95] Holloway, P.F., Sterrett, J.R.: "Effect of Controlled Surface Roughness on Boundary-Layer Transition and Heat Transfer at Mach Numbers of 4.8 and 6.0". Tech. rep. (1964)

[96] Fujii, K.: "Experiment of the Two-Dimensional Roughness Effect on Hypersonic Boundary-Layer Transition". Journal of Spacecraft and Rockets, 43(4):731–738 (2006)

[97] Duan, L., Wang, X., Zhong, X.: "Stabilization of a Mach 5.92 Boundary Layer by Two-Dimensional Finite-Height Roughness". AIAA journal, 51(1):266–270 (2013)

[98] Fong, K.D., Wang, X., Zhong, X.: "Stabilization of Hypersonic Boundary Layer Waves using 2-D Surface Roughness". 43rd AIAA Fluid Dynamics Conference, p. 2985 (2013)

[99] Fong, K.D., Wang, X., Zhong, X.: "Parametric Study on Stabilization of Hypersonic Boundary Layer Waves using 2-D Surface Roughness". 53rd AIAA Aerospace Sciences Meeting, p. 0837 (2015)

[100] Tang, Q., Zhu, Y., Chen, X., Lee, C.: "Development of second-mode instability in a Mach 6 flat plate boundary layer with two-dimensional roughness". Physics of Fluids, 27(6) (2015)

[101] Wheaton, B.M., Berridge, D.C., Wolf, T.D., Stevens, R.T., McGrath, B.E.: "Boundary Layer Transition (BOLT) Flight Experiment Overview". 2018 Fluid Dynamics Conference, p. 2892 (2018)

[102] Berry, S.A., Wheaton, B.M., Chynoweth, B.C.: "Secondary Side Considerations for Boundary Layer Transition Flight Experiment". Journal of Spacecraft and Rockets, 58(1):18–25 (2021)

[103] Chynoweth, B.C., Schneider, S.P., Wheaton, B.M.: "Transition Measurements with Forward and Aft Facing Steps on the BOLT Geometry at Mach 6". AIAA Scitech 2020 Forum, p. 1560 (2020)

[104] Wheaton, B.M., Berridge, D.C., Wolf, T.D., Araya, D.B., Stevens, R.T., McGrath, B.E., Kemp, B.L., Adamczak, D.W.: "Final Design of the Boundary Layer Transition (BOLT) Flight Experiment". Journal of Spacecraft and Rockets, 58(1):6–17 (2021)

[105] Melcher, J.T., Radcliffe, E.J., Butler, C., Wheaton, B.M.: "Effects of Aeroelasticity on Flight Dynamics in the Boundary Layer Transition (BOLT) Experiment". AIAA Aviation 2022 Forum, p. 3748 (2022)

[106] Berridge, D.C., McKiernan, G., Wadhams, T.P., Holden, M., Wheaton, B.M., Wolf, T.D., Schneider, S.P.: "Hypersonic Ground Tests In Support of the Boundary Layer Transition (BOLT) Flight Experiment". 2018 Fluid Dynamics Conference, p. 2893 (2018)

[107] Berry, S.A., Semper, M.T., Riha, A.K., Mullen, C.D., Reed, H.L., Dufrene, A.T., Fasel, H.F.: "Development of the BOLT II Roughness Experiment for Flight". Journal of Spacecraft and Rockets, 61(5):1362–1374 (2024)

[108] Anderson, B., Campbell, C., Saucedo, L., Kinder, G., Berger, K.: "Boundary Layer Transition Flight Experiment Overview and In-Situ Measurements". 48th AIAA Aerospace Sciences Meeting Including the New Horizons Forum and Aerospace Exposition, p. 240 (2010)

[109] Berger, K., Anderson, B., Campbell, C., Garske, M., Saucedo, L., Kinder, G., Micklos, A.: "Boundary Layer Transition Flight Experiment Overview". 42nd AIAA Thermophysics Conference, p. 3323 (2011)

[110] Charbonnier, J.M., Boerrigter, H.: "Contribution to the Study of Gap Induced Boundary Layer Transition in Hypersonic Flow". 5th International Aerospace Planes and Hypersonics Technologies Conference, p. 5111 (1993)

[111] Schiller, L.: "Strömung in Rohren. Handbuch der Experimentalphysik, herausgegeben von W. Wien und F. Harms" (1932)

[112] Reda, D.C.: "Correlation of Nosetip Boundary-Layer Transition Data Measured in Ballistics-Range Experiments". AIAA Journal, 19(3):329–339 (1981)

[113] Dirling, JR, R., Swain, C., Stokes, T.: "The Effect of Transition and Boundary Layer Development on Hypersonic Reentry Shape Change". 10th Thermophysics Conference, p. 673 (1975)

[114] Berry, S.A., Horvath, T.J.: "Discrete-Roughness Transition for Hypersonic Flight Vehicles". Journal of Spacecraft and Rockets, 45(2):216–227 (2008)

[115] Reda, D.C.: "Review and Synthesis of Roughness-Dominated Transition Correlations for Reentry Applications". Journal of spacecraft and rockets, 39(2):161–167 (2002)

[116] Passaro, A., Baccarella, D.: "Roughness Induced Transition in Hypersonic Regime over a Flat Plate". 17th AIAA International Space Planes and Hypersonic Systems and Technologies Conference, p. 2375 (2011)

[117] Passaro, A., Cifali, G.: "Experimental Characterization of Roughness-Induced Transition on a Flat Plate at Mach 6 in the European ATLLAS-2 Programme". 8th Aerothermodynamics Symposium, pp. 2–6 (2015)

[118] Bertin, J.J., Stetson, K.F., Bouslog, S.A., Caram, J.M.: "Effect of Isolated Roughness Elements on Boundary-Layer Transition for Shuttle Orbiter". Journal of spacecraft and rockets, 34(4):426–436 (1997)

[119] Anderson, A.D.: "Passive Nosetip Technology (PANT) Program, Interim Report, Volume X, Appendix A: Boundary Layer Transition on Nosetips with Rough Surfaces". Tech. Rep. TR-74-86, SAMSO (1975)

[120] Van Driest, E., Blumer, C.: "Boundary-Layer Transition at Supersonic Speeds - Three-Dimensional Roughness Effects (Spheres)". Journal of the Aerospace Sciences, 29(8):909–916 (1962)

[121] Schrijer, F., Scarano, F., Van Oudheusden, B., Bannink, W.: "Experiments on Hypersonic Roughness Induced Transition by means of Infrared Thermography". Proceedings of the Fifth European Symposium on Aerothermodynamics for Space Vehicles (ESA SP-563). 8-11 November 2004, Cologne, Germany. Editor: D. Danesy., p. 255, vol. 563, p. 255 (2005)

[122] Tirtey, S., Walpot, L., Chazot, O.: "Characterization of Hypersonic Roughness Induced Transition for the EXPERT Flight Experiment". 16th AIAA/DLR/DGLR International Space Planes and Hypersonic Systems and Technologies Conference, p. 7215 (2009)

[123] Potter, J.L., Whitfield, J.D.: "Effects of slight nose bluntness and roughness on boundary-layer transition in supersonic flows". Journal of Fluid Mechanics, 12(4):501–535 (1962)

[124] King, R.A., Kegerise, M.A., Berry, S.A.: "Version 2 of the Protuberance Correlations for the Shuttle-Orbiter Boundary Layer Transition Tool". Tech. Rep. TP-2009-215951, NASA (2009)

[125] Reshotko, E.: "Is Re_ϑ/M_e a Meaningful Transition Criterion?". AIAA journal, 45(7):1441–1443 (2007)

[126] Van Driest, E., Blumer, C., Wells Jr, C.: "Boundary-Layer Transition on Blunt Bodies - Effect of Roughness.". AIAA Journal, 5(10):1913–1915 (1967)

[127] Wool, M.R.: "Final Summary Report Passive Nosetip Technology (PANT) Program". Tech. Rep. TR-75-250, SAMSO (1975)

[128] McGilvray, M., Doherty, L.J., Neely, A.J., Pearce, R., Ireland, P.: "The oxford high density tunnel". 20th AIAA international space planes and hypersonic systems and technologies conference, p. 3548 (2015)

[129] Wylie, S., Doherty, L., McGilvray, M.: "Commissioning of the Oxford High Density Tunnel (HDT) for Boundary Layer Stability Measurements at Mach 7". 2018 Fluid Dynamics Conference, p. 3074 (2018)

[130] Hillyer, J., Doherty, L., Hambidge, C., McGilvray, M.: "Extension of Test Time in Ludwieg Tunnels". Second International Conference on Flight Vehicles, Aerothermodynamics and Re-Entry Missions and Engineering, FAR, Heilbronn, Germany. European Space Agency (2022)

[131] Hillyer, J., Doherty, L., Hambidge, C., McGilvray, M.: "Enhancing the Test Time Performance of Ludwieg Tunnels". AIAA SCITECH 2024 Forum, p. 2754 (2024)

[132] Jones, T.V., Schultz, D.L., Hendley, A.D.: "On the Flow in an Isentropic Light Piston Tunnel" (1973). ARC 34217, HYP 933

[133] Oldfield, M.L.G., Jones, T.V., Schultz, D.L.: "A Ludwieg Tube with Isentropic Compression Heating" (1973). ARC 34255, HYP 935

[134] East, R.A., Qasrawi, A.M.S.: "A Long Isentropic Free Piston Hypersonic Wind Tunnel" (1978)

[135] Purple, A.D.: "On the Operation and Performance of a Ludwieg Tube With Isentropic Compression Heating at Syracuse University". AIAA 25th Aerospace Sciences Meeting. AIAA, Reno, Nevada (1987)

[136] Magari, P.J., LaGraff, J.E.: "An isentropic compression-heated Ludweig tube transient wind tunnel". Experimental thermal and fluid science, 4(3):317–332 (1991)

[137] Buttsworth, D.R.: "Ludwieg Tunnel Facility with Free Piston Compression Heating for Supersonic and Hypersonic Testing". Proceedings of the 9th Australian Space Science Conference. University of Southern Queensland (2010)

[138] Swann, P., Buttsworth, D., Jahn, I.H., Frith, R., Moran, J., Webb, A., Noller, L.: "Reconfiguring the TUSQ Hypersonic Facility for Lower Mach Number". AIAA AVIATION FORUM AND ASCEND 2024, p. 4198 (2024)

[139] Moran, J., Buttsworth, D.R., Noller, L.: "Mach 6 and Mach 7 conditions in TUSQ at Reynolds numbers up to 30 million". AIAA AVIATION FORUM AND ASCEND 2024, p. 4197 (2024)

[140] Buttsworth, D.: "Gun Tunnels". Experimental Methods of Shock Wave Research, pp. 381–396. Springer (2015)

[141] Chen, F.J., Malik, M., Beckwith, I.: "Boundary-Layer Transition on a Cone and Flat Plate at Mach 3.5". AIAA journal, 27(6):687–693 (1989)

[142] Baehr, H.D., Stephan, K.: Heat and Mass Transfer. Springer, Berlin, Heidelberg (2006)

[143] Naved, I., Hermann, T., McGilvray, M., Ewenz Rocher, M., Hambidge, C., Doherty, L., Le Page, L., Grossman, M., Vandeperre, L.: "Heat Transfer Measurements of a Transpiration-Cooled Stagnation Point in Transient Hypersonic Flow". Journal of Thermophysics and Heat Transfer, 37(2):296–308 (2023)

[144] Naved, I., Hermann, T., Hambidge, C., Saad Ifti, H., Falsetti, C., McGilvray, M., Tirichenko, I.S., Vandeperre, L.: "Transpiration-Cooling Heat Transfer Experiments in Laminar and Turbulent Hypersonic Flows". Journal of Thermophysics and Heat Transfer, 37(2):281–295 (2023)

[145] Astarita, T., Carlomagno, G.M.: Infrared Thermography for Thermo-Fluid-Dynamics. Springer Science & Business Media (2012)

[146] Zaccara, M., Edelman, J.B., Cardone, G.: "A general procedure for infrared thermography heat transfer measurements in hypersonic wind tunnels". International Journal of Heat and Mass Transfer, 163:120419 (2020)

[147] Ochs, M., Horbach, T., Schulz, A., Koch, R., Bauer, H.: "A novel calibration method for an infrared thermography system applied to heat transfer experiments". Measurement Science and Technology, 20(7):075103 (2009)

[148] Zahoor, S.: (2024). Private Communication

[149] "Spectroscopy of Atmospheric Gases" (2023). URL `https://spectra.iao.ru/home`

[150] Mikhailenko, S., Babikov, Y.L., Golovko, V.: "Information-calculating system Spectroscopy of Atmospheric Gases. The structure and main functions". Atmos. Oceanic Opt., 18:685–695 (2005)

[151] Hetnarski, R.B., et al.: Encyclopedia of Thermal Stresses. Springer Netherlands Dordrecht (2014)

[152] Schultz, D.L., Jones, T., et al.: "Heat-transfer measurements in short-duration hypersonic facilities". AGARD (1973)

[153] Oldfield, M.: "Impulse Response Processing of Transient Heat Transfer Gauge Signals". Journal of Turbomachinery (2008)

[154] Leontiev, A., Lushchik, V., Makarova, M., Popovich, S.: "Temperature Recovery Factor in a Compressible Turbulent Boundary Layer". High Temperature, 60(3):409–431 (2022)

[155] Coleman, H.W., Steele, W.G.: Experimentation, Validation, and Uncertainty Analysis for E ngineers. John Wiley & Sons (2018)

[156] Welch, P.: "The use of fast Fourier transform for the estimation of power spectra: a method based on time averaging over short, modified periodograms". IEEE Transactions on audio and electroacoustics, 15(2):70–73 (1967)

[157] Hermann, T., McGilvray, M., Hambidge, C., Doherty, L., Buttsworth, D.: "Total temperature measurements in the oxford high density tunnel". International conference on flight vehicles, aerothermodynamics and re-entry missions and engineering, FAR, Monopoli, Italy (2019)

[158] Bustard, A.: "The Development of a Model-Alignment Probe for the Oxford High Density Tunnel" (2096). Master's Thesis

[159] White, F.M., Majdalani, J.: Viscous Fluid Flow, vol. 3. McGraw-Hill New York (2006)

[160] Qiao, L., Bai, J.Q., Xu, J.K., Xu, J.L., Zhang, Y.: "Modeling of supersonic/hypersonic boundary layer transition using a single-point approach". International Journal of Nonlinear Sciences and Numerical Simulation, 19(3-4):263–274 (2018)

[161] Reshotko, E., Tucker, M.: "Approximate Calculation of the Compressible Turbulent Boundary Layer with Heat Transfer and Arbitrary Pressure Gradient". Tech. rep. (1957)

[162] Huang, P., Bradshaw, P., Coakley, T.: "Skin Friction and Velocity Profile Family for Compressible Turbulent Boundary Layers". AIAA journal, 31(9):1600–1604 (1993)

[163] Roy, C.J., Blottner, F.G.: "Review and assessment of turbulence models for hypersonic flows". Progress in aerospace sciences, 42(7-8):469–530 (2006)

[164] Van Driest, E.R.: The Problem of Aerodynamic Heating. Institute of the Aeronautical Sciences Los Angeles (1956)

[165] Buttsworth, D.: "Nitrous oxide decomposition for supersonic combustion experiments in the USQ Ludwieg tube facility". Proceedings of the Australian Combustion Symposium (ACS 2009), pp. 1–4. University of Queensland (2009)

[166] McGrath, D.: "Developing the Light Isentropic Compression Heating Mode for the Oxford High Density Tunnel" (2016). Master's Thesis

[167] Taylor, C.F.: "The Internal Combustion Engine in Theory and Practice, Volume I" (1985)

[168] Bergman, T.L., Incropera, F.P., Dewitt, D.P., Lavine, A.S.: Fundamentals of heat and mass transfer. John Wiley & Sons (2011)

[169] Keyes, F.G.: "A Summary of Viscosity and Heat-Conduction Data for He, A, H_2, O_2, N_2, CO, CO_2, H_2O, and Air". Transactions of the American Society of Mechanical Engineers, 73(5):589–595 (1951)

[170] Laderman, A.: "Review of Wind-Tunnel Freestream Pressure Fluctuations". AIAA Journal, 15(4):605–608 (1977)

[171] Birch, B., Choudhury, R., Stern, N., Buttsworth, D.: "Pressure Fluctuations in a Hypersonic Ludwieg Tube with Free Piston Compression Heating". 22nd AIAA International Space Planes and Hypersonics Systems and Technologies Conference, p. 5266 (2018)

[172] Masutti, D., Spinosa, E., Chazot, O., Carbonaro, M.: "Disturbance Level Characterization of a Hypersonic Blowdown Facility". AIAA journal, 50(12):2720–2730 (2012)

[173] Ali, S.R., Wu, J., Radespiel, R., Schilden, T., Schroeder, W.: "High-Frequency Measurements of Acoustic and Entropy Disturbances in a Hypersonic Wind Tunnel". 44th AIAA Fluid Dynamics Conference, p. 2644 (2014)

[174] Steen, L.C.E.: "Characterization and Development of Nozzles for a Hypersonic Quiet Wind Tunnel". Ph. D. Thesis (2010)

[175] Lafferty, J., Norris, J.: "Measurements of Fluctuating Pitot Pressure," Tunnel Noise," in the AEDC Hypervelocity Wind Tunnel No. 9". 2007 US Air Force T&E Days, p. 1678 (2007)

[176] Guizar-Sicairos, M., Thurman, S.T., Fienup, J.R.: "Efficient subpixel image registration algorithms". Optics letters, 33(2):156–158 (2008)

[177] Akima, H.: "A New Method of Interpolation and Smooth Curve Fitting Based on Local Procedures". Journal of the ACM (JACM), 17(4):589–602 (1970)

[178] Stetson, K.F.: "Hypersonic Boundary-Layer Transition". Advances in Hypersonics: Defining the Hypersonic Environment Volume 1, pp. 324–417. Springer (1992)

[179] Simeonides, G.: "Laminar-Turbulent Transition Correlations in Supersonic/Hypersonic Flat Plate Flow". 24th International Congress of the Aeronautical Sciences, vol. 29 (2004)

[180] Deem, R., Murphy, J.: "Flat Plate Boundary Layer Transition at Hypersonic Speeds". 2nd aerospace sciences meeting, p. 128 (1965)

[181] "Knife Grinders - Sharpness Chart". `http://knifegrinders.com.au/Manuals/Sharpness_Chart.pdf`. Accessed: 2024-05-13

[182] Hedley, T.B., Keffer, J.F.: "Turbulent/non-turbulent decisions in an intermittent flow". Journal of Fluid Mechanics, 64(4):625–644 (1974)

[183] Saric, W.S.: "Görtler Vortices". Annual Review of Fluid Mechanics, 26(1):379–409 (1994)

[184] Lu, X., Yi, S., He, L., Liu, X., Niu, H.: "Experimental Investigation of the Hypersonic Boundary Layer Transition on a 45 Swept Flat Plate". Fluid Dynamics, 55(1):111–120 (2020)

[185] Bowcutt, K.G., Anderson, J.D., Capriotti, D.: "Viscous Optimized Hypersonic Waveriders". 25th AIAA Aerospace Sciences Meeting, p. 272 (1987)

Appendices

A
De-Risk Experiments

Prior to the experimental work presented in the main body of this work, a de-risk experimental campaign was undertaken. The experimental setup and some results are summarised in this Appendix.

A.1 Experimental Model

A.1.1 Mechanical Design

A smaller version of the flat plate model used in the main body of work was used in the de-risk experiments. An exploded CAD view of the top plate is shown in Figure A.1.

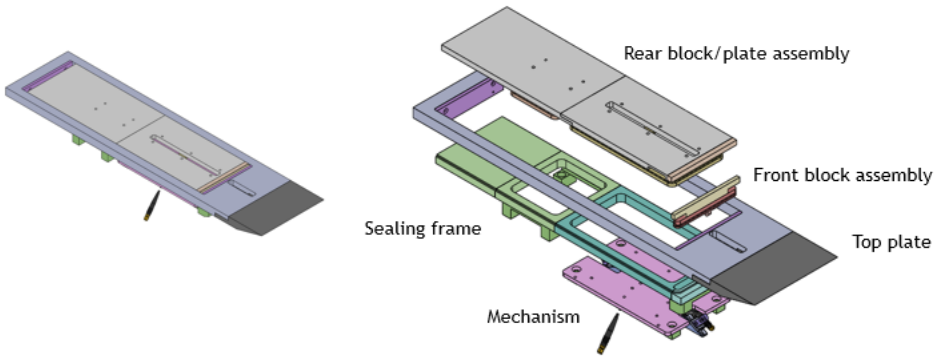

Figure A.1: Exploded view of the de-risk model.

The model featured the same overall design as the new model, with two individually actuated blocks. However, the mechanism for the rear plate was very unstable and it was not possible to move it remotely between tests. Additionally, the rear plate vibrated severely during shots. For these reasons, the rear plate was fixed at a height of 0 mm and only the front block was altered for this campaign.

A.1.2 Instrumentation

The de-risk model used largely similar instrumentation as the new model. However, IR thermography development was in its infancy at the time so heat flux measurements relied on TFGs. The same upstream array was used as that used in the new model. For the downstream array, 24 individually housed gauges were mounted in a 3D printed support.

A.2 Experimental Setup

A.2.1 Facility

The Oxford High Density Tunnel (HDT) was used and operated in Ludwieg mode. The nominal freestream condition used is outlined in Table A.1 - the required instrumentation to measure Mach number and total temperature was not used so these values are estimated based on historical data. This condition produced a laminar boundary layer as far as the most downstream TFG at $x = 275$ mm.

Table A.1: A summary of the test conditions used for testing in turbulent boundary layers.

Mach number	p_0 [bar]	T_0 [K]	Re_{unit} [10^6/m]	# of tests
6	38.5	450	34.4	9

A.2.2 Model Configurations

As stated above, only the front block was adjusted during the campaign. This resulted in only fence and cavity geometries being tested. Table A.2 shows the heights tested.

Table A.2: Range of geometries tested

Geometry	Size mm
Flat plate	-
Step	0.50
	0.75
	1.00
	1.28
Cavity	0.5
	1.00
	2.00

A.3 Results

Results take the form of heat flux and surface pressure fluctuation measurements.

A.3.1 Surface Heat Flux

Figures A.2a and A.2b show the Stanton number distributions along the length of the model for steps and cavities, respectively. Also plotted are the van Driest and Eckert estimates for flat plate laminar and turbulent heating [164, 11]. The heat flux far upstream of the step location follows the laminar flat plate correlations closely, indicating that the boundary layer upstream of the step is laminar in every test.

The presence of a step causes a decrease in heat flux upstream of the step, with the magnitude of this decrease increasing with larger steps. This is consistent with the literature [42] and the limited laminar data from the new experiments. Downstream of the step, there is a consistent increase in heat flux. It is unclear whether this is due to reattachment of the boundary layer following separation or the beginning of boundary layer transition. However, at step heights of 1 mm and 1.28 mm the heat flux approaches the predicted turbulent level.

Cavities appear to have very little effect on heat flux compared to steps of similar sizes. There is no apparent difference between flat plate heat flux data and cavities of any size tested. Any differences are more likely due to variation of tunnel conditions between shots, due to similar difference upstream of the cavity.

In the heat flux data downstream of the step there is a large amount of scatter between adjacent gauges. This is most likely due to very slight differences in how the gauges were mounted into the plate. This theory is supported by the coherence of the scatter of different cavity depths in Fig. A.2b. Some gauges were recessed while some protruded from the surface, whereas the gauges upstream of the step were painted onto a single piece of Macor. Although the differences in the heights of the gauges were small (<50 µm), the effect on heat flux is apparently significant. Additionally, flow disturbances originating from upstream gauges would have caused more scatter and uncertainty in downstream gauges.

A.3.2 Surface Pressure Fluctuations

Surface pressure fluctuations were captured using PCB132 pressure transducers. Figure A.3 shows the summary of the pressure fluctuation data, displayed PSDs as described in Section 3.3.3. Each plot shows the spectra for a single test at a single step height or cavity depth. The gauges are numbered 1 to 8, in increasing distance from the leading edge. Gauge 1 is upstream of the step and gauges 2 to 7 are all downstream.

These plots show the frequency composition of pressure fluctuations in the boundary layer and serve two purposes: they can give an indication of what disturbance may be present and if there is a specific disturbance causing transition; and they can show whether or not the boundary layer is laminar or turbulent.

For the flat plate and steps (Figures A.3a to A.3d), there is always some evidence of turbulent growth towards the rear of the plate, with the last gauge/s showing more energetic fluctuations than the upstream gauges (which are assumed to be laminar based on heat flux measurements). This turbulent growth generally appears as a broadband increase, suggesting that there is no particular disturbance/frequency which ultimately leads to turbulence. In the two larger steps there appears to be a coherent peak at around 110 kHz upstream of the step, suggesting a particular flow feature is forming upstream of the step. The trend for larger steps is that the location of full turbulence moves upstream, although the 0.50 mm step appears to have little

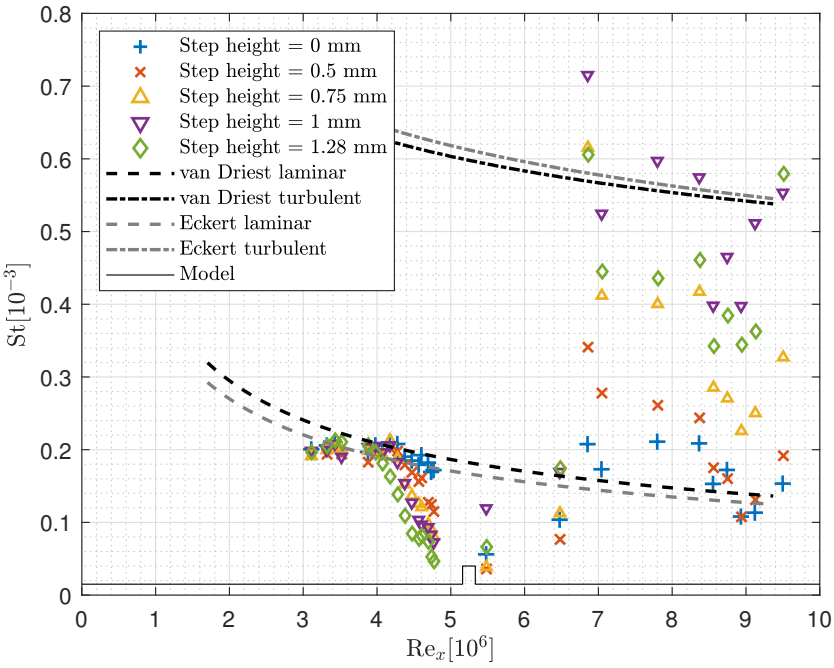

(a) Steps

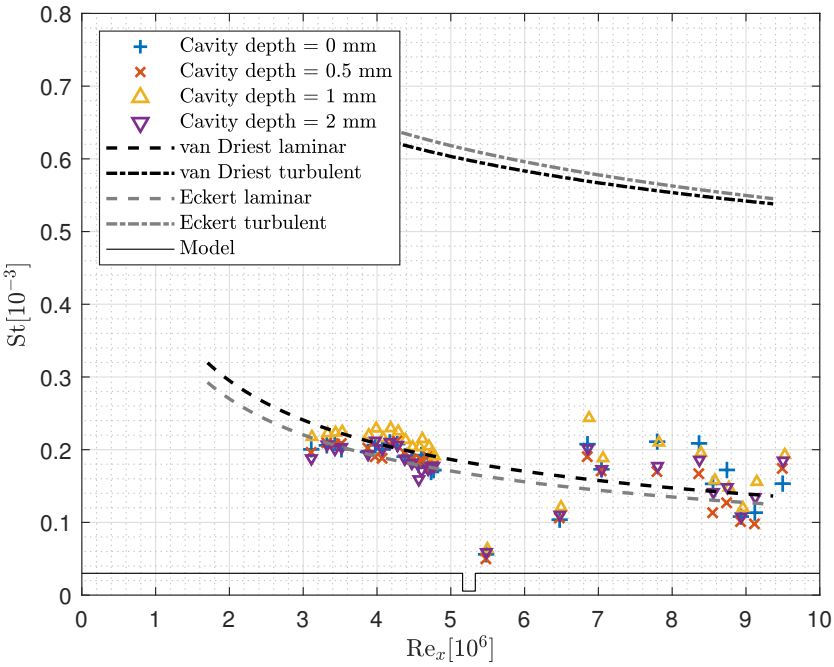

(b) Cavities

Figure A.2: Stanton number vs Reynolds number plots for all the geometries tested, compared to laminar and turbulent flat plate correlations. The location of the step/cavity is shown at the bottom of each plot.

effect. In fact, it is possible that some disturbances may even be damped compared with the flat plate. This could possibly be explained by a study by Fong [99] which found that a small protuberance can sometimes dampen a second mode disturbance.

As with heat flux, cavities have a much smaller influence on pressure fluctuations than fences. In Figures A.3e and A.3f there is even an apparent stabilising effect with cavities: gauges 7 and 8 are at a lower level compared with the flat plate. It is unclear why this is the case. Only data for the 0.50 mm and the 2.00 mm cavities are shown as some of the gauges in the 1.00 mm test experienced large non-flow disturbances which highly affected the PSDs.

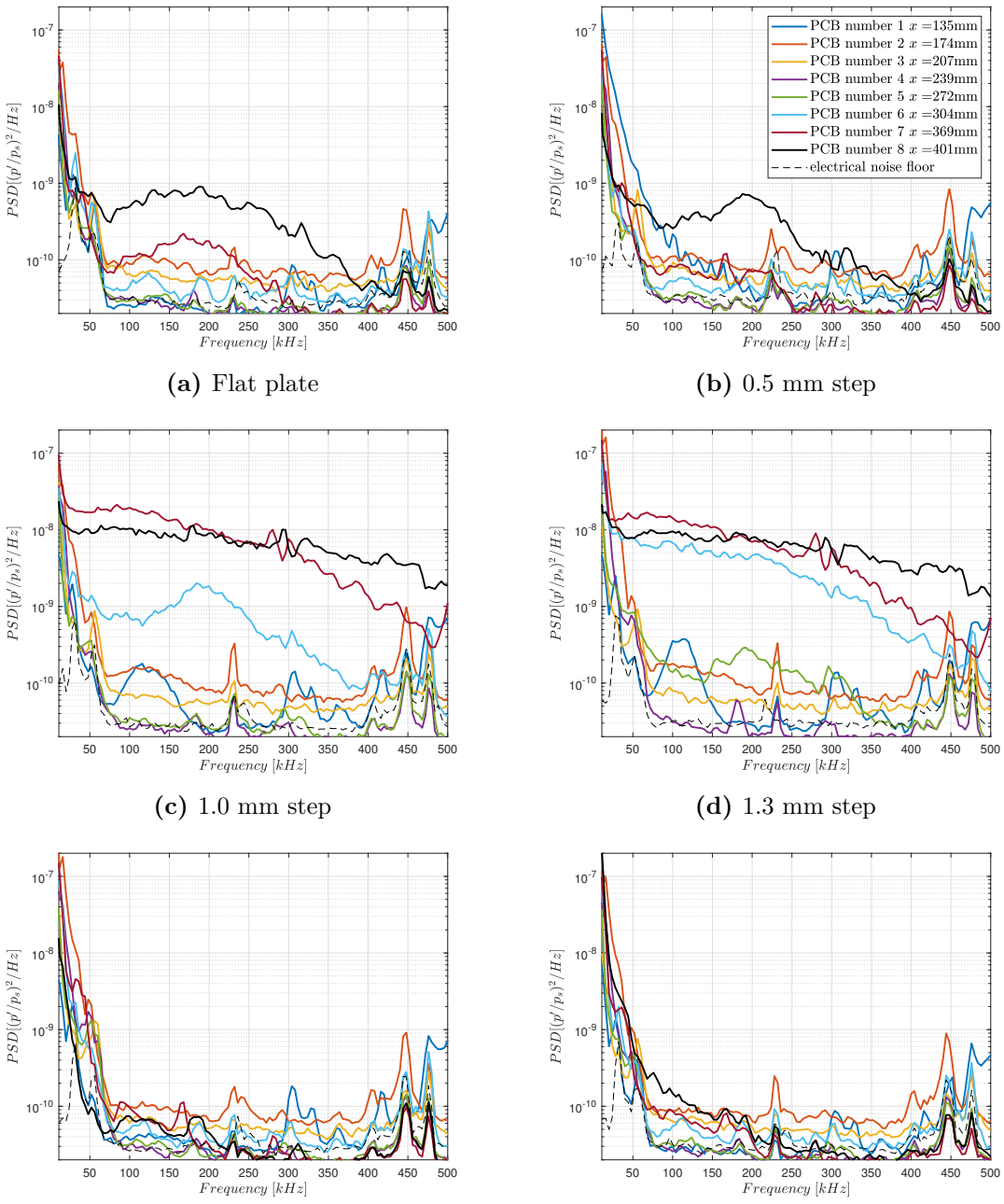

(a) Flat plate

(b) 0.5 mm step

(c) 1.0 mm step

(d) 1.3 mm step

(e) 0.5 mm cavity

(f) 2 mm cavity

Figure A.3: Power spectra of surface pressure fluctuations for different geometries.

B

Deem & Murphy's Method for Estimating Transition

Deem & Murphy [180] proposed that the effect of leading edge bluntness on flat plate transition can be described by three distinct behaviours. This is illustrated in Figure B.1.

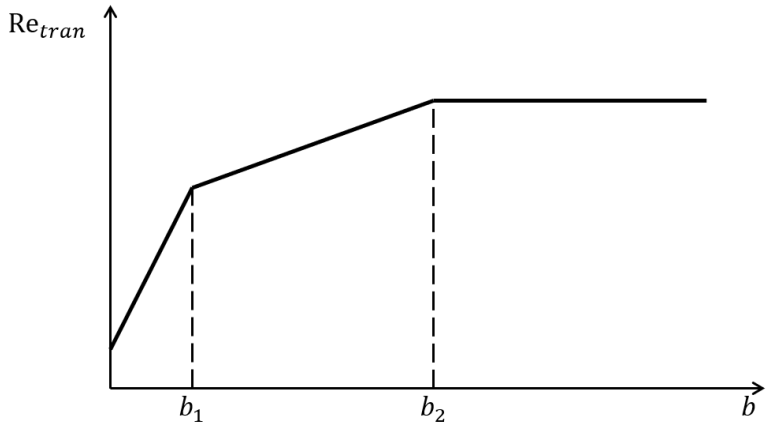

Figure B.1: Effect of leading edge bluntness, b, on transition Reynolds number, Re_{tran}.

In the first regime, where $b < b_1$, transition is strongly dependent on the bluntess. For $b_1 < b < b_2$, the dependence is weaker. Finally, when the bluntness becomes large enough, $b > b_2$, the transition location is independent of the leading edge bluntness.

The thesholds b_1 and b_2 are calculated using the following equations:

$$b_1 = \frac{2.545}{3}\left(1 - \frac{Y_c}{\delta}\right)\left[\frac{1.73}{M^2}\frac{T_w}{T} + 0.1328 + \frac{4.27}{M^2}\right]M^2 ... \\ \sqrt{\left(\frac{T_w}{T}\right)^{1/2}\left(\frac{T + 110.3}{T_w + 110.36}\right)}\frac{\mathrm{Re}_{tran}^{1/2}}{\mathrm{Re}_{unit}} \quad \text{(B.1)}$$

Where the ratio $Y_c/\delta = 0.848, 0.892, 0.908$ for $M = 5, 6, 7$.

$$b_2 = 2.545\left[\frac{1.73}{M^2}\frac{T_w}{T_n} + 0.1328\frac{4.27}{M_n^2}\right]M_n^2 ... \\ \sqrt{\left(\frac{T_w}{T_n}\right)^{22}\left(\frac{T_n + 110.3}{T_w + 110.36}\right)}\frac{\mathrm{Re}_{tran}^{1/2}\left[\frac{\mathrm{Re}_n}{\mathrm{Re}_{unit}}\right]^{1/2}}{\mathrm{Re}_{unit}\left[\frac{\mathrm{Re}_n}{\mathrm{Re}_{unit}}\right]} \quad \text{(B.2)}$$

Where

$$\frac{\mathrm{Re}_n}{\mathrm{Re}_{unit}} = \left[\frac{1 + 0.2M_n^2}{1 + 0.2M^2}\right]^2 \frac{M_n}{M}\left[\frac{\frac{T_0}{1+0.2M_n^2} + 110.3}{\frac{T_0}{1+0.2M^2} + 110.3}\right] \quad \text{(B.3)}$$

and

$$M_n = \left[5\left\{\left(\frac{6}{7M^2 - 1}\right)^{5/2}\left(\frac{6M^2\left(M^2 + 5\right)}{5\left(M^2 + 5\right)}\right)^{7/2}\right\}^{2/7} - 5\right]^{1/2} \quad \text{(B.4)}$$

Once the bluntness thresholds are calculated, transition can be estimated using the following:

$$\log_{10}\mathrm{Re}_{tran} = c_1 + 0.4\log_{10}\frac{\mathrm{Re}_{unit}}{39.37} \quad \text{(B.5)}$$

Where the constant, c_1, depends on the bluntness regime. For $b < b_1$

$$c_1 = \log_{10}\left\{\left[10^6 + 0.36 \times 10^6\left(M - 3\right)^{3/2}\right] ... \right. \\ \left.\left[1 + \frac{\mathrm{Re}_{unit}}{\mathrm{Re}_n}\frac{b}{b_1}\frac{10^6 + 0.36 \times 10^6\left(M_n - 3\right)^{3/2}}{10^6 + 0.36 \times 10^6\left(M - 3\right)^{3/2}} - \frac{b}{b_1}\right]\right\} - 2.19 \quad \text{(B.6)}$$

For $b_1 < b < b_2$

$$c_1 = \log_{10}\left\{\left[10^6 + 0.36\times10^6\left(M_n - 3\right)^{3/2}\right]\frac{\mathrm{Re}_{unit}}{\mathrm{Re}_n}\ldots \left[1 + \frac{b-b_1}{b_2-b_1}\frac{10^6 + 0.36\times10^6\left(M_3\right)^{3/2}}{10^6 + 0.36\times10^6\left(M_n - 3\right)^{3/2}} - \frac{b-b_1}{b_2-b_1}\right]\right\} - 2.19 \quad \text{(B.7)}$$

Finally, for $b_2 < b$

$$c_1 = \log_{10}\left\{10^6 + 0.36\times10^6\left(M - 3\right)^{3/2}\right\} - 2.19 \quad \text{(B.8)}$$

In order to predict transition using this method, firstly an estimate for Re_{tran} must be made. The bluntness regime is calculated, followed by the corresponding constant c_1. A new estimate for Re_{tran} is then calculated using Equation B.5. The process is iterated until convergence of Re_{tran}.